ISTANBUL TECHNICAL UNIVERSITY ★ GRADUATE SCHOOL

DESIGN AND PRODUCTION OF BIOMASS-DERIVED ANODE ACTIVE MATERIALS FOR LITHIUM ION BATTERIES

Ph.D. THESIS

İpek TUNÇ

Department of Metallurgical and Materials Engineering

Metallurgical and Materials Engineering Programme

DECEMBER 2024

ISTANBUL TECHNICAL UNIVERSITY ★ GRADUATE SCHOOL

DESIGN AND PRODUCTION OF BIOMASS-DERIVED ANODE ACTIVE MATERIALS FOR LITHIUM ION BATTERIES

Ph.D. THESIS

İpek TUNÇ
(506172411)

Department of Metallurgical and Materials Engineering

Metallurgical and Materials Engineering Programme

Thesis advisor: Prof. Dr. Özgül KELEŞ

DECEMBER 2024

İSTANBUL TEKNİK ÜNİVERSİTESİ ★LİSANSÜSTÜ EĞİTİM ENSTİTÜSÜ

LİTYUM İYON BATARYALAR İÇİN ORGANİK ATIKLARDAN ANOT AKTİF MALZEME TASARIMI VE ÜRETİMİ

DOKTORA TEZİ

İpek TUNÇ
(506172411)

Metalurji ve Malzeme Mühendisliği Anabilim Dalı

Metalurji ve Malzeme Mühendisliği Programı

Tez Danışmanı: Prof. Dr. Özgül KELEŞ

ARALIK 2024

İpek TUNÇ, a Ph.D. student of ITU Graduate School student ID 506172411, successfully defended the dissertation entitled "DESIGN AND PRODUCTION OF BIOMASS-DERIVED ANODE ACTIVE MATERIALS FOR LITHIUM ION BATTERIES", which she prepared after fulfilling the requirements specified in the associated legislations, before the jury whose signatures are below.

Thesis Advisor : **Prof. Dr. Özgül KELEŞ** .....
Istanbul Technical University

Jury Members : **Assoc. Prof. Dr. Billur Deniz KARAHAN** .....
Istanbul Technical University

Prof. Dr. Nilgün KARATEPE YAVUZ .....
Istanbul Technical University

Prof. Dr. Selmiye ALKAN GÜRSEL .....
Sabancı University

Prof. Dr. Ömer Suat TAŞKIN .....
Istanbul University

Date of Submission : 02 December 2024
Date of Defense : 24 December 2024

To my dear family…

FOREWORD

I would like to express my deepest gratitude to Prof. Dr. Özgül KELEŞ, who has always guided me throughout my doctoral research, whose endless support I have felt at every moment, and who has been much more than a thesis advisor to me. I am truly grateful to her for transforming me into the engineer I am today.

Endless thanks to my esteemed mentor, Assoc. Prof. Dr. Billur Deniz KARAHAN, who has always inspired me with her passion for the profession, from whom I have learned so much while working together, and who has always been a source of guidance and support.

I would also like to extend my deepest gratitude to Prof. Dr. Süheyla AYDIN, a valuable mentor, whom I am proud to be a student of, and who holds a very important place in my life. I am very fortunate to have had her guidance.

I would like to sincerely thank Prof. Dr. Ömer Suat TAŞKIN for his continuous support and guidance throughout my thesis research.

Special thanks to Dr. Arda KOCAMAN, who I am proud to work with, whose out-of-the-box thinking, invaluable ideas, and inspiration have always encouraged both me and those around him.

I would like to thank my dear colleagues Dr. Demet AYDOĞMUŞ, Dr. Leyla YANMAZ, Dr. Kağan BENZEŞIK, MSc. Utku Orçun GEZICI, Dr. Faruk KAYA, MSc. Selçuk KAN, Dr. Erçin Çağan DURAN, Dr. Burçak AVCI, MSc. Göksel HIZLI, MSc. Duygu YEŞILTEPE, Dr. Sıddıka MERTDINÇ ÜLKÜSEVEN, and all the research assistants and staff of the Department of Metallurgical and Materials Engineering at ITU for their endless support and valuable memories during my assistantship.

My sincere thanks go to my colleagues with whom I shared the same laboratory and worked together with great enjoyment: Dr. Emre ÇETINTAŞOĞLU, MSc. Barış Cem Alpay, MSc. Gençer KÜL, MSc. Reyhan SOLMAZ, MSc. Orhun OĞUZ, MSc. Eylem GÖK, MSc. Gültuğ YÜN, MSc. Humza ASHRAF, MSc. İbrahim Can TOPAKTAŞ, Yiğit BÜRÜMLÜ, Mehmet YILMAZ, Gülgün Zehra ŞENYURT, and Gizem Burcu BİLGİN.

I would like to express my deepest gratitude to my dear friends, who have been like a family to me over the last 18 years, and who have stood by me with endless support during every moment of my doctoral journey: Sena KOÇ, Baran İŞYAPAN, Volkan IŞIK, Emre ÖZDOĞAN, Eray TANRIVERİR, and Fırat BAŞARAN. My heartfelt thanks also go to my dear friends, Katia DI PERI, Martina PASINI TOPALOĞLU, and Bayram TOPALOĞLU, who have shown me that every moment we share is a celebration and that the distance doesn't matter.

I am incredibly grateful to my family in Istanbul, who have always been there for me, and who have celebrated life and all its blessings with me: MSc. İpek ERDEM, Nazan ERDEM, Mehmet ERDEM, Nur ÇAĞATAY, and our lovely cat Köfte.

Above all, I owe my deepest thanks and gratitude to my beloved mother, Hatice DEMİRTAŞ TUNÇ, my father, Hüseyin TUNÇ, my brother, Habib Can TUNÇ, and my grandmother, Nahide DEMİRTAŞ, for teaching me to be a good person first and foremost, and for their infinite love, patience, and support, which helped me become the person I am today.

Finally, I would like to express my sincere appreciation to the Regenerative and Restorative Medicine Research Center (REMER) at Istanbul Medipol University for supporting my experimental and characterization work, and to Dr. Alper YEŞİLÇUBUK and Prof. Dr. Bihter ZEYTUNCU for their helps in characterizations. I would like to thank the ITU Scientific Research Projects Unit for their financial support of this thesis under Project No. 42191.

December 2024

İpek TUNÇ
(Metallurgical and Materials Engineer)

TABLE OF CONTENTS

Page

ABBREVIATIONS

ATR-FTIR : Fourier transform infrared spectroscopy – attenuated total reflectance
CTAB : Cetyltrimethylammonium bromide
DMC : Dimethyl carbonate
EC : Ethylene carbonate
EV : Electric vehicle
FEC : Fluoro Ethylene Carbonate
LCO : Lithium cobalt oxide
LFP : Lithium iron phosphate
LIB : Lithium ion battery
$LiPF_6$: Lithium hexafluorophosphate
LMO : Lithium manganese oxide
LNO : Lithium nickel oxide
NMC : Lithium nickel manganese cobalt oxide
PC : Propylene carbonate
PEG : Polyethylene glycol
SDBS : Sodium Dodecyl Benzene Sulfonate
SEI : Solid electrolyte interface
SEM : Scanning electron microscopy
TEM : Transmission electron microscopy
XPS : X-ray photoelectron spectroscopy
XRD : X-ray diffraction
XRF : X-ray fluorescence

SYMBOLS

Si	**:** Silicon
SiO	**:** Silicon monoxide
SiO_2	**:** Silicon dioxide, silica
SiO_x	**:** Silicon suboxide
NaOH	**:** Sodium hydroxide
H_2SO_4	**:** Sulfuric acid
i	**:** maximum current measured at a selected voltage value
v	**:** scan rate
k_1	**:** diffusion constant
k_2	**:** capacitive constant

LIST OF TABLES

Page

LIST OF FIGURES

Page

DESIGN AND PRODUCTION OF BIOMASS-DERIVED ANODE ACTIVE MATERIALS FOR LITHIUM ION BATTERIES

SUMMARY

As technology advances, societies have seen a rise in energy demands, leading to a heavy reliance on fossil fuels to meet this growing need. However, the carbon dioxide and greenhouse gases released during these processes have contributed to global warming and climate change, becoming increasingly significant issues. According to the 2023 report by the U.S. Environmental Protection Agency, the largest portion of greenhouse gas emissions—28%—comes from gasoline and diesel transportation. In response, many countries have implemented policies to promote the widespread adoption of electric vehicles (EVs) as a means to mitigate the climate challenges posed by greenhouse gas emissions. The two most critical factors influencing the adoption of electric vehicles are the range per charge and the charging time, both of which are directly tied to the lithium-ion batteries used in these vehicles. To support the sustainable growth of electric vehicles, it is also essential that the components of lithium-ion batteries are sourced sustainably. Graphite is the predominant anode material used in commercial lithium-ion batteries. With its high electrical conductivity, graphite is valuable across various industries and is listed among the Critical Raw Materials by the European Union. However, as the demand for electric vehicles rises, experts predict a shortage of graphite supply beginning in 2026. Therefore, finding environmentally friendly and sustainable alternatives that can perform similarly to graphite is becoming increasingly crucial.

This thesis aims design and production of an anode active material for lithium-ion batteries using rice husk, an organic waste. Rice husk is a promising alternative to graphite due to its high silica content and worldwide annual production. However, the electrochemical performance of silica-based materials is often limited by their poor electrical conductivity. To enhance their performance, strategies such as reducing particle size to shorten the lithium diffusion path or creating composites with materials that have higher electrical conductivity can be employed. In this thesis, submicron silica particles and SiO_x/C nanocomposite biochars were synthesized using wet chemical methods and fast pyrolysis by induction heating. High During pyrolysis the organic components in rice husk decomposes and produces reducing gases such as CO, CH_4, and H_2, which partially reduce the silica to SiO_x. The high heating rates promote the formation of these reducing gases. For the first time in the literature, rice husk-derived anode active materials are synthesized using fast pyrolysis with induction heating. This study is significant because it has the potential for scalability and commercial application.

In the first part of the experimental studies, submicron silica particles were produced using leaching and precipitation methods using rice husk. The effects of pre-calcination, the solid-to-liquid ratio, and the addition of ethanol as a co-solvent on the silica particle sizes were examined. In this process, both rice husk and rice husk ash

were dissolved in a sodium hydroxide solution to obtain a sodium silicate solution, which is commonly used in silica production. By utilizing organic waste to derive the sodium silicate solution, the process aimed to reduce the overall carbon footprint. In the next stage of production, sulphuric acid was added to the sodium silicate solution to precipitate silica particles at a pH of 7. The resulting samples were characterized based on their structural, morphological, and electrochemical properties. FTIR and XRD analyses confirmed the existence of Si-O bonds and the amorphous silica structure. SEM images revealed that the particles were irregularly shaped and agglomerated. The sample that underwent calcination before leaching, with a solid-to-liquid ratio of 1/20 and no ethanol added, exhibited the smallest particle size. It was noted that low solid-to-liquid ratio leads to low SiO_2/Na_2O ratio, which is the key parameter to control particle growth. Moreover, adding ethanol increased particle size and shifted the distribution from monodisperse to polydisperse. This shift was attributed to the immiscibility of sodium silicate in ethanol, which led to local supersaturations. The sample with the smallest particle size delivered discharge capacities of 503, 167, and 145 mAh/g at the 1st, 100th, and 200th cycles, respectively. The improvement in electrochemical performance was attributed to the shorter lithium diffusion path. Additionally, the capacity drop observed after the 1st cycle in all samples is attributed to the formation of the solid electrolyte interface (SEI) layer and irreversible lithium silicates.

In the second part of the experimental studies, SiO_x/C nanocomposite biochar samples were synthesized using rice husk via induction-heated fast pyrolysis method with the aim of preserving the maximum carbon content to improve electrical conductivity. Three different pyrolysis temperatures (specifically, 700-750-800 °C) and two pyrolysis atmospheres (argon and argon-hydrogen mixture) were tested. Additionally, the sample with the highest carbon content was ball milled to reduce its particle size and achieve a more homogeneous elemental distribution. FTIR analysis confirmed the successful synthesis of silica, revealing the presence of Si-O-C, Si-O-Si, and Si-O bonds. XRD patterns showed that samples pyrolyzed at temperatures below 800 °C exhibited an amorphous phase, while above this temperature, crystallization began, and the cristobalite phase was formed. SEM images indicated that the samples had irregular morphologies; however, milling after pyrolysis resulted in smaller, more spherical particles. Raman spectroscopy confirmed the presence of both defective and graphitic carbon structures. As the pyrolysis temperature increased, the ratio of graphitization also increased, and milling further increased the I_D/I_G ratio by introducing additional defects into the structure. XPS analysis confirmed the formation of SiO_x, displaying peaks of Si^{+2}, Si^{+3}, and Si^{+4} in the Si 2p spectrum. TEM images showed that silicon-rich particles were uniformly distributed within the carbon matrix.

The pyrolysis conducted at 700 °C in the argon atmosphere resulted in the highest carbon content as 41.3 wt.% and delivered the best electrochemical performance as 1366, 340, and 275 mAh/g in the 1st, 100th, and 200th cycles, respectively. An increase in carbon content was associated with improved electrochemical performance. However, all samples exhibited a drop in capacity after the first cycle, attributed to the formation of the solid electrolyte interphase (SEI) layer and irreversible lithium silicates.

LİTYUM İYON BATARYALAR İÇİN ORGANİK ATIKLARDAN ANOT AKTİF MALZEME TASARIMI VE ÜRETİMİ

ÖZET

Gelişen teknoloji ile günümüzde toplumların enerji ihtiyaçları artmış ve bu artan ihtiyacın karşılanması için ağırlıkla fosil yakıtlara yönelinmiştir. Bu prosesler sonucu oluşan karbon dioksit ve sera gazları ise küresel ısınma ve iklim değişiminin daha büyük bir problem haline gelmesine yol açmıştır. A.B.D. Çevre Koruma Ajansı'nın 2023 yılındaki raporunda sera gazı yayınımında en büyük pay %28 ile benzin ve mazot bazlı ulaşıma aittir. Bu nedenle birçok ülke, sera gazı kaynaklı iklim sorunlarının azaltılması için elektrikli araçların yaygınlaşmasını destekleyen politikalar benimsemiştir. Bu araçların yaygınlaşabilmeleri için en önemli kriterler ise tek şarjla kat edilebilen menzil ve şarj süresi olarak görülmektedir. Bu iki kriter batarya paketlerinde kullanılan lityum iyon piller ile doğrudan ilişkilidir. Elektrikli araçların sürdürülebilir şekilde yaygınlaşması için lityum iyon pil bileşenlerinin de sürdürülebilir olması oldukça önemlidir. Ticari lityum iyon pillerde anot aktif malzeme olarak grafit yaygın olarak kullanılmaktadır. Yüksek elektrik iletkenliği ile birçok sektörde kendisine kullanım alanı bulan grafit, hali hazırda Avrupa Birliği'nin Kritik Hammade Listesi'nde yer almakta olup elektrikli araçlara artan taleple doğru orantılı olarak 2026 yılından itibaren grafit talebinin karşılanmasında sıkıntı yaşanacağı öngörülmektedir. Bu nedenle grafite yakın performans sergileyebilecek, çevre dostu ve sürdürülebilir alternatiflerin bulunması zorunluluk haline gelmiştir.

Bu tez çalışmasında bir organik atık olarak pirinç kabuğundan lityum iyon pillerde kullanılmak üzere anot aktif malzeme tasarımı ve üretimi gerçekleştirilmiştir. Pirinç kabuğu yüksek silika içeriği ve dünya çapında yıllık üretim miktarının yüksek olması sayesinde grafit anotlara alternatif olmak için önemli bir adaydır. Ancak silika esaslı malzemelerin elektrokimyasal performansı düşük elektrik iletkenlikleri nedeniyle sınırlıdır. Bu malzemelerin performanslarının iyileştirilmesi için partikül boyutları azaltılarak lityum iyonunun difüzyon mesafesinin kısaltılması ya da daha yüksek elektrik iletkenliğine sahip bir malzeme ile kompozit elde edilmesi uygulanabilecek stratejilerdendir. Bu bilgiler ışığında, bu tez çalışması kapsamında yaş kimyasal yöntemler (liç ve çöktürme) kullanılarak mikron altı silika partiküller ve piroliz yöntemi kullanılarak SiO_x/C nanokompozit biyokömür numuneler üretilmiştir. Piroliz sırasında indüksiyon fırını kullanılarak yüksek ısıtma hızları elde edilmiştir. İşlem sırasında, pirinç kabuğunun yapısındaki organik bileşenler bozunarak CO, CH_4, H_2 gibi redükleyici gazları oluştururken, yapıdaki silika bu redükleyici gazlar ile SiO_x'e indirgenmiştir. Yüksek ısıtma hızları ile redükleyici gazların oluşumu desteklenmiştir. Bu çalışma ile literatürde ilk defa pirinç kabuğu kullanılarak indüksiyon ısıtmalı hızlı piroliz yöntemi ile lityum iyon bataryalarda kullanılmak üzere anot aktif malzeme sentezi gerçekleştirilmiştir. Bu çalışma, prosesin yüksek gramajlarda çalışmaya ve ticarileşmeye uygun olması nedeniyle önemlidir.

Deneysel çalışmaların ilk kısmında pirinç kabuğu kullanılarak liç ve çöktürme metotları ile mikron altı silika partikül elde edilerek, liç öncesi kalsinasyon, liç sırasında katı/sıvı oranı, ve çözücü olarak etanol ilavesinin sentezlenen partikül boyutlarına etkisi incelenmiştir. Proses sırasında pirinç kabuğu ve pirinç kabuğu külü sodyum hidroksit çözeltisi içerisinde çözülerek ticari olarak da silika üretiminde kullanılan sodyum silikat çözeltisi elde edilmiştir. Organik atıkları kullanarak sodyum silikat çözeltisi eldesi ile prosesin karbon ayak izinin azaltılması hedeflenmiştir. Üretimin sonraki aşamasında, elde edilen sodyum silikat çözeltisine sülfirik asit eklenerek pH=7 değerinde silika partiküllerin çökmesi sağlanmıştır. Üretilen numuneler yapısal, morfolojik ve elektrokimyasal olarak karakterize edilmiştir. Üretim sırasında liç öncesi kalsinasyonun silika partikül üretiminin verimini artıracağı, düşük katı/sıvı oranlarının (düşük SiO_2/Na_2O oranına denk gelmektedir) daha küçük boyutlu partikül eldesini sağlayacağı ve etanol eldesinin çözelti yüzey gerilimini düşürerek daha küresel partikül eldesine yol açacağı hipotezleri kurulmuştur FTIR ve XRD analizleri, Si-O bağlarının varlığını ve amorf silika yapısını doğrulamıştır. SEM görüntüleri, partiküllerin düzensiz şekillerde ve birbirine yapışmış olduğunu göstermektedir. Partikül boyut analizi sonucunda en küçük partikül boyutu, liç öncesinde pirinç kabuklarının kalsine edildiği, katı/sıvı oranının 1/20 olarak seçildiği ve etanol eklenmeyen numunede ölçülmüştür. Etanol ilavesi ile partikül boyutlarının arttığı ve dağılımın monodispersten polidisperse kaydığı görülmüştür. Bunun sebebinin sodyum silikatın etanol içerisinde çözünmemesi nedeniyle aşırı doygun bölgeler oluşturması olduğu düşünülmektedir. Çevrimsel voltametri analizi tüm numunelerde 0,7 V civarında katı-elektrolit arayüzey (SEI) katmanı oluşumu ve 0,2 V altında lityumun yapıya girişini gösteren reaksiyonların varlığını göstermiştir. En küçük partikül boyutuna sahip numune birinci, yüzüncü ve iki yüzüncü çevrimlerinde sırasıyla 503, 167 ve 145 mAsa/g deşarj kapasitesi vermiştir. Kısalan lityum difüzyon mesafesinin elektrokimyasal performansta iyileşme sağladığı düşünülmektedir. Buna ek olarak, ilk çevrimlerden sonra tüm numunelerde görülen kapasite düşüşü katı-elektrolit arayüzey (SEI) katmanının ve tersinmez lityum silikatların oluşumuna atfedilmiştir.

Deneysel çalışmaların ikinci kısmında ise pirinç kabuğu kullanılarak indüksiyon ısıtmalı hızlı piroliz yöntemi ile SiO_x/C nanokompozit biyokömür numuneler sentezlenmiş ve lityum iyon pillerde anot olarak kullanım potansiyelleri incelenmiştir. Numunelerin elektrik iletkenliğinin iyileştirilmesi amacıyla yapıda en yüksek miktarda karbonun tutulması amaçlanmıştır. Bu amaçla üç farklı piroliz sıcaklığı (700-750-800 °C) ve iki farklı piroliz atmosferi (argon ve argon-hidrojen karışımı) denenmiştir. Son olarak en yüksek karbon içeriğine sahip numune partikül boyutunun küçültülmesi ve homojen element dağılımının elde edilmesi için bilyalı değirmende öğütülmüştür. FTIR analizi, tüm örneklerde Si-O-C, Si-O-Si ve Si-O bağlarını doğrulayarak silikanın başarılı bir şekilde sentezlendiğini göstermektedir. XRD paternleri, 800 °C'nin altındaki sıcaklıklarda amorf silika fazını, üzerindeki sıcaklıkarda ise silikanın kristalleşmesi sonucu kristobalit fazının oluşmaya başladığını göstermektedir. SEM görüntüleri, numunelerin düzensiz morfolojilere sahip olduğunu gösterirken, piroliz sonrası öğütme işlemi ile daha küçük boyutta ve yuvarlak morfolojide partiküllerin elde edildiği görülmüştür. Raman spektroskopisi, D ve G bantlarını göstererek hatalı ve grafitik karbon yapılarının varlığını doğrulamaktadır. Piroliz sıcaklıklarının artmasıyla grafitleşme oranı yükselirken, öğütme işlemi yapıdaki hata miktarını artırarak ID/IG oranında artışa neden olmuştur. 700 °C'de argon atmosferinde yapılan piroliz işlemi, ağırlıkça %41,3 karbon içeriği ile en iyi elektrokimyasal performansı vermiştir. XPS analizi ile, Si 2p spektrumunda

Si^{+2}, Si^{+3} ve Si^{+4} piklerinin varlığı ile SiO_x yapısının oluşumu doğrulanmıştır. TEM görüntüleri, 700 °C'de argon ve argon-hidrojen atmosferlerinde piroliz edilmiş numunelerde silisyumca zengin partiküllerin, karbon matris içerisinde homojen bir şekilde dağıldığını göstermektedir. En yüksek karbon içeriğine sahip numune (700 °C – argon atmosferi) birinci, yüzüncü ve iki yüzüncü çevrimlerinde sırasıyla 1366, 340 ve 275 mAsa/g deşarj kapasitesi vermiştir. Artan karbon içeriğiyle beraber elektrokimyasal performansta iyileşme görülmesine rağmen, tüm numunelerde ilk çevrimlerden sonra kapasite düşüşü görülmüştür. Bu düşüşün sebebinin katı-elektrolit arayüzey (SEI) katmanının ve tersinmez lityum silikatların oluşumu olduğu düşünülmektedir. Son olarak çamur kompozisyonu optimizasyonu, elektrolit katkısı ve elektrokimyasal aktivasyon ile elektrokimyasal performansın daha da iyileştirilmesi amaçlanmıştır. Çamur kompozisyonu olarak daha yüksek karbon içeriği sayesinde (aktif malzeme:karbon:bağlayıcı oranı) 60:25:15 kompozisyonu 80:10:10 kompozisyonuna göre daha yüksek spesifik kapasite sağlamıştır. Elektrokimyasal aktivasyon prosedürü, düşük akımlarla yapılan şarj/deşarj aşamaları sırasında daha homojen bir katı-elektrolit arayüzey tabakasının büyümesini teşvik ederken, şarj/deşarj limit voltajlarında uzun süre beklemek yapıya lityumun girişi ve çıkışı için yeterli zaman sağlayarak elektrokimyasal performansı iyileştirmektedir. Son olarak, elektrolit katkısı olarak FEC (Fluoro Ethylene Carbonate) eklenmesinin, katı-elektrolit arayüzey tabakasının stabilitesini artırarak kapasite korunumunu iyileştirdiği görülmüştür.

1. INTRODUCTION

Global energy consumption has shown accelerated growth in the last few decades. The worldwide primary energy consumption increased by 60% between 2000 and 2023 [1]. Using primary energy sources to meet this demand increases CO_2 and greenhouse gas emissions. The United States Environmental Protection Agency's report reveals that gasoline and diesel-based transportation, with a 28% share, is the primary source of these emissions [2]. The rising concerns about climate change and global warming due to greenhouse gas emissions have led governments and industries to develop new strategies based on all-electric vehicles (EVs). The practical use of these vehicles mainly depends on the maximum range and charging time, hence the performance of lithium ion batteries.

Commercial lithium ion batteries generally comprise graphite anode and lithium transition metal oxides or phosphates as cathodes. The sustainability of raw battery materials is critical in the continuous development of lithium ion battery chemistries. In this regard, graphite, used in many industries besides batteries, creates a bottleneck. Graphite has been on the European Union's Critical Raw Materials list for many years. Moreover, over 70% of global graphite is supplied by China, which makes it a geopolitically critical material. To address this issue, many researchers are studying alternatives to graphite.

Silicon-based anode active materials are great candidates for substituting graphite due to their high theoretical capacity, safe working potential, and abundance on Earth [3]. However, pure silicon anodes suffer from high volumetric changes (up to 375%) during cycling, limiting their use as anode active materials due to deterioration of anode resulting in performance failure. Therefore, SiO_2 and SiO_x anodes have recently drawn attention for having moderate volume changes, low cost, and greater cycle stability. The production of these anodes from biowaste under the zero-waste principle could significantly impact the environment and economy. Among the possible organic biowastes, such as bamboo leaf and horsetail plant, rice husk has the highest silica

content (up to 18-20 wt.%), which makes it the most suitable candidate for SiO_2 and SiO_x production.

So far, many processes have been proposed in the literature to synthesize SiO_2 and SiO_x anode active materials using rice husk, namely metallothermic reduction [4], pyrolysis [5], precipitation [6], hydrothermal or sol-gel synthesis [7], and mechanical milling [8]. Among them, the pyrolysis method with the resulting product of biochar and the precipitation method with the final product of pure SiO_2 particles stand out with high efficiency and safety for anode active material synthesis.

This thesis aims to produce alternative anode active materials using a biowaste, namely rice husk, by leaching, precipitation, and novel fast pyrolysis methods to substitute graphite in lithium ion batteries. The high silica and carbon content of the rice husk makes it a great source for anode active material synthesis. In general, silica-based anode active materials suffer from low electrical conductivity. Here, two possible solutions are proposed to overcome this challenge: decreasing particle size to shorten the lithium diffusion path and creating nanocomposites with a material that has higher electrical conductivity. Precipitation and pyrolysis-based two sets of experiments are designed to test the validity of proposed solutions. In the first set of samples, submicron silica particles are synthesized using a leaching and precipitation method to achieve the submicron particle size. In the second set of samples, SiO_x anode active materials are produced by a single-step fast pyrolysis method to preserve the maximum amount of carbon in the structure. The samples are characterized by their chemical, morphological, and structural properties. Finally, electrochemical performances are investigated in detail using galvanostatic tests, cyclic voltammetry, and electrochemical impedance spectroscopy.

In this study, for the first time in the open literature, a fast pyrolysis method using an induction furnace (>50 °C/min) is used for lithium ion battery anode active material production using rice husk as a biowaste. High heating rates are utilized to partially reduce SiO_2 to SiO_x during pyrolysis with the reducing gases produced while the transformation of organic content to carbon. The carbon and SiO_x in the resulting nanocomposite is expected to deliver higher electrochemical performance. This study is significant because it has the potential for scalability and commercial application.

1.1 Aim of the Thesis

This study aims to design and produce anode active materials using rice husk, which is a silica-containing organic waste, as a sustainable alternative to commercial graphite anodes in lithium ion batteries.

While literature indicates that silica reacts with lithium at low potentials, its low electrical conductivity reduces the performance of silica-based anode active materials. Here, two hypotheses addressing this problem are proposed: the first hypothesis is by reducing the particle size of silica-based anode materials to shorten the lithium ion diffusion path utilizing hydrometallurgical processes (leaching and precipitation), and the second is creating composite structure (SiO_x/C) via fast pyrolysis that has high both ionic and electrical conductivity.

As proposed above, in the first part, our solution has been set on synthesizing. Six silica samples have been made using leaching and precipitation methods. Various factors have been investigated including calcination, the silica-to-sodium oxide ratio, and ethanol addition, to produce submicron particles having spherical morphology.

In the second part, five SiO_x and carbon so-called composite biochar samples are produced through fast pyrolysis. For the first time in the literature, rice husk-derived anode active materials were synthesized via fast pyrolysis using induction heating. During the pyrolysis of rice husk, silica remains in the biochar while organic materials decompose and generate reducing gases such as CO, CH_4, and H_2. These gases also partially reduce silica to SiO_x. The process employs high heating rates (>50 °C/min) through induction heating to maximize carbon retention in the composite structure and enhance the production of reducing gases. With this aim, the effects of pyrolysis temperature and atmosphere on the biochar's carbon content and silicon's valence state in the synthesized anodes have been investigated. The effect of slurry composition, electrochemical activation, cut-off voltage, and electrolyte addition on the anodes' electrochemical performance are examined.

1.2 Literature Review

Upon reviewing the literature, it was observed that various materials derived from rice husk have been utilized in battery research. These materials can be categorized into three: pure carbon-based materials, pure silica particles, and biochars, which naturally

form SiO_2/C and SiO_x/C composites. The early studies concentrated on the synthesis of carbon-based materials, while recent trends have shifted towards SiO_x/C composites with various doping methods.

To the best of our knowledge, Fey et al. [9] were the first to synthesize rice husk-based active materials for lithium-ion batteries in 2001. They produced hard carbon anodes by pyrolysis followed by leaching and claimed a high reversible capacity of 1015 mAh/g at a current load of 75 mA/g. In subsequent years, the same research group [10] conducted another study aimed at increasing the porosity of the synthesized pyrolytic carbons by introducing pore-forming materials. Their findings revealed that pyrolysis at 600 °C, when combined with a 5 % pore-forming additive (porogen), resulted in the highest specific capacity of 2523 mAh/g at a current load of 0.1 C. In the following years, Wang et al. [11] successfully synthesized carbon fibers using rice husk by hydrothermal carbonization, heat treatment, and NaOH leaching. The dissolution of SiO_2 in rice husk ash leads to a higher surface area with micro, meso, and micropores [12]. While the sample delivered 789 mAh/g in the first discharge step, the capacity suddenly dropped to 396 mAh/g in the following cycles due to the decomposition of carbonate-based electrolyte and SEI layer formation. To increase the surface area, $ZnCl_2$ activation on lignin-derived carbon anodes using rice husk is conducted by Li et al. [13]. Their porous carbon anode delivered 469 mAh/g specific capacity at 0.2 C current after 100 cycles.

While most studies focus on synthesizing anode active materials using rice husk, Nilmoung et al. [14] successfully synthesized a V_2O_5/C composite cathode active material using carbon derived from rice husk. The carbon was produced through calcination and NaOH leaching of the rice husk, which was then combined with a vanadium oxide solution. After the mixture underwent gelation, heat treatment at different temperatures was applied, and the effect of temperature on the structural stability was investigated. The sample heat treated at 800 °C delivered the highest specific capacity of 350 mAh/g at 0.1 C current.

However, the low specific capacity of carbon has led researchers to explore the production of silica-based anode active materials using rice husk in the following years. This process typically involves air calcining the rice husk to remove its organic content. The resulting ash is then dissolved in a sodium hydroxide (NaOH) solution to create a sodium silicate solution (Na_2SiO_3). Subsequently, nano silica powder is

precipitated by adding acid until a neutral pH is reached. Amutha et al. [15] investigated the purity of the nano silica powders extracted from rice husk. Their results indicated that refluxing the material with acid solutions could produce nano silica particles approximately 80 nm in size with a purity of up to 98 wt.%. Yuvakkumar et al. [16] synthesized nano silica powders using the above method and achieved 25 nm average particle size and 99.9% purity. Rafiee et al. [17] focused on increasing the surface area of rice husk-derived silica particles. They claimed that refluxing rice husk with 1M HCl solution, followed by calcination at 700 °C, leads to the highest surface area and pore volume. In addition to previous optimization studies, Dominguez et al. [18] explored the addition of various alcohols as co-solvents to the size and morphology of precipitated silica particles.Their findings indicated that addition of ethanol decreases the solution polarity and surface tension due to having molecular bonds that are weaker than the water. This lower surface tension promotes the isotropic growth and formation of more spherical particles. Askaruly et al. [6] investigated the electrochemical behavior of two different types of silica powders derived from rice husks. They compared the performance of silica that was air-calcined to precipitated silica produced via NaOH leaching and acid precipitation. The precipitated silica anode delivered a specific capacity of 442 mAh/g after 50 cycles at a current of 50 mA/g. In contrast, the air-calcined silica only provided a specific capacity of 295 mAh/g under the same conditions. The enhanced electrochemical performance of the precipitated silica is attributed to its higher specific surface area and pore volume.

Unlike above, some researchers have focused on producing silicon nanoparticles from rice husks due to their high theoretical capacity (3580 mAh/g at room temperature) and the potential for lower production costs. However, breaking the strong covalent bonds between silicon and oxygen atoms in the silica structure of rice husks requires a significant amount of energy. To overcome this energy barrier, in 2013, Liu et al. [19] synthesized silicon nanoparticles through the magnesiothermic reduction of rice husk powder. After leaching the by-products, such as MgO, the resulting powders exhibited particle sizes ranging from 10 to 40 nm and a porous morphology. Notably, they achieved a high reversible capacity of 2790 mAh/g, with an 86% capacity retention after 300 cycles. While the starting material is very inexpensive, the highly exothermic nature of the reaction raises safety concerns. As an innovative design, Liu

et al. [20] introduced anode active materials using a combination of $Si@SiO_x/C$ synthesized from rice husk and coffee grounds. The $Si@SiO_x$ particles were produced through a process involving calcination followed by magnesiothermic reduction. These particles were then mixed with coffee grounds and subjected to heat treatment to form the $Si@SiO_x/C$ structure. The researchers determined that the optimal mixture ratio of $Si@SiO_x$ particles to coffee grounds was 1:2. The sample created with this ratio achieved a reversible capacity of 1125 mAh/g at a current of 100 mA/g. As a safer alternative to magnesiothermic reduction, Zhao et al. [21] employed zincothermic reduction to synthesize silicon/carbon (Si/C) anode active materials using rice husk as the starting material. They mixed carbonized rice husk powder with zinc powder and aluminum chloride ($AlCl_3$), which was then loaded into an autoclave and subjected to heat treatment at 300 °C. The resulting composite anode achieved a specific capacity of 1033 mAh/g at a current density of 1 A/g over 100 cycles.

Although silicon anode active materials have a potential for higher specific capacities, processes such as magnesiothermic reduction require safety precautions and additional post-processing. As a result, researchers have preferred more eco-friendly and safer methods, especially when using organic waste as starting materials. Additionally, the low capacities of pure carbon-based anode materials and the poor electrical conductivity of silica have motivated researchers to explore the synthesis of composite materials using rice husk via simple and efficient processes. Wang et al. [22] published a study on the production of a composite anode made from rice husk, which consists of carbon and silica. This composite was created through pyrolysis at 900 °C in a nitrogen atmosphere. The resulting material contained 41 wt.% carbon and 59 wt.% SiO_2, with silica particles ranging in size from 10 to 50 nm. The composite anode achieved a specific capacity of 325 mAh/g. In their study, the authors conducted separate electrochemical tests to evaluate the individual contributions of carbon and SiO_2 to the overall electrochemical performance. They found that the composite anode exhibited a higher capacity compared to both the carbon and silica anodes. This outcome demonstrated the successful design of the composite anode. Additionally, they noted that the increase in specific capacity observed in subsequent cycles is due to the activation of the inner parts of the silica anode. In the initial cycles, only the surface of the silica was electroactive, while in later cycles, the inner regions also became activated. Feng et al. [23] investigated the further enhancement of this

composite by synthesizing SiO_2/C composite anodes through carbonization in the N_2 atmosphere. They examined the impact of ball milling on the electrochemical performance. Their results showed that ball milling reduced the particle size from 1 micron to 400-500 nm and created a more uniform distribution of carbon and SiO_2 within the structure. The milled samples exhibited a reversible capacity of 827 mAh/g at a current rate of 100 mA/g over 300 cycles.

Recently, researchers have adopted a doping strategy to enhance the electrical conductivity of composite anode active materials. Zhang et al. [5] synthesized boron and nitrogen co-doped C/SiO_x composite anode using rice husk and $NH_4HB_4O_7$ as a pore-forming agent. This design allows for a porous structure that provides active sites for lithiation, while doping with boron and nitrogen improves electrical conductivity and enhances rate capability. The resulting doped anode active material exhibited specific capacities of 1165 mAh/g at a current of 0.1 A/g and 650 mAh/g at 1 A/g. In the study conducted by Zhang et al. [24], the electrochemical performance of phosphorus (P) and nitrogen (N)-doped C/SiO_x composite structures was investigated. They used $(NH_4)_3PO_4$ as a doping agent and rice husk as the sources of silicon (Si) and carbon (C). The researchers claimed that doping with P and N in the carbon matrix improves ion transport and enhances electrolyte penetration by creating defective sites. The doped sample exhibited a specific capacity of 1078 mAh/g at a current density of 0.1 A/g, with an initial Coulombic efficiency of 73%. Similarly, Cui et al. [25] incorporated sulfur (S) and nitrogen (N) into C/SiO_x structures, using thiourea as the doping source. This composite's specific capacity of 1150 mAh/g at 0.1 A/g is attributed to the improved electrical conductivity provided by the doping process. Additionally, during pyrolysis, SiO_2 transforms into SiO_x, resulting in an increase in capacity.

The summary of literature studies highlights the significance of composite anode designs due to the limited electrochemical performance of pure carbon and pure silica anodes. Rice husk serves as an excellent candidate for this purpose, as it is an organic waste material containing 20 wt.% silica and 80 wt.% organic compounds. The SiO_x/C composite anodes can be synthesized safely and effectively using a pyrolysis process. By optimizing the pyrolysis parameters, the quantity of carbon and the oxygen content of silica can be tailored for improved performance.

1.3 The Scope of the Thesis and Hypothesis

1.3.1 The scope of the thesis

The scope of this thesis includes the synthesis of anode active materials through two methods: the precipitation method, utilizing rice husk ash to create a sodium silicate solution for silica particle formation, and the pyrolysis method, where rice husk is subjected to fast induction heating in an inert argon atmosphere for biochar production. The study also evaluates the electrochemical performance of the synthesized materials, contributing to the development of more sustainable and efficient alternatives to conventional graphite anodes.

The experimental studies cover:

- Leaching and precipitation of submicron silica particles from rice husk: Rice husk powder is first leached in a sodium hydroxide (NaOH) solution, followed by acid precipitation to obtain submicron-sized silica particles. The study investigates the silica-to-sodium oxide ratio as a critical parameter that influences polymerization reactions and particle growth. Furthermore, the effect of calcination on silica extraction is examined, along with the impact of solvent polarity on particle morphology achieved by adding ethanol. The synthesized silica powders are characterized chemically, morphologically, and structurally. Finally, their electrochemical performance is evaluated using galvanostatic tests, cyclic voltammetry, and electrochemical impedance spectroscopy.
- Fast pyrolysis using induction heating to produce biochar composite that contains SiO_x and carbon: In this process, rice husk powder is pyrolyzed in an argon atmosphere with high heating rates (>50 °C/min) to promote the generation of reducing gases such as methane (CH_4), carbon monoxide (CO), and hydrogen (H_2). These gases facilitate the partial reduction of SiO_2 to SiO_x. To achieve these goals, the pyrolysis temperature and atmosphere are optimized to preserve the maximum amount of carbon in the resulting composite material, thereby enhancing its electrical conductivity. For further improvement, the sample with the highest carbon content is milled to reduce particle size. The synthesized powders are structurally, chemically, and morphologically characterized. Galvanostatic tests, cyclic voltammetry, and

electrochemical impedance spectroscopy are used to evaluate their electrochemical performances. The study also investigates the impact of slurry composition, electrochemical activation, discharge cut-off voltages, and the addition of FEC (Fluoro Ethylene Carbonate) as an electrolyte additive on the electrochemical performance of the optimized biochar sample.

1.3.2 The hypothesis of the thesis

The experiments conducted within the scope of this thesis are based on the following hypotheses:

The low electrical conductivity of silica adversely affects its electrochemical performance, limiting its effectiveness as an anode active material in lithium ion batteries. One approach to enhancing the electrochemical performance of silica-based materials is to reduce the particle size to shorten the lithium diffusion path or to create composites with materials that have higher electrical conductivity.

The leaching and precipitation methods are simple and effective for producing submicron silica particles. In this method, controlling the silica-to-sodium oxide ratio will lead to the production of smaller particles. This is because the silica-to-sodium oxide ratio is the key parameter for controlling particle size through polymerization and particle growth reactions. Moreover, calcination prior to leaching is expected to increase the silica precipitation efficiency, while the ethanol addition is expected to increase sphericity.

Incorporating a more electrically conductive material can enhance the electrochemical performance of silica-based anode active materials by reducing resistance. Fast pyrolysis is an effective method for synthesizing anode active materials from biomass. Using temperatures above 700 °C during pyrolysis, which exceeds the Boudouard reaction threshold, allows the organic compounds in rice husk to be converted into carbon while generating reducing gases such as carbon monoxide, hydrogen, and methane. Utilizing fast heating rates through induction heating promotes the formation of these reducing gases, which can partially reduce silica to SiO_x during pyrolysis. The resulting nanocomposite SiO_x/C anodes are expected to exhibit competitive performance compared to traditional graphite anodes.

2. LITHIUM ION BATTERIES

2.1 Working Principle

Lithium ion batteries have four main elements: anode (negative electrode), cathode (positive electrode), electrolyte, and separator. The anode and cathode act as lithium hosts during charge and discharge steps, while the electrolyte provides ionic mobility, and the separator prevents shortcuts between positive and negative electrodes [26]. In the charging step, lithium ions are released from the cathode active material and moved through the electrolyte to reach the anode active material. In this step, the electrical energy moves lithium ions from the cathode to the anode, which is stored as chemical energy. During the migration of lithium ions, electrons flow through the external circuit. In the discharging step, lithium ions stored in the anode migrate back to the cathode through the electrolyte. The resulting cell voltage is mainly related to the potential difference between the electrodes. The schematic drawing of lithium ion migration during charge and discharge steps is presented in Figure 2.1.

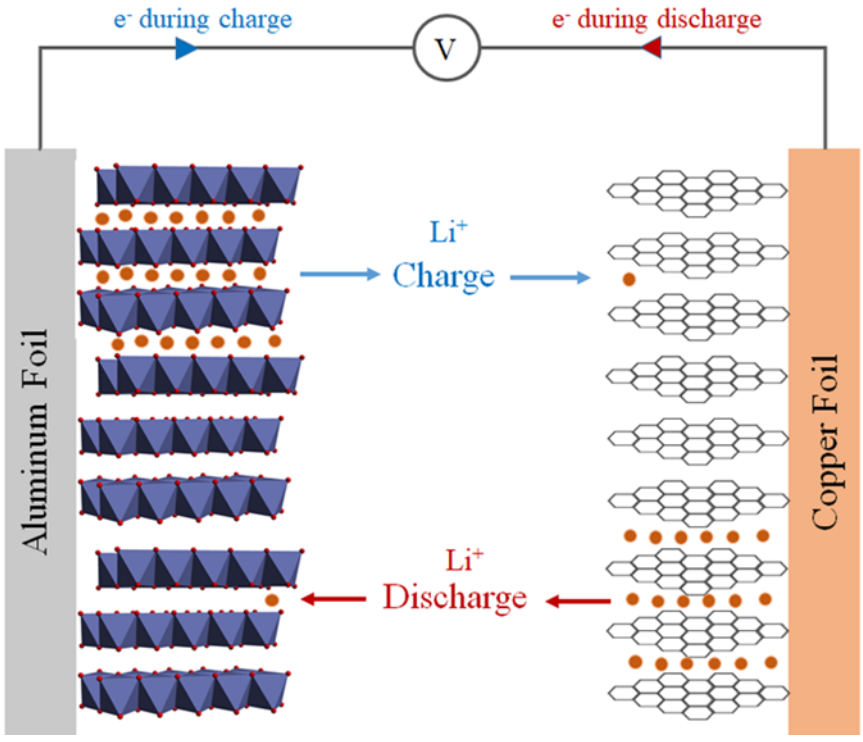

Figure 2.1 : Charge and discharge mechanism of lithium ion batteries.

2.2 Components

2.2.1 Anode active material

The anode is the negative electrode of lithium-ion batteries, which stores lithium ions in the discharge step at low voltages. General requirements of an anode material include good conductivity, durability, low working potential, low density, and cost-efficiency. As shown in Figure 2.2, anode active materials are usually classified according to their lithium storage mechanism.

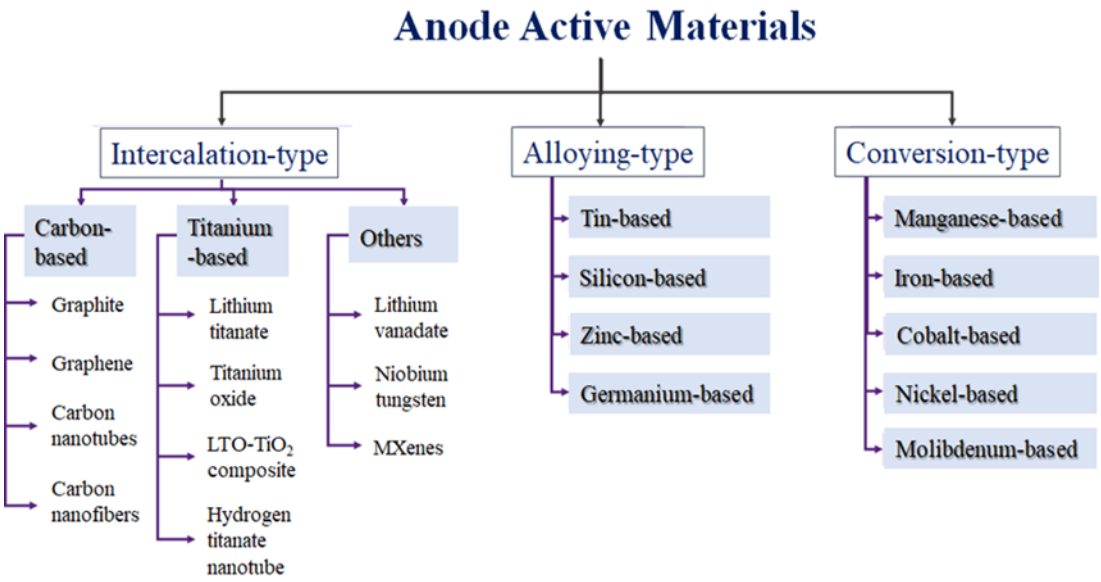

Figure 2.2 : Anode active materials based on lithiation mechanism.

Recently, Eftekhari [27] proposed classifying anode active materials based on their working potential. He classifies active materials into four groups. The potential window is determined by the potential range where the majority of capacity is derived. In the first group, group IV and V elements are listed as low-voltage anode materials (< 1 V vs. Li/Li^+). Secondly, transition metal oxide and chalcogenides are presented as mid-voltage anode active materials (1 – 2 V vs. Li/Li^+). The third group covers high-voltage anode active materials (>2 V vs. Li/Li^+). Finally, nanostructured and mixed-valence materials are covered in the fourth group as high-voltage anode materials (wide potential range as 0 - 3 V vs. Li/Li^+). Detailed information on the most commonly used anode active materials is given in Section 3 under “Anode Active Materials”.

2.2.2 Cathode active material

The cathode is the positive electrode that stores lithium ions during the charge step at higher voltages. The general requirements of a cathode active material include high theoretical capacity and working voltage, structural stability, easy production, and low cost.

In lithium ion batteries, cathode active materials are designed to intercalate for longer cycle life. Depending on the crystal structure, lithium diffusion occurs in various dimensions during intercalation. Lithium ions can diffuse only through 1 dimension in olivine structures, while they can move in 2D and 3D in layered and spinel cathodes, respectively [28]. The crystal structures of main intercalation-type cathodes are presented in Figure 2.3.

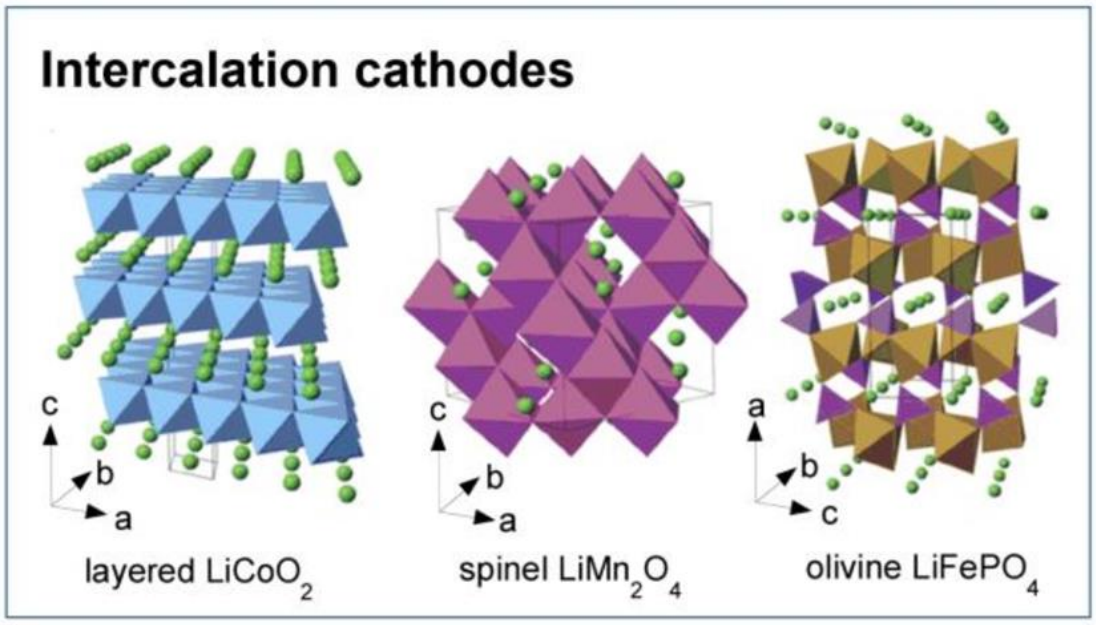

Figure 2.3 : Crystal structure of intercalation-type cathodes [28].

The first cathode active material proposed by Goodenough [29] in 1980, LCO ($LiCoO_2$), has a rock salt structure and working voltage window of 3-4.2 V vs Li/Li^+. The large size and charge differences between lithium and cobalt ions provide a beneficial ordering for 2D lithium diffusion. Good structural stability and electrical conductivity make LCO an ideal cathode active material. Although LCO cathodes have a high theoretical capacity (274 mAh/g), only 135 mAh/g specific capacity is achieved in practical applications [30]. The high cost and limited electrochemical performance of LCO cathodes required the development of new cathode chemistries. Nickel has lower prices and higher specific capacities to be used as LNO cathode

active materials. However, production difficulties and cation mixing effects due to similar sizes of Li^+ and Ni^{2+} hinder the use of LNO cathodes. They have a theoretical capacity of 275 mAh/g, but only a specific capacity of 150 mAh/g could be delivered in the voltage range of 2.5-4.2 V vs Li/Li^+ [31]. Lithium manganese oxide (LMO) is another type of basic cathode active material that provides higher stability in electrolytes with lower cost. LMO cathodes have 285 mAh/g theoretical and 200 mAh/g practical capacities in the 2.5-4.3 V range [32]. However, due to structural degradations, Jahn-Teller distortion limits the practical capacities to only 120 mAh/g. Additionally, the LMO structure transforms into a spinel structure with cycling, which causes rapid capacity drops. The drawbacks of each basic cathode active material require a balance with mixed chemistry. Today, NMC ($LiNi_{1-x-y}Co_xMn_yO_2$) cathodes are the most studied cathode chemistry. In this design, cobalt helps fast charge-discharge ability, nickel provides high capacity, and manganese functions to have structural stability. In Figure 2.4, NMC stoichiometries are presented in a ternary LCO-LNO-LMO system. NMC cathodes can deliver capacities around 200-210 mAh/g in the 3-4.3 V range [33].

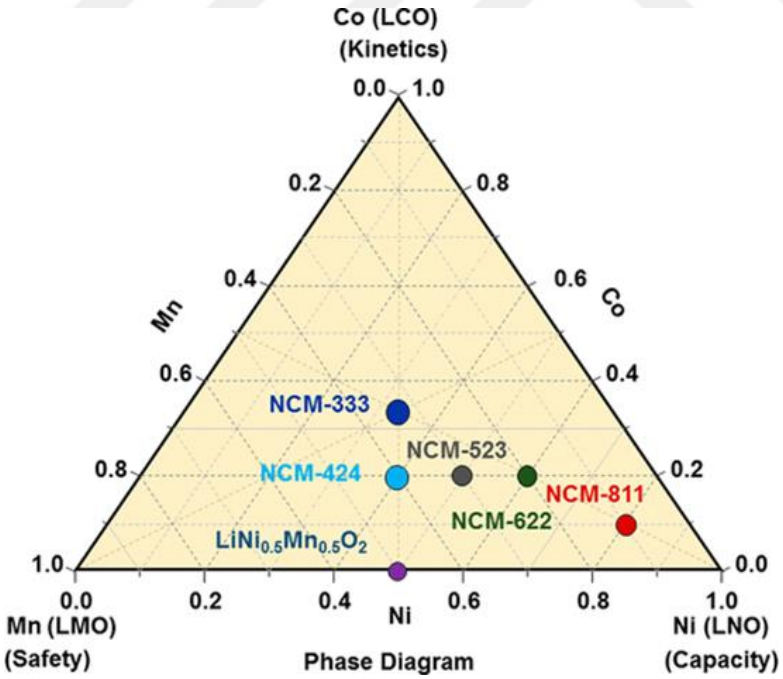

Figure 2.4 : NMC chemistries in LCO-LNO-LMO ternary system [33].

In recent years, aluminium has been used to synthesize NCA cathodes as a substitute for manganese. Here, aluminium provides thermal stability by inhibiting cation migration at high temperatures. Additionally, modification methods such as surface

coating, doping with various cations (e.g., Na^+, Zr^+, Ti^+, Mg^+), and anions such as F^- are under research to improve the structural stability of nickel-rich cathodes [33].

The last group covers cathode active materials with the olivine structure, $LiMPO_4$ (M = Fe, Mn, Ni, or Co). Today, mainly $LiFePO_4$ (LFP) cathodes are investigated to be used in lithium ion batteries. They are cheaper, less toxic, and safer than layered cathodes. The main drawback of LFP cathodes is their low capacity of 170 mAh/g [34]. To improve the electrochemical performance of LFP cathodes, recent studies focus on combining isomorphous elements into olivine structures such as Mn, Co, and Ni. The voltage capacity curves of various olivine cathodes are presented in Figure 2.5. Although their low capacity, olivine-based cathode active materials found their place in EVs.

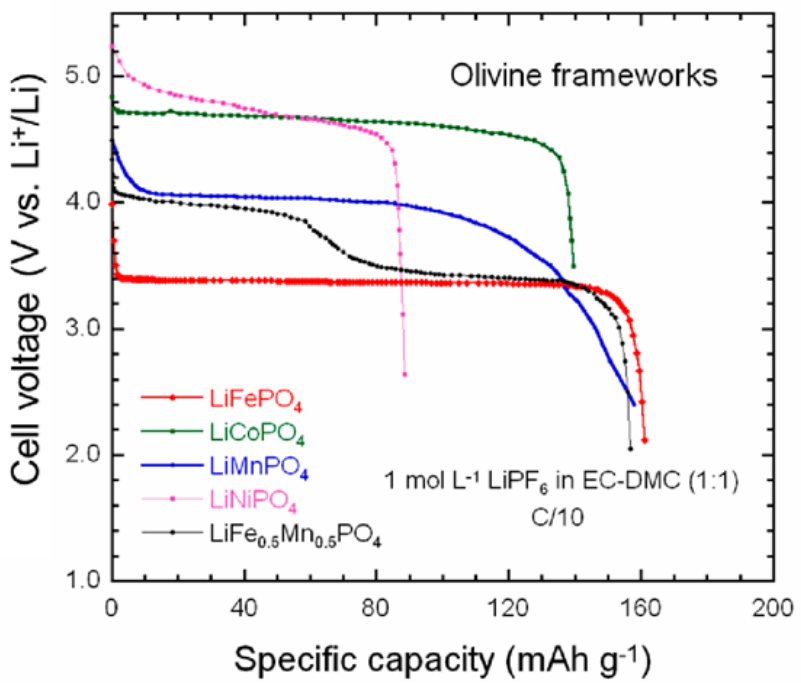

Figure 2.5 : Voltage capacity curves of various olivine cathodes [35].

2.2.3 Electrolyte

Electrolyte is one of the major components affecting battery performance due to its direct relationship with ion transportation and electrode surface passivation. Generally, an electrolyte is expected to have high ionic conductivity, wide electrochemical window, high thermal stability at a wide temperature range, high chemical stability, low electrical conductivity, low toxicity, and cost. Developing advanced electrolytes that can safely work at high voltages and promote the growth of a stable SEI layer could improve the electrochemical performance of batteries [36].

Liquid electrolytes are a mixture of solvents and lithium salts. Dipolar organic solvents are commonly used in electrolytes as solvents. A brief comparison is given in Table 2.1. Among them, alkyl carbonates are seen as the most suitable ones. DMC (dimethyl carbonate) and PC (propylene carbonate) are suitable solvents for their low viscosity and thermal stability. However, using these solvents solely is not possible due to their inability to form a passivation layer in the presence of lithium-based salts [37]. This requires the addition of ethylene carbonate (EC) to the solvent mixture to improve the formation of a good passivation layer on the graphite electrode surface.

Table 2.1 : Physicochemical properties of common alkyl carbonates [36,37].

Carbonate	Structure	Boiling point (°C)	Flash point (°C)	Dynamic viscosity (mPa)	Oxidation potential (V vs. Li/Li^+)
PC	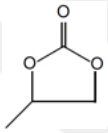	242	135.5	4.81	5.2
EC	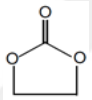	248	145.5	4.61	6.7
EMC	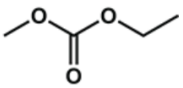	110	23.5	0.89	6.1
DMC	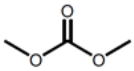	91	16	0.76	5.5
DEC	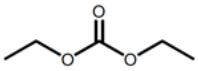	126	33	0.96	5.2

Lithium salts are essential in electrochemical performance as a complementary electrolyte part. The basic requirements of lithium salts are good solubility in suitable solvents, high ionic conductivity, chemical stability, low molecular weight and toxicity, effective SEI formation, and low cost. Some of the most commonly reported lithium salts are lithium hexafluorophosphate ($LiPF_6$), lithium tetrafluoroborate ($LiBF_4$), lithium bis (oxalate) borate (LiBOB), and lithium bis (trifluoromethane sulfonimide) (LiTFSI) [38]. Table 2.2 provides a comparison of lithium salts. $LiPF_6$ salts stand out when all parameters are taken into account.

Table 2.2 : Comparison between lithium salts [38].

Property	Excellent	Very good	Good	Fair	Poor
Ion mobility	$LiBF_4$	$LiPF_6$	$LiAsF_6$	LiTf	LiTFSI
Thermal stability	LiTFSI	LiTf	$LiAsF_6$	$LiBF_4$	$LiPF_6$
Chemical inertness	LiTf	LiTFSI	$LiAsF_6$	$LiBF_4$	$LiPF_6$
SEI formation	$LiPF_6$	$LiAsF_6$	LiTFSI	$LiBF_4$	-
Al dissolution	$LiAsF_6$	$LiPF_6$	$LiBF_4$	LiTf	LiTFSI

A different approach is modifying electrolytes with additives to prevent the formation of lithium dendrites and promote more stable SEI layer formation. Fluoro ethylene carbonate (FEC), vinylene carbonate (VC), and ethylene sulfate (DTD) could be named as a few of the many electrolyte additives. Numerous studies have been presented in the literature that electrolyte additives improve performance by promoting SEI stability and the formation of self-healing electrostatic shield on electrodes [39].

2.2.4 Separator

In lithium ion batteries, the separator aims to prevent physical contact between positive and negative electrodes. Although they do not directly participate in chemical reactions, their properties significantly impact a battery's performance. The general requirements of a separator are high ionic conductivity, thermal and mechanical stability, high wettability, having a pore size of less than 1 micron, uniform thickness, and porosity [40]. Additionally, separators are expected to close their pores at high temperatures to prevent further ion passing and thermal runaway. Expected properties from separators are listed in Table 2.3.

Porous membranes currently used in lithium ion batteries could be fabricated via polymers and/or ceramics. Although ceramic based separators provide high thermal stability, several drawbacks, such as high production cost and poor mechanical stability, limit their use in batteries. Therefore, commercial separators are often based on polymer materials. They have high ionic conductivity and ion transfer number. However, their thermal stability and wetting ability need further improvements [42]. Different types of separators used in lithium ion batteries are presented in Figure 2.6.

Table 2.3 : Ideal properties of separators [41].

Parameter	Expected Value	Affected property	Testing method
Thickness (micron)	<25	Mechanical strength	Micrometer
Ionic conductivity (S/cm)	$>10^{-4}$	Power and energy density of the battery	Impedance spectroscopy
Porosity (%)	40-60	Swelling of separator	Pycnometer
Pore volume (micron)	<1		Scanning electron microscopy
Wettability	High	Ionic transfer	Contact angle
Tensile strength (%)	<2% offset at 6894 kN/m^2	Mechanical strength	Dynamic mechanical analyzer
Shrinkage (%)	<5%	Dimensional stability	Thermal mechanical analysis

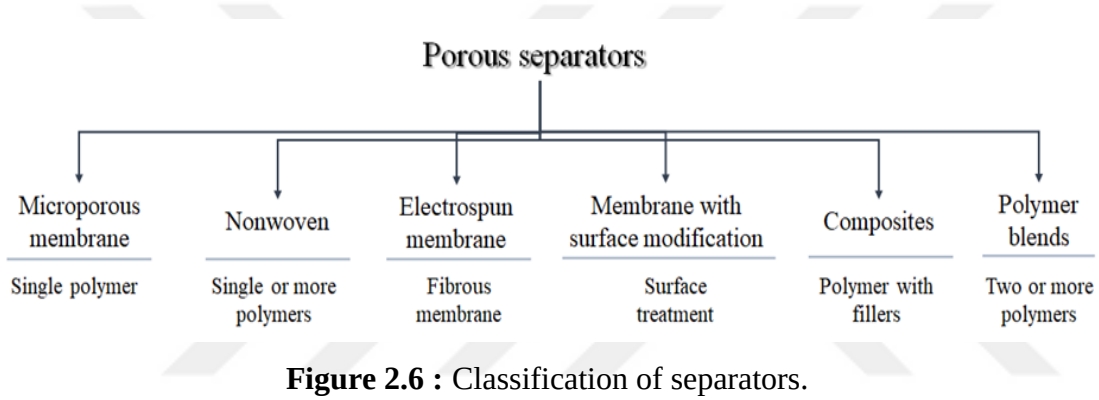

Figure 2.6 : Classification of separators.

Table 2.4 compares different types of separators. Microporous separators are the most common type used in lithium ion batteries.

Table 2.4 : Comparison between different type separators [43].

Type of Separator	Advantages	Disadvantages
Microporous	High chemical stability High mechanical properties Good conductivity	Some polymers (e.g. PVDA, PAN) exhibit low wettability
Composite	High mechanical strength, wettability, ionic conductivity, thermal stability	Thicker separators could be produced due to coating leading to increased resistance
Nonwoven mats	Usually show good cycling and rate performance	Might have lower porosity and lower pore size than 1 micron
Gel-polymer electrolytes	Can work as separator and electrolyte Very good ionic conductivity	Poor mechanical strength and electrochemical performance

Microporous separators are commercially available due to their advantages and ease of production. Commercial separators usually have a 20-25 micron thickness, 40-60% porosity, and pore sizes lower than 1 micron. Table 2.5 gives a general comparison of commercial microporous separators.

Table 2.5 : Comparison between commercial microporous separators [44].

Properties	**Celgard 2730**	**Celgard 2400**	**Celgard 2320**	**Celgard 2325**	**Asahi Hipore**
Structure	Single layer	Single layer	Trilayer	Trilayer	Single layer
Composition	PE	PP	PP/PE/PP	PP/PE/PP	PE
Thickness (µm)	20	25	20	25	25
Porosity (%)	43	40	42	42	40
Melting temperature (°C)	135	165	135/165	135/165	138

3. ANODE ACTIVE MATERIALS

Metallic lithium was the first anode material used in lithium-ion batteries due to its very high theoretical capacity. However, safety concerns led to the discontinuation of its use in battery applications, leading the way for the rise of graphite as a preferred material. Graphite was first utilized as an anode by Sony in commercial batteries in 1991, and its adoption grew rapidly thereafter.

Over time, research has expanded to include various carbon-based materials, metal oxides, lithium titanate, and more recently, silicon-based anodes [45]. Today, while graphite remains the primary anode material used commercially, lithium titanate is also employed depending on the specific application. Additionally, a mixture of graphite and silicon has recently found its way into commercial applications (Figure 3.1).

Table 3.1 and Figure 3.2 compare anode active materials [46]. Metallic lithium and silicon gain attention for their high theoretical capacities, while graphite anodes step forward with a low working potential against lithium. Lithium titanate anodes find applications with low volumetric change, hence their high safety.

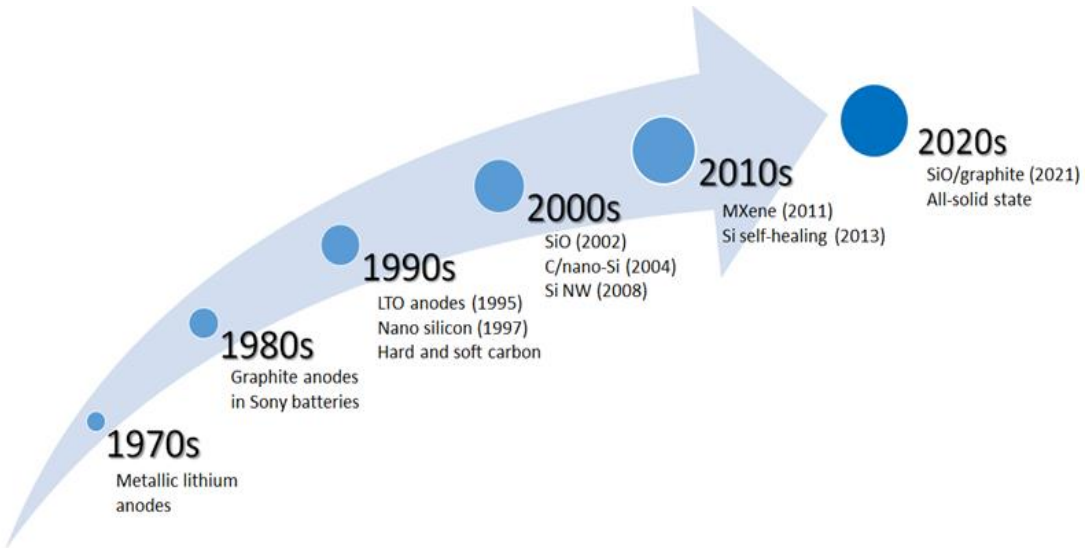

Figure 3.1 : Historical development of anode active materials.

Table 3.1 : General comparison of anode active materials [46].

Materials	Lithium metal	Graphite	Lithium Titanate	Silicon
Theoretical capacity (mAh/g)	3862	372	175	3579
Theoretical Energy Density (mAh/cm^3)	2047	837	613	9786
Volumetric change (%)	100	12	1	320
Density (g/cm^3)	0.53	2.25	3.5	2.33
Working potential (vs. Li^+/Li)	0	0.05	1.6	0.4
Lithiated structure	Li	LiC_6	$Li_7Ti_5O_{12}$	$Li_{4.4}Si$

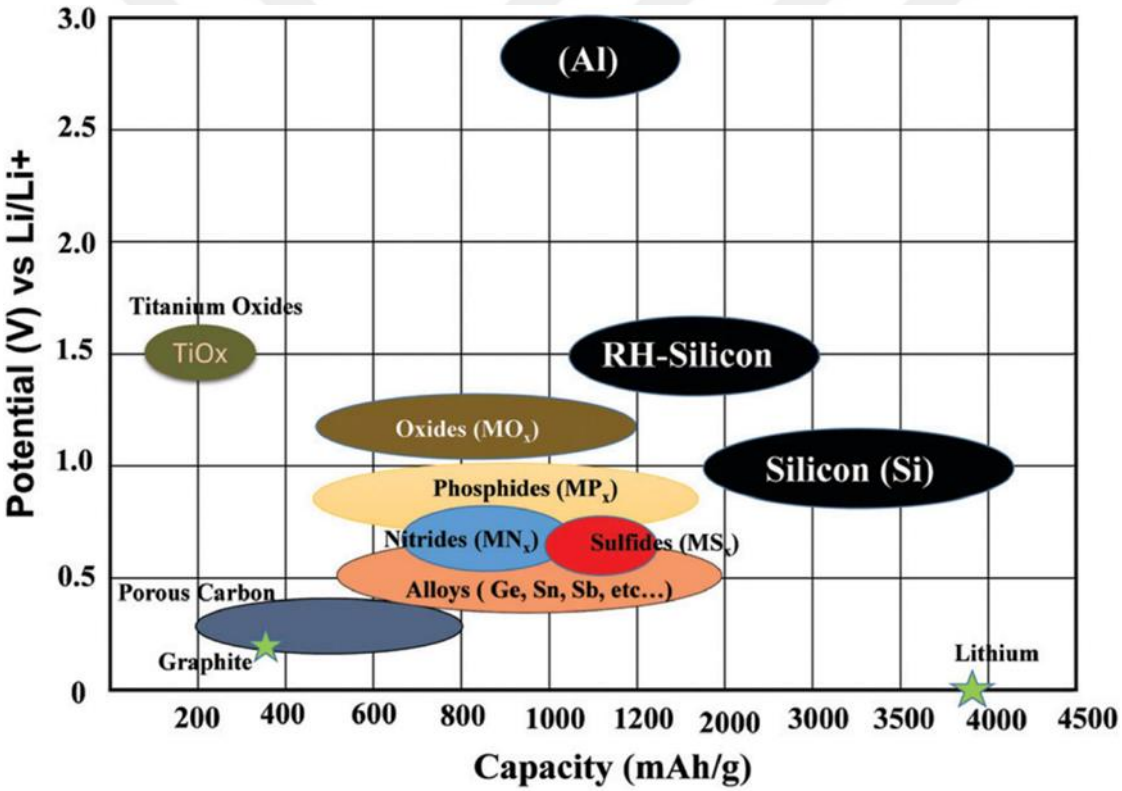

Figure 3.2 : Voltage capacity diagram of common anode active materials [47].

3.1 Lithium Metal

Due to its high theoretical capacity (3862 mAh/g), lithium metal is a great candidate for anode active material in lithium ion batteries. The redox reaction as dissolution and deposition of lithium takes place during the charge and discharge steps and given in Equation 3.1 below [48]:

$$xLi \leftrightarrow xLi^{+} + xe^{-} \tag{3.1}$$

However, having only one electron on its outer shell makes lithium highly reactive and thermodynamically unstable [49]. Additionally, its nonporous and flat surface results in high local current densities caused by the electric field lines perpendicular to its surface, which leads to forming dendrites, an unstable SEI layer, and electrolyte decomposition [50,51]. All these undesired side reactions, studied by Tikekar et al. [52] in Figure 3.3, raise safety concerns about metallic anodes.

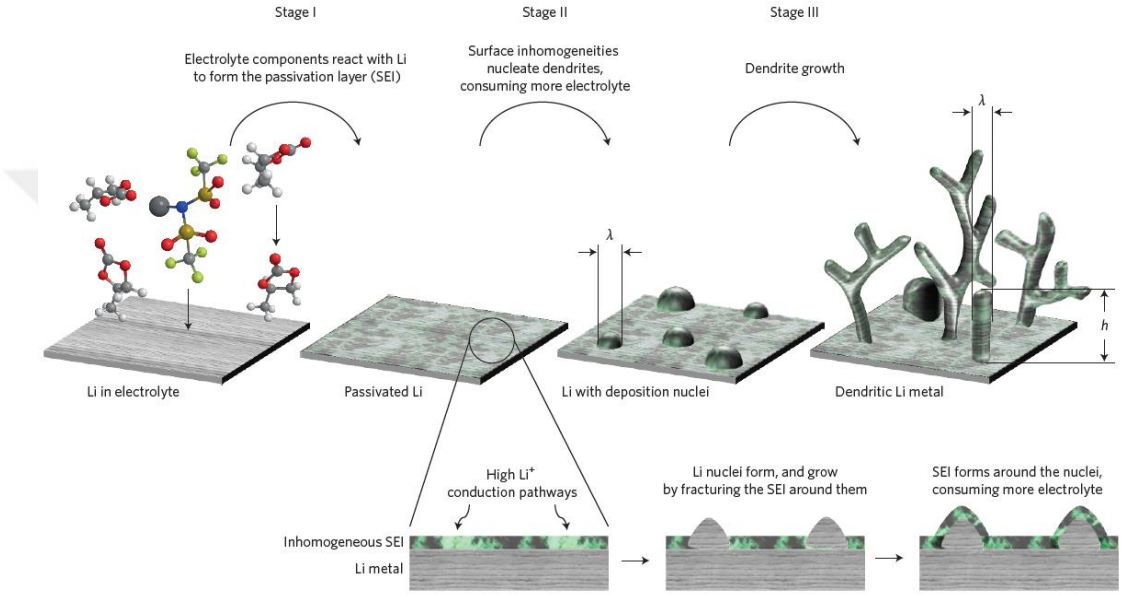

Figure 3.3 : Schematic drawing of lithium metal failure mechanisms [52].

Lithium metal reacts with almost all types of electrolytes, including solid electrolytes. Tasaki et al. [53] conducted ab initio calculations to investigate the reactivity of lithium metal in the presence of various electrolytes and additions (e.g., ethylene carbonate, vinylene carbonate, propylene carbonate, vinyl ethylene carbonate). According to their calculations, electrolytes and additives undergo exothermic and spontaneous reactions in the presence of lithium. Later, many studies confirmed these reaction products as Li_2O, LiF, LiOH, Li_2CO_3, $(CH_2OCO_2Li)_2$, CH_3OCO_2Li, $CH_2{=}CH_2$ [54,55].

Another problem with lithium metal anodes is volume changes during the charge and discharge steps. The volume changes (about 100%) observed during cycling could severely affect lithium metal anodes and cause pulverization, hence capacity loss. Lithium ions leave the metal surface during charging by passing through the SEI layer and dissolving in the electrolyte. During cathodic polarization with a stable SEI layer, these ions migrate and deposit uniformly back to the metal surface. However, when

the SEI layer loses its integrity, these lithium ions can deposit on the metal surface unevenly, resulting in dendrite formation. Later, fresh lithium ions react with electrolytes to form a new layer of SEI, which will fracture again in the following cycles. As shown in Figure 3.4, this cycle of constantly losing lithium ions and consuming electrolytes leads to capacity fade and stability problems [56].

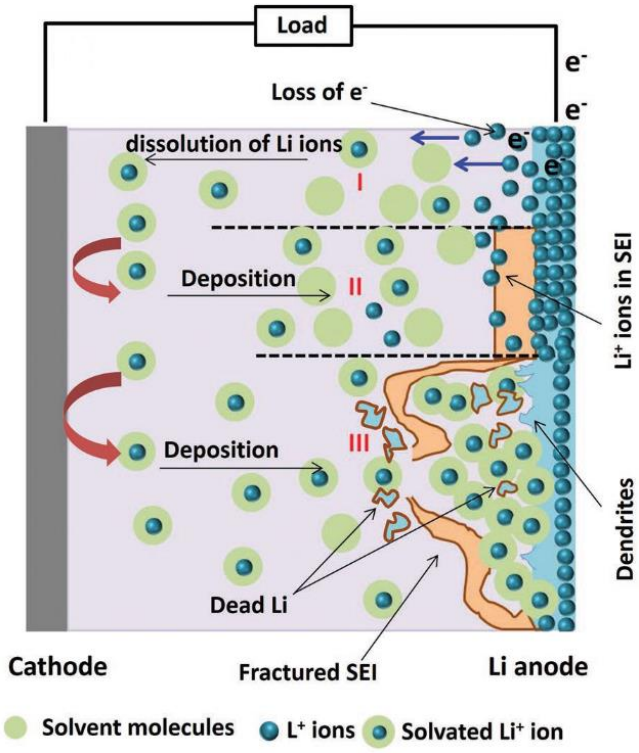

Figure 3.4 : Schematic presentation of SEI fracture and irregular Li deposition of surface [57].

Some strategies to overcome these problems could be summarized as modification of lithium, obtaining a stable SEI layer, and developing new electrolytes for lithium metal anodes. The high local current densities on the lithium metal surface cause non-uniform lithium nucleation and significant volume changes. Therefore, surface modification of lithium metal is a promising method. Zhu et al. [58] coated lithium metal surfaces with polydimethylsiloxane (PDMS) by sol-gel method. Later, the nanoporous surface is improved by acid treatment to improve ion diffusibility. Their results show good stability of lithium metal anodes with around 95% Coulombic efficiency after 200 cycles. In another study, Sun et al. [59] investigated the effect of nano-scale organic-inorganic coating on the electrochemical stability of lithium metal anodes. They claim the hybrid organic-inorganic coating provides high stability and uniform lithium deposition on the metal surface with around 98% Coulombic

efficiency after 350 cycles. With a similar aim, Chen et al. [60] synthesized flower-shaped lithium nitrate (Li_3N) coated lithium metal anodes using the facile plasma activation method. The robust Li_3N protective layer helped to block electrolyte and lithium metal contact. It provided good capacity retention as 96% and higher specific capacity at a 5C rate compared to pristine lithium metal anode. Chen et al. [61] coated the lithium metal surface with an Al_2O_3 layer using atomic layer deposition in another research. The authors report that Al_2O_3 coating has helped reduce electrolyte consumption and improved the anode's Coulombic efficiency.

Designing 3D composite electrodes is another promising way to control volume exchange and inhibit dendrite formation in Li anode half cells. Metal, lithium, and carbon-based materials are the most commonly used hosts for lithium deposition. Zhu et al. [62] produced a unique anode design (CuFG@Li) with graphene-nested copper foam as a lithium host. This design uses graphene to create micron-sized cages within the copper foam used as a lithium deposition matrix. The anode provided high Coulombic efficiency (98%) for 200 cycles at 1 mA/cm^2 current load. In another study, Liu et al. [63] used N-doped graphitic carbon foams (NGCFs) to promote uniform Li nucleation in lithium metal anodes. The resulting 3D carbon-based design provided a high Coulombic efficiency of 99.6% over 300 cycles.

In addition to electrode design, a distinct effort is made to design electrolytes for more stable lithium metal anodes. Numerous studies about both liquid and solid electrolytes could be found in the literature [64,65]. When liquid electrolytes are used, the SEI layer is formed, and it contains many organic and inorganic components as a result of the decomposition of the electrolyte. While the organic components, such as polyolefins, decrease the electrical conductivity but increase flexibility, the inorganic components, such as LiF and Li_2CO_3, provide relatively better lithium ion conductivity [66]. An ideal mixture of organic and inorganic components is necessary for optimum Li metal anode performance for protective SEI design.

Very recently, gel and solid electrolytes have gained remarkable interest in eliminating the stability problems of liquid electrolytes. Gel electrolytes could have poly(methyl methacrylate)-PMMA, polyvinylidene fluoride-PVDF, and poly(vinylidene fluoride-cohexafluoropropylene) (PVDF-HFP) based matrixes [66]. Today, gel electrolytes provide a wide working potential window, good compatibility with anode and cathode active materials, and moderate ionic conductivity. Along with these advantages,

further improvements are needed to find a balance between mechanical strength and ionic conductivity [67].

Solid electrolytes are the newest members of the electrolyte family and can be categorized as solid polymer and solid ceramic electrolytes. PEO (Poly(Ethylene Oxide)) for polymer electrolytes, perovskite, and sulfides for ceramic electrolytes [66].

3.2 Carbon-Based Anode Active Materials

Carbon-based anode active materials gain attention due to their low density, structural and chemical stability, high abundance, and low cost. Based on their structure, they can be divided into two groups: graphitic and non-graphitic carbon. Graphitic carbons are crystalline materials that exhibit a long-range order in 3D. On the other hand, non-graphitic carbons are amorphous materials and could be described as hard and soft carbon. While soft carbons can be transformed into graphitic materials by high temperature processes, the same procedure is not possible for hard carbons [68]. Schematic representations of carbon-based materials and their electrochemical properties are presented in Figure 3.5 and Table 3.2, respectively. As seen in Figure 3.5, graphite exhibits a layered structure composed of many graphene layers, while soft and hard carbons consist of a larger fraction of less ordered layers.

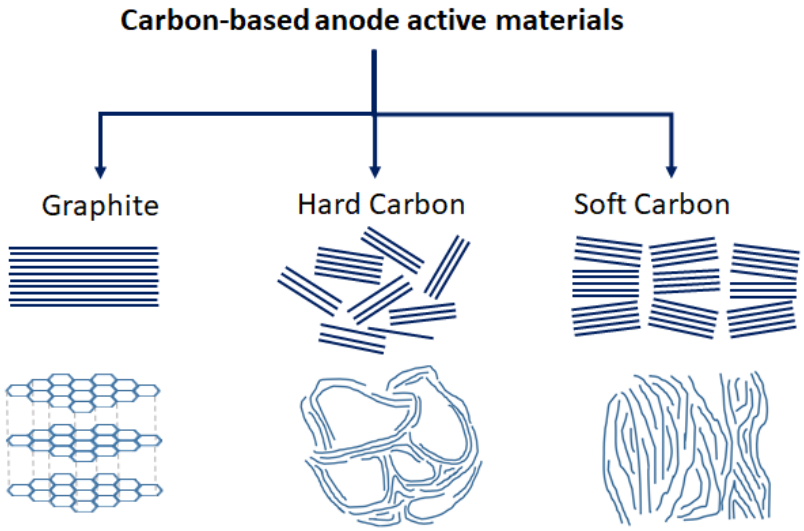

Figure 3.5 : Schematic drawing of carbon-based anode active material structures.

Table 3.2 : Comparison of the electrochemical properties of carbon-based anode active materials [68].

Materials	Graphite	Hard Carbon	Soft Carbon
Raw material	Natural graphite, pitch, petroleum coke	Resin, pitch, biomass	Pitch, petroleum coke
Theoretical capacity (mAh/g)	372	500-700	372
Density (g/cm^3)	~2.2	1.4-1.8	~2.2
Interlayer distance (nm)	~0.335	0.37-0.42	0.34-0.37
Initial Coulombic efficiency (%)	Very good	Poor	Very good
Volume change (%)	~10	~1	1-10
Cost	Low	High	Medium
Common application areas	Li-ion batteries	Li/Na/K-ion batteries	Na/K-ion batteries

3.2.1 Graphite

Graphite is the most commonly used commercial anode active material. The lithium storage capability of graphite has been known since 1975. However, using propylene carbonate (PC) electrolytes results in failure due to the exfoliation of graphite electrodes. In 1983, Yazami and Touzain incorporated graphite anodes using solid polymer electrolytes. Later, in the 1990s, Dahn et al. successfully achieved the reversible intercalation in graphite anodes when ethylene carbonate (EC) was used due to stable SEI layer formation. In 1991, Sony introduced the first commercial lithium ion battery using PC electrolyte and coke anode. A more suitable EC/DMC (dimethyl carbonate) electrolyte and graphite anode combination was developed by Guyomard and Tarascon in 1993 and is still used in many commercial lithium ion batteries today [69]. A summary of graphite anode developments is presented in Figure 3.6.

Graphite consists of sp^2 hybridized graphene layers connected by Van der Waals forces. These layers could be stacked in hexagonal ABAB form (thermodynamically stable form) or rhombohedral ABCABC stacking [70]. The weak van der Waals forces allow reversible intercalation of secondary species such as Li^+. The resulting LiC_6 alloy, the highest lithium content at room temperature conditions, leads to 372 mAh/g theoretical and 850 mAh/cm^3 volumetric capacities of graphite anodes [69]. The insertion of lithium ions into the layered structure increases the interlayer distance

between graphene layers from 3.35 Å to 3.70 Å, which accounts for around 10% volumetric change [71].

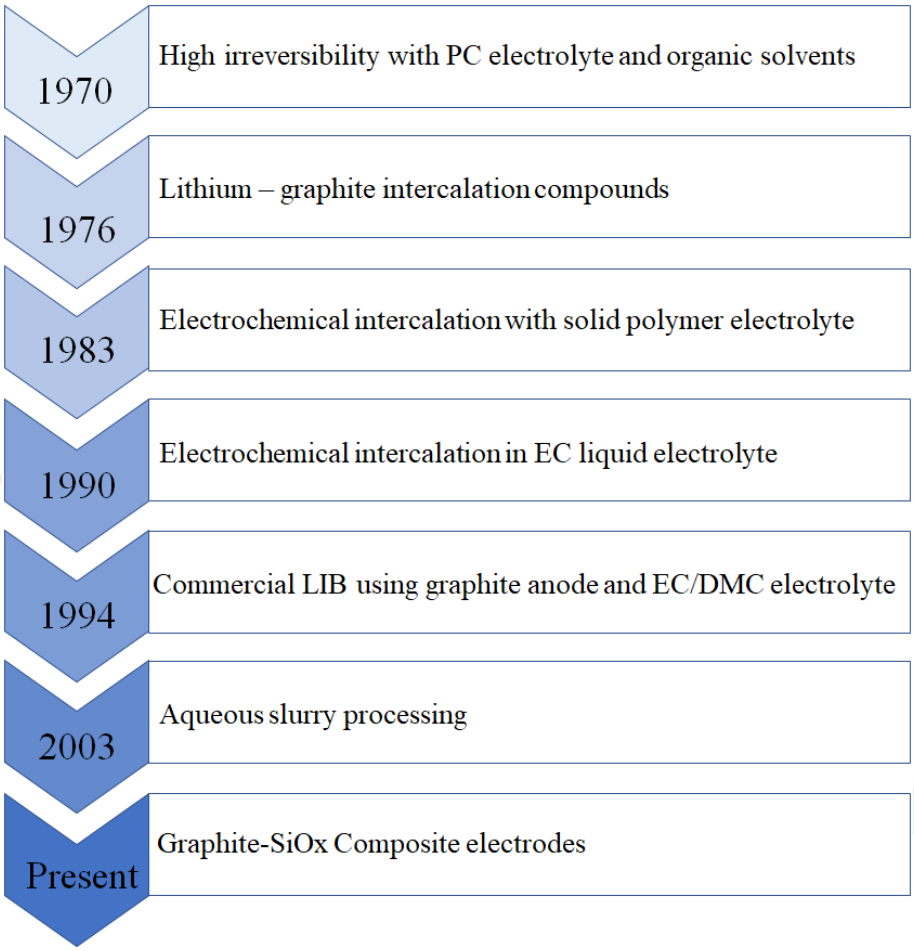

Figure 3.6 : Developments in graphite anodes.

The lithium intercalation into graphite occurs between 0.01 and 0.25 V vs. Li/Li^+ according to Equation 3.2 below. The reversibility of intercalation reactions is highly related to the stable SEI layer formed on graphite anodes. Many organic carbonate-based electrolytes decompose around 0.8 V vs. Li/Li^+. Outside of the electrochemical stability window of an electrolyte, intercalation of solvent ions and electrolyte decomposition on the graphite surface at low potentials result in exfoliation of graphene layers and lead to capacity fade [72].

$$C_6 + xLi^+ + xe^- \rightarrow Li_xC_6 \tag{3.2}$$

The voltage capacity curve of graphite is presented in Figure 3.7. The voltage plateau around 0.2 V vs. Li/Li^+ is seen. This plateau provides the majority of the graphite's capacity.

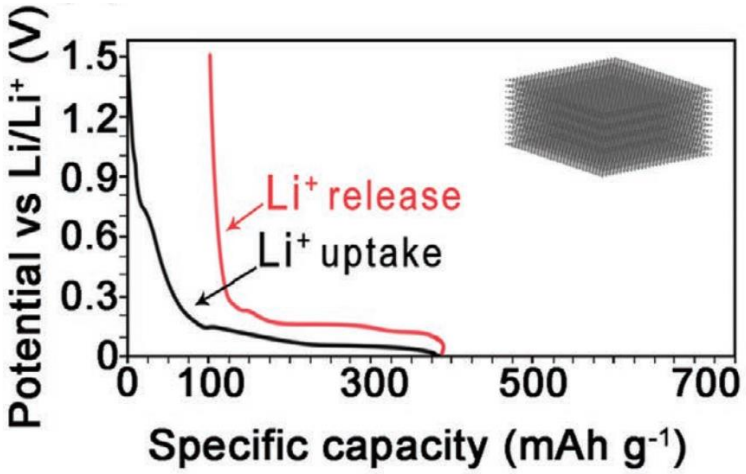

Figure 3.7 : A typical capacity voltage curve of graphite [73].

The energy density of a battery is a function of both the specific capacity and the working potential of active materials. Therefore, graphite's low working potential creates an advantage over other anode active materials. Among other anodes, it has the second lowest working potential (0.2 V vs. Li/Li^+) after lithium metal. On the other hand, the rate capability of graphite anodes remains a challenge. High rates cause the risk of lithium plating on the electrode surface and lead to safety risks. Many studies relate the rate capability of graphite anodes with their particle size and morphology [74,75]. Therefore, modifying the electrode properties could enhance the electrochemical performance. A significant drawback of graphite anode is irreversible capacity loss during the first cycle, which results from the lithium consumption during electrolyte decomposition. Different strategies, such as graphite surface modification or electrolyte additives, are being explored to promote the growth of a more stable SEI layer to improve capacity retention.

As studied by Kim et al. [76], one approach involves etching the graphite surface with KOH to create pores and increase active sites for lithium intercalation. The modified surface helped to achieve higher specific capacity and better rate performance. In another study, Hai et al. [77] embraced ion implantation for nitrogen doping to improve the electrochemical performance of graphite anodes. They reported a 29% increase in volumetric capacity for nitrogen-doped graphite anodes due to increased lattice distance and defects. Additionally, many studies show that electrolyte additives improve cycling performances by deactivating defective sites and helping build a stable SEI layer on electrode surfaces [78–80].

The graphite used in lithium ion batteries could be classified as natural graphite (NG) and synthetic graphite (SG). Both are polycrystalline materials that consist of an enormous number of single-crystalline domains [81]. While a more oriented structure is seen in natural graphite, it is more random in synthetic graphite. For comparison, SEM images of natural and synthetic graphite are presented in Figure 3.8.

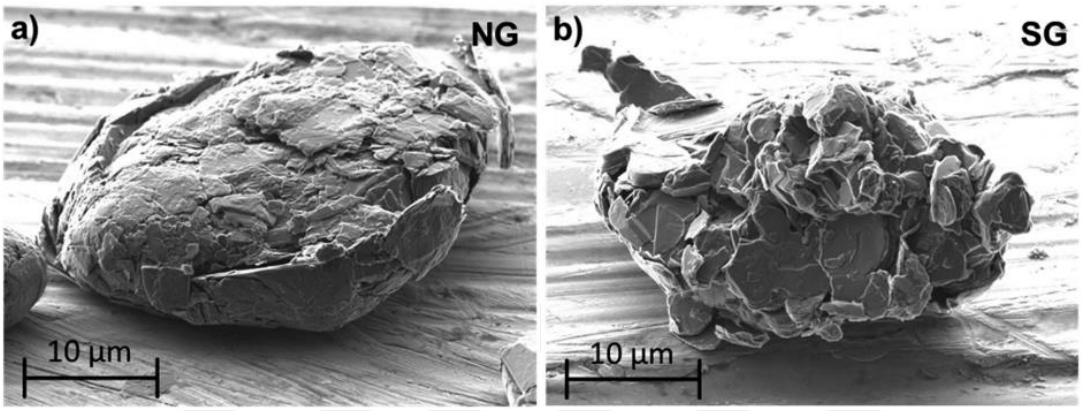

Figure 3.8 : SEM images of natural graphite (NG) after processing and synthetic graphite (SG) [69].

The production processes for natural and synthetic graphite have some distinct differences. The production of natural graphite begins with mining and flotation, which helps to remove impurities such as silicon (Si), sulfur (S), potassium (K), and nitrogen (N), achieving a purity level of 95%. Following this, the spheroidization process is employed to produce micron-sized spherical graphite particles. Finally, either acid leaching or high temperature processing is used to reduce the impurity level to below 500 ppm. Additionally, the surface of the graphite particles is coated with carbon to enhance their electrochemical performance. An overview of the general steps involved in the natural graphite production route can be seen in Figure 3.9.

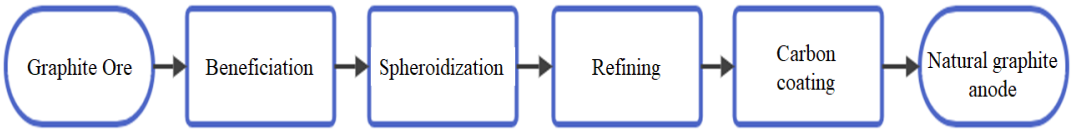

Figure 3.9 : Natural graphite anode production flow chart.

On the other hand, synthetic graphite is produced in three main steps. First, precursors such as coal are calcined around 800-1200 °C to obtain soft carbon, followed by grinding and sorting depending on particle sizes. Later, a second heat treatment step, around 2500 °C, is applied for graphitization. In the final step, particles are coated with

carbon to improve electrochemical properties [82]. The production flow chart is presented in Figure 3.10.

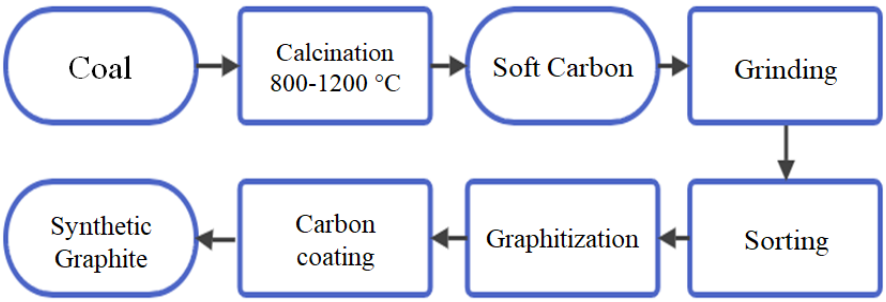

Figure 3.10 : Synthetic graphite anode production flow chart.

The world's graphite reserves and productions are presented in Tables 3.3 and 3.4. Among all countries, China has the highest annual graphite production. In recent years, increased pollution has led China to shut down many factories and has directly influenced the graphite market. Although the large graphite reserves are located in Türkiye, the amorphous nature of ores makes them challenging to use in battery production. Since 2004, graphite has been listed in the European Union's critical raw material list [83]. Considering the increased demand for electric vehicles, a natural graphite supply shortage is expected by 2026 [84]. Therefore, finding alternative anode active materials to substitute graphite has increased importance.

Table 3.3 : World graphite reserves by country, 2022 [85].

Country	Million tonnes	Percentage of total
Türkiye	90	27.3
Brazil	74	22.4
China	52	15.8
Madagascar	26	7.9
Mozambique	25	7.6
Tanzania	18	5.5
India	8	2.4
Uzbekistan	7.6	2.3
Canada	5.9	1.8
Mexico	3.1	0.9
Other countries	20.4	6.2
Total	330	100%

Table 3.4 : World graphite production by country, 2022 [85].

Country	Thousand tonnes	Percentage of total
China	850	65.6
Mozambique	170	13.1
Madagascar	110	8.5
Brazil	87	6.7
Russia	15	1.2
Canada	13	1
Norway	10	0.8
India	8.3	0.6
North Korea	8.1	0.6
Ukraine	3	0.2
Other countries	21.6	1.6
Total	1296	100%

3.2.2 Hard carbon

Hard carbons, also known as non-graphitizable carbon-based materials, could be associated with a structure consisting of large fractions of curved graphene sheets, which are arranged randomly. Even at ultrahigh temperatures such as 3000 °C, these layers cannot be rearranged to form an ordered graphitic structure [68]. This property is assigned to cross-linking and covalent bonds of C-O-C. During pyrolysis, hard carbon precursors such as resin or pitch form rigid bonds, defects, and micropores that inhibit the growth of ordered graphene sheets to form graphite structure. Because of these, hard carbon structure is generally rich in pores, defects, and edges with only a small range of graphite domains. Different structural models proposed for hard carbons are presented in Figure 3.11.

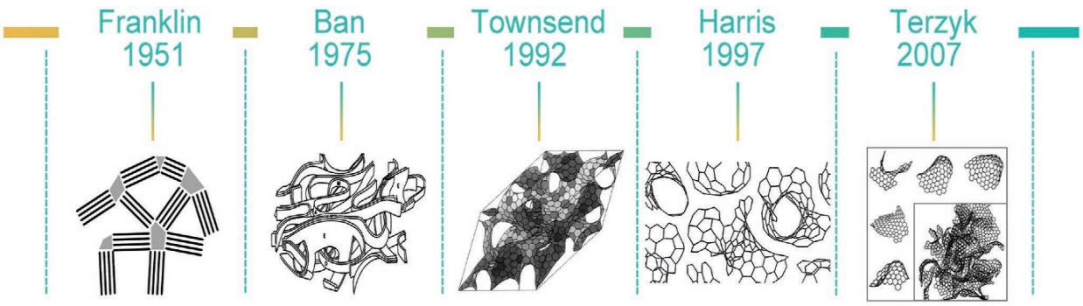

Figure 3.11 : Proposed hard carbon structures in literature [68].

The disordered and porous structure of hard carbons benefits lithium diffusion and creates active sites for charge transfer reactions. These result in high charge and rate capacity and good performance at low temperatures. Two lithiation mechanisms are proposed for hard carbons. In the model proposed by Sato et al. [86], Li^+ ions are located at ionic and covalent sites on the carbon structure. There, Li_2 covalent molecules with saturated LiC_2 are formed, which results in high energy density. In another model, Besenhard et al. [73] proposed that Li^+ ions react with graphitic sites and cavities, which results in a high reversible capacity to hard carbons. A schematic presentation of lithium storage in hard carbons is presented in Figure 3.12. Lithium adsorption occurs at defective sites; here, lithium ions occupy pore sites and intercalation reactions occur in graphitic domains.

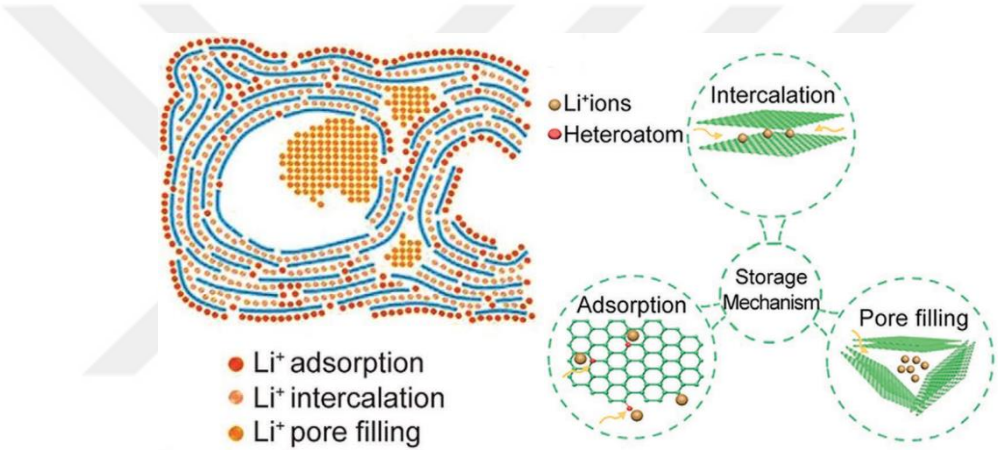

Figure 3.12 : Lithium storage mechanism of hard carbons [87,88].

Winter et al. [73] investigated the voltage capacity curves of carbon-based materials. In Figure 3.13, the intercalation of lithium ions starts at 0.8 V vs. Li/Li^+, and there is no distinct plateau; rather, a visible slope is seen. The slope is found to be related to the heterogeneous structure of hard carbons, which have graphitic and disordered domains.

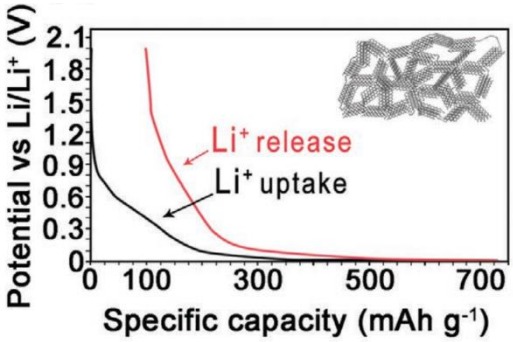

Figure 3.13 : A typical capacity voltage curve of hard carbon [73].

According to the study conducted by Yang et al. [89], a high slope seen at high voltages is related to surface adsorption, resulting in a high diffusion coefficient. At lower voltages, insertion instead of adsorption becomes the dominant reaction for lithium storage (see Figure 3.14).

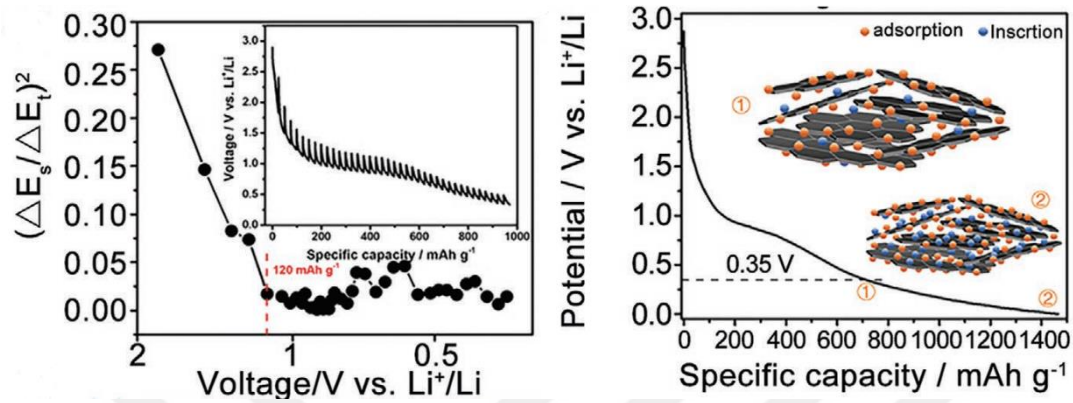

Figure 3.14 : Change in the diffusion coefficient and specific capacity according to voltage [89].

The electrochemical performance of hard carbons is highly affected by the precursor. Despite their high price, resin-based hard carbons are seen to deliver the best electrochemical performance due to their pore structures and surface chemistries. Therefore, research is mainly focused on synthesizing the desired structure with improved electrical conductivity. Qian et al. [90] synthesized P-doped resin-based hard carbon anodes using phosphoric acid and resin. The synthesized anode delivered 1294 mAh/g specific capacity with 60% initial Coulombic efficiency. Pitch is another precursor used in hard carbon synthesis at more reasonable prices than resin. The coal tar pitch (CTP) is mainly used for hard carbon synthesis due to its easy-to-graphitize structure. Guo et al. [91] produced CTP-based hard carbon anodes with 829 mAh/g initial charge capacity using oxidation and carbonization processes.

3.2.3 Soft carbon

Soft carbons exhibit similar properties to both graphite and hard carbons. While they possess a larger fraction of graphitic domains than hard carbons, they still do not fully consist of long-range 3D order. Soft carbons could be produced by heat treatment of carbonaceous materials at high temperatures, such as pitch and petroleum coke. The carbonization process takes place in three steps: pyrolysis, carbonization, and graphitization. During pyrolysis, carbonaceous materials decompose, and volatile components such as CO, CO_2, H_2O, and CH_4 are removed as gaseous products [92].

When the decomposed material possesses a semifluid state, the graphitization process occurs easily at high temperatures (1000-2000 °C) and forms soft carbons.

A structural comparison of graphite, soft, and hard carbons is studied by Adams et al. [93], and the results are presented in Figure 3.15. Further investigation of the carbon structure by Raman spectroscopy shows that all samples have D and G bands representing ordered and disordered structures. Contrarily, the 2D band is only seen in graphite, indicating the lower number of stacked graphene layers in hard and soft carbons. XRD patterns further confirm the disordered structure. A single peak is seen in the graphite sample, while amorphous structures associated with broad peaks are observed in hard and soft carbon spectra.

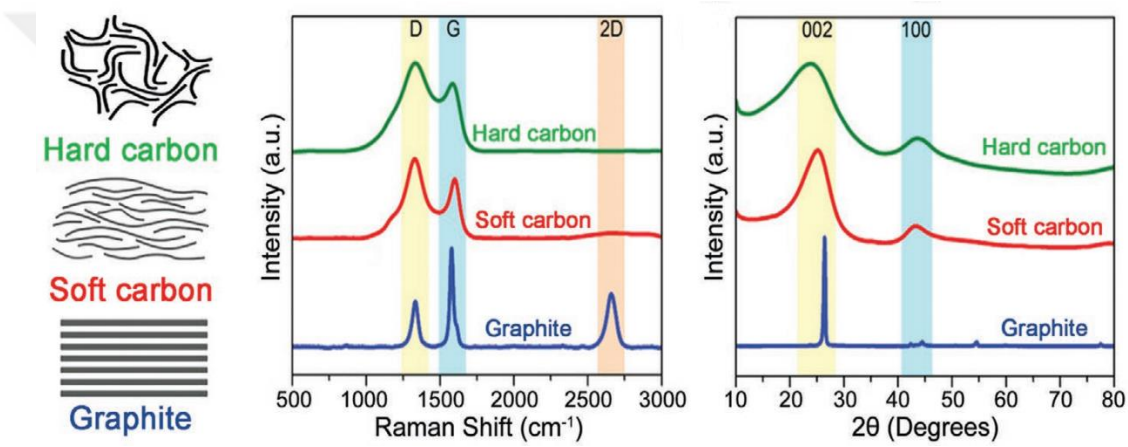

Figure 3.15 : Structural comparison between graphite, soft and hard carbons [93].

The lithiation mechanisms of soft carbons are found to be similar to those of hard carbons. The intercalation of lithium ions starts at 1 V vs Li/Li^+, with no visible plateau. The voltage and specific capacity show a linear change, which results in lower specific capacity (see Figure 3.16).

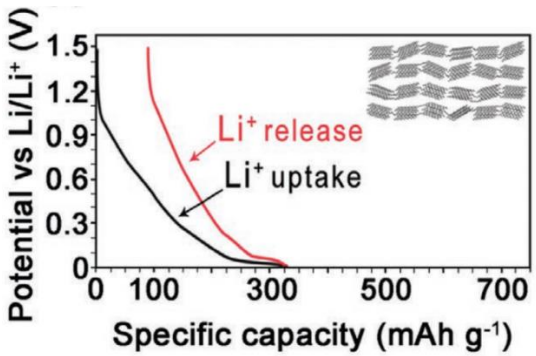

Figure 3.16 : A typical capacity voltage curve of soft carbon [73].

So far, different precursors have been used to produce anode-active materials. Kim et al. [94] prepared pitch-based anode active materials and investigated the effect of pitch crystallinity and softening point on the electrochemical performance. The samples delivered 300-350 mAh/g specific capacity with 70-78% initial Coulombic efficiency. According to their results, pitch with a high softening point resulted in an increased crystallinity, and it delivered better capacity and rate performance. In another study, Ko et al. [95] synthesized anode active materials using petrochemical waste, namely pyrolysis fuel oil (PFO). PTO-based soft carbon anode delivered 366 mAh/g reversible capacity with 99% capacity retention over 100 cycles. Soft carbon gained popularity with its high capacity retention. By combining silicon anodes with soft carbons, high energy density anodes exhibiting good retention could be achieved [96].

3.3 Lithium Titanate ($Li_4Ti_5O_{12}$)

Lithium titanate (LTO), first reported by Jonker in 1956, finds its place in practical battery applications due to its high safety and cycle stability [97]. The high working voltage of these anodes (around 1.55 vs. Li/Li^+) lies inside the stability window of most electrolytes, therefore minimizing the SEI layer formation. The flat reaction plateau caused by a two-phase lithiation/delithiation mechanism and almost no volume change provides cycle stability with a long life [98]. Although its merits, low electrical conductivity (around 10^{-8} to 10^{-13} S/cm) and lithium diffusion coefficient (about 10^{-8} to 10^{-13} cm^2/s) limits the rate performance of LTO anodes [99].

The lithiation reactions of LTO are given in Equation 3.3. The galvanostatic curve is presented in Figure 3.17. Its theoretical capacity is calculated as 175 mAh/g using Equation 3.3 [97]. The lithiation reaction of LTO is believed to be a two-phase mechanism. During discharge, lithium ions insert 16c octahedral sites in the crystal structure; the same reaction occurs for lithium ions present in 8a sites. In conclusion, 16c sites are equally filled by lithium ions inserted from outside and transferred from 8a sites [100].

$$Li_4Ti_5O_{12} + 3Li^+ + 3e^- \leftrightarrow Li_7Ti_5O_{12} \quad (3.3)$$

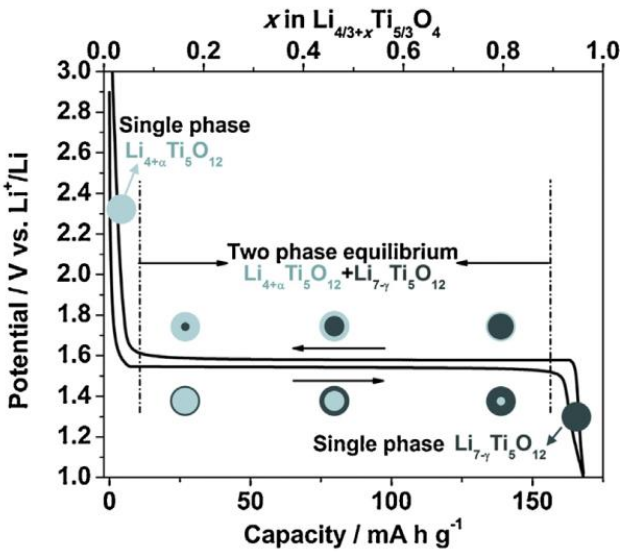

Figure 3.17 : Two-phase lithiation of LTO anodes presented in voltage capacity curve [97].

The resulting $Li_7O_5Li_{12}$ phase can host more lithium ions in empty 8a sites. However, to provide cycling stability, the cut-off voltage for discharge is often selected as 1 V. The study conducted by Huang et al. [101] proves the intercalation of more lithium ions when LTO anodes are further discharged to 0.5 V. Another study by Yao et al. [102] shows discharging LTO to near 0 V results in higher reversible capacities around 250 mAh/g. The lithium insertion and extraction from the spinel LTO crystal structure are shown in Figure 3.18.

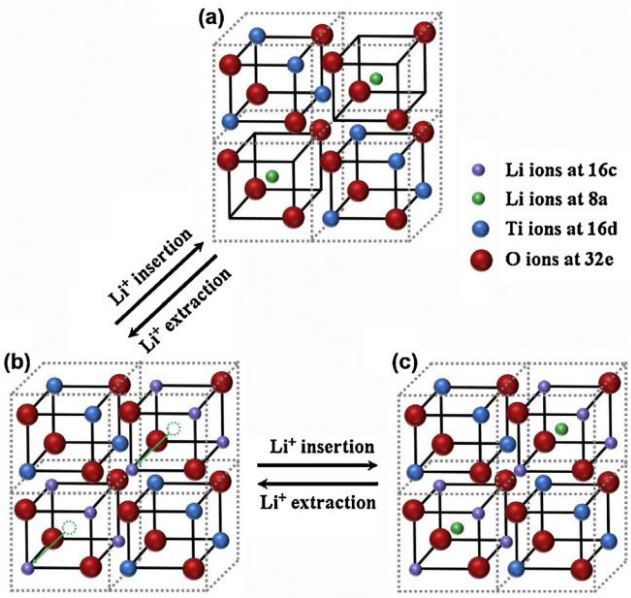

Figure 3.18 : Spinel LTO crystal structure with lithium insertion **a)** at 3 V **b)** between 1-3 V **c)** between 0.01 - 1 V [103].

The cycle performance of LTO anodes can be improved by different strategies such as nanostructuring, coating, and doping. Generally, spinel LTO is produced by the solid-state reaction of TiO_2 and a lithium source such as LiOH or Li_2CO_3 at high temperatures (above 800 °C) for a long period (12-24 hours) [104]. Although the long reaction time provides high purity, the particles produced are usually large in size and low in surface area. The particle size of LTO could be decreased to shorten the lithium diffusion path and improve the electrochemical performance of LTO anodes. Venkateswarlu et al. [105] synthesized $Li_4Ti_5O_{12}$ particles with 39 nm particle size and high purity using titanium isopropoxide and lithium acetate. The particles delivered 255 and 142 discharge and charge capacities, respectively, at 0.1 C rate between 0.01-1.75 V. In another study, Khomane et al. [106] produced CTAB (Cetyl Dimethyl Ethyl Ammonium Bromide)-assisted $Li_4Ti_5O_{12}$ nanoparticles and tested their electrochemical performance. Their results show that CTAB-assisted LTO delivered 174 mAh/g at 0.2 C rate, while the sample produced without CTAB provided only 140 mAh/g specific capacity. Another way to shorten the lithium diffusion path is to introduce porosity into the structure. Lin et al. [107] produced porous LTO using LiCl and $TiCl_4$ as precursors. Oxalic acid is used for pore formation. The synthesized active materials delivered 167 mAh/g at 0.5 C and 133 mAh/g at 1 C rate with high capacity retention over 200 cycles. Surface coating over LTO particles is highly preferred for improving electrical conductivity. Carbon coating is the most common method using various precursors, including glucose, starch, super P, and sucrose.

Hu et al. [108] investigated the best carbon source for LTO@C anodes. According to their results, PAA is found to provide the best electrochemical performance. The LTO@C (3.5 wt% C) anodes delivered 168, 143, and 132 mAh/g at 0.2, 8, and 10 C rates, respectively. Huang et al. [109] studied the surface modification of LTO with Ag particles by thermal decomposition of $AgNO_3$. The 5 wt.% Ag resulted in the highest reversible capacity as 182 mAh/g in the potential range of 0.5 – 2.5 V. Similar to surface modification, metal ions are also used for doping to enhance the electrical conductivity of LTO anodes. Moreover, further improvement using electrolyte modifications is possible. $LiPF_6$ is the most commonly used lithium salt in EC/DMC or EC/EMC electrolytes. A combination of different additives and solvents could be beneficial for increasing thermal stability, safety, and working potential. For example,

sulfone-based electrolytes could be a more suitable alternative for LTO anodes due to their stability at high voltages [110].

3.4 Silicon-based Anode Active Materials

The first investigation of Li-Si alloys was conducted by Axel et al. in the 1960s [111,112]. Later, in the 1970s, the reversibility of the Li-Si system was shown by Sharma et al. [113]. In the late 1990s, Bourderau et al. [114] and Li et al. [115] developed the first silicon thin films and nanoparticles for lithium ion batteries, respectively. Wilson et al. [116] used CVD to produce nanosilicon-dispersed carbon anodes (up to 11 at. % Si). In the following years, different morphologies, such as nanowires [117], hollow nanospheres [118], and yolk/shell designs [119], are proposed to improve the capacity retention of silicon anodes. Recently, new binders and electrolytes have been under research to improve the performance of silicon anodes [120]. The historical developments in silicon anodes are shown in Figure 3.19. A more detailed investigation of silicon-based anode active materials is presented in Section 4 under the title "SiO_x ($0 \leq x \leq 2$) Anodes".

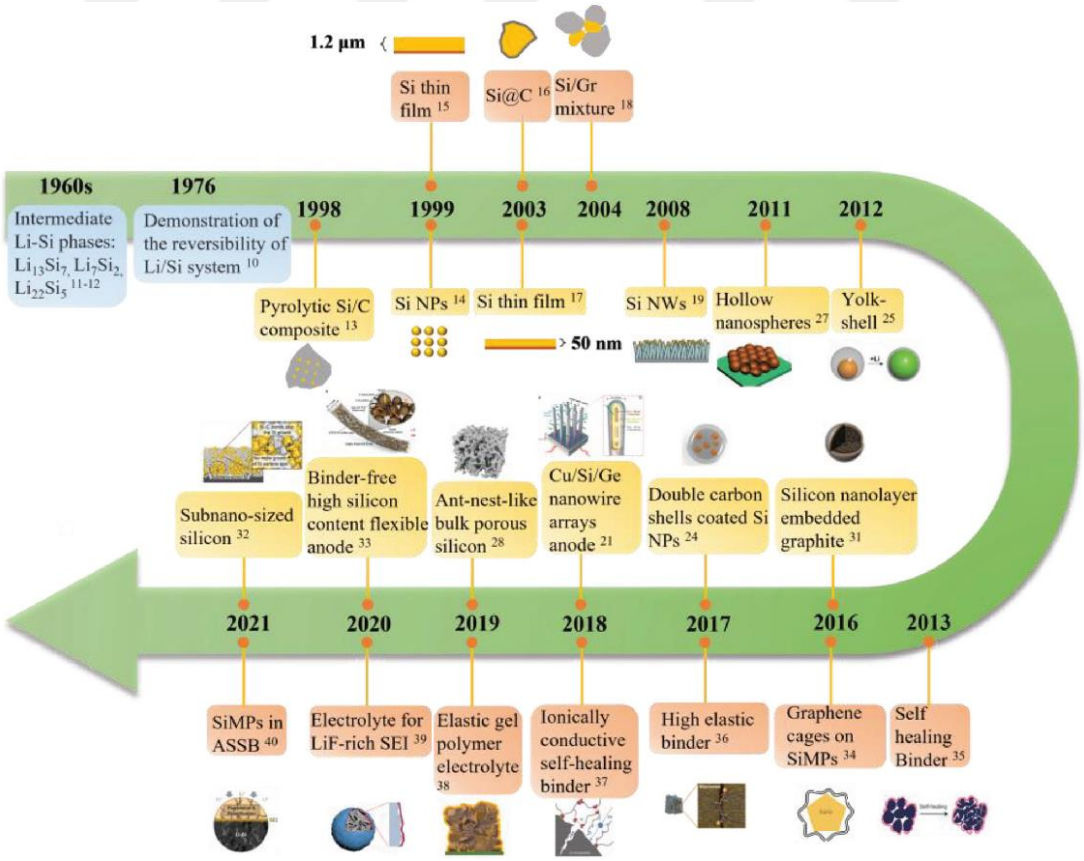

Figure 3.19 : A brief history of silicon-based anodes [120].

3.5 Other Materials

Many metals or alloys exhibit lithium storage by intercalation, alloying, or conversion reactions. Titanium oxide, tin, zinc, manganese, iron, cobalt, nickel, molybdenum-based materials, and MXenes are studied in the literature. Among intercalation type anodes, titanium oxide anodes gain attention with their low toxicity, high cycle life, and low volume changes (around 2-3%). They have a higher theoretical capacity (335 mAh/g) in comparison to LTO anodes (175 mAh/g) [121]. However, low electrical conductivity and poor rate performance of titanium oxide anode active materials need further improvements. Various strategies, including nanostructuring, doping, and constructing 3D structures with a high surface area, are suggested to enhance the electrochemical performance of titanium oxide anodes [121].

A new type of anode active material, such as 2D transition metal carbide and carbonitrides, namely MXenes, has been under detailed research since 2011. Generally, MXenes are produced by selective etching of the A layer from MAX phases, where M is a transition metal (Ti, V, and Nb), A is an A group element, and X is either carbon or nitrogen [122]. The high electrical conductivity and layered structure of MXene materials make them good candidates for energy storage applications. Ti_2C-based MXene ($Ti_3C_2T_x$) is the most studied anode, first reported by Naguib et al. [123] in 2012. The material delivered 225 and 80 mAh/g at C/25 and 3C rates, respectively. Recent reports indicate that the electrochemical performance of MXene materials requires enhancement through the adjustment of production parameters.

Alloying-type anodes provide high specific capacities due to alloying/dealloying reactions with lithium. Tin (Sn) anodes draw interest with their high theoretical capacity of 994 mAh/g when $Li_{4.4}Sn$ alloy is formed. Unfortunately, similar to silicon anodes, high volumetric changes (up to 300%) cause mechanical instability and poor capacity retention [124]. Synthesizing nanostructures or forming composites are proposed to solve this problem [125].

Many transition metal oxides, selenides, phosphides, nitrides, sulfides, and fluorides exhibit conversion type lithiation. Among them, iron oxides (hematite and magnetite) have low cost, high availability, and reversibility of conversion reactions. The theoretical capacities of hematite and magnetite are 926 and 1007 mAh/g, respectively

[126,127]. Xu et al. [128] synthesized mesoporous Fe_2O_3 and Fe_3O_4 microspheres to improve their electrochemical performance. The mesoporous structure is preferred to shorten the lithium diffusion path and increase the electroactive surface area. The synthesized magnetite and hematite anodes delivered 1307 and 1453 mAh/g initial discharge capacity at 0.2 C rate.

4. Si AND SiO_x ($0 \leq x \leq 2$) ANODES

The inadequate performance and expected supply problems of graphite, the safety risks of metallic lithium, and the low energy density of lithium titanate anodes draw attention to silicon-based anodes. Silicon's high abundance in the earth's crust, low toxicity, and low prices make it a great candidate for anode active material to be used in lithium ion batteries. In Table 4.1, a brief comparison of silicon-based anode active materials is given. While silicon has the highest theoretical capacity, its extreme volumetric changes (up to 300 %) during cycling create major problems with capacity retention. The increased O/Si ratio provides structural stability to the active material by compromising its capacity.

Table 4.1 : Silicon-based anode active materials [3].

Materials	**Si**	**SiO**	**SiO_x**	**SiO_2**
Theoretical capacity (mAh/g)	3579	2600	1965-3579	1965
Volumetric exchange (%)	300	150	100-300	100
Initial Coulombic efficiency (%)	100	68.7	52.4-100	52.4

4.1 Silicon

Silicon remains one of the main substitutes for graphite in anode materials due to its high abundance in the earth's crust, low cost, and low toxicity. It delivers high specific capacity by forming multiple alloys with lithium, which allows it to achieve high electrochemical performance with low electrode thickness and weight [129,130].

The lithiation mechanism of silicon has been studied extensively due to the potential use of Li-Si molten salt electrolytes at high working temperatures (> 400 °C) and lithium ion batteries as anode active materials at room temperature. Many studies have investigated the Li-Si phases formed at room and high temperature conditions [131–133]. They conclude that equilibrium intermetallic compounds such as $Li_{12}Si_7$, Li_7Si_3, $Li_{13}Si_4$, and $Li_{22}Si_5$ are formed at higher temperatures, resulting in a stepped voltage profile (Figure 4.2). On the other hand, metastable amorphous Li_xSi phases are

observed at room temperature. Because the development of equilibrium phases is kinetically inhibited, solid-state amorphization takes place, resulting in the production of the amorphous phases, which have a lower Gibbs free energy than the reactants [134]. Therefore, Li_xSi ($0<x<3.75$) alloys are formed at room temperature, leading to a plateau in voltage profile below 0.1 V, leading to the theoretical capacity of 3598 mAh/g after full lithiation [135].

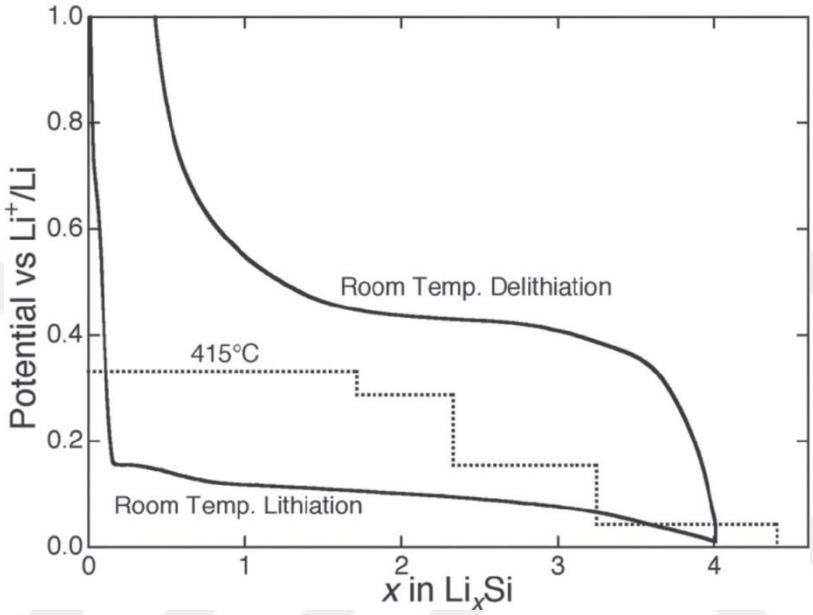

Figure 4.1 : Lithiation mechanism of silicon powder at room temperature (solid line) and 415 °C (dashed line) [136].

During the discharge step, between 50 mV - 2 V, the voltage plateau could be ascribed to lithiation reactions of crystalline silicon and the formation of amorphous Li_xSi as given in Equation 4.1 [137,138]. When the voltage decreases further than 50 mV, the amorphous Li_xSi converts to crystalline Li_xSi, as presented in Equation 4.2 [139]. In delithiation, a voltage plateau around 0.4 V depicts the reversible reactions given in Equation 4.3. First, the crystalline $Li_{15}Si_4$ is converted to an amorphous phase. Then, lithium ions are extracted to form amorphous silicon. After cycles, the reactions only occur between amorphous $Li_{15}Si_4$ and silicon atoms [140].

$$Si\ (crystalline) + xLi^+ + xe^- \rightarrow\ Li_xSi\ (amorphous) \quad (4.1)$$

$$4Li_xSi\ (amorphous) + (15-4x)Li^+ + (15-4x)e^- \rightarrow Li_{15}Si_4(crystalline) \quad (4.2)$$

$$Li_{15}Si_4\ (crystalline) \leftrightarrow 15Li^+ + 15e^- + 4Si\ (amorphous) \quad (4.3)$$

Unfortunately, the high capacity in the first cycles was only preserved for a few more cycles. The high number of lithium ions forming silicon alloys causes high volumetric

changes (up to 300 % at full lithiation) during these cycles [141]. Therefore, the significant expansion and shrinkage of silicon particles results in pulverization and active material loss. In the meantime, newly-created Si particle surfaces help to continue cycling, and demolition of the SEI layer has occurred, as shown in Figure 4.3. Consequently, poor rate performance and low Coulombic efficiency limit the use of pure silicon anodes in lithium ion batteries [142].

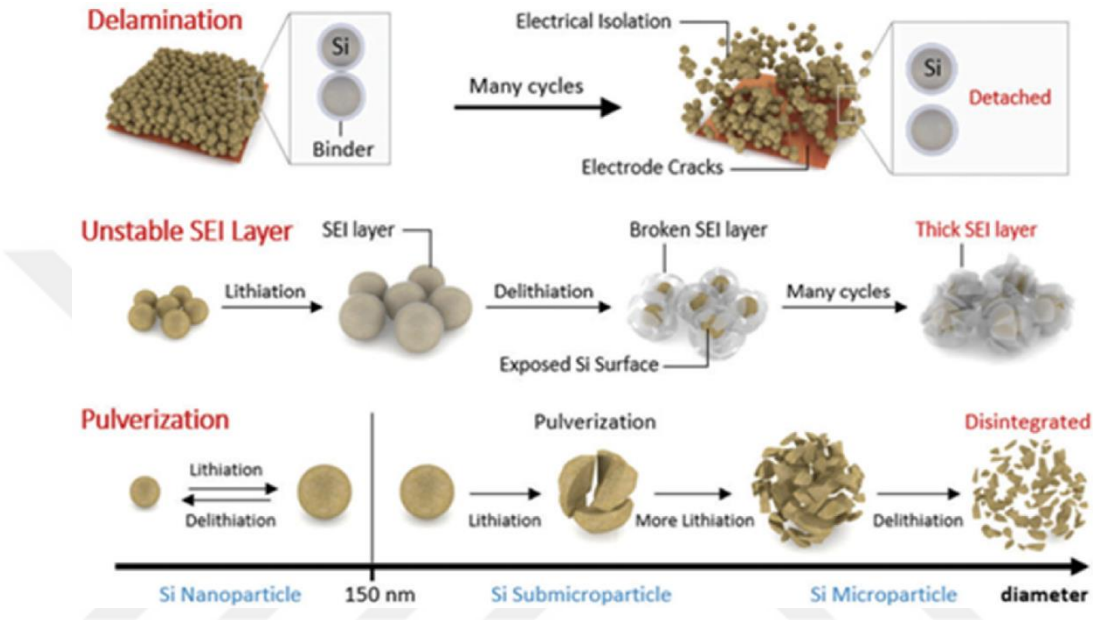

Figure 4.2 : Common failure mechanisms of silicon anodes [143].

To overcome these problems, different strategies are proposed, such as decreasing particle size, increasing porosity, metal doping, composite formation, and carbon coating [139,144,145]. Silicon particles having a diameter below 150 nm are found to maintain their structural stability during repeated cycles. These particles can endure mechanical stress caused by volumetric changes, providing better capacity retention [136]. Different geometries, such as nanowires, could provide the same effect as small particles do, which helps to buffer the volumetric changes.

Thin film production methods are also used to produce Si anodes with different geometries and compositions. Polat et al. [146] synthesized compositionally graded Si-Cu helical arrays and achieved 1228 mAh/g specific capacity at 0.1 A/g current load at the 100th cycle. The Cu-rich layer improves the adhesion, while helices help accommodate volumetric expansion in cycling. Chan et al. [117] synthesized silicon nanowires with a diameter of around 90 nm to be used as lithium ion battery anode active material and achieved 3193 mAh/g specific capacity at C/20 current load with

73 % initial Coulombic efficiency. The lithium storage capacity of nanowires was found to be stable after 10 cycles, proving the strategy's efficiency. However, the synthesis of nano-scale particles by PVD (physical vapor deposition) is relatively expensive. Therefore, the production of micron-scale porous powders is proposed to improve cycle life and rate capability of silicon anodes by buffering volume exchange and shortening the lithium ion diffusion path [147]. Pathak et al. [148] synthesized nano-porous silicon by selective leaching of aluminum from hypereutectic Al-Si alloy. They achieved around 1000 mAh/g specific capacity after 300 cycles at C/3 current load, proving the porous structure's efficiency. In another study, Jia et al. [149] produced spherical micron sized porous silicon anodes using magnesiothermic reduction of silica pomegranate structure. The anode active materials delivered 1467 mAh/g reversible capacity at 2.6 A/g current load with good rate capability. Core/shell designs are another path for achieving a porous structure. The space between the core and shell helps to alleviate the volume changes and to form a more controlled SEI layer on active materials. While many studies are focusing on different core/shell structures, Si/C composition could be marked as the most studied chemistry [150–152].

Low electrical conductivity is another reason behind the limited rate performance of silicon anodes. Metal doping and carbon coating are efficient methods to improve conductivity. Zhang et al. [153] produced Cu-doped silicon anodes using the hydrothermal method and ball milling. The Cu/Cu_3Si alloy aims to increase electrical conductivity and strengthen the structure of the $Si/Cu/Cu_3Si/C$ composite. The amorphous carbon layer is added to inhibit particle agglomeration and side reactions. The active material delivered 984 mAh/g reversible capacity at 0.5 C current load after 500 cycles. Nulu et al. [154] investigated the effect of nickel and manganese doping on the electrochemical performance of silicon nanoparticles. Their results show that Mn and Ni doping improves the electrical conductivity and creates ionic channels to accelerate lithium ion diffusion. The Mn and Ni-doped Si nanoparticles provided 2324 and 2561 mAh/g specific capacity at 200 mA/g current load after 100 cycles.

The carbon coating method is commonly used as another way of improving silicon anodes's electrical conductivity. It helps to provide a more stable surface, promote electron transfer, and provide a barrier layer on silicon particles. Qi et al. [155] studied the adequate carbon layer thickness for improved electrochemical performance of silicon nanoparticles. Carbon coating thickness (2-30 layers) and deposition time in

the CVD process are investigated. The optimum C coating thickness of Si/C composite is around 1 nm (2-3 layers) for inhibiting unstable SEI layer formation and extreme volume change. When used as anode active material, it provided 3019 and 1647 mAh/g specific capacities at 0.2 and 5 A/g current loads, respectively.

4.2 Silicon Monoxide - SiO

SiO anodes draw attention with lower volumetric changes compared to pure silicon anodes. C. F. Mabery published the first SiO reports in 1887 [156]. Commercial SiO is obtained by heating the mixture of silica and silicon at high temperatures and condensing the gaseous SiO vapor [157]. While there are many debates, Hohl et al. [158] proposed an interface cluster mixing (ICM) model shown in Figure 4.4. Here, black regions are silicon clusters, white areas are SiO_2 clusters, and grey interfaces are suboxide transition areas. SiO structure is thermodynamically unstable and tends to disassociate to SiO_2 and Si.

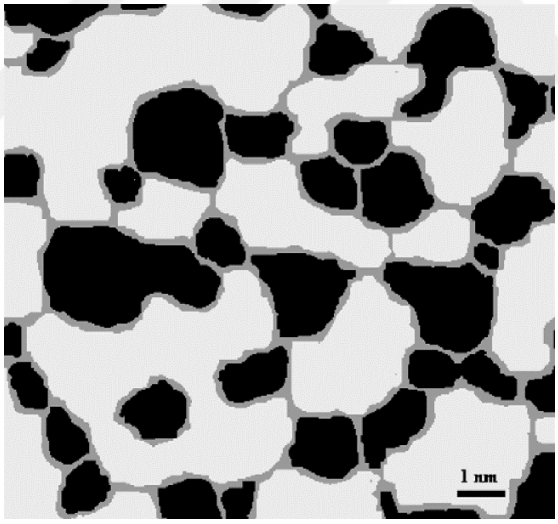

Figure 4.3 : ICM model of amorphous SiO [158].

The lithiation mechanism of SiO could be classified as conversion reactions (SiO and Li^+) and alloying reactions (Si and Li^+) [159]. In the first reaction step, lithium oxide and lithium silicates are formed. Many of the lithium silicates formed in this step are electrochemically inactive, which results in low Coulombic efficiency. In the second step, lithiation reactions in newly generated silicon take place. The reactions could be summarized in Equation 4.4-4.9 [160,161]:

$$SiO + 2Li^+ + 2e^- \rightarrow Li_2O + Si \quad (4.4)$$

$$4SiO + 4Li^+ + 4e^- \rightarrow Li_4SiO_4 + 3Si \quad (4.5)$$

$$3SiO + 2Li^+ + 2e^- \rightarrow Li_2SiO_3 + 2Si \quad (4.6)$$

$$7SiO + 6Li^+ + 6e^- \rightarrow Li_6Si_2O_7 + 5Si \quad (4.7)$$

$$5SiO + 2Li^+ + 2e^- \leftrightarrow Li_2Si_2O_5 + 3Si \quad (4.8)$$

$$Si + xLi^+ + xe^- \leftrightarrow Li_xSi \quad (4.9)$$

The crystal structure of lithium silicates as a result of lithiation reactions of SiO is presented in Figure 4.5a. Jung et al. [162] claim the silicon-rich core of SiO transforms into electrochemically active Li_xSi alloy, while the surrounding silicon suboxide transforms into electrochemically inactive lithium silicates and lithium oxide during lithiation as seen in Figure 4.5b. This outer matrix mainly comprises lithium silicates, while lithium oxide only constitutes a minority. According to their calculations, they speculate that the formation of the Li_2O phase is thermodynamically more favorable. However, kinetic limitations inhibit the transformation of lithium silicates into lithium oxide. Another remarkable outcome of their study is the comparison of lithium diffusion coefficients of various lithium silicates and lithium oxide. Lithium ions seem to diffuse faster in lithium oxide rather than lithium silicates which may lead Li_2O to work as a fast lithium diffusion path.

Studies show that the lithiation products of SiO are highly related to reaction rate and lithiation depth. Lee et al. [159] asserted that the irreversible capacity loss rises with the increased depth of lithiation. Even though electrochemically inactive components such as lithium silicates and lithium oxide serve as buffers during cycling, they result in low initial Coulombic efficiency and volume expansion of around 150%, causing pulverization of SiO anodes. To overcome these problems, strategies such as doping, carbon coating, and synthesis of nano-scale and porous electrodes are proposed. Yang et al. [163] synthesized porous SiO/Ni composite anodes and tested their electrochemical performance. They claimed that increased porosity helps to buffer volume changes of SiO anodes, while nickel deposition improves electrical conductivity. With a different approach, Park et al. [164] produced mesoporous SiO anodes via mechanochemical oxidizing followed by acid etching methods using Si and ZnO powders. The use of micron-sized silicon powder as a precursor resulted in higher reversible capacity than nano-sized Si precursors.

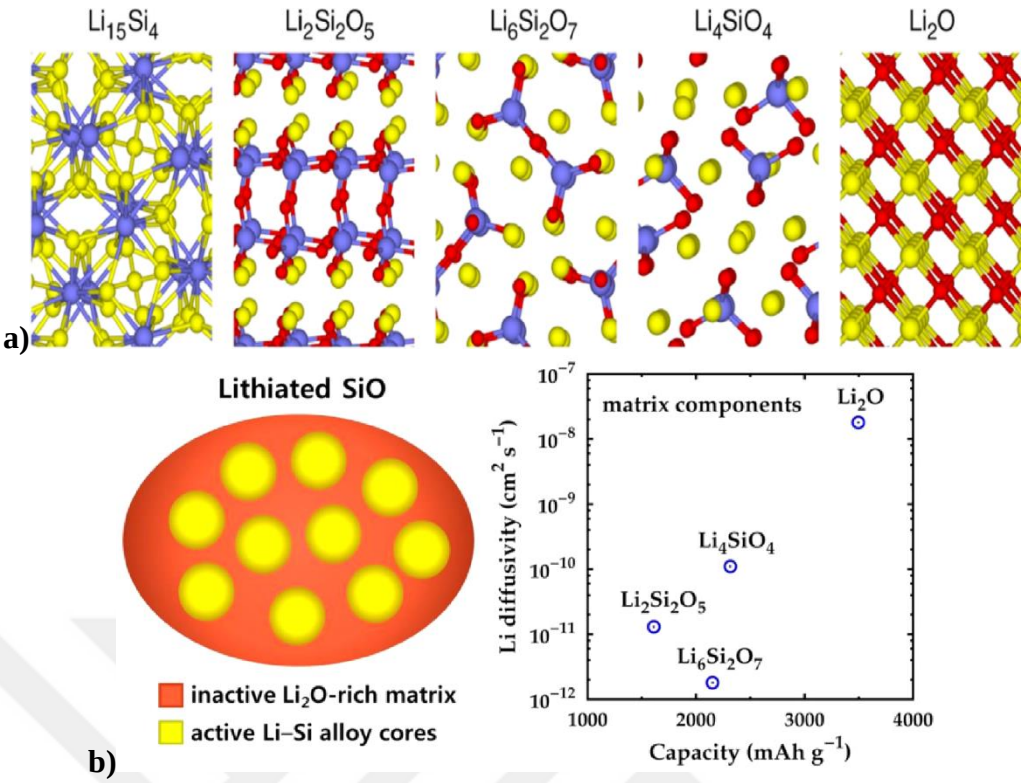

Figure 4.4 : a) Crystal structure of various lithium silicates and lithium oxide **b)** Schematic drawing of lithiated SiO structure and lithium diffusion coefficients of lithium silicates and lithium oxide [162].

In 2017, Woo et al. [165] conducted a detailed study on doping to enhance the electrochemical performance of SiO anodes by comparing boron doping and carbon coating. Here, assumptions were that the carbon coating lowers the internal resistance by providing electrical conductive pathways while the boron-doping increases electrochemical activity by creating lithium ion pathways within the material. Their results show that boron-doping improves the lithium diffusion kinetics and provides better long term stability than carbon coating. Miyachi et al. also [166] investigated the effect of different dopants, namely nickel, iron, and titanium. The initial discharge capacities are found to be 1556, 1335, 1270, and 1260 mAh/g for Ni-doped, Fe-doped, Ti-doped, and pristine SiO anodes, respectively. They claim that metal doping may form amorphous silicon, amorphous silica, and metal-rich domains. In this structure, metal doping works as an electron transporter, hence eases the lithium diffusion reactions.

4.3 Silicon Suboxide - SiO_x (0<x<2)

Non-stoichiometric SiO_x anodes gained popularity in recent years for their high theoretical capacity (2680 mAh/g) and capacity retention [167]. Similar to SiO, the structure of SiO_x has been a topic of recent years. Detailed characterizations conducted by Hirata et al. [168] helped deconstruct the SiO_x structure. They found that the silicon suboxide and silica surround the silicon core, as seen in Figure 4.6 [169].

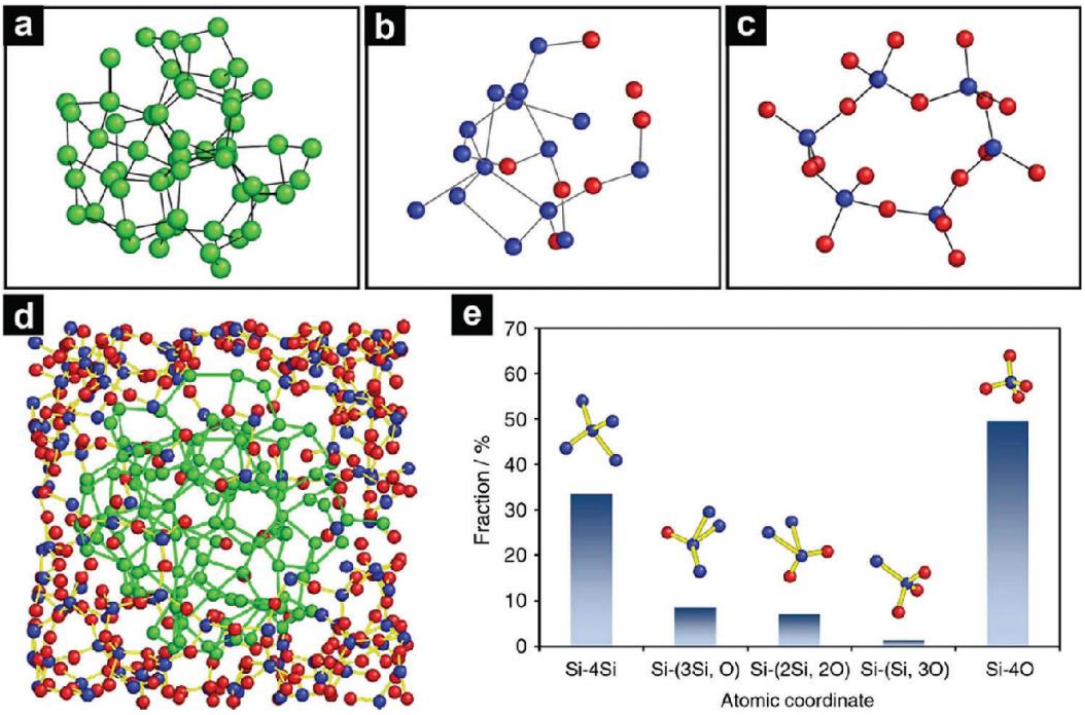

Figure 4.5 : Atomic array of **a)** silicon **b)** silicon suboxide **c)** silica **d)** The proposed atomic model of SiO **e)** ratio among the Si-clusters [168].

Moon [170] conducted density functional studies to investigate the oxygen content in silicon anode lithiation products. The Li-Si-O phase diagram presented in Figure 4.7 shows that the Li-Si system mainly consists of stable crystalline alloys such as LiSi, $Li_{12}Si_7$, $Li_{13}Si_4$, and $Li_{15}Si_4$. Lithiation reaction products of silica could also be Li_2O, Li_4SiO_4, Li_2SiO_3, $Li_2Si_2O_5$, etc.

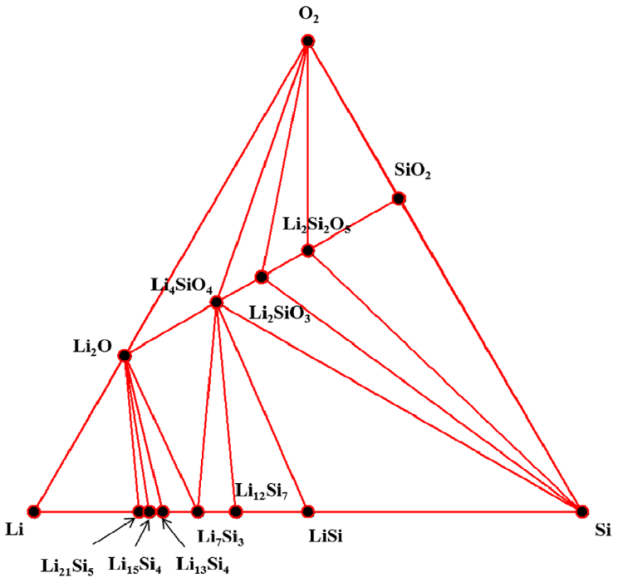

Figure 4.6 : Li-Si-O ternary phase diagram [170].

Lithium oxide and silica formation are observed during the lithiation reactions of SiO_x, similar to SiO and SiO_2. The formation of Li_2O and some of the lithium silicate phases are irreversible reactions. In the first step, lithium oxide, lithium silicates, and newly generated silicon are formed. In the second step, lithiation reactions occur between the generated silicon and reversible lithium silicates. The sum of reactions is presented in Equation 4.10-4.14 [171–173].

$$SiO_x + 2xLi^+ + 2xe^- \rightarrow xLi_2O + Si \quad (4.10)$$

$$SiO_x + xLi^+ + xe^- \rightarrow (x/4)\, Li_4SiO_4 + (1 - x/4)Si \quad (4.11)$$

$$SiO_x + (6x/7)Li^+ + (6x/7)e^- \rightarrow (x/7)\, Li_6Si_2O_7 + (1 - 2x/7)Si \quad (4.12)$$

$$SiO_x + (2x/5)Li^+ + (2x/5)e^- \leftrightarrow (x/5)Li_2Si_2O_5 + (1 - 2x/5)\, Si \quad (4.13)$$

$$Si + xLi^+ + xe^- \leftrightarrow Li_xSi \quad (4.14)$$

Yu et al. [173] investigated the phases during discharge and charge reactions via ex-situ High-Resolution Transmission Electron Microscopy (HRTEM). When the voltage is decreased to 0.4 V, $Li_2Si_2O_5$ and $Li_6Si_2O_7$ phases are formed. Further decrease of voltage to 0.15 V resulted in the formation of Li_4SiO_4. Finally, at 0 V, LixSi alloy generates. During charging, when the voltage rises to 2 V, reversible $Li_2Si_2O_5$ alloy is no longer detected; only irreversible Li_4SiO_4 and $Li_6Si_2O_7$ alloys are found.

The electrochemical performance of these materials is directly related to their oxygen content. Lower oxygen ratios ($0<x<1$) lead to higher specific capacity, while higher silicon content results in lower capacity retention. Although silicon provides high

capacity, its volume changes cause less cycling stability. On the other hand, higher oxygen ratios (1<x<2) lead to lower specific capacity but better retention due to the formation of higher amounts of Li_2O phase [174]. Li_2O acts as a buffer for volume changes but causes low Coulombic efficiency by consuming lithium ions and electrolytes [175]. The structural evolution of $Li_xSiO_{1/3}$ is presented in Figure 4.8 by Chou et al. [176] using density functional theory calculations. As the lithium content increases, Si-O-Si bonds start to break, and O atoms are covered with lithium atoms. The intensity of Si-O and Si-Li peaks are decreased, while Si-Li and Li-O peaks are increased. The formation of lithium oxide and lithium silicates is claimed to be directly related to the oxygen content of these anodes. Tang et al. [177] systematically studied the electrochemical performance of SiO_x/C anodes (x = 0.61, 0.71, 0.81, and 0.95) with varying O/Si ratios. The oxygen ratio is controlled by the magnesiothermic reduction process. The highest initial discharge capacity is obtained in the sample $SiO_{0.61}$/C with 2526 mAh/g. In the following cycles, the capacity of $SiO_{0.61}$/C decreased gradually. Samples with higher oxygen ratios performed higher cycling stability. It can be concluded that higher SiO_2 content and carbon shell can buffer the volume expansion of SiO_x anodes by forming lithium silicates. Thus, cycle life is improved.

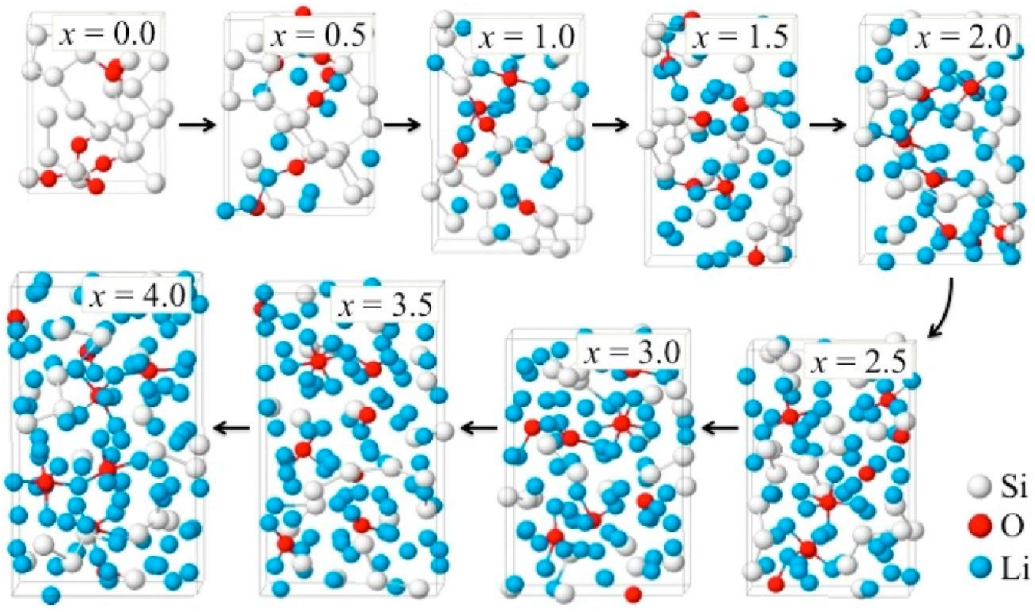

Figure 4.7 : Structural changes with increasing lithium content from x = 0 to 4 in amorphous $Li_xSiO_{1/3}$ [176].

Like all Si-based anodes, SiO_x anodes suffer from volumetric changes, poor electrical conductivity, and low Coulombic efficiency. Solving these problems could help SiO_x

to be used as a high energy density anode in commercial lithium ion batteries. Dressler and Dahn [8] used an oxidizing ball milling method for producing SiO_x anode active materials from crystalline silicon powder. While the process is effective for obtaining SiO_x anodes, the high surface area of the powders resulted in irreversible capacity loss due to SEI layer formation. Introducing porosity to SiO_x anode active materials for alleviating volume expansion is studied by Yu et al. [173]. Micron-sized SiO powders are heat treated, milled, and etched with NaOH to obtain a porous SiO_x structure. Only heat treated samples exhibit low electrochemical performance due to the increased amount of SiO_2, which inhibits lithium diffusion. Ball milling after heat treatment allows exposing the active silicon surfaces within the silica matrix. Finally, increased porosity resulted in better rate performance (890 mAh/g at 1 C current load) and capacity retention by buffering the volume changes and allowing faster lithium diffusion thanks to electrolyte-filled pores. The synthesis of porous SiO_x/C (p-SiO_x/C) anodes with optimum carbon coating was studied by Sun et al. [178]. Anode active material is obtained via zincothermic reduction of silicon-containing precursors (mixture of APTES ((3-Aminopropyl) triethoxysilane) and terephthalaldehyde (TA)) followed by carbonization. The authors claim that the carbon layer obtained by carbonization of organics present in the host material provides a more uniform coating than physical mixing with carbon sources. The p-SiO_x/C anode active materials exhibited a discharge capacity of 2002 mAh/g at 0.1 A/g current load. The XPS analysis on the SEI layer formed on cycled p-SiO_x/C electrodes reveals that the major components are Li_2O, Li_2CO_3, LiF, and RCO_xLi. A 3D porous Al-doped Si/SiO_x anode active material is synthesized by Wang et al. [179] using chemical etching of Al-Si alloys. An orthogonal experimental design including three parameters (acid concentration, reaction time, and temperature) is proposed to optimize the chemical etching process. In 3D particle morphology, primary silicon particles act as cores that are interconnected by eutectic silicon rods. These rods grow out from the cores, and the structures account for 82 % of the pore volume. This design alleviates volume expansions, and the residual aluminium enhances electrical conductivity.

Im et al. [180] developed a sandwich design as P-doped SiO_x/Si/SiO_x to improve reversible capacity. The phosphorus doping improves electrical conductivity; the SiO_x layers limit the interface area between the electrolyte and Si layer to provide higher SEI layer stability. The proposed anode delivered 3534 mAh/g initial discharge

capacity with 90% initial Coulombic efficiency, indicating a successful strategy. In another study, Kwon et al. [181] investigated the effect of vanadium and aluminum doping to improve the electrical conductivity of SiO_x/C anode active materials. They claim vanadium doping provides around two times higher electrical conductivity (up to $1.4e^{-3}$ S/m) and lithium diffusion coefficient than aluminum doping. The superiority of vanadium doping is explained by having more electrons in outer shells that act as charge carriers. The homogeneous distribution of vanadium ions and carbon coating of V-doped SiO_x@C anodes resulted in 910 mAh/g specific capacity at 1 A/g current load. In another study, Ma et al. [182] produced self-standing N-doped SiO_x/C films as anode active materials using electrospinning and carbonization methods with TEOS and PVP as starting materials. The 3D carbon network structure is believed to provide good rate capability with 488 mAh/g specific capacity at 0.6 A/g current load after 200 cycles. Also, eliminating the need to use a binder and current collector eases the adaptation of these anodes in lithium-ion batteries. Xie et al. [183] investigated the C, N, and P co-doped SiO_x anodes and their rate performance. Graphite and citric acid are carbon sources, while phytic acid and melamine are P and N sources, respectively. Authors believe carbon provides structural stability at high current rates, while P and N-doping lower charge transfer resistance, resulting in enhanced rate capability. 20 % phytic acid addition resulted in the best electrochemical performance as 1089 mAh/g specific capacity at 0.2 A/g current load. Moreover, 370 mAh/g reversible capacity is achieved at 5 A/g current load. The above studies prove the beneficial effects of introducing porosity, doping, and carbon coating on the specific capacity and rate performance of SiO_x anodes.

4.4 Silicon Dioxide (Silica) - SiO_2

In early studies, silica is considered inactive to react with lithium due to the strong covalent bond between silicon and oxygen atoms [184]. Commonly, it is only used for buffering volume changes. However, Gao et al. [185] later proved the electrochemical activity of silica in the voltage range of 0 – 1 V vs. Li/Li^+. They obtained around 400 mAh/g specific capacity using silica powders with 7 nm particle size. Since then, many studies have been conducted to enhance the electrochemical performance of silica anodes.

Similar to all silicon-derived anodes, silica goes through a two-step lithiation process. In the first step, electrochemically active lithium silicates and metallic silicon are formed along with inactive lithium silicates and lithium oxide. In the second step, metallic silicon is reacted with lithium to generate Li_xSi. The lithiation reactions are given in Equations 4.15-4.19 below [186,187]:

$$5SiO_2 + 4Li^+ + 4e^- \leftrightarrow 2Li_2Si_2O_5 + Si \quad (4.15)$$

$$3SiO_2 + 4Li^+ + 4e^- \rightarrow 2Li_2SiO_3 + Si \quad (4.16)$$

$$2SiO_2 + 4Li^+ + 4e^- \rightarrow Li_4SiO_4 + Si \quad (4.17)$$

$$SiO_2 + 4Li^+ + 4e^- \rightarrow 2Li_2O + Si \quad (4.18)$$

$$Si + xLi^+ + xe^- \leftrightarrow Li_xSi \quad (4.19)$$

Lener et al. [188] conducted DFT studies to further investigate the products of silica lithiation reactions. The calculations show that $Li_2Si_2O_5$ and Li_2SiO_3 phases are more likely to be formed at higher voltages at room temperature. They added that lithium silicate structures are more stable than lithium oxide.

The electrochemical performance of silica is highly affected by particle size. Guo et al. [189] claimed that larger SiO_2 particles form Li_4SiO_4, while smaller particles tend to form Li_2O. Liang et al. [190] obtained nano and micron-scale SiO_2 powders by ball milling desert sand and tested the effect of milling time (36-108 h) on their electrochemical performance. According to their results, there is a direct relation between milling time and initial discharge capacity. However, the best cycling stability is seen in the sample milled for 72 hours. The results show that higher milling time leads to smaller particles, which exhibit better performance. Additionally, inactive silica present in the anode is inadequate for buffering all volume changes that occur in cycling, causing capacity loss in later cycles. Many studies report that nano-scale silica performs better than bulk particles for shortening lithium diffusion path. Han et al. [191] investigated the ways to improve the performance of micron-scale SiO_2 by thermal prelithiation. They claim prelithiated micron-scale silica particles outperform the nano silica anodes in terms of specific capacity and retention. In another study, Lepoivre et al. [192] studied various prelithiation methods, namely controlled short-circuit, plating, and potentiostatic discharge, to increase the reversible capacity of Si/SiO_2 anodes. Authors speculate that the prelithiation process helps to crack the SiO_2

shell and reduce SiO_2 to metallic silicon, which increases the electroactivity of the electrode.

Another design strategy to overcome the low electrical conductivity of silica anodes is producing hollow structures. Yan et al. [193] synthesized silica hollow cubes in nano-size using a hard template method. They claim the hollow structure helps to alleviate the volume changes and shorten the diffusion path during charge and discharge reactions. The hollow structure provided 919 mAh/g reversible capacity. In another study, Yu et al. [194] obtained hollow SiO_2 spheres using a hydrothermal method using TEOS (Tetraethyl orthosilicate) as the starting material. Cao et al. [195] combined hollow silica spheres with a porous carbon matrix to provide fast lithium ion transportation with increased electrical conductivity. The anode delivered 910 mAh/g specific capacity at 200 mA/g current load after 150 cycles.

The low electrical conductivity of silica anodes makes it necessary to create composite structures with more conductive materials. Carbon coating is the facile method among the others to increase the conductivity of silica anodes. Liu et al. [196] produced SiO_2@C hollow spheres using TEOS (Tetraethyl orthosilicate) and PAA (Poly(acrylic acid)) precursors. The highest specific capacity is obtained as 649 mAh/g after 150 cycles containing 67 wt.% SiO_2, while SiO_2 hollow spheres only deliver 90 mAh/g. Lv et al. [197] produced amorphous SiO_2@C anode active materials using the sol-gel method followed by milling and heat treatment. They claim that the amorphous SiO_2 anodes exhibit better electrochemical performance than the SiO_2 powders with nano-crystalline domains. The ball milled amorphous SiO_2/C anodes delivered the best specific capacity of 600 mAh/g.

To conclude, research indicates that silicon-based anode active materials are a strong candidate to replace graphite for their high abundance, environmental friendliness, and electrochemical performance. Although the use of pure silicon anode is limited due to its irreversible capacity loss caused by high volumetric changes, silicon oxides-based anode ($0<x\leq2$) active materials promise hope. Anode active materials with desired electrochemical performances could be obtained by tailoring the oxygen content and morphological properties.

5. WASTE-DERIVED ANODE ACTIVE MATERIALS

In recent years, increased energy demand and the significant effects of climate change have led governments to take necessary precautions. For example, the European Union's Green Deal aims to make Europe a climate-neutral continent, and the Fit for 55 package seeks to reduce greenhouse gas emissions by 55% until 2030 [198,199]. These policies support the growth of the electric vehicle (EV) market and promote a cleaner transportation system. In electric vehicles, lithium ion batteries are the key components. Therefore, the raw materials used in the production of these batteries have a direct impact on the EV market. Currently, 90% of global graphite mining has been done in China (Figure 5.1); this makes the rest of the world open to possible supply chain problems and limitations, enhancing the importance of the circular economy.

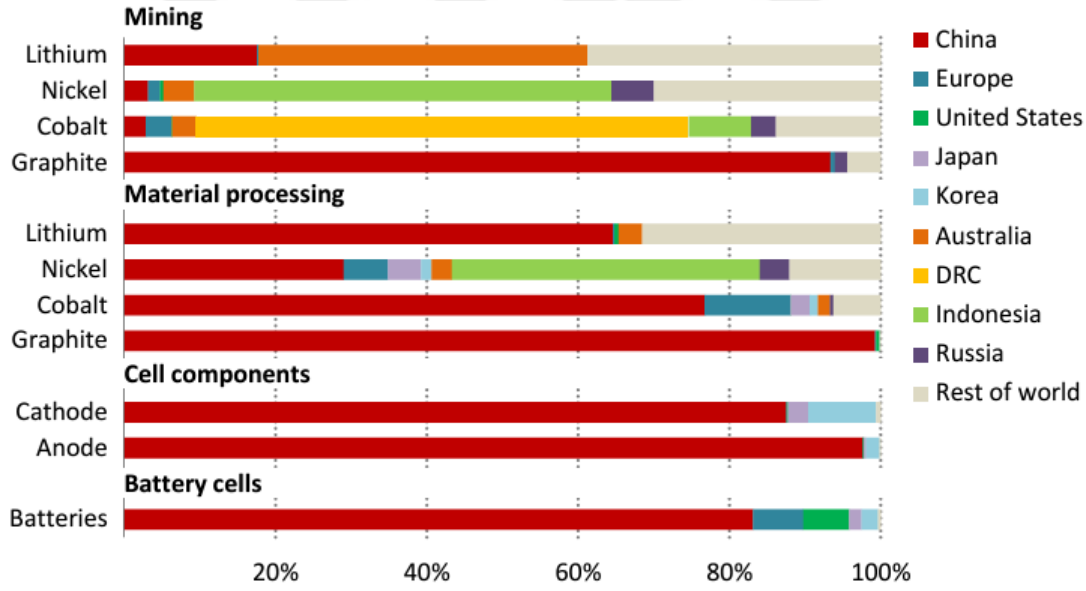

Figure 5.1 : Global battery supply chain according to countries [200].

The circular economy and the limited and geographically localized reserves of battery raw materials have led researchers to investigate alternative production routes for active materials using existing waste rather than ores. Motivated by this, many studies are conducted using both industrial and organic wastes. Table 5.1 presents a brief list of inorganic wastes used in anode active material synthesis.

5.1 Organic Wastes

The globally increased production rate leads many industries to recycle their defective and end-of-life products to increase self-sufficiency. Therefore, the use of industrial wastes in anode active material synthesis could be interrupted due to industrial recycling demands for lowering production costs. Organic wastes, on the other hand, are usually discarded and deposited on large lands to compost piles. Deposition of these organic wastes in landfills results in the creation of methane gas, pollution, and an economic burden. Instead, a zero-waste policy could use these wastes to produce high-value battery active materials.

Another significant advantage of organic wastes is their porous nature, which results in high surface area and pore volume. Additionally, the high carbon content of organic materials eases the formation of composite structures with homogeneous elemental distribution. Due to all these reasons, the production of active materials using organic wastes has high research value and gained importance in recent years. Table 5.2 shows various organic wastes incorporated into battery active material synthesis. While many organic wastes could be used for carbon-based battery materials, their limited capacity has led researchers to focus on more diverse and rich wastes in terms of elemental composition. In this context, rice husk is a great candidate for containing around 20 wt.% silica.

Table 5.1 : Industrial waste-derived anode active materials.

Authors	Waste type	Process	Synthesized anode active material	1st discharge capacity	Capacity retention	Ref.
Naskar et al.	Automobile tire	Pyrolysis	Carbon	545 mAh/g @ 0.1 C	71%	[201]
Veldevi et al.	Automobile tire	Chemical activation Pyrolysis	Turbostratic carbon	1420 mAh/g @ 50 mA/g	81%	[202]
Shilpa et al.	Automobile tire	Pyrolysis Surface activation	Activated carbon	880 mAh/g @ 50 mA/g	80%	[203]
Ding et al.	Bicycle tire	HCl-assisted carbonization	Honeycomb-shaped carbon	533 mAh/g @ 100 mA/g	61%	[204]
Bao et al.	Si wafer slicing sludge	Spray drying Ball milling	Nano Si with graphene	1007 mAh/g @ 450 mA/g	98%	[205]
Kasukabe et al.	Si wafer sawdust	Beads milling	C-coated Si nanoflakes	1200 mAh/g @ 1 A/g	98%	[206]
Wang et al.	Si wafer diamond wire cutting waste	Chemical treatments (oxide and organic layer removal, acid leaching)	C-coated micron Si	1096 mAh/g @ 100 mA/g	46.5%	[207]
Sreenarayanan et al.	Photovoltaic and semiconductor-grade Si scrap	Wet grinding Surface coating Heat treatment	Spherical Si-C composite	1600 mAh/g @ 0.1 C	75.7 %	[208]
Wang et al.	Si sludge from Si wafer cutting	NH_4F treatment Calcination	Porous Si	2886 mAh/g @ 1 A/g	74 %	[209]

Table 5.1 (continued) : Industrial waste-derived anode active materials.

Authors	Waste type	Process	Synthesized anode active material	1st discharge capacity	Capacity retention	Ref.
Zhang et al.	Crystalline Si solar panel	Ball milling Molten salt treatment	Porous Si	2427 mAh/g @ 1 A/g	91.5%	[210]
Sim et al.	Photovoltaic waste	Leaching	Si	1745 mAh/g @ 1 C	62.3%	[211]
Chun et al.	Iron slag	Magnesiothermic reduction	C-coated mesoporous Si	1521 mAh/g @ 1 A/g	97%	[212]
Yang et al.	Spent carbon anode of aluminium reduction cell	Alkali fusion method	Carbon	991.8 mAh/g @ 1 C	-	[213]
Karahan	Electric arc furnace dust	Hydrometallurgical processes (leaching, cementation, distillation, chemical precipitation) Calcination	(1) Zinc oxide (2) Zinc ferrite (3) Nanocomposite	(2) 1183 mAh/g (3) 1950 mAh/g @ 50 mA/g	(2) 62% (3) 50%	[214]
Karahan	EAF dust	Pyrolysis	C-coated EAF dust	1000 mAh/g @ 50 mA/g	60%	[215]
Gulcan et al.	EAF Flue dust	Mechanical activation Pyrolysis	C-coated EAF dust	1470 mAh/g @ 50 mA/g	50%	[216]
Cao et al.	Al-Si Alloy	Selective leaching	Spongy Si@C	1909 mAh/g @ 0.05 C	84%	[217]
Liu et al.	Ti blast furnace slag	Acid leaching Aluminothermic reduction	Porous micro Si/Si-Ti alloy	2202 mAh/g @ 500 mA/g	50.7%	[218]

Table 5.1 (continued) : Industrial waste-derived anode active materials.

Authors	Waste type	Process	Synthesized anode active material	1st discharge capacity	Capacity retention	Ref.
Hou et al.	Vermiculite as mining waste	Exfoliation Aluminothermic reduction	Si/C composite	2581 mAh/g @ 100 mA/g	76%	[219]
Li et al.	Glass bottles	Magnesiothermic reduction	C-coated Si	1420 mAh/g @ 0.5 C	97%	[220]
Ehi-Eromosele et al.	PET bottles	Ionothermal synthesis	Activated carbon	460 mAh/g @ 100 mA/g	98%	[221]
Sun et al.	PET	Solvothermal treatment	Micron PET particles	200 mAh/g @ 100 mA/g	35.2%	[222]
Villagómez-Salas et al.	LDPE and HDPE plastic bags	Solvothermal treatment Carbonization	Amorphous carbon chips	230 and 350 mAh/g @ 0.2 C	-	[223]

Table 5.2 : Organic waste-derived anode active materials.

Authors	Waste type	Process	Synthesized anode active material	1st discharge capacity	Capacity retention	Ref.
Liu et al.	Rice husk	Acid leaching Magnesiothermic reduction	Si nanoparticles	2790 mAh/g @ 0.1 C	86%	[19]
Li et al.	Rice husk	Alkali treatment Acid precipitation	Porous carbon	1280 mAh/g @ 0.2 C	39%	[13]
Liu et al.	Rice husk Coffee ground	Carbonization Magnesiothermic reduction	Si@SiO_x/C	2500 mAh/g @ 100 mA/g	56%	[20]
Zhao et al.	Rice husk	Zincothermic reduction	Si/C composite	2000 mAh/g @ 1 A/g	63%	[21]
Agarkar et al.	Sugarcane bagasse	Chemical activation Microwave heating	Porous active carbon	1465 mAh/g @ 100 mA/g	52%	[224]
Zheng et al.	Duckweed	Carbonization	N-doped porous C	2407 mAh/g @ 100 mA/g	47%	[225]
Sankar et al.	Green tea	Chemical activation	Spherical mesoporous activated carbon	781 mAh/g @ 100 mA/g	69%	[226]
Sekar et al.	Green tea	Carbonization Chemical activation	Graphitic carbon nanoflakes	706 mAh/g @ 100 mA/g	56%	[227]
Hernández-Rentero et al.	Cherry pit	Chemical activation Pyrolysis	Disordered activated carbon	910 mAh/g @ C/3	35%	[228]
Yu et al.	Corn straw	Carbonization Chemical activation	Porous carbon nanospheres	1275 mAh/g @ 0.2 C	42%	[229]

Table 5.2 (continued) : Organic waste-derived anode active materials.

Authors	Waste type	Process	Synthesized anode active material	1st discharge capacity	Capacity retention	Ref.
Cheng et al.	Cotton	Pyrolysis	Hollow structured carbon	578 mAh/g @ 100mA/g	58.8%	[230]
Jagdale et al.	Cotton	Pyrolysis	2D carbon fiber	450 mAh/g @ 0.5 C	88%	[231]
Muruganantham et al.	Mango peel	Carbonization	Porous hard carbon	801 mAh/g @ 100 mA/g	78%	[232]
Salimi et al.	Leather shavings	Pyrolysis Acid leaching	Biochar	2063 mAh/g @ 100 mA/g	38%	[233]

5.1.1 Rice husk as a valuable organic waste

In 2022-2023, global rice production was estimated to exceed 500 million tonnes, with approximately 20% of this weight consisting of rice husk. Given these production figures, finding value in this by-product is crucial. Some potential applications for rice husk include its use as absorbents, fillers in concrete and cement, insulation materials in the steel and refractory industries, rubber fillers, and in energy applications [234].

Bazargan et al. [235] characterize the chemical composition of raw rice husks as approximately 32% cellulose, 18% hemicellulose, 28% lignin, 17% silica, and 5% moisture. Mussato and Teixeira [236] describe the structure of rice husks as a complex arrangement where cellulose forms the structural framework, hemicellulose encases it, and lignin adds further support (Figure 5.2).

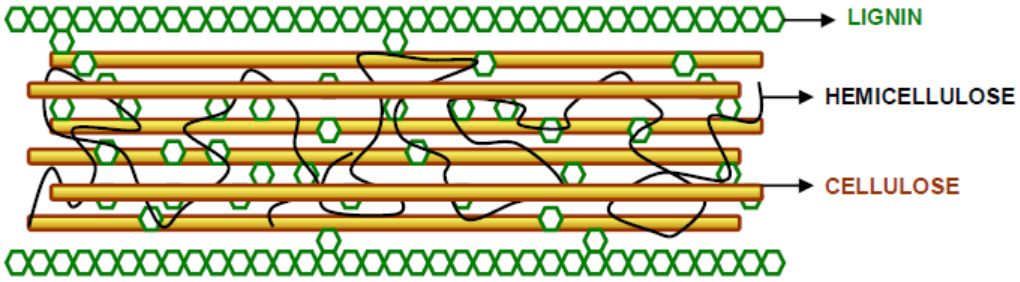

Figure 5.2 : Rice husk structure with cellulose, hemicellulose, and lignin [236].

The organic content of rice husk corresponds to 80% of the total weight. Inorganic materials comprise the remainder of 20 wt.%, mainly silica and other minor impurities such as potassium, calcium, and iron. Patel et al. [237] reported that while the majority of silica in rice husk is present as free amorphous silica, some silicon may be bonded with monosaccharides. Supporting this, Toda et al. [238] reported homogeneous elemental distribution within the rice husk ash using EDX elemental mapping.

An essential characteristic of rice husk is its naturally porous structure. A study by Araque et al. [239] examined the microstructural properties of rice husk. As seen in Figure 5.3, they reported that the outer layer called the epidermis, consists of convex cells with a symmetrical arrangement. These cells are separated by grooves, with silicon particles scattered across the surface. In contrast, the inner layer typically comprises thin-walled cells and small pores. This inner layer provides structural support and resilience, protecting the seed from strain.

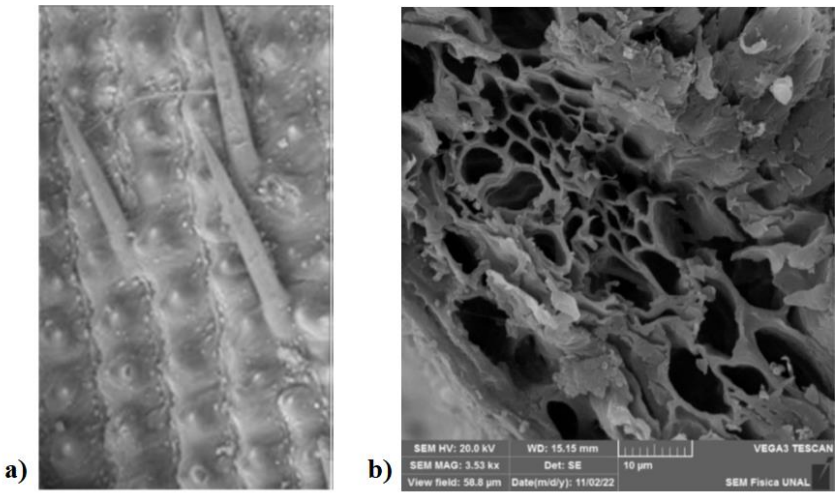

Figure 5.3 : SEM images of rice husk **a)** Outer layer **b)** Inner layer [239].

All the inherited properties and high abundance of rice husk make it an excellent candidate for energy applications. Upon reviewing the literature, pyrolysis and wet chemical methods emerged as the most commonly utilized techniques for synthesizing active materials from rice husk in lithium ion battery applications. The two processes are discussed in detail below.

5.1.1.1 The wet chemical method

The wet chemical method is a commercially available process for producing silica particles. Here, sodium silicate solution is used as a starting material, and the neutralization of the sodium silicate solution with acid addition is used to produce silica particles. This process can easily be adapted to use rice husk as a starting material. It involves calcination of rice husk to obtain ash, leaching this ash in NaOH solution to obtain sodium silicate solution, and precipitating silica by adding sulphuric acid until neutral pH. The chemical reactions regarding dissolution and precipitation are given in Equations 5.1 - 5.3 [6,240,241].

$$SiO_2 \text{ (rice husk ash)} + 2NaOH = Na_2SiO_3 + H_2O \quad (5.1)$$

$$Na_2SiO_3 + H_2SO_4 + H_2O = Si(OH)_4 + Na_2SO_4 \quad (5.2)$$

$$Si(OH)_4 = SiO_2 + H_2O \quad (5.3)$$

In the first step, rice husk dissolves in sodium hydroxide solution to form sodium silicate solution, also known as water glass. Sodium silicate is a complex solution with components (water, negatively charged silicate species, and sodium ions) under a dynamic equilibrium [240]. The critical characteristics of sodium silicate solutions are

SiO_2 concentration and SiO_2/Na_2O ratio. The colored area marked in Figure 5.4 shows the stable sodium silicate region within the suitable solubility and viscosity limits of the ternary Na_2O-SiO_2-H_2O phase diagram. The commercial sodium silicate solutions also fall within this marked area, with a SiO_2/Na_2O molar ratio (R_M) of 1.6 - 3.75. Moreover, the optimum ratio for colloidal and finely divided silica particles is considered to be 3.25 [241]. While sodium silicate glasses, quartz sand, and vitreous silica could be used to obtain sodium silicate solution, in recent years, the incorporation of by-products such as rice husks or waste glasses has been studied to decrease the process's carbon footprint. The sodium silicate solutions derived from rice husk ash demonstrated similar properties to commercial alternatives [242,243].

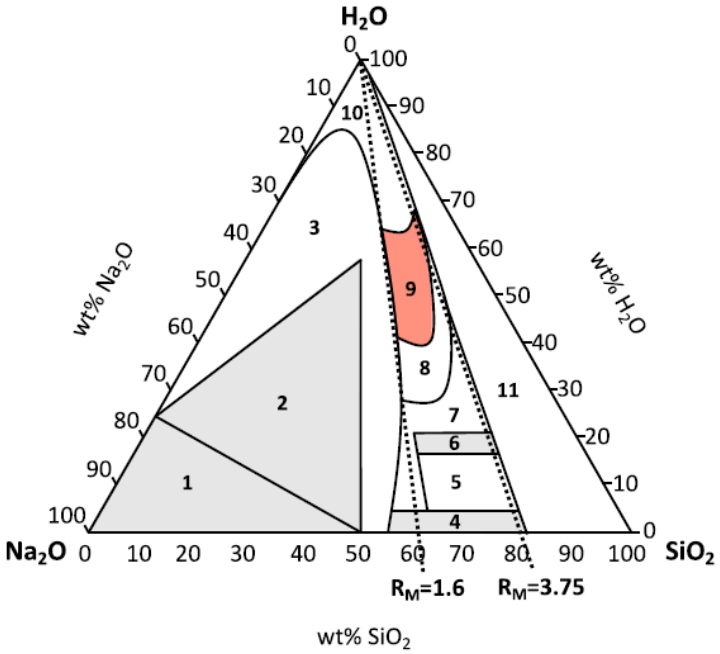

Figure 5.4 : Ternary Na_2O-SiO_2-H_2O phase diagram [240].

Like amorphous solids, silicate structures in aqueous solutions also have $(SiO_4)^{4-}$ tetrahedral units. They bond at their corners by sharing one oxygen atom, known as bridging oxygen (BO), which forms various networks, including chains, rings, and three-dimensional structures. Sodium ions, on the other hand, break Si-O-Si bonds and create non-bridging oxygens (NBO). Research using NMR and Raman spectroscopies has demonstrated that the silicate groups in sodium silicate solutions possess significantly different chemical structures. Knight et al. [244] conducted the most extensive research on this topic. They identified 48 different structures, which are believed to correspond to 85% of the silicon species in the silicate solutions. Here,

researchers used “Q-units” or “Q^n” to define silicate species, where Q represents a silicon atom coordinated by four bonds, while n represents the number of silicon atoms connected through an oxygen atom. Q^0 represents a monomeric silicate tetrahedron in this context, while Q^4 indicates a silicon atom bonded to four other silicon atoms. Silicate structures with bridging and non-bridging oxygens and Q units are presented in Figure 5.5.

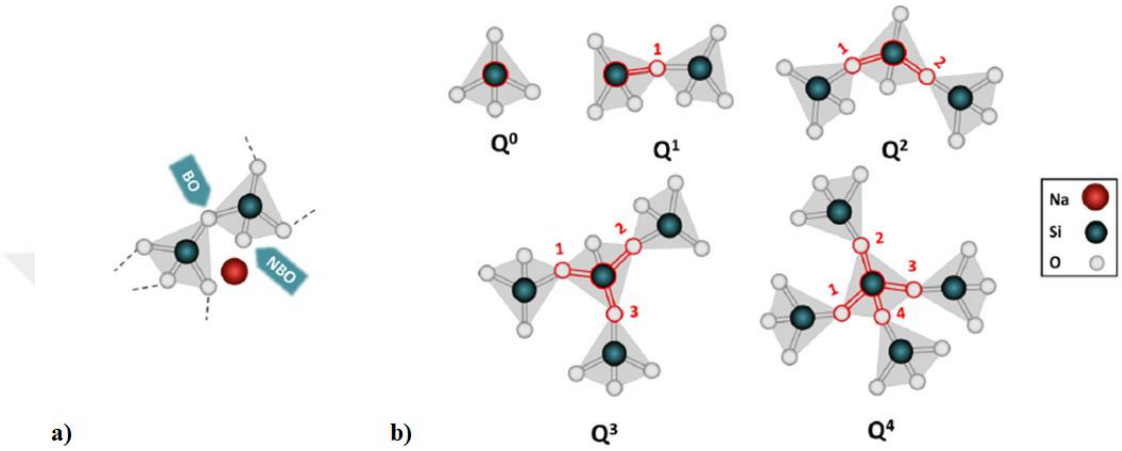

Figure 5.5 : Silicate structures a) Bridging (BO) and non-bridging oxygens (NBO) b) Q units [240].

The complex distribution of Q units in silicate solutions is believed to be affected by two reactions: the acid-base equilibria (Equation 5.4) and the polymerization-depolymerization equilibria (Equations 5.5 and 5.6) as below [245]:

The Acid-Base Equilibria

$$\equiv Si{-}OH + H2O \leftrightarrow \equiv Si{-}O^- + H3O^+ \quad (5.4)$$

The Polymerization-Depolymerization Equilibria

$$\equiv Si{-}OH + OH{-}Si \leftrightarrow \equiv Si{-}O{-}Si \equiv + H2O \quad (5.5)$$

or

$$\equiv Si{-}OH + \equiv Si{-}O^- \leftrightarrow \equiv Si{-}O{-}Si \equiv + OH^- \quad (5.6)$$

The polymerization reactions mainly involve the condensation of silanol groups and the dominance of the above reactions. Therefore, the connectivity of silicon atoms depends on many parameters: solution concentration, silica-to-sodium oxide ratio (SiO_2/Na_2O), pH, and temperature could be given to name a few [246]. Based on the literature findings, the effects of the parameters on Q units are discussed below.

The composition of the solution, specifically the SiO_2/Na_2O ratio in silicate solutions, is a crucial parameter that influences the distribution of Q units. A detailed examination revealed that the complexity and quantity of silica species increase with higher silica concentrations. When the ratio (R_M) is above 1.5, Q^3 species become more dominant. Additionally, for R_M values greater than 3.5, cross-linked Q^4 species, which have Q^3 surface units, are more prevalent. This is because monosilicic acid is only stable in an aqueous solution if its concentration is below 100 ppm. At higher silicic acid concentrations, higher molecules, such as oligomers, are formed [246].

The pH level is a crucial factor influencing the quantity of Q units in sodium silicate solutions. When the pH decreases, Q^3 and Q^4 units are encouraged to be formed instead of Q^1 and Q^2. In simpler terms, as the pH drops, oligomers with higher order and larger particle sizes are generated. Additionally, the gelation process begins as the pH continues to decrease (around pH=10). Contrarily, increasing the pH causes the breaking of Si-O-Si bonds by OH^- ions, thus leading to the depolymerization of silicate species into smaller, more reactive, and more ionic forms [240].

Research also indicates that higher temperatures, while less significant than other factors, promote depolymerization reactions, producing monomers rather than larger particles. The effect of the parameters on the Q^n distribution is briefly shown in Figure 5.6.

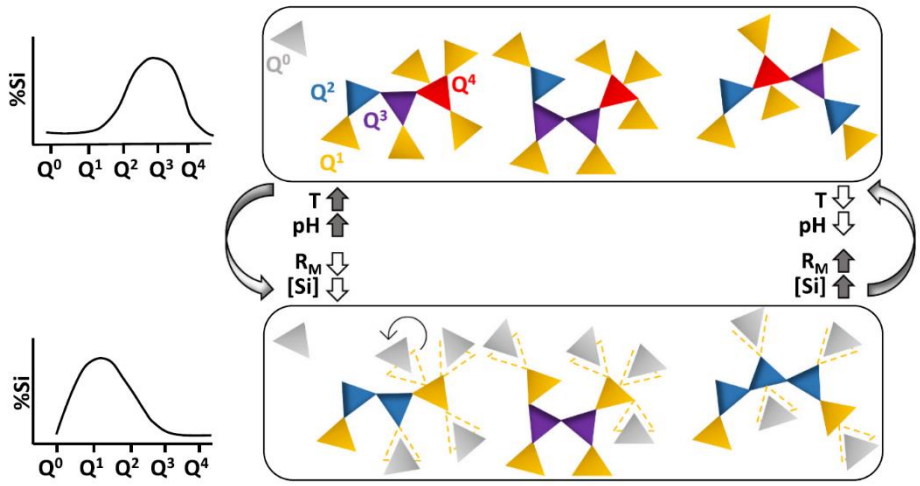

Figure 5.6 : Q^n distribution according to temperature, pH, R_M, and solution concentration [240].

Q^4, the most compact Q unit in silicate solutions, is only found in high-concentration solutions where the R_M value exceeds 2. In these solutions, colloidal silica is the major

component, with particle sizes ranging from 1 to 1000 nm. The core of the colloidal silica particles consists of Q^4 units, while Q^3 groups are present on the surface. At high solution concentrations or R_M values, silicate particles tend to aggregate into fractal structures, forming a gel. While the existence of colloidal silica in high concentration solutions is acknowledged, the precise critical concentration necessary for forming these particles remains unknown. A schematic representation of different silicate species in sodium silicate solution is given in Figure 5.7. The gray-colored sphere symbolizes a colloidal silica particle.

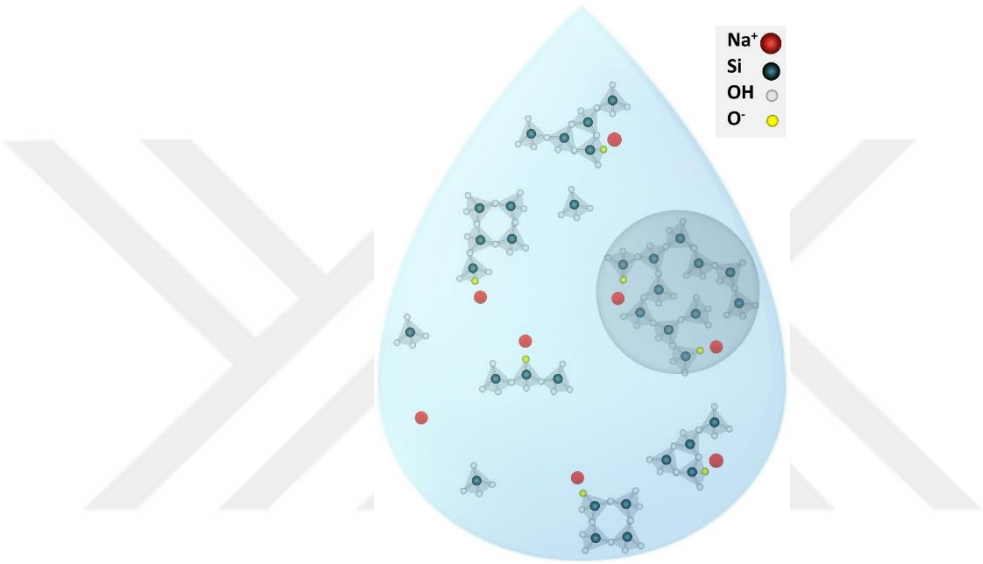

Figure 5.7 : Representation of silicate species in sodium silicate solution [240].

Iler [241] proposed a theory suggesting that silica polymerization occurs due to electrostatic forces between silicic acid monomers. According to him, polymerization occurs in three stages:

1. The polymerization of $Si(OH)_4$ monomers into oligomers, followed by the formation of particles,
2. The growth of these particles,
3. The aggregation of particles into branched chains and networks, which ultimately create a gel structure that extends throughout the liquid medium.

In the first stage, 3D particles form in the solution. These particles later grow due to reactions between reactive SiOH surface groups, driven by the Ostwald ripening effect. When cations are present—such as in a neutralized sodium silicate solution mixed with acid, particularly at lower pH values—the charge repulsion between the

negatively charged silicate particles decreases. This reduction allows the particles to aggregate and form a gel structure, as illustrated in Figure 5.8. The growth of silica aggregates is expected to be anisotropic due to the random distribution of the surface reactive groups [247].

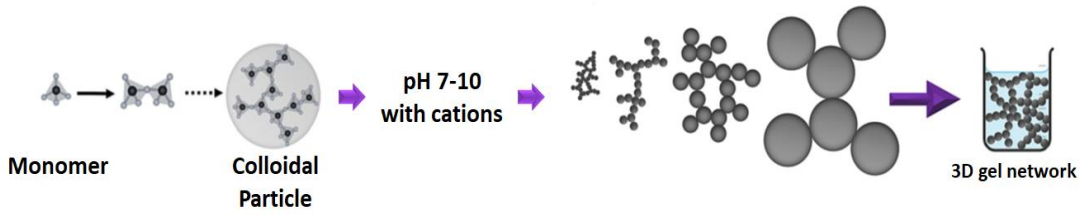

Figure 5.8 : Growth mechanism of silica particles [240].

Schlomach and Kind [248] investigated the aggregation in semi-batch acid precipitation of silica and how the various parameters affect particle size. Their experimental results showed that primary particles quickly aggregate at the beginning of the precipitation process. Over time, contrary to what is expected, smaller secondary particles are not seen in the particle size analysis. This phenomenon can be explained by aggregated particles, which have a large surface area and directly absorb the newly formed primary particles, preventing the formation of secondary particles. In another study, Gorrepati et al. [249] investigated the effect of acid molarity, pH, and salt addition on silica precipitation. Particle formation was observed to accelerate exponentially as acid molarity increased. Furthermore, all salt additives were found to enhance the formation and growth of particles. Notably, $AlCl_3$ was the additive with the most significant effect due to increased ionic strength. A study conducted by Baldyga et al. [250] investigated the pH-dependent aggregation problem during the precipitation of amorphous silica. The results showed that at low pH values, such as 3.5, particles tend to form aggregates over extended periods compared to higher pH values, such as 9.3 and 10.5. Consistent with previous research, Baldyga et al. also found that adding NaCl increases the mean particle diameter at all temperatures. This occurs due to the higher concentration of Na^+ cations, which enhances the electrostatic attraction between the particles.

Hessein et al. [251] utilized rice husk ash to prepare a sodium silicate solution for silica precipitation in their study. They employed sulfuric acid to adjust the pH to 7 during precipitation. Additionally, they added sodium dodecyl sulfate (SDS), an anionic surfactant, to control the size of the precipitated silica particles. The optimal

concentration of SDS was 200 ppm, along with 30% Na_2SiO_3 and 4% H_2SO_4, resulting in spherical particles with an average size of 18 nm.

Likewise, Al-Abboodi et al. [252] used rice shell ash to generate a sodium silicate solution, which was subsequently utilized to produce silica nanoparticles. Their findings indicated that increasing the concentration of NaOH solution from 1M to 2M led to a slight increase in the mean particle size of SiO_2, from 13 nm to 16 nm.

In addition to the parameters mentioned above, some researchers have explored using different alcohols as co-solvents to improve the sphericity of silica particles. Dominguez et al. [253] investigated the effects of short-chain polar co-solvents (ethanol, methanol, propanol, and acetone) on silica particle morphology. They found that adding ethanol and propanol leads to the formation of spherical particles due to their lower surface tension and the negative variation in surface free energy. This allows the particles to grow freely in an isotropic environment, resulting in a spherical shape. In contrast, adding methanol and acetone does not decrease surface free energy as effectively as ethanol or propanol. This is because methanol and acetone have a higher tendency to form hydrogen bonds and exhibit strong polar characteristics. As a result, silica particles grow under non-isotropic conditions, leading to non-spherical morphologies, such as elliptical or cylindrical shapes. Unlike earlier studies, Godoi et al. [254] and Jung et al. [255] used alcohol as a precipitating agent in sodium silicate solutions. They suggested that the chain lengths of alcohol influence particle morphologies. Similarly, Harris et al. [256] concluded that the type of alcohol solvent has a greater effect on particle size than the dispersion of particle sizes.

Wen et al. [257] conducted a systematic study on this topic, investigating the effects of sodium silicate concentration, surfactants, and ethanol addition on silica particle yield and morphology. Their results indicated that higher sodium silicate molarity leads to the formation of larger particles with more irregular shapes. Lower concentrations produce less silicic acid, making the growth process more dominant than nucleation. They found that a mixture of anionic and non-ionic surfactants provides optimal stability with minimal aggregation. Lastly, they noted that adding ethanol helps prevent agglomeration by forming hydrogen bonds, inhibiting the creation of Si-O-Si structures.

In summary, silica production from sodium silicate solutions is a complex process influenced by several factors. One of the most critical elements is the SiO_2/Na_2O ratio, which significantly impacts the final product by controlling polymerization reactions and regulating the growth of silica particles. Thus, optimizing this ratio is essential for managing the size and development of the silica particles.

Additionally, process yield and the sphericity of the resulting particles can be improved through calcination and the addition of alcohol. Finally, using more sustainable sources, such as rice husk ash, to produce sodium silicate solutions can help reduce the carbon footprint of this process.

5.1.1.2 Pyrolysis

Pyrolysis is a thermal decomposition process that occurs in the absence of oxygen. When biomass is converted through pyrolysis, it produces biochar with a high surface area, various functional groups, and excellent adsorption qualities [258]. These characteristics make biochar suitable for various applications, including waste management, energy production, soil enhancement, and pollutant removal. Most research has focused on utilizing biochar's strong surface sorption and ion exchange capabilities to remove contaminants. However, biochar also has significant potential as a green battery active material due to its high carbon content and abundance.

Although the temperature-related transformation mechanism of biomass-derived biochar has yet to be clearly discovered, different researchers have presented theories. Among these, the dynamic molecular structure proposed by Keiluweit et al. [259] is one of the most widely accepted theories for applying to all plant-derived biochars. In this study, Keiluweit et al. examined the mechanism of biochar formation using wood and grass based on temperature. They classified the reactions involved in biochar formation into four distinct stages (Figure 5.9). According to the model, only dehydration reactions occur at lower temperatures, and the material's main structure remains unchanged. In the next stage, the material experiences depolymerization reactions, leading to the production of volatile compounds. The resulting material, transition chars, has an amorphous center structure within a crystalline matrix. As the temperature increases, intermediate compounds with polyaromatic units are formed, enriching the stable aromatic lignin residues. Also, the loss of less heat-resistant compounds in the biochar results in a decreased char yield. Additionally, the

depolymerization of cellulose is almost completed, and the resulting structure is a highly amorphous carbon phase. In the third stage, X-ray diffraction (XRD) patterns reveal the formation of graphene sheets within turbostratic carbon crystallites. The main structure remains amorphous, but the lateral growth of graphene-like sheets leads to a sharp increase in pore sizes. The graphitic crystallites are denser at this stage than the original amorphous carbon matrix. Consequently, the transformation of amorphous carbon into graphitic crystallites results in nanopores smaller than 2 nm. The final stage is called turbostratic chars, which consist of turbostratic crystallites containing nanopores. A long-range order of these turbostratic crystallites forms at higher temperatures, indicating an increase in crystalline structure. Bourke et al. [260] investigated the differences between biochar and graphite, concluding that the primary distinctions include higher heteroatom content, enhanced electrical conductivity, and increased surface area.

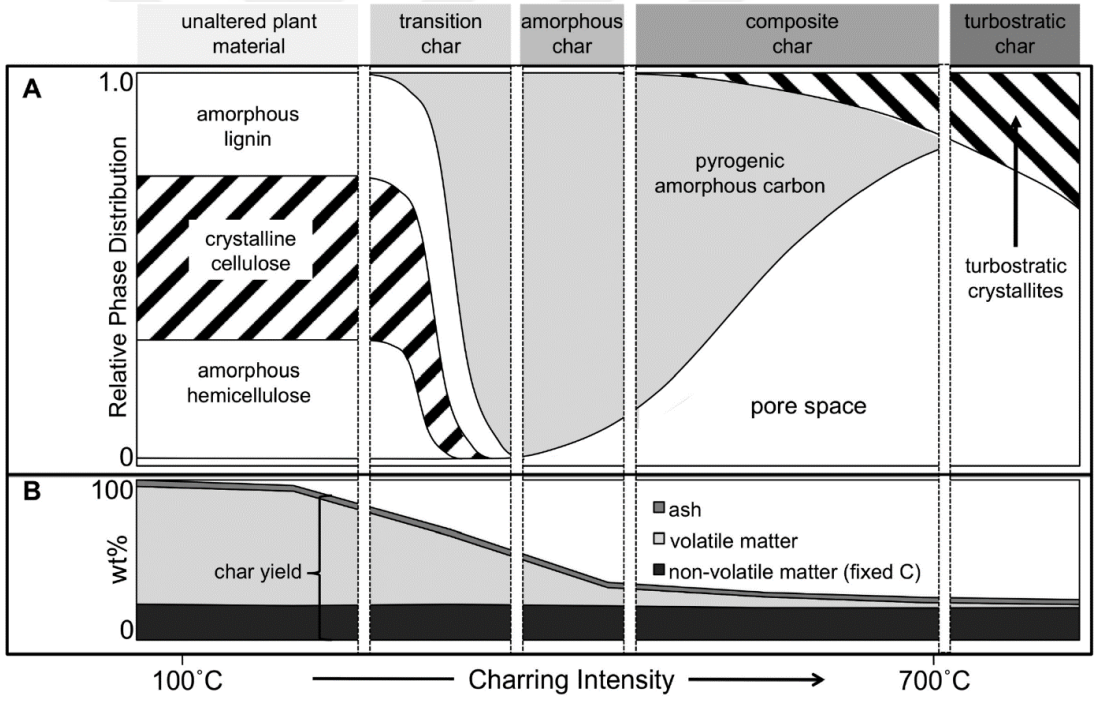

Figure 5.9 : Dynamic molecular structure of biomass-derived biochar formation stages and characteristics [259].

Like many biomass, rice husk consists of three main biopolymers as building blocks: cellulose, hemicellulose, and lignin. The weight percentage of these biopolymers and other components in rice husk is approximately 25-30 wt.% cellulose, 18-21 wt.% hemicellulose, 25-30 wt.% lignin, 15-20 wt.% silica, and 10-15 wt.% moisture

[261,262]. The molecular structure of cellulose, hemicellulose, and lignin is presented in Figure 5.10.

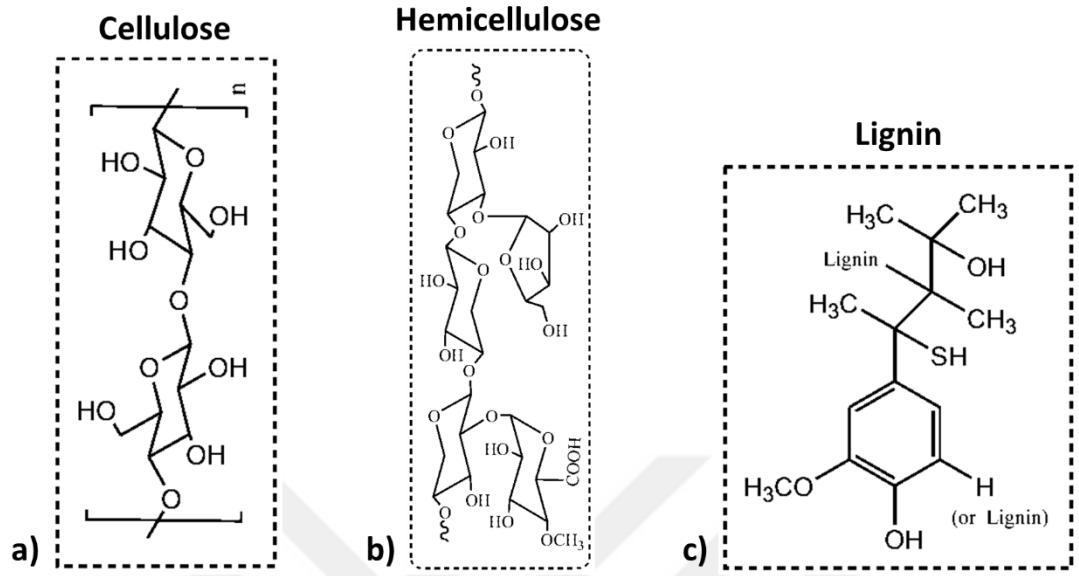

Figure 5.10 : Molecular structures **a)** Cellulose **b)** Hemicellulose **c)** Lignin [92].

During pyrolysis of rice husk, silica remains in the structure while the organic components break down, producing various gaseous by-products. Collard and Blin [263] studied the thermal conversion of cellulose, hemicellulose, and lignin, which are the basic building blocks of organic structures. They classified the reactions occurring during pyrolysis into primary and secondary reactions. During primary reactions, chemical bonds in the polymers break, releasing volatile chemicals while the residue matrix undergoes rearrangement. As seen in Figure 5.11, the three main pathways in primary reactions can be characterized as char formation, depolymerization, and fragmentation. Here, char formation occurs by intermolecular rearrangements of biopolymers, resulting in a higher stability residue. In this pathway, benzene rings are formed, leading to polycyclic structures with the release of water or incondensable gas. The second pathway is depolymerization. In this step, bonds between the monomer units are broken, which reduces the degree of polymerization of the chains, ultimately producing volatile molecules. Finally, fragmentation involves linking numerous covalent bonds within the polymer, including those in the monomer units. This process results in the formation of non-condensable gases and a variety of small organic compounds that can condense at room temperature.

When the volatile compounds formed due to the primary reactions are unstable under the reactor's temperature conditions, they can undergo secondary reactions, such as cracking or recombination. Cracking reactions involve breaking chemical bonds within the volatile compounds, forming lower molecular weight (MW) molecules. Recombination or recondensation reactions, on the other hand, combine volatile compounds to form a higher molecular weight (MW) molecule, which may become non-volatile under the reactor's temperature conditions. During these reactions, maintaining pyrolysis temperatures below 500 °C and slow heating rates promotes char formation, while temperatures above 600 °C and higher heating rates enhance the production of CH_4, CO, and H_2 gases [264,265].

A closer examination of how the heating rate affects the pyrolysis process made it clear that only low-energy chemical bonds can be broken at slower heating rates. As a result, the rearrangement reactions lead to the formation of a more stable biochar structure. At high heating rates, various types of chemical bonds break simultaneously, releasing volatile gases before any rearrangement reactions can occur. Additionally, smaller particle sizes enhance the efficiency of volatile gas formation.

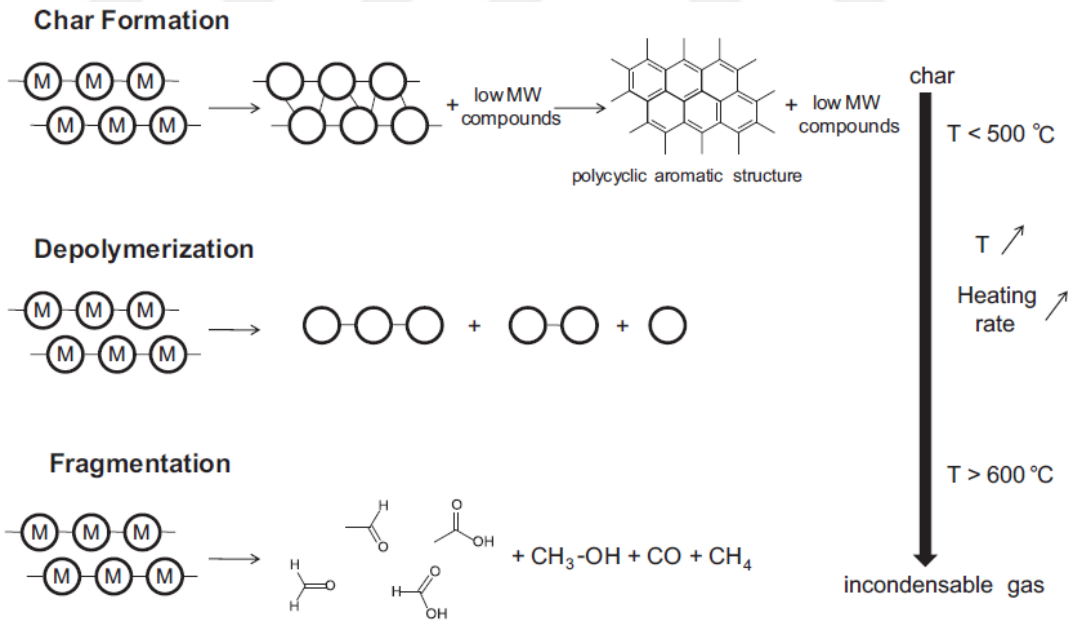

Figure 5.11 : Primary reactions of biomass pyrolysis [263].

Similarly, pyrolysis mechanisms of cellulose, hemicellulose, and lignin are studied by Chen et al. [92], and the generated volatiles are investigated via FTIR analysis. According to their study, the volatile gases, mainly CO, CH_4, and H_2, produced during pyrolysis were derived from the decomposition of hemicellulose, cellulose, and lignin,

in that order, reflecting their thermal stability. Additionally, when examining the biochars created through the pyrolysis at different temperatures, it was observed that most surface functional groups disappeared at temperatures above 600 °C for all samples. Additionally, similar FTIR spectra were obtained above this temperature. Furthermore, XRD patterns indicated that graphitization began in the biochars pyrolyzed above 500 °C for all materials.

Chen et al. [92] proposed possible decomposition mechanisms for cellulose, hemicellulose, and lignin by considering the thermal decompositions and generated products. They claimed that cellulose primarily degrades at low temperatures (below 300 °C) by breaking hydrogen bonds between the molecules and dehydrating hydroxyl groups. As the temperature rises, some pyran rings decompose, and oligosaccharides, acids, ketones, CO_2, CO, and other products are formed. Above 500 °C, intense deoxygenation reactions result in removing oxygen-containing functional groups, increasing CO gas production. Simultaneously, the continued dehydration of oligomers leads to the rapid formation of a benzene ring structure. These reactions result in biochar formation with a highly disordered cross-linked structure. Between 600 and 800 °C, the aromatic ring structure of biochar transforms into a macromolecular carbon structure, increasing its graphitization.

During the thermal decomposition of hemicellulose at low temperatures (below 250 °C), unstable carbohydrate chains are removed, and reactions such as dehydroxylation and decarboxylation occur. These processes lead to the formation of carbon dioxide (CO_2) gas. As the temperature increases above 400 °C, aromatic cyclization reactions form a ring structure. When the temperature surpasses 600 °C, condensation reactions produce a fused ring structure, which releases hydrogen (H_2) and methane (CH_4) gases.

The decomposition of lignin primarily occurs through free radical reactions. At temperatures between 200 and 300 °C, the cleavage of side chain bonds in lignin takes place, forming carbon monoxide (CO) and carbon dioxide (CO_2) gases. As the temperature increases, aromatic hydrocarbons and methane (CH_4) gas are produced. At temperatures above 500 °C, the aromatic ring structures open, leading to condensation reactions and the release of hydrogen H_2, CO, and CO_2 gases. Subsequently, more fused ring structures are formed at temperatures between 600 and 800 °C.

The study by Claoston et al. [266] investigates the effect of pyrolysis temperature on the physicochemical properties of rice husk. They conducted pyrolysis at three different temperatures: 350, 500, and 600°C. The results indicated that as the temperature increased, the porosity, ash content, and electrical conductivity of the rice husk biochar also increased. This increase in porosity is attributed to the volatilization of organic compounds, which creates new pores, and the breakdown of micropores, resulting in larger and more open pore structures. Conversely, carbon, hydrogen, and nitrogen content decreased in samples that were pyrolyzed at higher temperatures. The authors noted that the reduction in carbon content is due to diminishing carbonization reactions at elevated temperatures. Hidayat et al. [267] reported similar results, observing a decreasing trend in carbon content with increased temperature. According to the XRF analysis results, they also showed that silica is the main inorganic content of rice husk-derived biochar.

The morphological changes observed during pyrolysis processes at higher temperatures (700-900°C) were studied by Gao et al. [268]. Scanning electron microscopy (SEM) images reveal significant structural collapse due to melting when pyrolysis is conducted at 900°C, forming closed pores. The authors noted that the volatiles produced during pyrolysis can escape freely from the naturally porous raw material at lower temperatures. However, at temperatures exceeding 900°C, more volatiles become trapped within the structure, causing substantial collapse and decreased surface area and porosity. Gao et al. also explored the impact of temperature on graphitization. The higher intensity ratio (I_D/I_G) from Raman spectra indicates that increased pyrolysis temperatures enhance graphitization. Morin et al. [269] obtained similar results in their study of beech bark pellets and beech stick chars. They attributed the I_D/I_G ratio increase to a rise in the concentration of aromatic rings, particularly those with at least six fused benzene rings, which arise from dehydrogenation reactions. They concluded that higher pyrolysis temperatures lead to a greater number of aromatic rings within each ordered cluster.

Phuong et al. [270] investigated the effects of pyrolysis temperature and heating rate on biochar yield and its properties. They selected three different pyrolysis temperatures (350, 450, and 550 °C) and two heating rates (10 and 50 °C/min) for their study. The results indicated that increasing the pyrolysis temperature led to a higher carbon content, while higher heating rates increased the surface area for rice husk biochars.

The increase in volatile production at higher heating rates may explain these findings. The study by Collard et al. [263] provides a theoretical background for this phenomenon. Higher temperatures and heating rates lead to larger amounts of volatile compounds, such as CH_4, CO, and H_2, due to cellulose, hemicellulose, and lignin decomposition, the main components of rice husk and other biomass. A common characteristic of these generated gases is their reducing nature. These reducing gases are naturally produced during the pyrolysis of rice husk and can partially reduce the silica present in the biochar, resulting in SiO_x. SiO_x has a higher theoretical capacity and reactivity than silica, making it a promising candidate for use as an anode active material in lithium ion batteries.

Researchers have employed induction heating during pyrolysis to achieve higher heating rates. Tsai et al. [271] utilized a laboratory-scale fast pyrolysis system with induction heating to examine biochar and bio-oil derived from rice husk. Their investigation focused on the effects of heating rate, pyrolysis temperature, holding time, and particle size on the char yield and chemical composition. While induction heating has been used in previous pyrolysis studies, similar to Tsai et al.'s, these studies typically concentrate on the yield of biochar or bio-oil. To the best of our knowledge, pyrolysis of rice husk via induction heating and using this biochar as an anode active material in lithium ion batteries has not been studied yet. The fast heating rates achieved through induction heating will facilitate the generation of higher amounts of reducing gases during pyrolysis, which can be utilized to partially reduce silica to SiO_x. The end product will be a natural nanocomposite composed of carbon and SiO_x. This method could be used to produce high value-added anode active materials using organic wastes quickly and without harmful chemicals.

A detailed examination of research on rice husk-derived biochars and precipitated silica particles as anode active materials is presented in the literature review.

6. EXPERIMENTAL STUDIES

In this thesis, rice husk-derived anode active materials are synthesized, and the experimental studies are conducted in two different sets. In the first set of experiments, submicron SiO_2 particles are synthesized using rice husk via leaching and precipitation. The effect of calcination on precipitation efficiency, the solid-to-liquid ratio on precipitated particle size, and the ethanol addition on particle morphology are investigated. The samples are characterized and tested for their electrochemical performance. In the second set of experiments, a biochar composite consisting of SiO_x and C is produced via fast pyrolysis of rice husk. Fast heating is embraced to promote the generation of reducing gases. The effect of pyrolysis temperature and atmosphere on the carbon content of biochar and the valence state of silicon is investigated. The optimized sample is ball milled to reduce particle size. Finally, the electrochemical performances of biochar active materials are investigated.

6.1 Characterization of Pristine Rice Husk

The rice husk used in experiments is purchased from a local mill in Corum, Türkiye. Rice husk is ball milled at 800 rpm for 15 minutes in a stainless steel jar with stainless steel balls, taking the ball: powder ratio of 10:1. This powder is used in all experiments without further purification. In Figure 6.1, images of pristine rice husk and rice husk powder are given. In Figure 6.2, SEM images of pristine rice husk and elemental mapping results show that rice husk is composed of uniformly distributed C, O, and Si.

Figure 6.1 : Images of pristine rice husk rice husk powder obtained after ball milling.

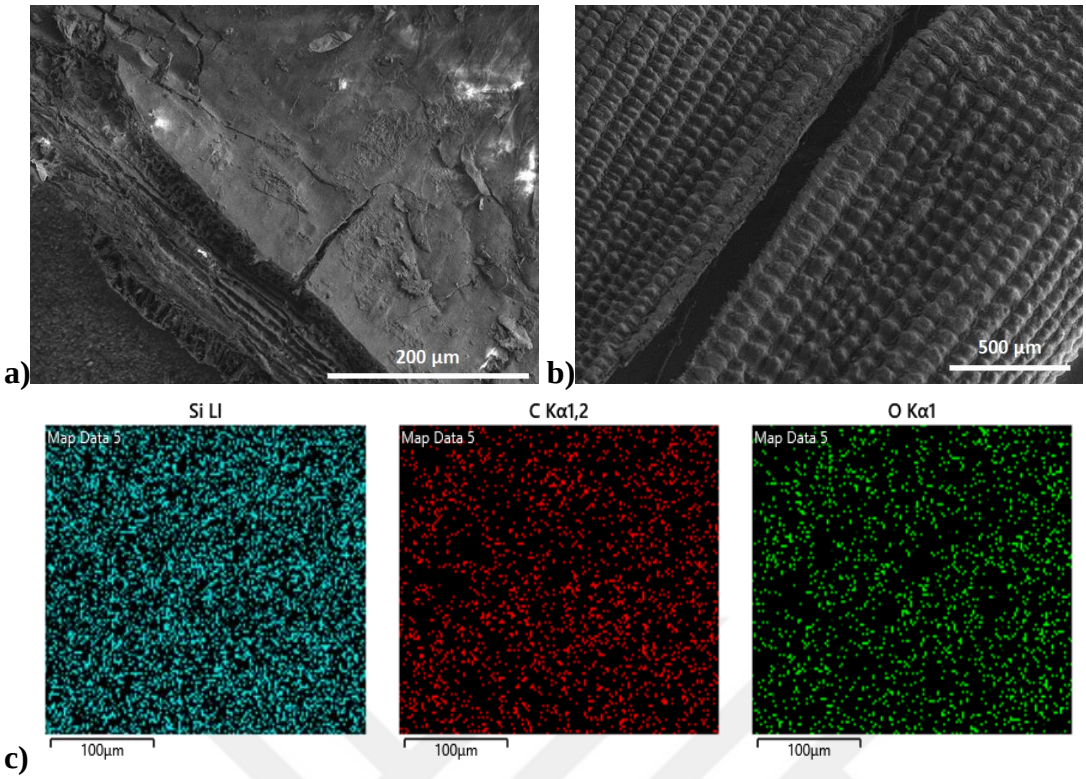

Figure 6.2 : SEM image of pristine rice husk **a)** inner shell **b)** outer shell **c)** EDS mapping of outer shell.

In Figure 6.3, SEM images of rice husk powder and EDS analysis results taken from analysis spots are given in Table 6.1. The average of the elemental results of three analysis points shows that the rice husk powder contains an average of 58% carbon, 32% oxygen, and 9% silicon.

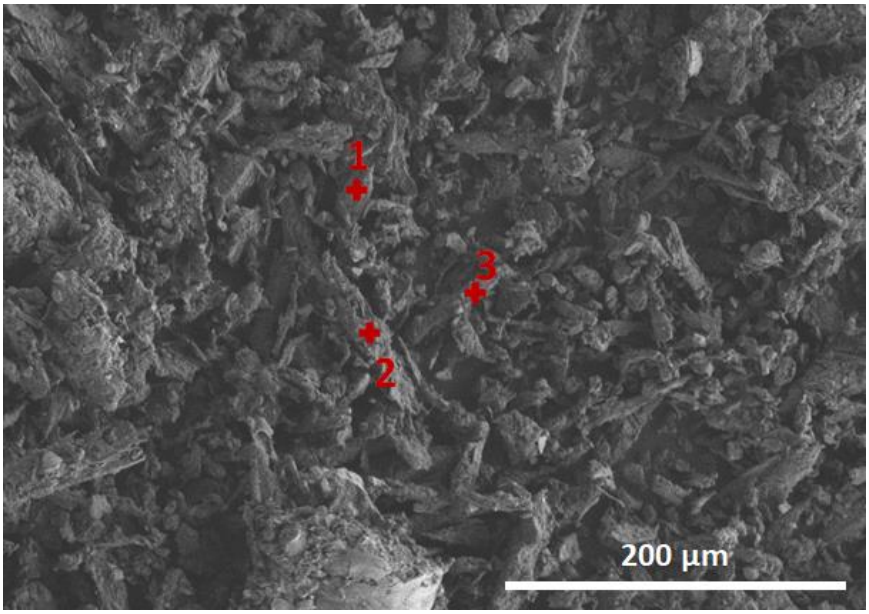

Figure 6.3 : SEM image of ball-milled rice husk powder.

Table 6.1 : EDS analysis results of rice husk powder.

Elements	Analysis 1 (wt.%)	Analysis 2 (wt.%)	Analysis 3 (wt.%)
C	45.9	50.3	78.9
O	40.7	39.9	17.1
Si	13.3	9.8	4.1

The thermal characterization of pristine rice husk powder is made by thermogravimetric analysis (TGA) between 25-900 °C in the air atmosphere with a 5 °C/min heating rate by using PerkinElmer TGA 4000, and the result is given in Figure 6.4. A weight loss of approximately 10% until 200 °C is ascribed to the removal of physically bonded water. A significant loss of 54% until 450 °C is observed and related to the decomposition of hemicellulose and cellulose. Later, at higher temperatures, a progressive weight loss until 900 °C is detected and attributed to the decomposition of lignin in the structure. TGA result shows that most organic components could be removed by heat treating rice husk at 600 °C.

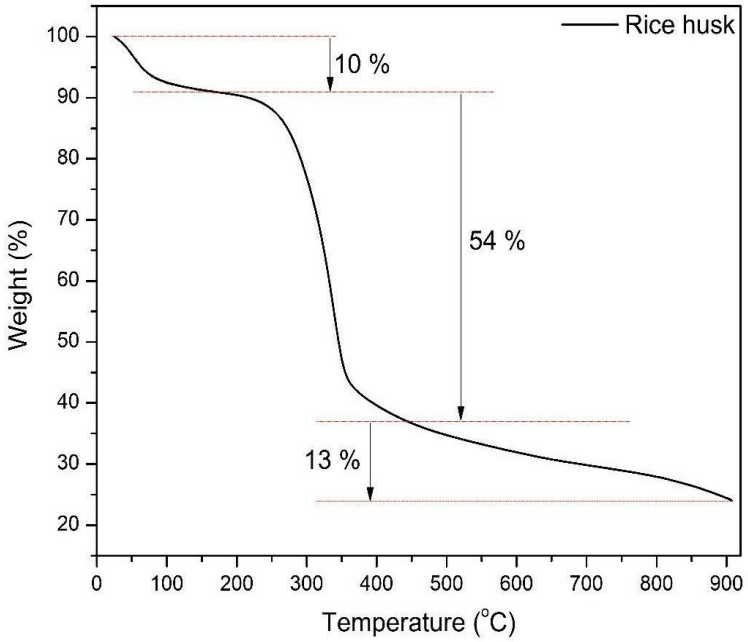

Figure 6.4 : TGA result of pristine rice husk powder.

To investigate the inorganic content, the rice husk powder is heat treated at 600 °C, and the elemental composition of the ash is determined by X-ray fluorescence (XRF) analysis (Bruker S8 Tiger) and presented in Table 6.2. The rice husk ash is mainly SiO_2 (87 wt.%) with minor amounts of impurities such as K_2O, CaO, Fe_2O_3, and MgO.

Table 6.2 : Chemical analysis of rice husk ash.

Oxides	**SiO_2**	**K_2O**	**CaO**	**Cl**	**SO_3**	**P_2O_5**	**MnO**	**Fe_2O_3**	**MgO**	**NiO**	**Rest**
wt.%	87.90	5.59	1.64	1.29	1.01	0.69	0.67	0.65	0.28	0.19	0.09

6.2 Submicron SiO_2 Anode Active Material Synthesis

In the first set of experiments, pristine rice husk powder and rice husk ash are used for the leaching process. To prepare the ash, rice husk powder is calcined at 600 °C for 3 hours to remove organic compounds. The resulting white powder, known as rice husk ash (RHA), is then added to a 2M NaOH solution. This mixture is subjected to continuous stirring at 80 °C for 3 hours to facilitate the leaching process. Afterward, the sodium silicate solution is obtained through filtration.

Next, 2.5M H_2SO_4 is added to the sodium silicate solution until the pH reaches 7, causing the formation of white precipitates. These precipitated particles are collected using centrifugation and washed with ethanol and deionized (DI) water at least three times. Finally, the precipitate is again calcined at 600 °C for 3 hours.

To see the effect of calcination on precipitation efficiency, the solid/liquid ratio on precipitated particle size, and ethanol addition on particle morphology, six samples in four sets are synthesized (see Table 6.3). The process flow chart and images of process products are given in Figures 6.5 and 6.6, respectively.

Table 6.3 : Experimental design of submicron SiO_2 particle synthesis.

Sample Code	Calcination	Solid/liquid ratio	Ethanol/water ratio		
PS-1	-	1/10	-		
PS-2	600 °C – 3 hours		-		
PS-3		1/20	-		
PS-4			1/2	1/1	2/1

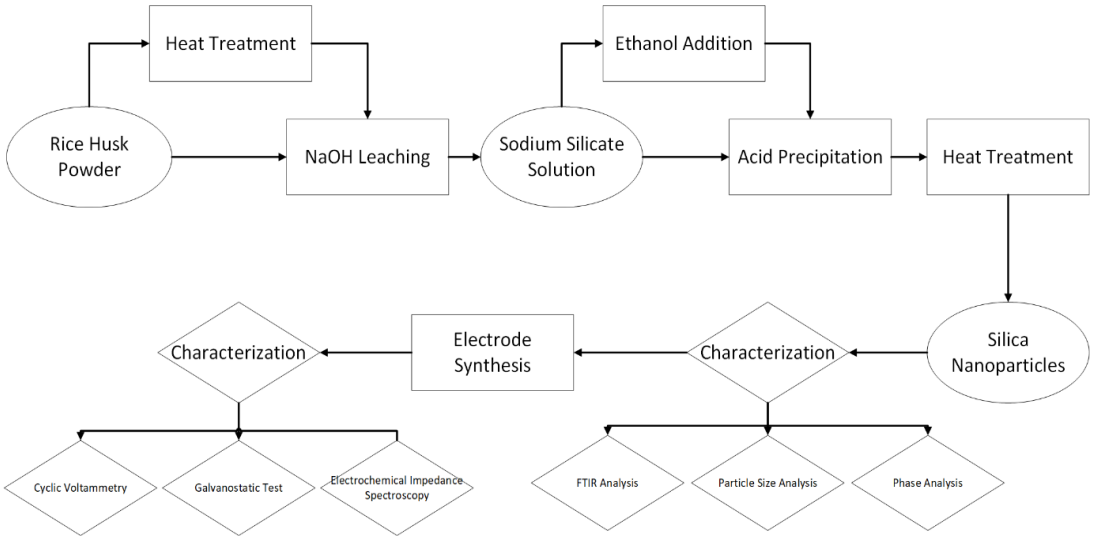

Figure 6.5 : The process flow chart of submicron SiO_2 particle synthesis.

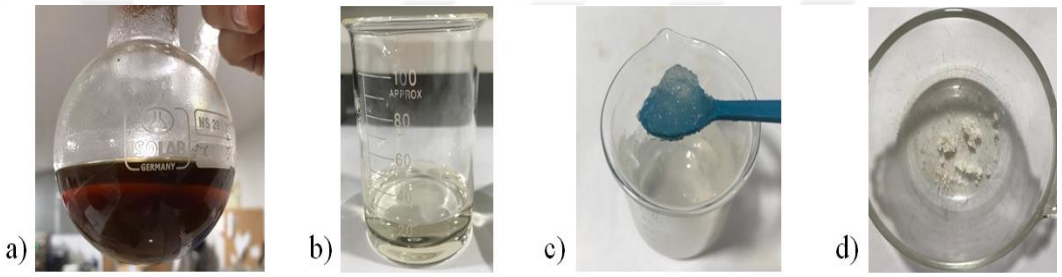

Figure 6.6 : Images of **a)** Pregnant leach solution **b)** Filtered sodium silicate solution **c)** Precipitated gel **d)** Dried precipitate.

6.3 Production of Nanocomposite Biochar Anode Active Materials Containing SiO_x and C via Fast Pyrolysis

In the second set, rice husk powder is pyrolyzed in an induction furnace via fast heating (>50 °C/min) under a controlled atmosphere to obtain biochar. Fast heating is embraced to promote the generation of reducing gases during pyrolysis. The duration is set to 90 minutes. For process optimization, rice husk powder is pyrolyzed at various temperatures (700-750-800 °C) under argon (Ar) or varigon (95% Ar + 5% H_2) atmospheres. The sample with the highest carbon content was later ball-milled to obtain a smaller particle size with a more homogeneous elemental distribution. The experimental parameters are given in Table 6.4. The process flow chart of biochar production and sample images taken after pyrolysis is shown in Figures 6.7 and 6.8, respectively.

Table 6.4 : Pyrolysis conditions of nanocomposite biochars.

Sample Code	Temperature (°C)	Duration (minutes)	Atmosphere	Milling after Pyrolysis
800-Ar	800	90	Argon	-
750-Ar	750			
700-Ar	700			
700-Ar-H			Varigon	
700-Ar-M			Argon	800 rpm – 12 hours

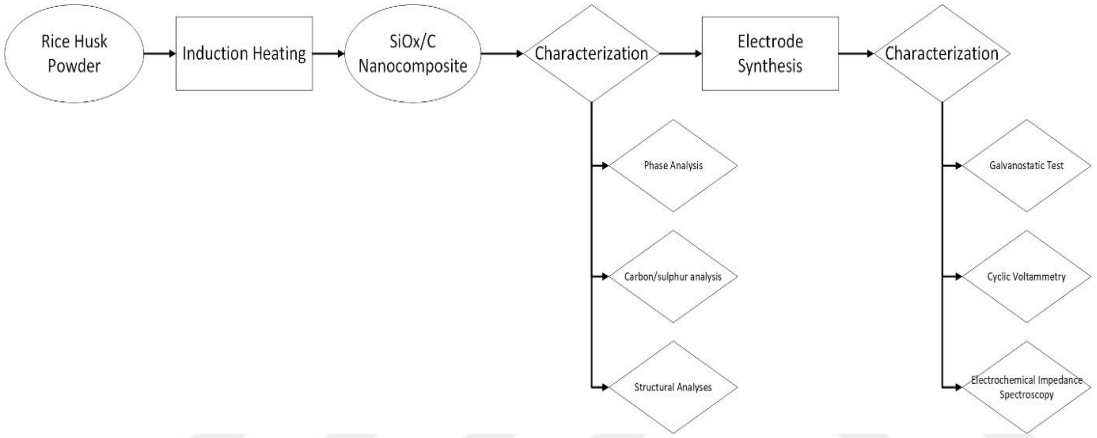

Figure 6.7 : The process flow chart of nanocomposite biochar production.

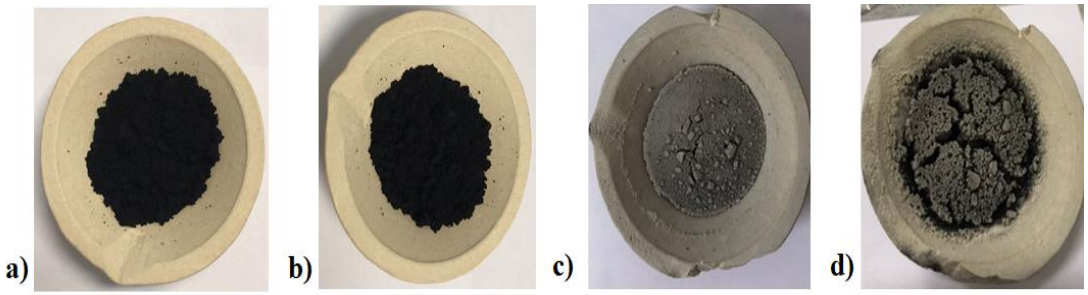

Figure 6.8 : Synthesized biochars **a)**700-Ar **b)**700-Ar-H **c)**750-Ar **d)**800-Ar.

6.4 Characterizations

6.4.1 Structural, chemical and morphological characterizations of powders

The structural characterizations of synthesized active materials are conducted via Fourier transform infrared spectroscopy – attenuated total reflectance (ATR-FTIR, Perkin Elmer UATR Two), X-Ray diffraction (Bruker D2 Phaser, using Cu-Kα in 2θ=10-90°), and Raman spectroscopy (Renishaw inVia, 532 nm laser wavelength).

The amount of carbon present in the active materials is determined by carbon/sulphur analyzer (Eltra). The binding energies of Si, C, and O are determined by XPS spectrometer (Thermo Scientific K-Alpha).

Particle morphologies are investigated by scanning electron microscopy (SEM, Zeiss Gemini 500). The electrode morphologies of fresh and cycled cells are investigated by ex-situ SEM images. After 200 cycles, cells are disassembled in a glove box, and electrodes are washed with Dimethyl carbonate (DMC) solution several times. The same images are taken from fresh electrodes for comparison. Particle sizes are measured by dispersing samples in deionized water using Malvern Panalytical Zeta Ultra. Diffraction patterns and bright/dark field images are collected using high-resolution transmission electron microscopy (HR-TEM, Jeol Jem 2100).

6.4.2 Electrochemical characterizations

A slurry is prepared for electrochemical characterizations by dispersing active materials synthesized, poly(vinylidene fluoride), and carbon black in N-Methyl-Pyrrolidone (NMP) with a 60:25:15 ratio. The slurry is coated on copper foil with a wet thickness of 50 µm. The coated electrodes are dried in a vacuum oven at 70 °C for 4 hours, followed by 120 °C overnight. Dry electrodes are rolled to 30 µm thickness and punched in 12 mm diameter (Figure 6.9). To investigate the effect of slurry composition on electrochemical performance, two slurry compositions, 60:25:15 and 80:10:10, were prepared for the sample optimized.

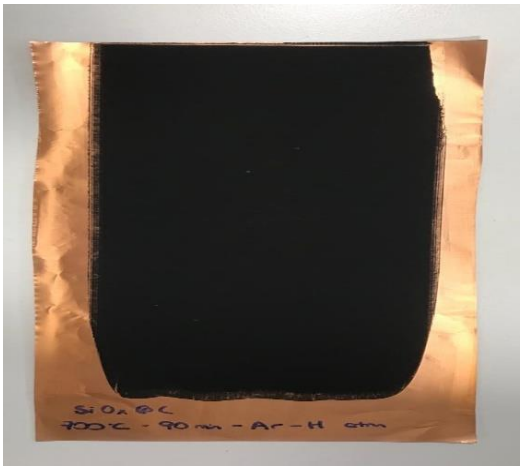

Figure 6.9 : Dry electrodes.

Coin cells (CR2032) are assembled in an argon-filled glove box (MBraun Labmaster) using metallic lithium as the counter electrode, Celgard 2400 as the separator, and

EC:DMC (v:v 50/50) solution containing 1M $LiPF_6$ as the electrolyte, as shown in Figure 6.10. Additionally, 10 v.% FEC is used as electrolyte addition in the sample optimized.

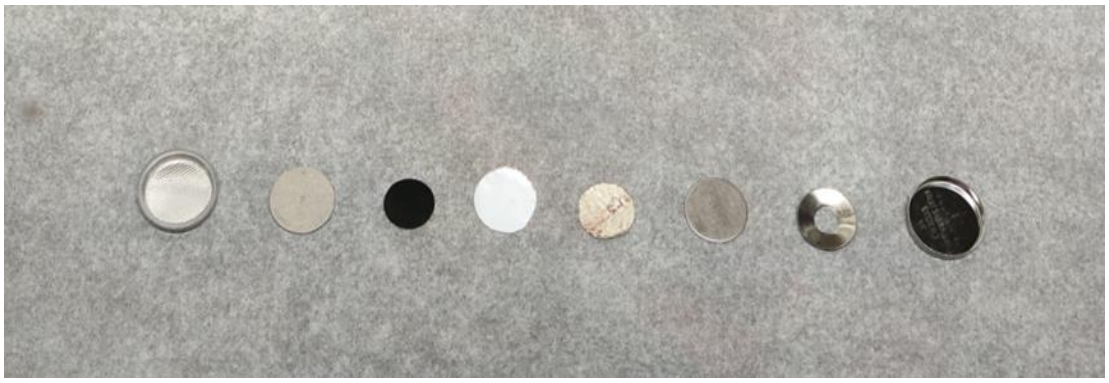

Figure 6.10 : Half cell assembly in glove box.

Prior to galvanostatic tests, the half cells are cycled between 2mV-2V vs. Li/Li^+ with a current density of 10 mA/g with 48 h holding at the cut-off voltages for 5 cycles to promote the growth of a stable SEI layer. Following the conditioning step, current density is increased to 50 mA/g, and cells are cycled between the same voltage window for 200 cycles. Some half cells are cycled in the same voltage window with a current density of 50 mAh/g without holding at cut-off voltages to investigate the effect of formation on the cell performances.

The reaction mechanism is investigated by cyclic voltammetry analysis between 2 mV - 3 V with a scan rate of 0.1 mV/s. The energy storage mechanism is examined in detail by cyclic voltammetry analysis at varying scan rates. The contribution of capacitive and diffusion behaviors in lithium storage is investigated by Equation 6.1 given below:

$$i(v) = k_1 v + k_2 v^{1/2} \tag{6.1}$$

$$i(v)/\, v^{1/2} = k_1 v^{1/2} + k_2 \tag{6.2}$$

In the above equations, v is the scan rate, i is the maximum current measured at a selected voltage value, and k_1 and k_2 are diffusion and capacitive constants, respectively. The $k_1 v$ reveals the portion of the surface-controlled pseudocapacitive process, while $k_2 v^{1/2}$ corresponds to the diffusion-controlled intercalation processes. The k_1 value is determined from the slope of the Equation 6.2.

Impedance values are measured after 1st and 3rd discharge steps by electrochemical impedance spectroscopy using Gamry Interface 1000 Potentiostat between 10^{-2} – 10^5

Hz with 5 mV perturbation potential. For discharging before EIS measurements, the cells are discharged to 2 mV at 50 mA/g current load and held at this voltage for 2 hours to ensure stabilization. The Gamry Echem Analyst software is used to model the EIS data.

7. RESULTS AND DISCUSSION

7.1 Submicron SiO_2 Anode Active Materials

This section studies the relations between the calcination and precipitation efficiency, solid-to-liquid ratio and particle size, ethanol addition and particle morphology. The process is optimized to achieve the minimum particle size to decrease the lithium diffusion path and improve electrochemical performance.

7.1.1 Structural characterizations

The structure of the synthesized particles is characterized by FTIR spectroscopy. As seen in Figure 7.1, all samples exhibit similar spectra. Three characteristic bands for silica are present in each sample, located around 450, 800, and 1060 cm^{-1}, confirming the SiO_2 structure. These bands correspond to the bending of Si-O bonds, as well as the symmetric and asymmetric stretching vibrations of Si-O-Si bonds, respectively [272]. When ethanol is added to the sodium silicate solution to synthesize PS-4 samples, a slight red shift in the Si-O band around 450 cm^{-1} is observed. This shift to lower wavenumbers may be attributed to the reduced stability of Si-O bonds caused by decreased solution polarity. Moreover, the absence of additional organic or inorganic bands confirms the high purity of the synthesized silica particles. According to Sankar et al. [273], most unwanted inorganic phases are eliminated during the post-precipitation heat treatment step, resulting in highly pure silica powder.

The X-ray diffraction (XRD) patterns of the synthesized submicron SiO_2 particles are presented in Figure 7.2. All samples exhibit an amorphous structure, as indicated by the amorphous halo observed around 23°. Despite washing all samples three times with deionized (DI) water and ethanol after precipitation, a small peak around 34° was detected in some samples. This peak is attributed to the untransformed sodium silicate phase (ICDS card no: 01-1007). Kim et al. [274] noted that residual sodium silicate can be removed by washing the samples with diluted acetic acid.

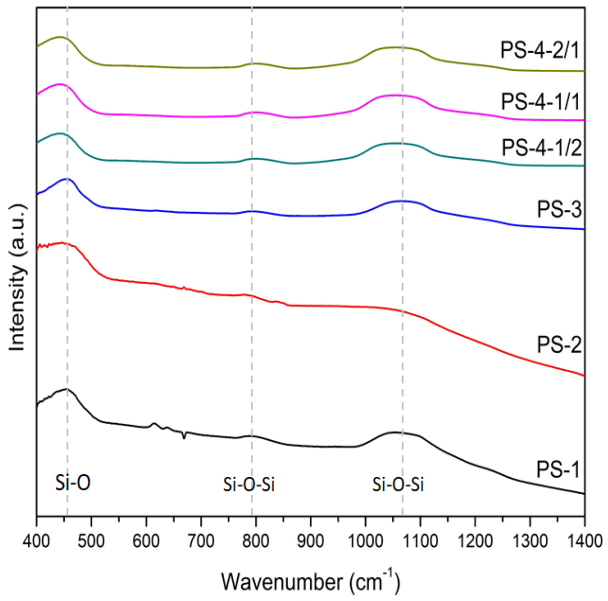

Figure 7.1 : FTIR spectra of submicron SiO_2 anode active materials.

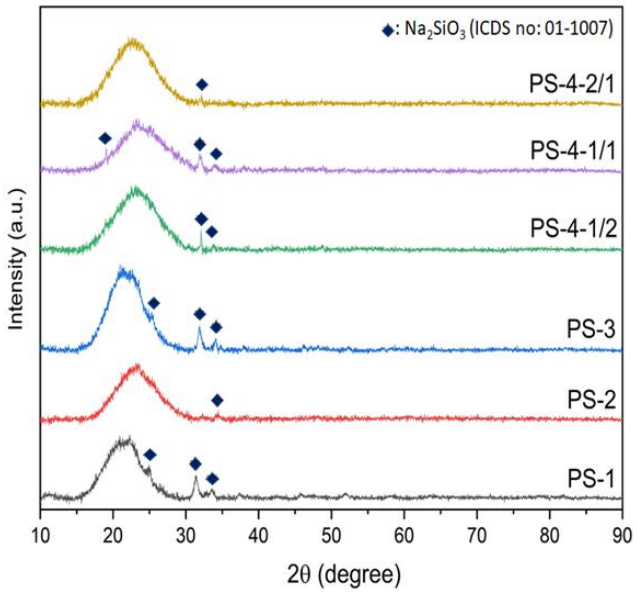

Figure 7.2 : XRD patterns of SiO_2 anode active materials.

7.1.2 Morphological characterizations

Figure 7.3 displays the measured particle sizes for various samples. During the production of the PS-1 and PS-2 samples, rice husk powder and its ash were utilized in the leaching stage, respectively. Although both samples exhibited large sizes, the size distribution in the PS-2 sample was more narrow. Additionally, rice husk powder contains only 20% silica by weight, which results in a lower yield during precipitation. Considering these factors, it was determined that using rice husk ash in the leaching process is more advantageous. Notably, PS-3 exhibited the smallest particle size and the narrowest size distribution among all the samples. The results suggest that using

rice husk ash for leaching at a solid-to-liquid ratio of 1:20 produces the smallest particle size. A lower solid-to-liquid ratio corresponds to a decreased SiO_2/Na_2O ratio. This outcome is expected, as the SiO_2/Na_2O ratio is a key factor influencing the complexity of silica units (Q^n) in sodium silicate solutions, ultimately affecting the final particle size.

Moreover, ethanol addition to sodium silicate solution led to an increase in particle size and a wider distribution. This broader distribution arises from the miscibility of sodium silicate in ethanol, which increases sodium silicate concentration in water, causing local supersaturation, as explained by Cui et al. [275]. Supporting our results, they observed that as the amount of ethanol increased, the distribution and particle sizes also enlarged.

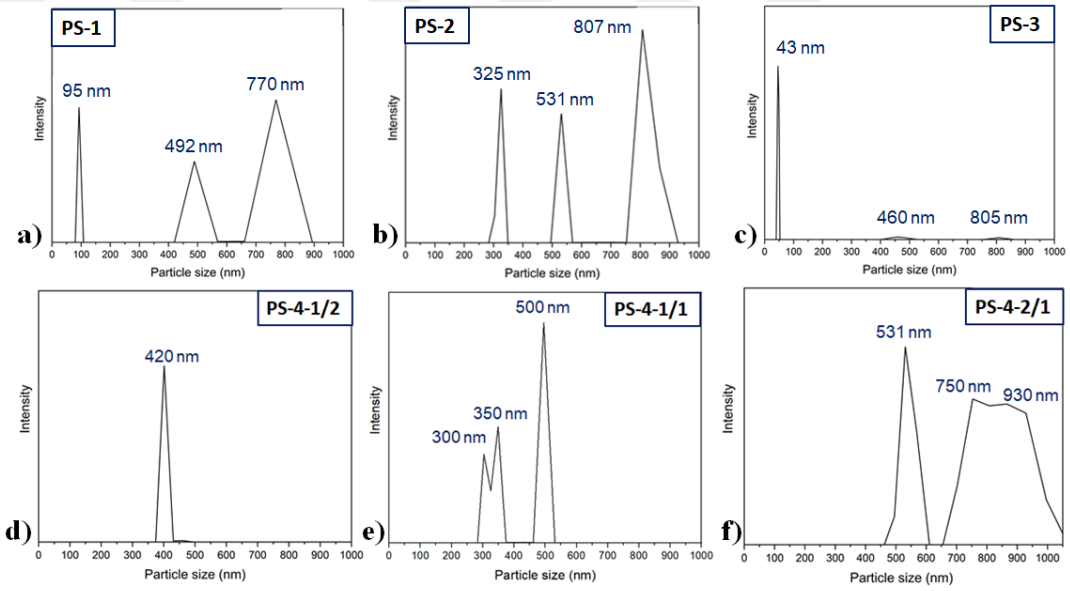

Figure 7.3 : Particle size measurements of submicron SiO_2 anode active materials.

The morphologies of the particles were further examined using scanning electron microscopy. As shown in Figure 7.4, agglomerated particles with angular shapes were observed. The PS-3 sample displayed smaller, rod-like particles (see Fig. 7.4c). During the formation of silica particles, monomeric silicic acid undergoes polymerization reactions to convert into oligomeric silicic acid. This process leads to the formation of primary particles ranging in size from 20 to 50 nm [276]. Subsequently, these primary particles begin to aggregate, resulting in larger particles. Although the concentration of the sodium silicate solution used in the PS-3 sample is similar to that of commercial solutions, it may be too high, potentially causing particle agglomeration and non-isotropic growth. To prevent this agglomeration issue, using solutions with lower

concentrations or addition of surfactants could be beneficial. This approach would further contribute to reducing particle sizes.

Dominguez et al. [253] claimed that using ethanol in a sodium silicate solution as a co-solvent could promote the formation of more spherical particles due to its lower surface tension, which results in isotopic growth. However, agglomeration was more dominant than particle globularization due to decreased viscosity in our results.

For further analyses, only the PS-4-1/2 sample was used due to its smaller particle size among the ethanol-added samples (PS-4).

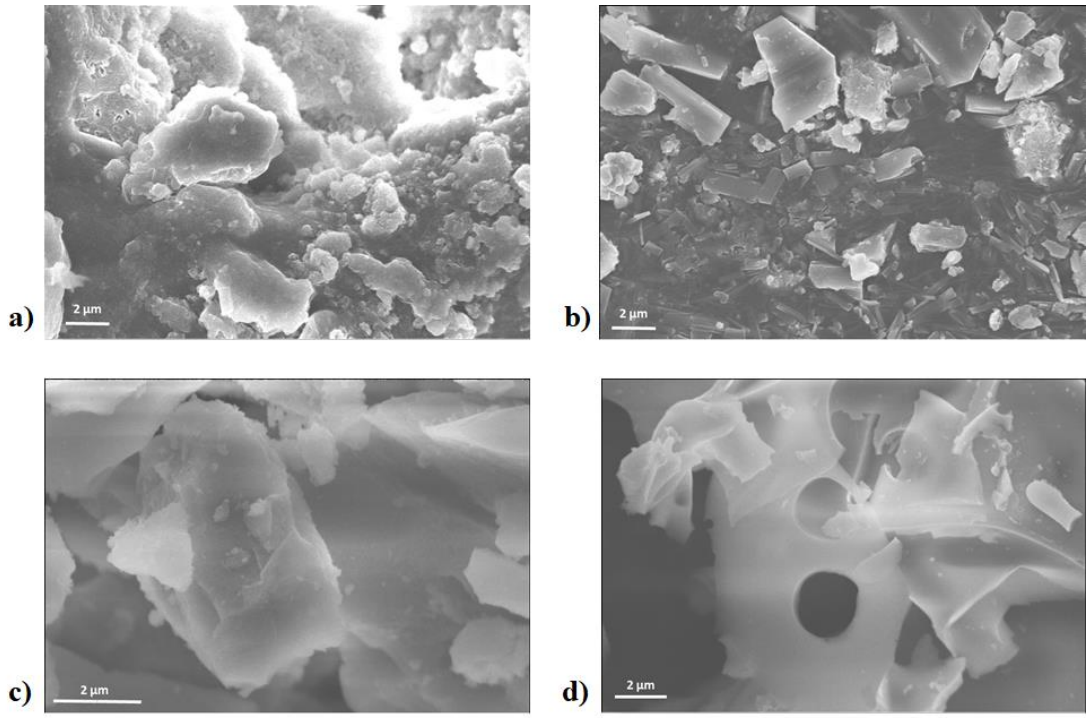

Figure 7.4 : SEM images of synthesized active materials **a)** PS-1 **b)** PS-2 **c)** PS-3 **d)** PS-4-1/2.

7.1.3 Electrochemical characterizations

The electrochemical performance of synthesized submicron SiO_2 anode active materials was evaluated through galvanostatic tests. Figures 7.5-7.8 illustrate that the charge-discharge curves display a small shoulder around 0.7 V and a voltage plateau below 0.2 V, indicating the formation of a solid electrolyte interphase (SEI) layer and lithium storage, respectively [277]. The first discharge capacities recorded for samples PS-1, PS-2, PS-3, and PS-4-1/2 are 356, 205, 503, and 265 mAh/g, respectively. The PS-3 sample with the smallest particle size demonstrated the highest initial discharge capacity. However, the low lithium diffusion coefficient and electrical conductivity of

silica are believed to contribute to the reduced specific capacity of the samples [278]. The smaller particle size may improve capacity by shortening the lithium diffusion pathway. Additionally, all samples showed a sudden drop in capacity after the first cycle, which may be linked to the formation of irreversible phases during the lithiation reactions of SiO_2 [278].

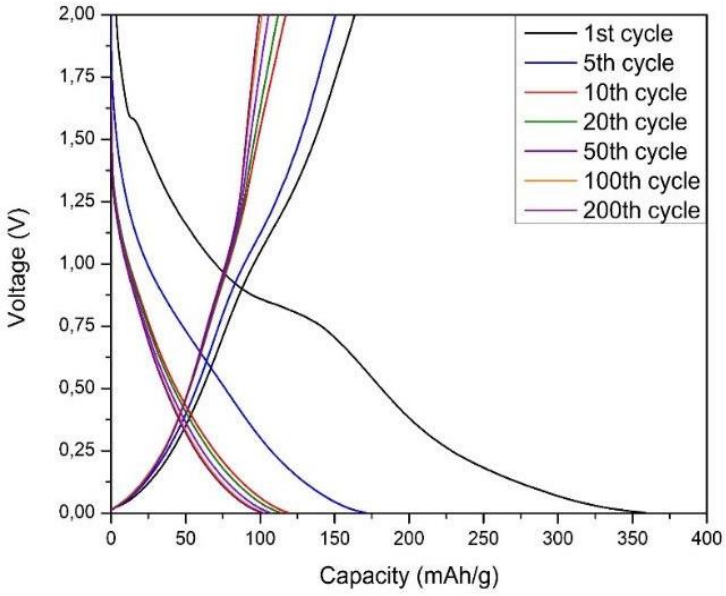

Figure 7.5 : Voltage-capacity curve of PS-1.

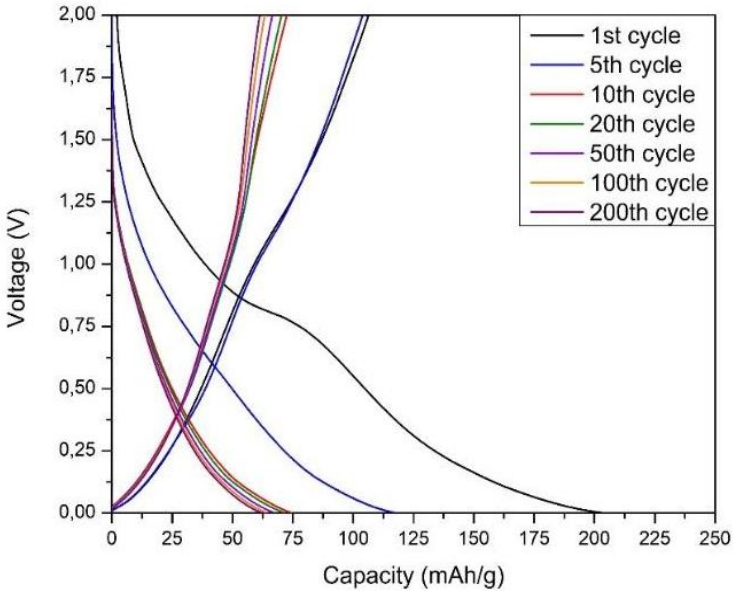

Figure 7.6 : Voltage-capacity curve of PS-2.

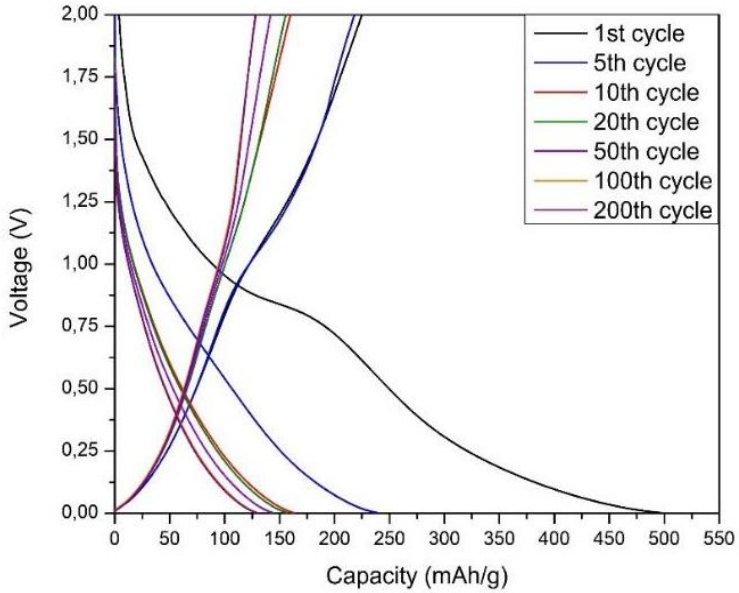

Figure 7.7 : Voltage-capacity curve of PS-3.

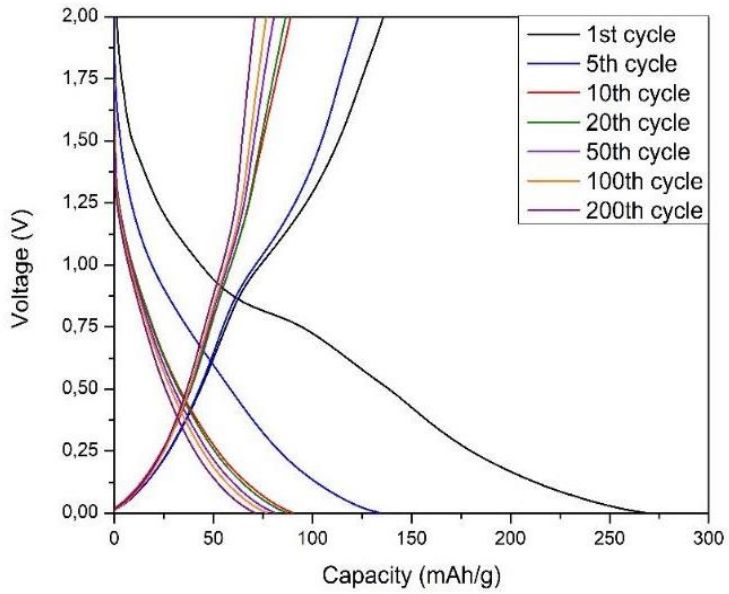

Figure 7.8 : Voltage-capacity curve of PS-4-1/2.

The capacity retention of the anode active materials is evaluated through their cycle performance, as shown in Figure 7.9. Among the samples, PS-3 exhibits the highest reversible capacity after 200 cycles. The initial Coulombic efficiency (CE) for all samples is approximately 70%. However, in subsequent cycles, the CE increases to nearly 100%. Similar to galvanostatic tests, the low initial CE is attributed to the formation of irreversible phases and the growth of the solid electrolyte interphase (SEI) [278].

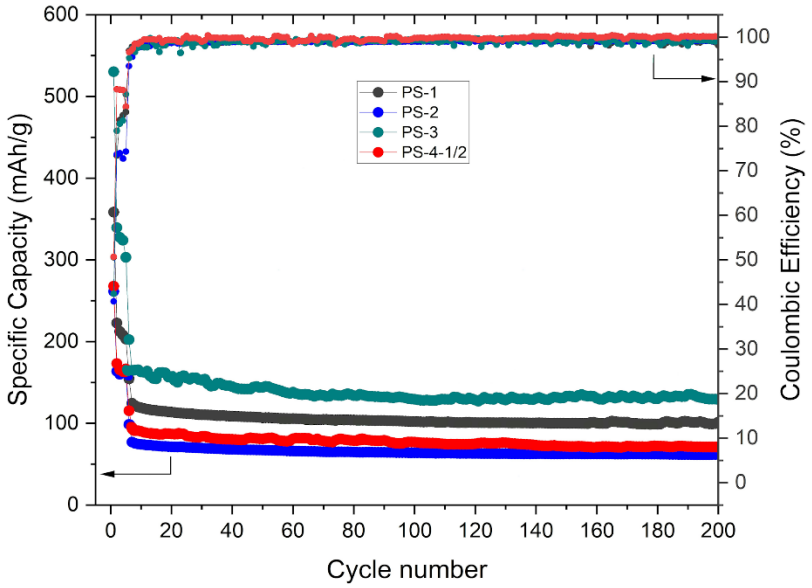

Figure 7.9 : Capacity retention of submicron SiO_2 anode active materials.

The lithiation mechanisms of submicron SiO_2 anode materials have been further examined using cyclic voltammetry (CV) analyses. The CV curves are illustrated in Figures 7.10-7.13. The anodic peak around 0.1 V can be assigned to delithiation, while the peak at approximately 1.2 V corresponds to the conversion of $Li_2Si_2O_5$ to SiO_2 [279]. The cathodic peak near 0.7 V is attributed to the formation of the solid electrolyte interphase (SEI) layer, while the cathodic peak below 0.4 V is associated with lithiation reactions. Overall, low current values are observed in all samples, indicating the low activity of SiO_2 anode materials, which is a result of their low electrical conductivity and low lithium mobility [280]. The reduction in peak currents after the first cycle is believed to arise from the formation of inactive components.

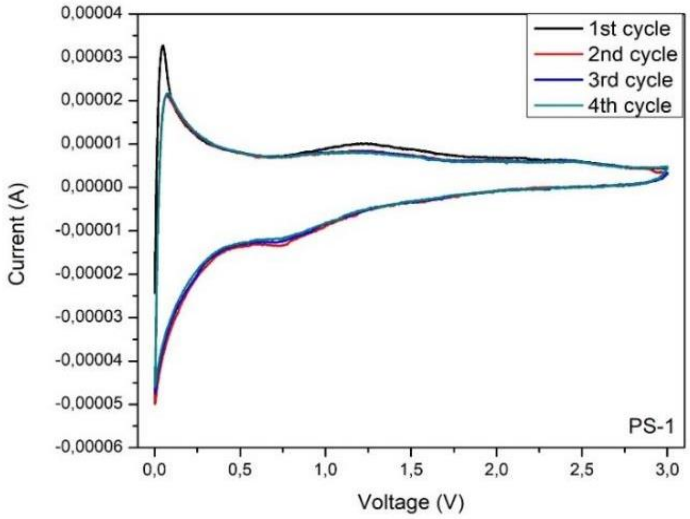

Figure 7.10 : Cyclic voltammetry curve of PS-1.

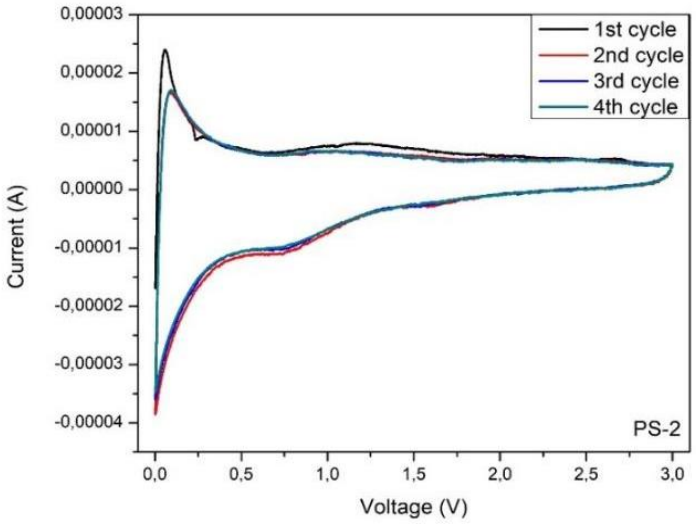

Figure 7.11 : Cyclic voltammetry curve of PS-2.

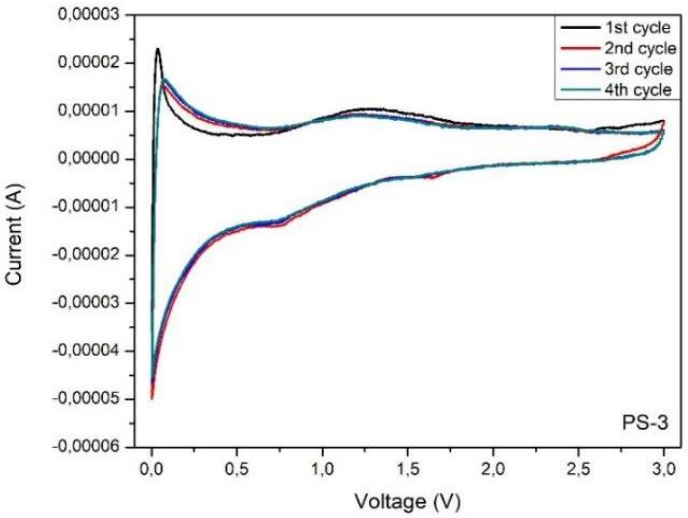

Figure 7.12 : Cyclic voltammetry curve of PS-3.

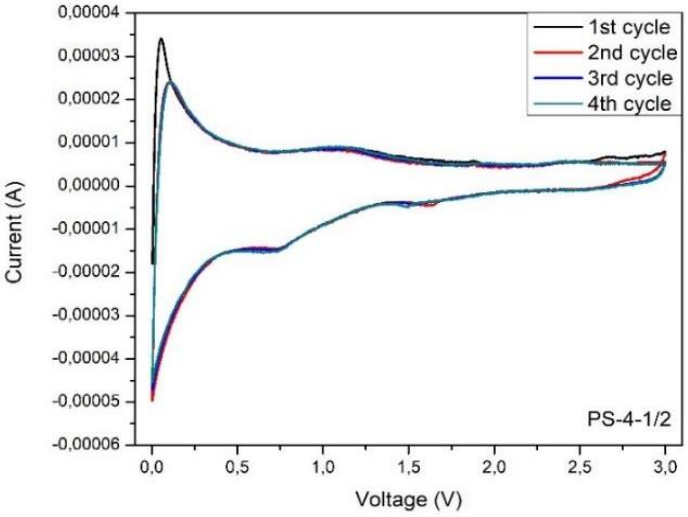

Figure 7.13 : Cyclic voltammetry curve of PS-4-1/2.

The impedance spectra of submicron SiO_2 anode active materials and equivalent circuit used in modeling are given in Figures 7.14-7.18. All samples exhibited a depressed semicircle with Warburg diffusion. The circuit consists of a solution resistance, constant phase element and resistance of SEI layer and charge transfer reactions followed by Warburg impedance. In all samples, charge transfer and SEI resistance values are increased after cycling, indicating increased resistance due to the growth of a stable SEI layer and the formation of lithium silicates, which decreases the electrical conductivity. In coherence with galvanostatic results, the lowest SEI and charge transfer resistance values are observed in the sample with the smallest particle size, namely PS-3. Smaller particles are believed to ease Li^+ diffusion in silica by shortening the diffusion path, resulting in lower impedance values [278].

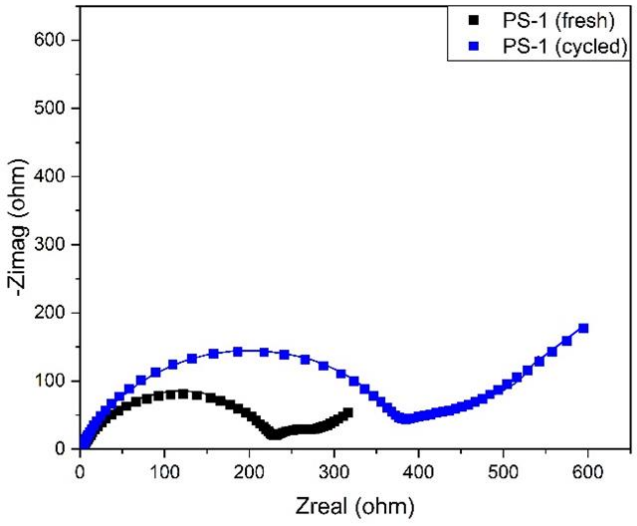

Figure 7.14 : Impedance spectra of PS-1.

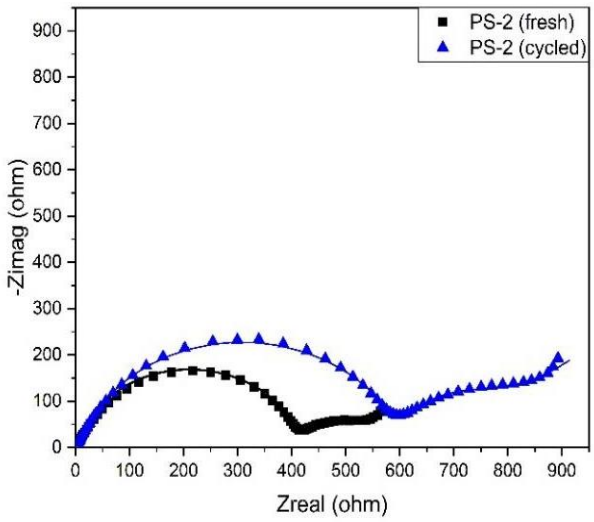

Figure 7.15 : Impedance spectra of PS-2.

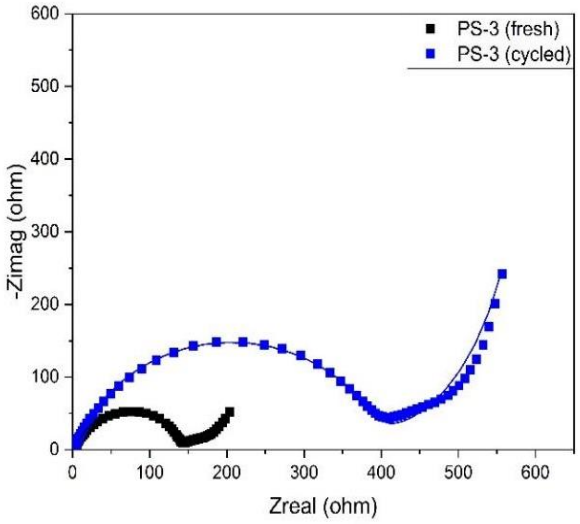

Figure 7.16 : Impedance spectra of PS-3.

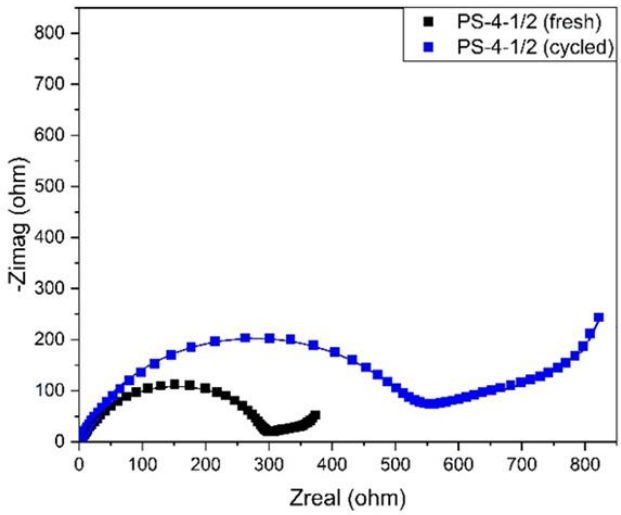

Figure 7.17 : Impedance spectra of PS-4-1/2.

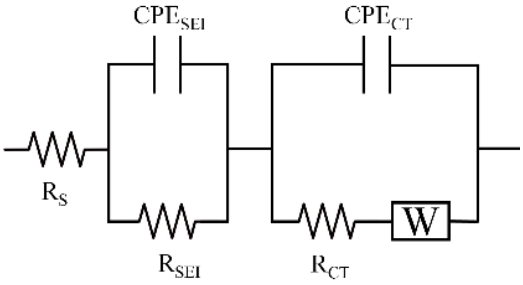

Figure 7.18 : Equivalent circuit.

7.2 Nanocomposite Biochar Anode Active Materials Containing SiO_x and C via Fast Pyrolysis

This section describes the synthesis of nanocomposite biochar anode active materials from rice husk powder using a fast pyrolysis method with induction heating. In this

process, the organic content of the rice husk is converted into carbon and reducing gases through decomposition. The fast heating promotes the formation of these reducing gases, which are then used to partially reduce silica to SiO_x. Formation of SiO_x resulted in an increase in capacity due to improved electron transport. In the resulting nanocomposite, carbon enhances electrical conductivity, while SiO_x serves as the electroactive material. Therefore, the process is optimized to preserve the maximum amount of carbon in the biochar. The effect of pyrolysis atmosphere/temperature and milling on the electrochemical performance of SiO_x anode active materials is investigated.

7.2.1 Structural characterizations

The IR spectra given in Figure 7.19 reveal the Si-O and C-related bonds in all samples. In general, similar spectra are observed for all synthesized nanocomposite biochars. The broad peak observed at 1055 cm^{-1} is associated with asymmetric and symmetric stretching of Si-O-C and Si-O-Si bonds, the broad hump around 800 cm^{-1} is attributed to Si-O-Si stretching mode, while two peaks at 418 and 505 cm^{-1} are related with Si-O bending mode [7,281,282]. Functional groups are similar in samples pyrolyzed at 700-750-800 °C, only with increased peak intensities at higher temperatures. The partially reducing atmosphere (Ar-H) did not majorly affect the functional groups. According to Keiluweit et al. [259], most functional groups are lost, resulting in similar spectra at biomass pyrolyzed at 600 °C and above temperatures.

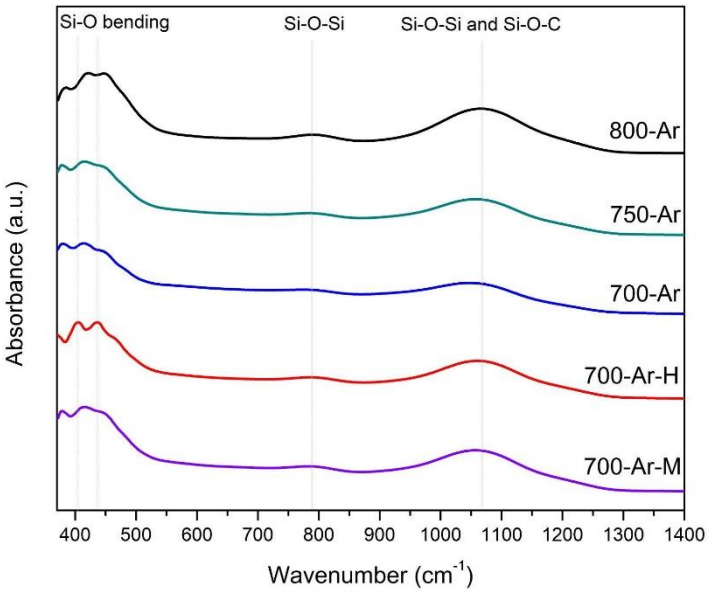

Figure 7.19 : IR spectra of nanocomposite biochars.

Carbon structure is investigated in detail via Raman spectroscopy (Figure 7.20). Two characteristic peaks, namely D and G bands, at 1340 and 1575 cm^{-1} are observed in all samples. The D band is related to the disordered or defective type of carbon, while the G band is related to ordered graphitic carbon. No peak is detected in pristine rice husk samples, but distinct D and G bands are seen in all pyrolyzed samples. This shows the successful transformation of the rice husk into nanocomposite biochar. The graphitization ratio of samples (I_D/I_G ratio) is calculated and found as 0.87, 0.89, 0.81, 0.84, and 0.96 for 700-Ar-M, 700-Ar-H, 700-Ar, 750-Ar, and 800-Ar samples, respectively. As expected, milling after pyrolysis increased the I_D/I_G ratio by creating defects in the sample [23]. Higher I_D/I_G ratios observed at increased pyrolysis temperatures could be explained by the increment in aromatic ring concentrations containing a minimum of six fused benzene rings. The change in the I_D/I_G ratios as a result of pyrolysis temperature is investigated by Morin et al. [269] using beech bark pellet and beech stick chars. Higher I_D/I_G ratios could be explained by the increased number of aromatic rings due to the dehydrogenation of hydroaromatics. Similarly, higher graphitization degrees are obtained by Gao et al. [268] using rice husk biochars. Higher graphitization is expected to increase electrical conductivity, hence improved electrochemical performance [283].

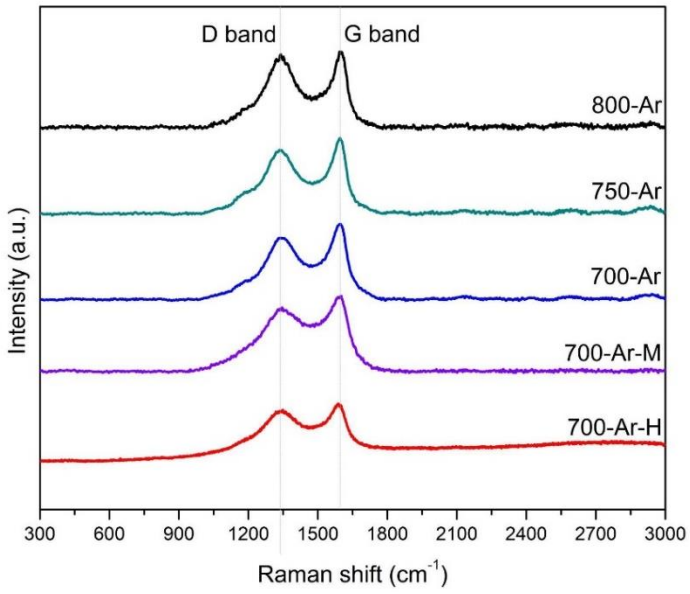

Figure 7.20 : Raman spectra of nanocomposite biochars.

XRD patterns presented in Figure 7.21 reveal that all samples exhibit an amorphous structure. The broad peak around 23° is associated with amorphous SiO_x and carbon. When the pyrolysis temperature is raised to 800 °C, crystallization of amorphous

phases and formation of cristobalite (ICDS:98-003-3086) is detected [284]. Additionally, a small bump around 43° is attributed to graphitic carbon.

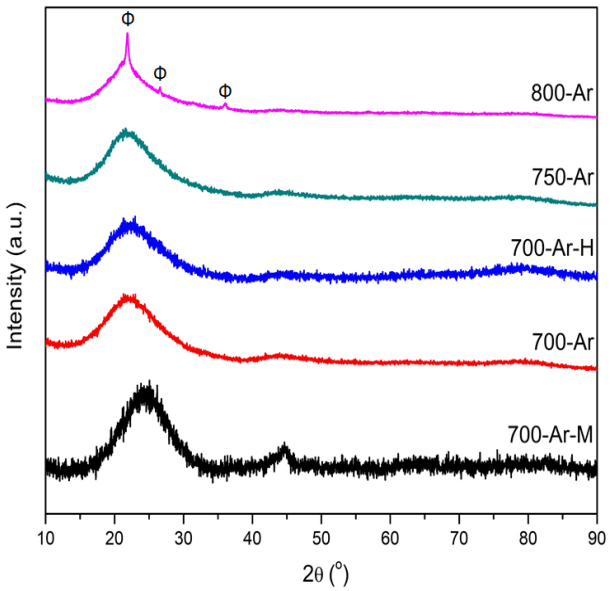

Figure 7.21 : XRD patterns of nanocomposite biochars.

7.2.2 Chemical characterizations

The carbon preserved in the biochar structure after pyrolysis is determined by carbon/sulfur analysis, and results are given in Table 7.1. According to the results, the highest carbon is detected in the sample pyrolyzed at 700 °C under an argon atmosphere, similar to the results obtained in other studies [267]. The weight measurements after pyrolysis are found to be in coherence with this result. Conducting pyrolysis at a partially reducing atmosphere (Ar-H) leads to higher carbon loss, as expected.

Table 7.1 : Carbon content of biochars.

Sample Code	Carbon content (wt.%)	Weight loss during pyrolysis (%)
700-Ar-H	37.3	71.4
700-Ar	41.3	66.8
750-Ar	32.5	72.6
800-Ar	20.5	78.6

XPS analysis was conducted on the sample with the maximum carbon content (700-Ar) to investigate the Si-O bonding under the existence of C in the material. The XPS spectrum of the 700-Ar sample shown in Figure 7.22 exhibits O 1s, C 1s, Si 2s, and Si

2p peaks at 533, 285, 154, and 103 eV, respectively. The O 1s spectrum (Figure 7.23) shows three peaks: HO-C=O at 530.88 eV, Si-O at 532.50 eV, and C=O at 534.08 eV [25]. In the C 1s spectrum (Figure 7.24), five peaks are observed as O-C=O at 287.68 eV, O-C-O at 286.28 eV, C-O at 285.08 eV, C-C sp^3 at 283.98 eV, and C-C sp^2 at 283.68 eV [285]. The deconvolution of the Si 2p spectrum (Figure 7.25) reveals three peaks as Si^{2+} at 103.08 eV, Si^{3+} at 103.63 eV, and Si^{4+} at 105.13 eV, which indicates the successful partial reduction of SiO_2 to SiO_x by pyrolysis. The reducing gases such as CO and H_2 are released during pyrolysis upon the decomposition of rice husk powder, resulting in the reduction of SiO_2 [25]. The formation of SiO_x phases is expected to improve the electrochemical performance because of its higher theoretical capacity than SiO_2 anodes [286].

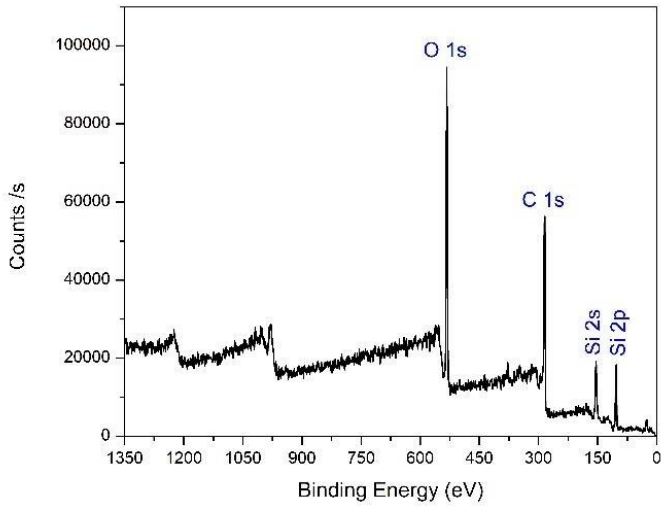

Figure 7.22 : XPS spectra of the 700-Ar.

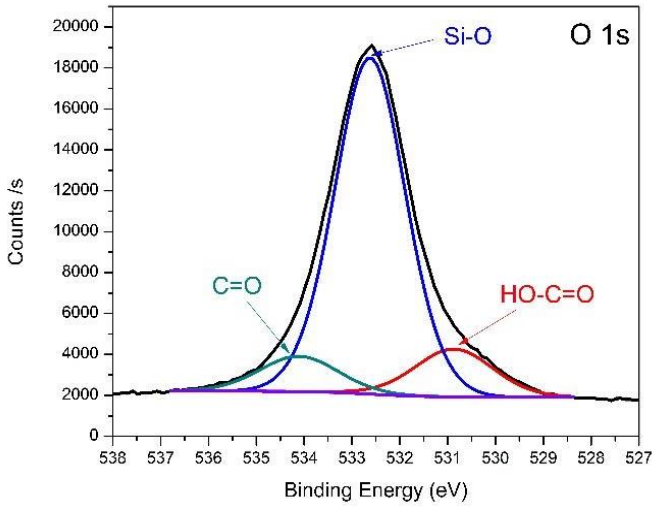

Figure 7.23 : O 1s spectra of the 700-Ar.

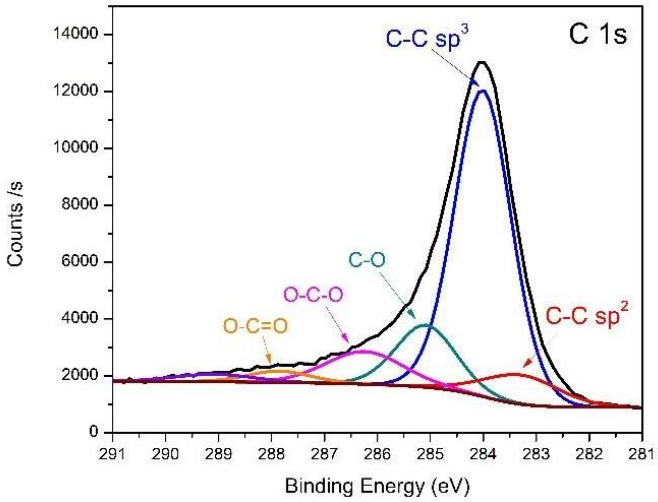

Figure 7.24 : C 1s spectra of the 700-Ar.

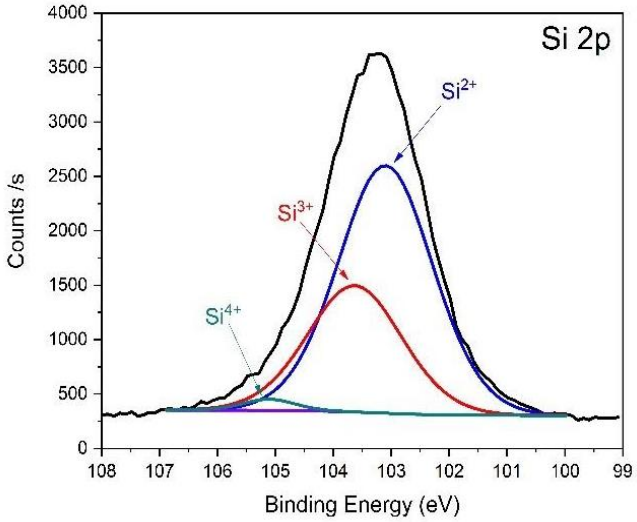

Figure 7.25 : Si 2p spectra of the 700-Ar.

7.2.3 Morphological characterizations

Scanning electron microscopy (SEM) images of the sample surfaces reveal micron-sized particles with heterogeneous morphology (Figure 7.26). It is known that pyrolysis temperatures exceeding 800 °C can lead to melting and fragmentation as volatile components exit the structure, resulting in porosities [268,283]. Temperatures reaching up to 900 °C can cause the formation of closed pores due to collapsing and melting processes. Additionally, according to Wang et al. [287], reducing atmospheres such as hydrogen (H_2) lead to an increased pore volume compared to inert atmospheres during pyrolysis. Furthermore, the 700-Ar-M sample, which ball-milled after pyrolysis, is tend to agglomerate more due to increased surface area.

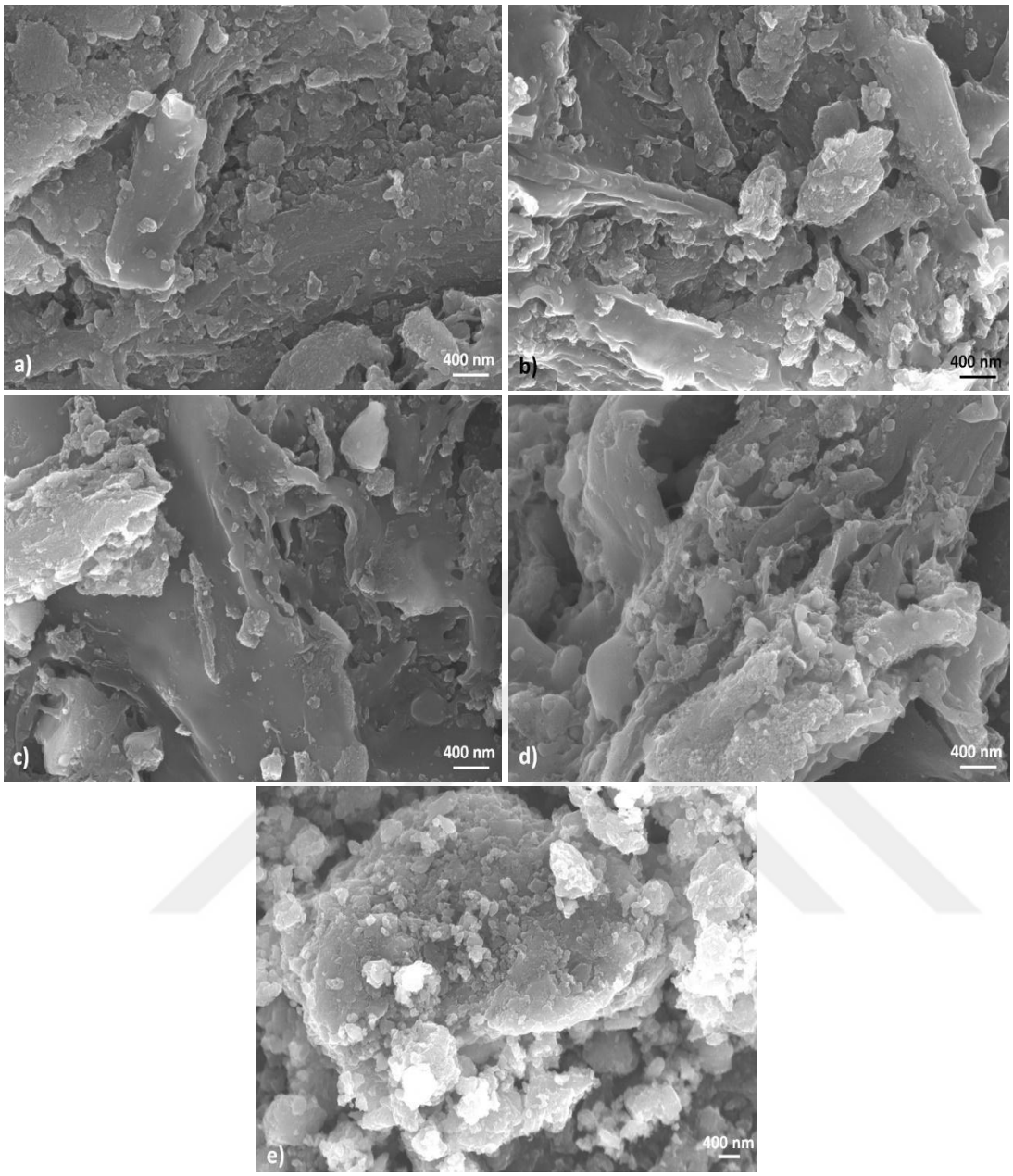

Figure 7.26 : SEM images of nanocomposite biochars **a)** 700-Ar **b)** 700-Ar-H **c)** 750-Ar **d)** 800-Ar **e)** 700-Ar-M.

HR-TEM images (Figures 7.27 and 7.28) show that in both 700-Ar and 700-Ar-H samples, dark-colored silicon-rich particles are homogeneously distributed on the light-colored carbon matrix. The SAED patterns further prove the amorphous nature of both samples, in coherence with XRD analyses. EDS analyses given in Tables 7.2 and 7.3 show that the samples mainly consisted of Si, C, and O with the addition of minor impurities (e.g., Ca, K, etc.) originating from pristine rice husk powder.

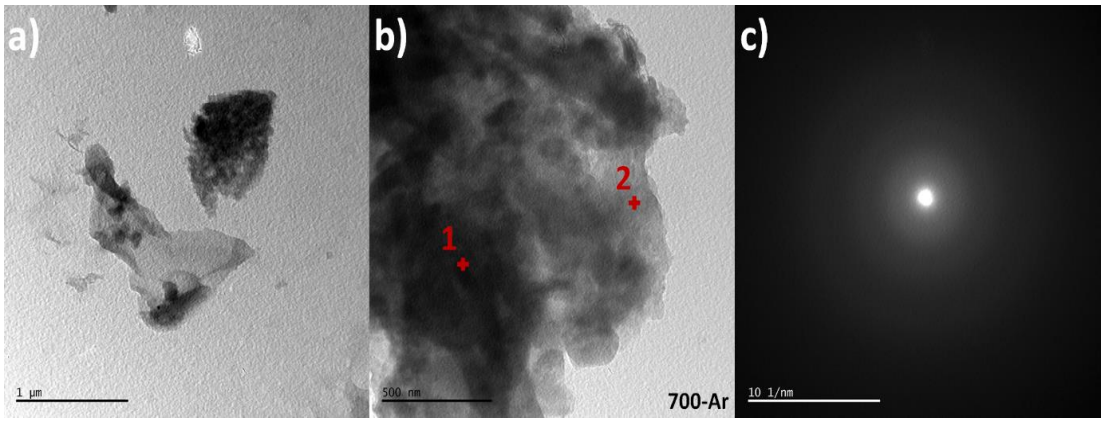

Figure 7.27 : TEM images and SAED patterns of 700-Ar **a,b)** Bright field images **c)** SAED pattern.

Table 7.2 : EDS analysis results of 700-Ar.

Elements	Analysis 1 (at.%)	Analysis 2 (at.%)
C	34.3	91.5
O	46.1	5.7
Si	19.0	2.4
K	0.6	0.2
Ca	-	0.1

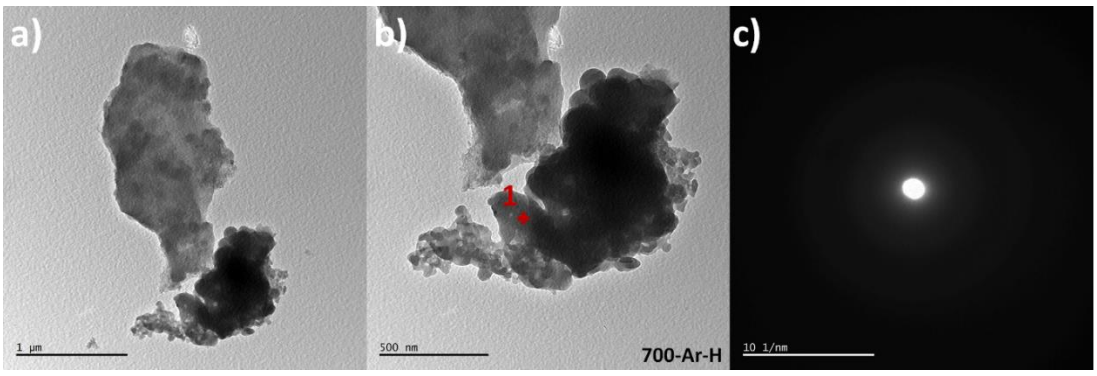

Figure 7.28 : TEM images and SAED patterns of 700-Ar-H **a,b)** Bright field images **c)** SAED pattern.

Table 7.3 : EDS analysis result of 700-Ar-H.

Elements	Analysis 1 (at.%)
C	74.1
O	18.3
Si	7.5
K	0.1
Ca	-

After electrode production, electrochemical tests are conducted. Later, the sample that delivered the best electrochemical performance (700-Ar) is investigated by ex-situ SEM. Figure 7.29 shows that the SEI layer formed during cycling is well-connected to the electrode and homogeneous. The coating thickness is confirmed by cross-section SEM images and found to be 2.5 and 10 microns in fresh and cycled samples, respectively (Figures 7.29 a,b). Additionally, surface images given in Figure 7.29c prove that the nanocomposite anode active materials are well-adherent with conductive carbon chains. After cycling, a continuous SEI layer holds the structure together by creating a network with few cracks due to volume exchange in discharge/charge steps (Figure 7.29d).

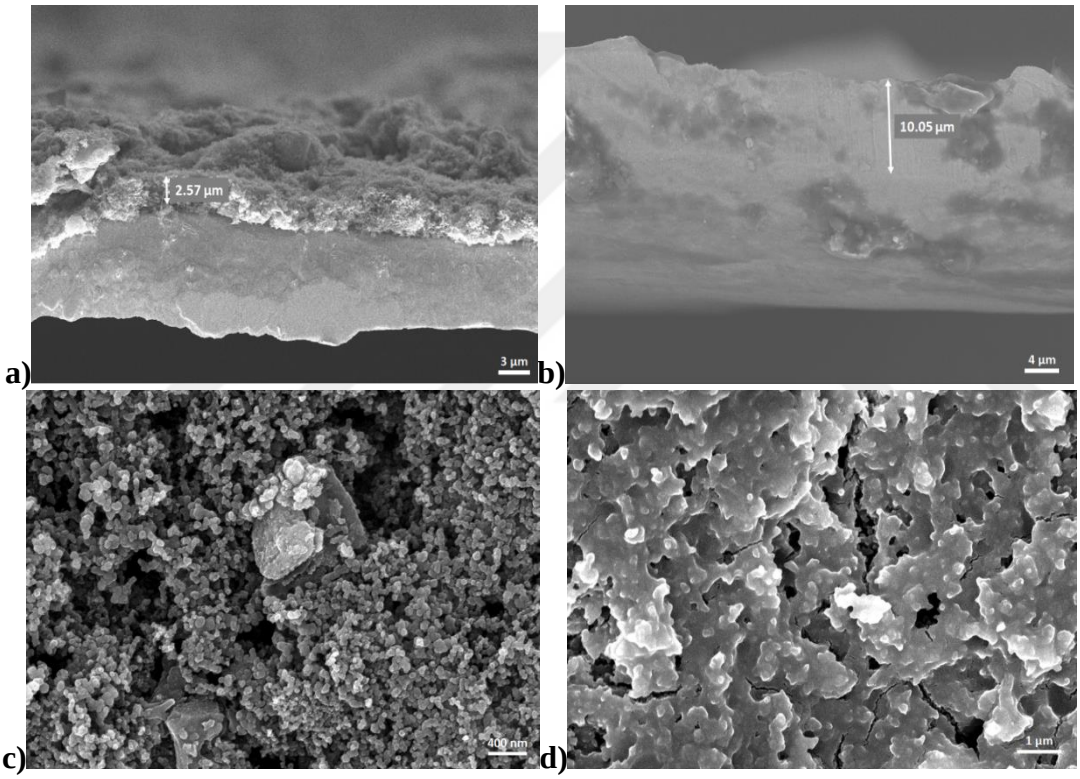

Figure 7.29 : Post-mortem SEM images of 700-Ar electrode **a,c)** before cycling **b,d)** after cycling.

7.2.4 Electrochemical characterizations

The voltage-capacity curves of samples in Figures 7.30-7.34 show that all samples have higher specific capacity than graphite anodes in the first discharge step. A small shoulder around 0.7 V is attributed to SEI layer formation, while the voltage plateau below 0.2 V is ascribed to lithiation reactions. Sample 700-Ar, which has the highest carbon content, delivered the best electrochemical performance with 1366, 800, 340, and 275 mAh/g specific capacity in the 1st, 5th, 100th, and 200th cycles. The enhanced

electrochemical performance is related to the carbon present in the structure, which improves the electrical properties by providing conductive pathways. Conducting pyrolysis at higher temperatures and partially reducing atmospheres leads to more carbon loss and lower specific capacities due to poor conductivity [279]. As seen in Figure 7.35, the initial Coulombic efficiencies (CE) of all samples are about 65% and rapidly increased to 95% in the later cycles. The formation of irreversible phases and growth of the SEI layer is linked with the low initial CE [3].

Jo et al. [288] produced composite anode active material by mixing synthetic SiO_x and graphite powder. It delivered 440 mAh/g specific capacity in the first discharge, followed by a rapid capacity drop after the 50th cycle. In our study, higher specific capacities are achieved by using organic rice husk compared to synthetic SiO_x powder as a starting material. In another study, Lee et al. [289] produced SiO_x/C anodes by NaCl-assisted mechanical milling and calcination of rice husks. The catalytic graphitization provided by NaCl is tested. The results showed that the addition of NaCl promoted graphitization and resulted in 915 mAh/g of first discharge capacity at 50 mA/g of current load. In this study, superior discharge capacities are achieved without additives.

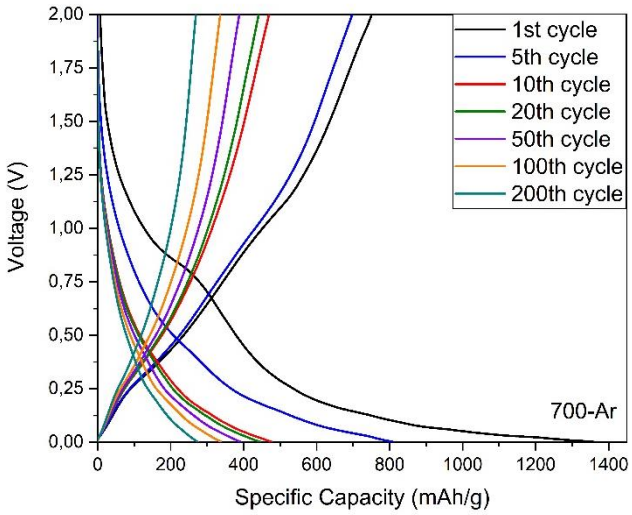

Figure 7.30 : Voltage-capacity curve of the 700-Ar.

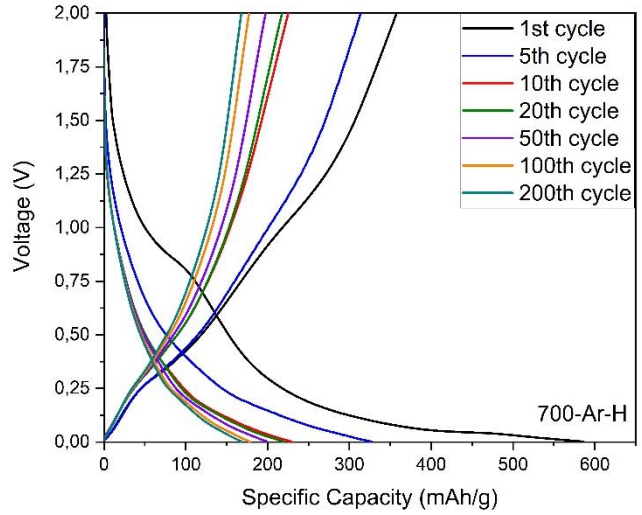

Figure 7.31 : Voltage-capacity curve of the 700-Ar-H.

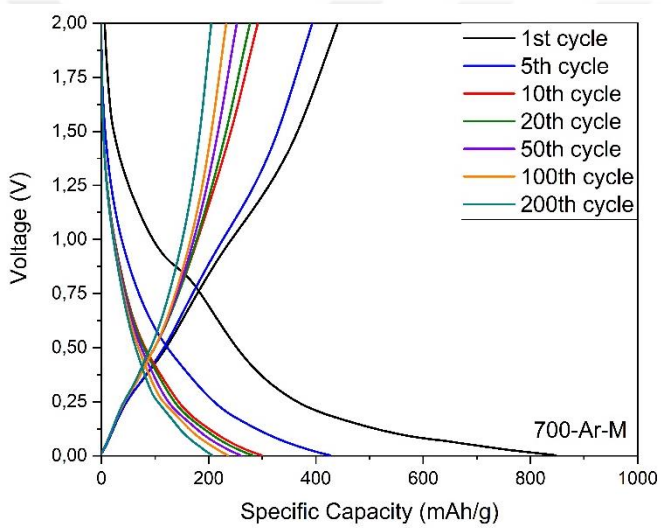

Figure 7.32 : Voltage-capacity curve of the 700-Ar-M.

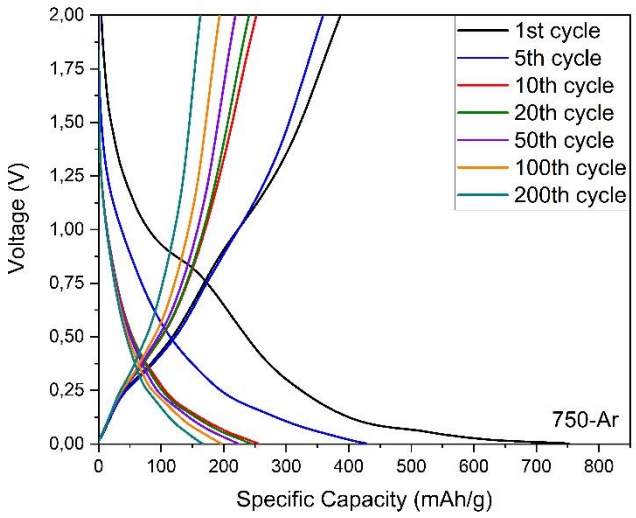

Figure 7.33 : Voltage-capacity curve of the 750-Ar.

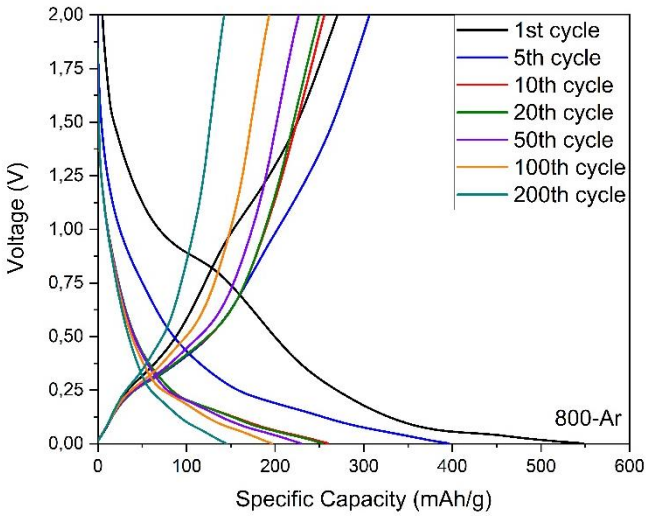

Figure 7.34 : Voltage-capacity curve of the 800-Ar.

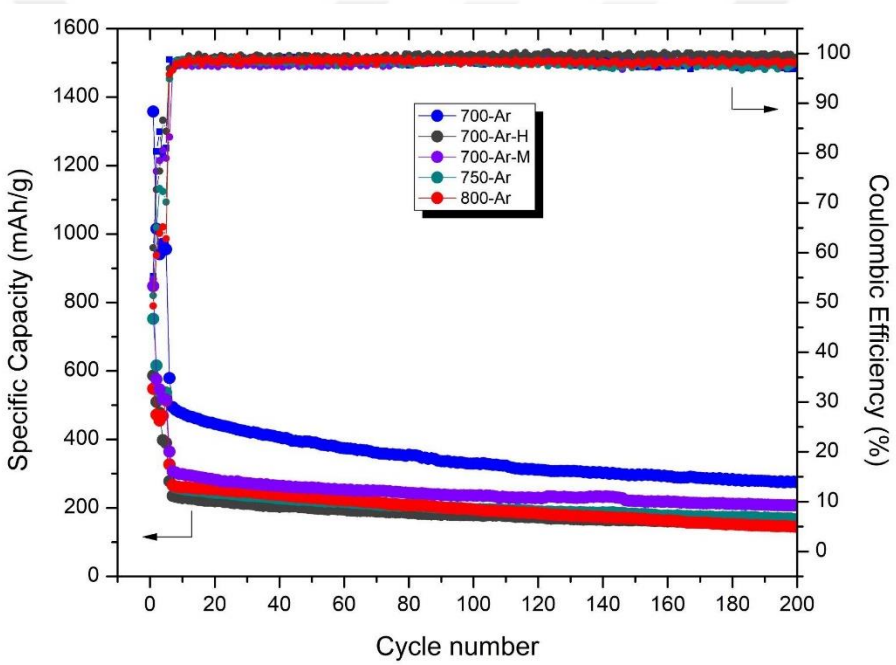

Figure 7.35 : Capacity retention of nanocomposite biochars.

Cyclic voltammetry analysis results are shown in Figures 7.36-7.40. In coherence with galvanostatic test results, higher peak currents are measured in sample 700-Ar, proving that the sample is more electrochemically active. The anodic peak around 0.5 V could be attributed to a delithiation reaction. The weak peak around 1.15 V could also be assigned to transformation of the $Li_2Si_2O_5$ phase to SiO_2 [279]. In the cathodic region, the peaks below 0.4 V and 0.7 V could be related to lithiation and SEI formation, respectively. Supporting the galvanostatic tests, the decreased currents after the first cycle could be explained by the irreversible reactions of SEI layer growth and the formation of electrochemically inactive phases such as $LiSiO_4$ and Li_2O [290].

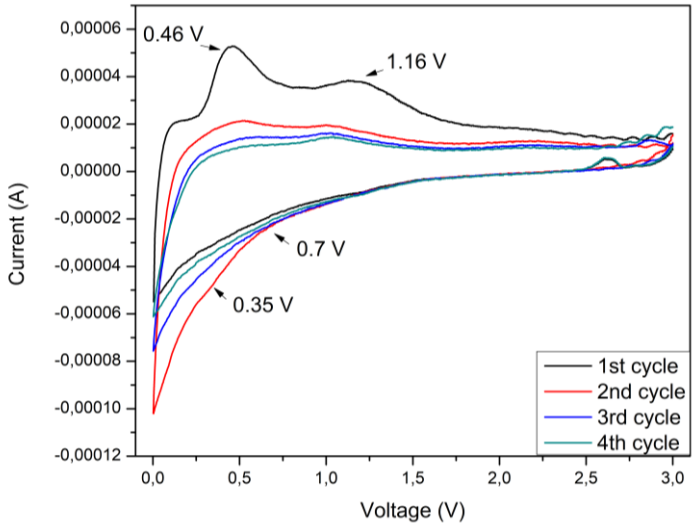

Figure 7.36 : Cyclic voltammetry curve of the 700-Ar.

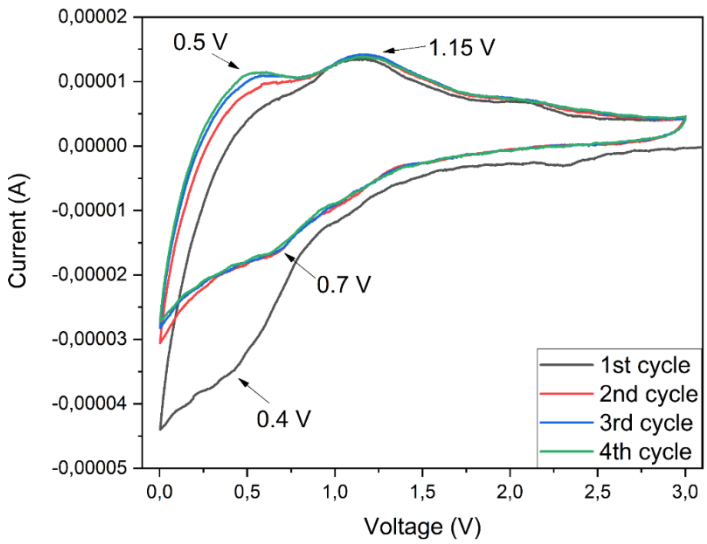

Figure 7.37 : Cyclic voltammetry curve of the 700-Ar-H.

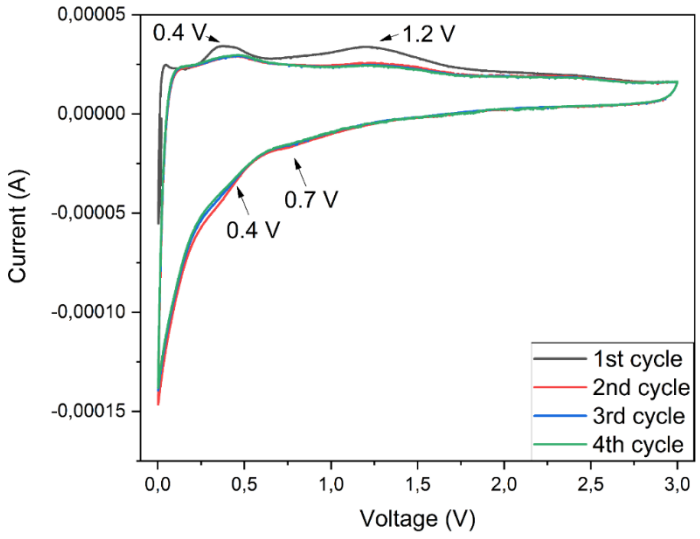

Figure 7.38 : Cyclic voltammetry curve of the 700-Ar-M.

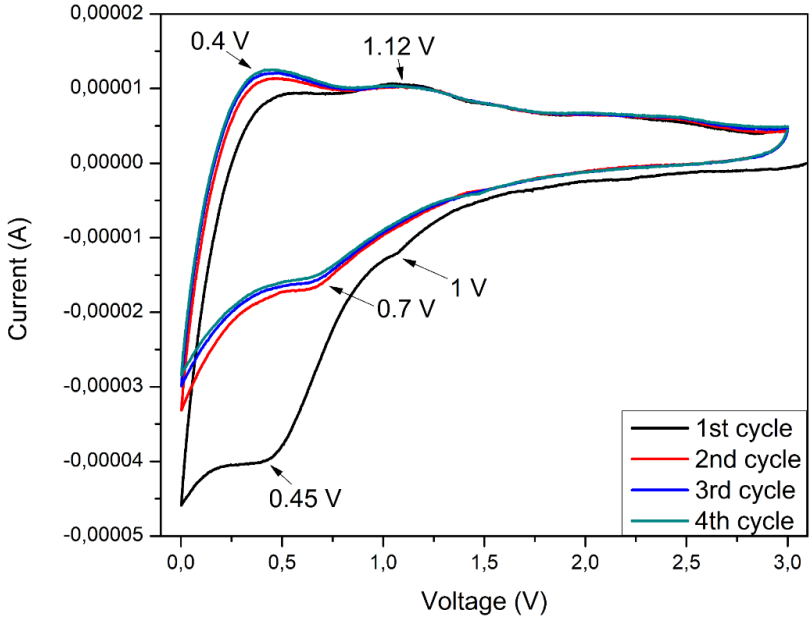

Figure 7.39 : Cyclic voltammetry curve of the 750-Ar.

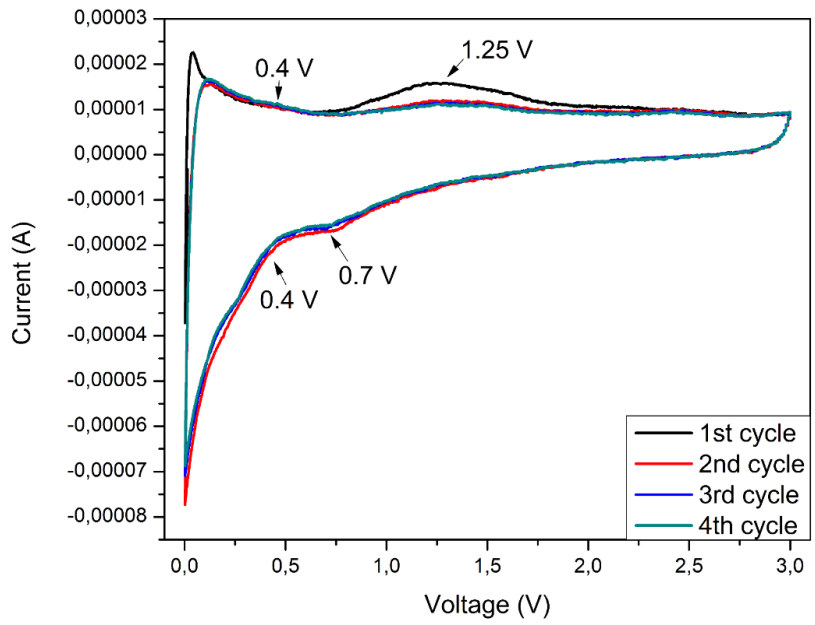

Figure 7.40 : Cyclic voltammetry curve of the 800-Ar.

The electrochemical impedance of synthesized anode active materials and the equivalent circuit are given in Figures 7.41-7.46. In all samples, a depressed semicircle with Warburg diffusion is observed. The circuit consists of a solution resistance, constant phase element and resistance of SEI layer and charge transfer reactions, followed by Warburg impedance. The lowest impedance values are obtained in the 700-Ar sample, which preserves the maximum carbon in the structure. Higher resistance values are observed in all samples after cycling. This could be related to the growth of the SEI layer [278,291].

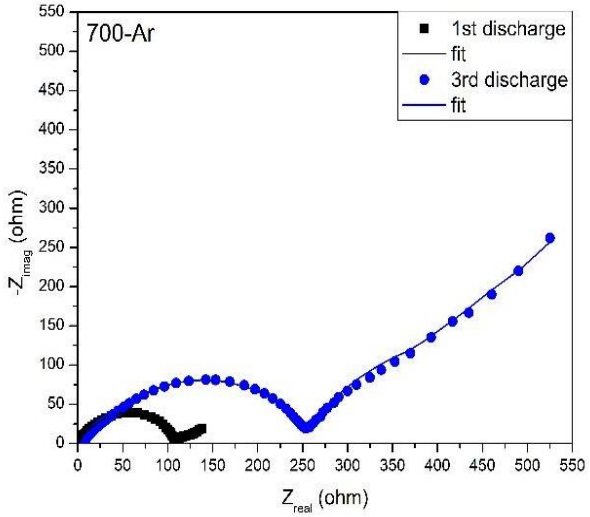

Figure 7.41 : Impedance spectra of 700-Ar sample.

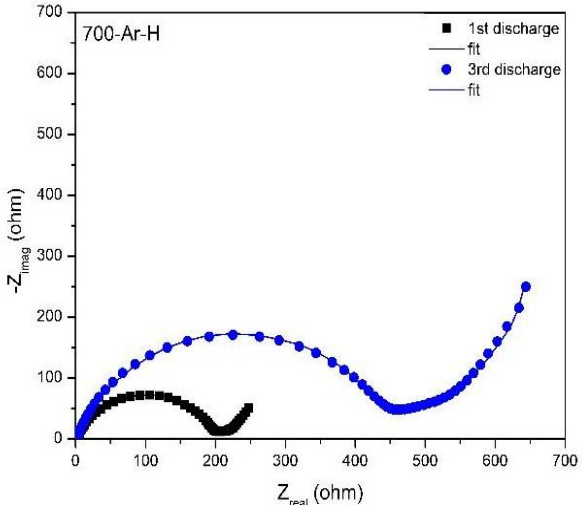

Figure 7.42 : Impedance spectra of 700-Ar-H sample.

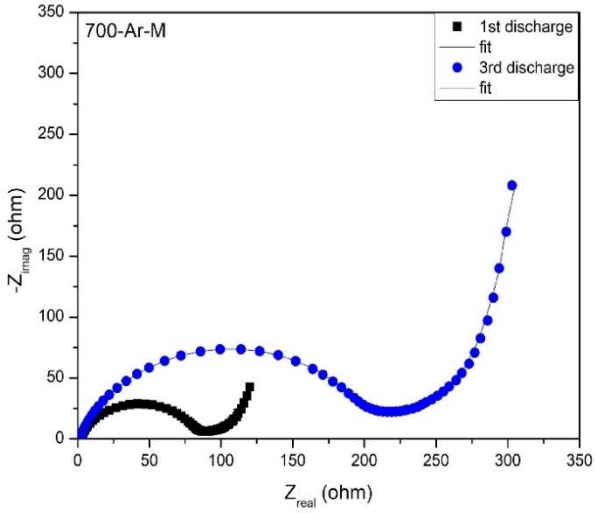

Figure 7.43 : Impedance spectra of 700-Ar-M sample.

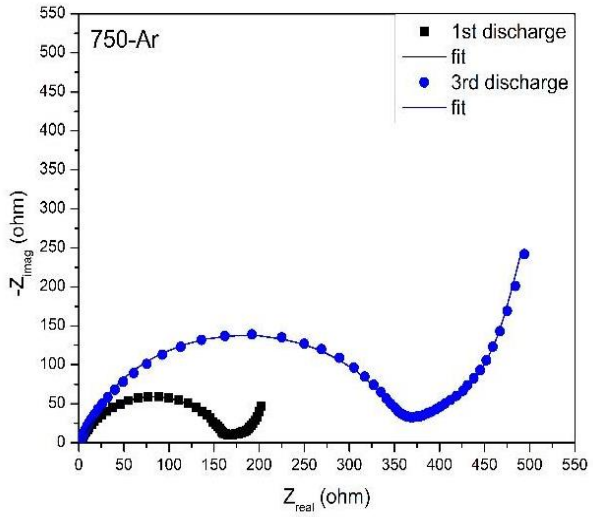

Figure 7.44 : Impedance spectra of 750-Ar sample.

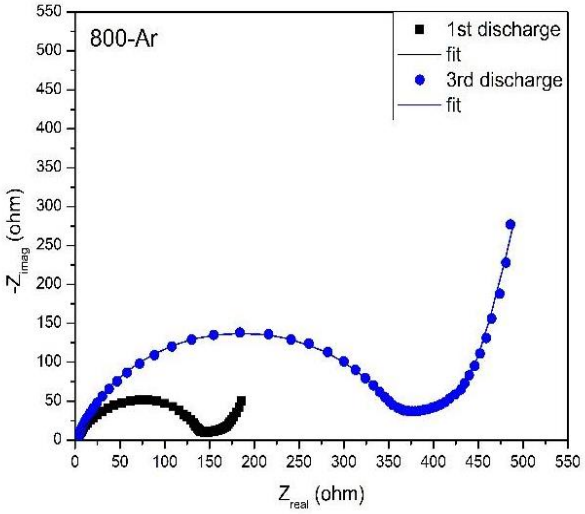

Figure 7.45 : Impedance spectra of 800-Ar sample.

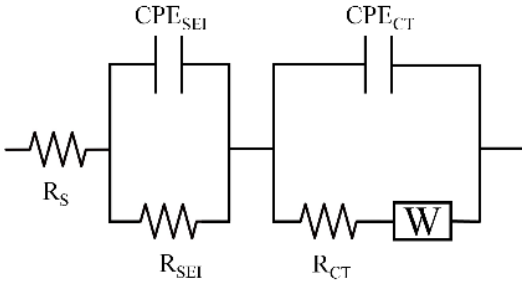

Figure 7.46 : Equivalent circuit.

The energy storage mechanism is detailed by cyclic voltammetry analysis at varying scan rates for the sample with the best electrochemical performance (700-Ar). CV curves are well-preserved at increased scan rates, as seen in Figure 7.47. The peak current values and the square root of scan rates are plotted and fitted to calculate the

k_1 value in Equation 2 (Figure 7.48). As seen in Figure 7.49, at low scan rates, the reactions are found to be diffusion-dominated. At the same time, the capacitive contribution is measured to increase at higher scan rates, which indicates the good capacitive behavior of the 700-Ar sample. Although lithiation reactions are diffusion-dominated in active materials, the high capacitive contribution is expected to lead to better capacity retention at high current loads [292,293].

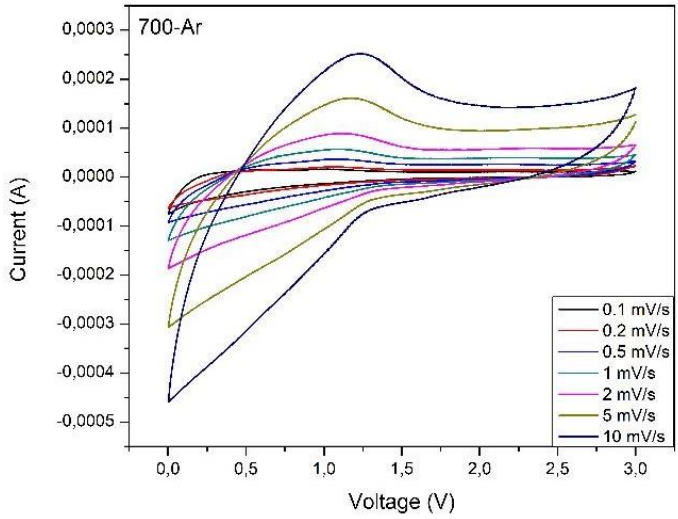

Figure 7.47 : Cyclic voltammetry curves of the 700-Ar at different scan rates from 0.1 to 10 mV/s.

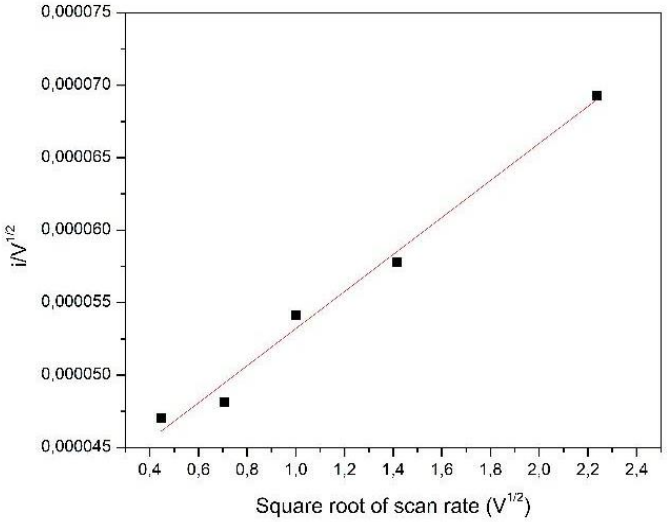

Figure 7.48 : Peak current values and square root of scan rate plot.

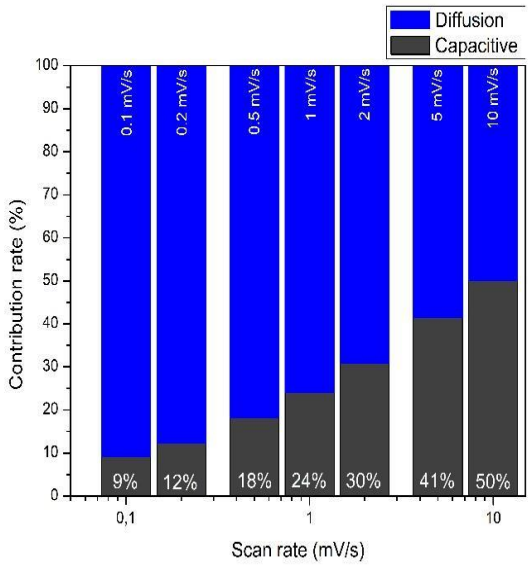

Figure 7.49 : Diffusion and capacitive contribution ratios of the 700-Ar at different scan rates.

The rate test of the 700-Ar given in Figure 7.50, indicates the positive effect of increased capacitive contribution on the specific capacity at high current loads. Here, the pre-conditioned half-cells (described as formation in the experimental section) are subjected to rate test using current loads ranging from 50 to 800 mA/g. Although there was some capacity loss as the current load increased, the sample still exhibited an average capacity of 110 mAh/g at a current load of 800 mA/g. When the current load was decreased to 50 mA/g after the rate test, the capacity stabilized around 140 mAh/g. This capacity loss suggests that high current loads lead to permanent deformations in the structure. Techniques such as doping effectively improve the performance rate of SiO_x anodes by improving electrical conductivity [25,285].

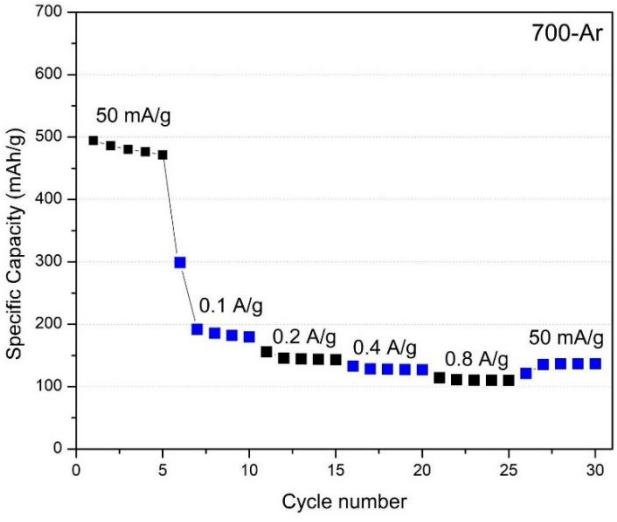

Figure 7.50 : Rate test of the 700-Ar.

Optimizing the electrode production and conducting electrochemical tests are just as crucial as process optimization for achieving the best electrochemical performance from active materials. With this reason, various slurry compositions were prepared, and galvanostatic tests were performed using the 700-Ar sample, demonstrating the best performance. To evaluate this performance, the standard slurry composition of 60:25:15 (active material: carbon: binder) is compared with an alternative composition of 80:10:10, as illustrated in Figure 7.51. The results clearly show that the 60:25:15 slurry composition outperforms the 80:10:10 composition. Orozco-Gallo et al. [294] claim that the carbon ratio in the slurry significantly affects the cycle performance of the anode active materials and leads to higher specific capacities. Additionally, they emphasize that the binder ratio is crucial for achieving more homogeneous electrodes with strong adhesion, particularly for active materials with flake-like morphologies due to their high surface area. Our results support the outcomes of Orozco-Gallo, as an increased carbon content leads to higher specific capacities due to improved electrical conductivity.

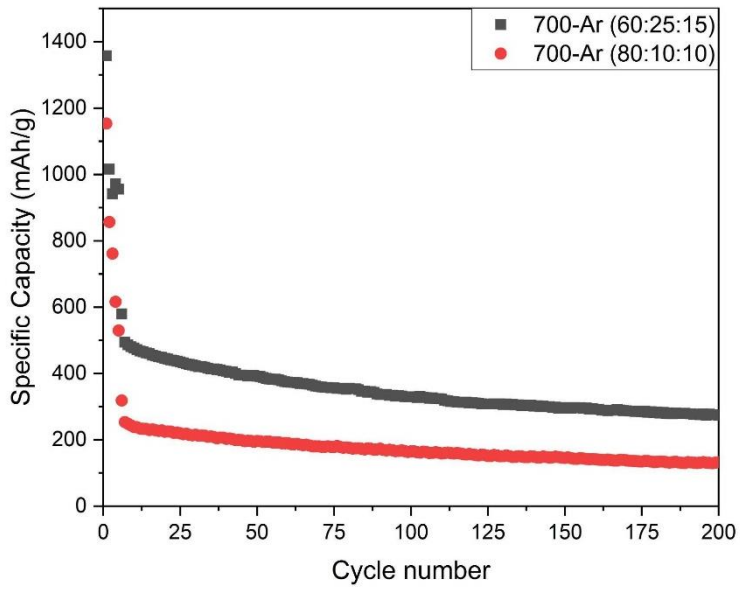

Figure 7.51 : Cycle performance of 700-Ar with different slurry compositions (Active material : carbon : binder).

A stable SEI layer is crucial for stable electrochemical performance, especially for active materials with working voltages lower than the electrolyte decomposition (approximately 1 V), such as SiO_x [295]. The most commonly used methods in the literature to create a stable and homogeneous SEI layer are electrolyte additives and electrochemical activation via constant current-constant voltage (CC/CV) sequences

(referred as formation). Here, the constant current step is a standard galvanostatic charge-discharge procedure with a low current load to promote the growth of a compositionally and morphologically homogeneous SEI layer, while constant voltage step provides potentiostatic holding steps at cut-off voltages which give sufficient time for lithiation/delithiation reactions [296]. Ren et al. [296] describe how the constant current/constant voltage (CC/CV) procedure facilitates the restructuring of electrode materials through the migration of lithium within the particles, leading to enhanced electrochemical performance. While this method can achieve higher specific capacities, it still experiences irreversible capacity loss during the initial cycles. This loss is attributed to a significant amount of lithium being trapped in the solid electrolyte interphase (SEI) layer and the formation of inactive components. Moreover, the study conducted by Liu et al. [297] shows that using the CC/CV protocol results in a denser and more stable SEI layer with higher inorganic content. This results in lower lithium consumption and higher cycle stability. Similar to the outcomes of Ren et al., the 700-Ar sample achieves higher specific capacities when electrochemical activation is applied (Figure 7.52). However, both samples still show a significant capacity loss.

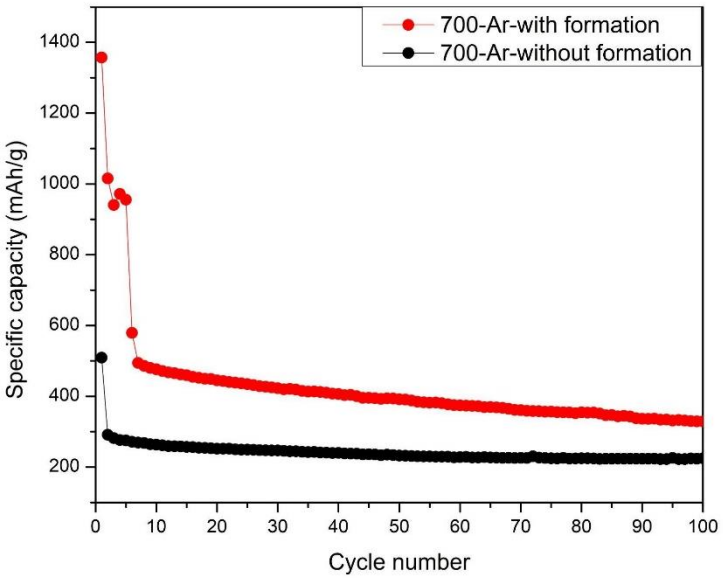

Figure 7.52 : Effect of formation on the cycle performance of the 700-Ar.

To further improve the cycle performance, half cells were cycled using various lower cut-off voltages (2-100 mV), and the results are shown in Figure 7.53. Since lithiation reactions occur at low voltages in silica-based active materials, increasing the lower cut-off voltage is expected to decrease the specific capacities. Conversely, discharging to excessively low voltages can lead to electrode degradation [297]. Therefore, it is

essential to find a balance between these two factors. According to the results, the highest initial capacity is achieved when cells are discharged to 2 mV, while the lowest one belongs to 100 mV. However, when the long-term stability of the cells is compared, a slightly higher specific capacity is achieved when the lower cut-off voltage is set to 10 mV.

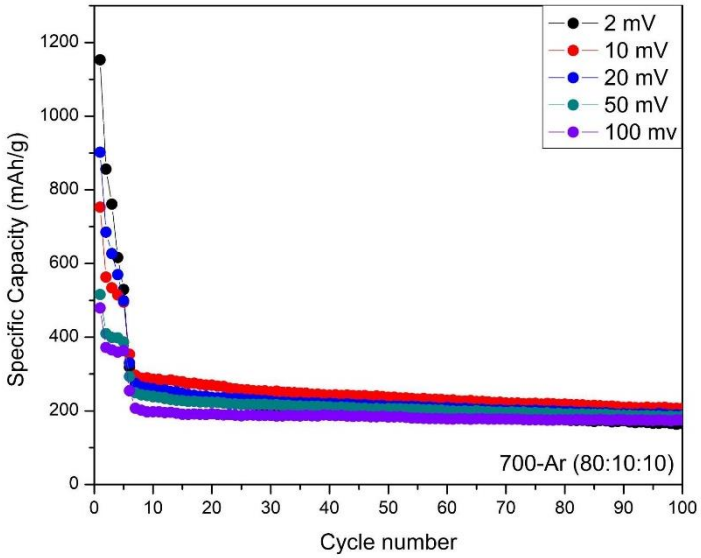

Figure 7.53 : Effect of lower cut-off voltage on the cycle performance of the 700-Ar.

Finally, the effect of electrolyte additives on the capacity retention is investigated. Fluoroethylene carbonate (FEC) is a well-known additive that promotes the formation of a stable LiF-rich SEI layer with high ionic conductivity [298]. The stable SEI layer inhibits further $LiFP_6$ decomposition at low voltages, thus helping to increase capacity retention and Coulombic efficiency. However, studies in the literature indicate that adding insufficient or excessive amounts of FEC may lead to more damaging results [299,300]. Therefore, it is essential to optimize the FEC quantity. Figure 7.54 presents the cycle performances of the cells with and without the FEC addition. As seen from the figure, cycle stability and capacity retention increases with FEC addition, similar to the results of Jaumann et al. [301]. Furthermore, they noted that only a slight increase in specific capacity was observed in the FEC-doped samples compared to the undoped sample. The primary benefit of FEC doping was its ability to enhance cycling stability by forming a dense solid electrolyte interphase (SEI) film and improving lithium ion conductivity.

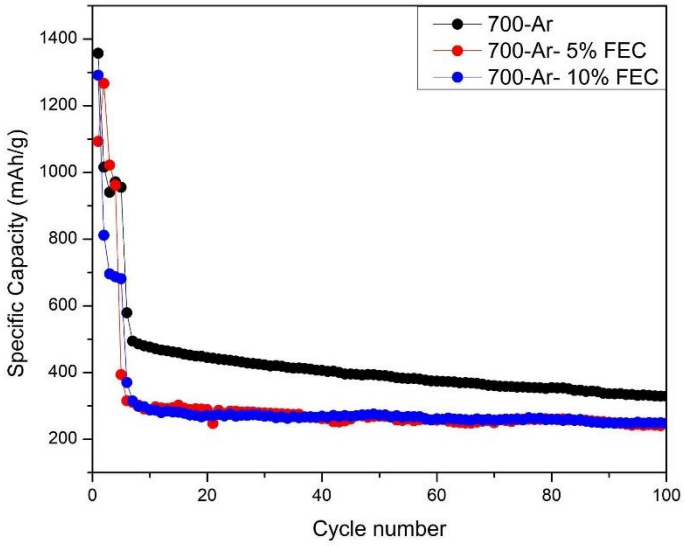

Figure 7.54 : Effect of FEC addition on the cycle performance of the 700-Ar.

8. CONCLUSION

This thesis focuses on utilizing rice husk, which contains the highest silica content among organic wastes, to produce anode active materials as a substitute for graphite. Although silica has low electrochemical performance due to its poor electrical conductivity, two strategies have been proposed to enhance its performance. The first strategy involves decreasing the particle size to shorten the lithium diffusion path. The second strategy proposes designing composites with materials that have high electrical conductivity.

In the first set of experiments, submicron silica particles are synthesized via leaching and precipitation of rice husk. In the second set, for the first time in the literature, fast pyrolysis by induction heating is conducted to produce nanocomposite biochars containing SiO_x and C. Here, high heating rates are embraced to promote the generation of reducing gases such as CH_4, CO, and H_2. These gases partially reduce silica to SiO_x during pyrolysis, and the resulting active material exhibits enhanced electrochemical performance, while retained carbon in the structure improves the electrical conductivity. After synthesis, all samples are characterized for their chemical, structural, and morphological properties. Finally, their electrochemical performances are evaluated using galvanostatic tests, cyclic voltammetry, and electrochemical impedance spectroscopy. The results are summarized as follows:

1. In the first set, silica particles are successfully synthesized using rice husk via leaching and precipitation. Process parameters such as calcination prior to leaching, solid-to-liquid ratio, and ethanol addition as co-solvent are optimized to obtain the smallest particle sizes.

2. FTIR analysis showed that all samples have Si-O bonds, namely Si-O bending, Si-O-Si symmetric, and asymmetric stretching bonds, proving the silica structure. XRD analyses revealed that samples exhibit an amorphous nature with a small amount of retained sodium silicate phase. SEM images showed that irregular-shaped particles are agglomerated. Additionally, rice husk resulted in a lower precipitation efficiency than rice husk ash due to its low silica content.

3. The effect of changing process parameters is mainly seen in particle size analysis results. According to these results, a decreased solid-to-liquid ratio, which also means a low SiO_2/Na_2O ratio, produces smaller particles due to being the key parameter for controlling particle size through polymerization and particle growth reactions. A higher SiO_2/Na_2O ratio promotes the polymerization reactions, thus the growth of particles. The ethanol addition as a co-solvent resulted in an increased particle size. This is believed to be caused by the immiscibility of sodium silicate in ethanol, which causes local supersaturation. Moreover, as the ethanol amount increases, the particle size distribution shifts from monodisperse to polydisperse. A sodium silicate solution with a lower SiO_2/Na_2O ratio could be beneficial for observing the globulization of particles with ethanol addition due to the decreased surface tension of the solution, which promotes isotropic growth. Among all samples, calcination of rice husk powder at 600 °C for 3 hours before leaching, with a solid-to-liquid leaching ratio of 1/20 and no ethanol addition, resulted in the smallest particle size.

4. Cyclic voltammetry analysis results show that all samples exhibit a shoulder around 0.7 V and a plateau below 0.2 V, which indicate the formation of the SEI layer and lithium storage reactions, respectively. For electrochemical performance, PS-3, as the sample with the smallest particle size, has the lowest impedance values, and it delivers the highest specific capacities of 503, 167, and 145 mAh/g in the 1st, 100th, and 200th cycles. A shorter lithium diffusion path could explain the enhanced electrochemical performance. The sudden capacity drop after the first cycle, seen in all samples, could be explained by the formation of the SEI layer and irreversible lithium silicates.

5. In the second set, nanocomposite biochars containing SiO_x and C are successfully synthesized by fast pyrolysis of rice husk via induction heating. Fast heating is embraced to promote the generation of reducing gases such as CH_4, CO, and H_2 during pyrolysis due to the decomposition of organic content in rice husk. These gases are used to partially reduce SiO_2 to SiO_x and improve electrochemical performance. Additionally, the carbon preserved in the structure after pyrolysis is intended to improve electrical conductivity. Therefore, the pyrolysis process was optimized to have the maximum amount of carbon by changing the pyrolysis temperature (700-750-800 °C) and atmosphere (Ar-Varigon). For further

improvement, the sample with the highest carbon content is milled to achieve smaller particle sizes with a more homogeneous elemental distribution. Finally, the effect of slurry composition, electrochemical activation, discharge cut-off voltage, and electrolyte addition are investigated to enhance electrochemical performance.

6. FTIR analysis results show that all samples have Si-O bending, Si-O-Si, and Si-O-C bonds regardless of pyrolysis temperature and atmosphere, proving the synthesis of silica. All samples exhibit an amorphous nature below 800 °C according to the XRD patterns. Above that temperature, silica starts to crystallize and form the cristobalite phase. Additionally, a slight bump around 43° is seen in all samples, which could indicate the graphitic carbon. SEM images of pyrolyzed samples show particles with irregular sizes and morphologies. Additionally, milling after pyrolysis helps to form more rounded morphologies with smaller particles.
7. The carbon structures investigated via Raman spectroscopy reveal that all samples have D and G bands representing the defective and graphitic carbon structures. The graphitization ratio calculated by I_D/I_G shows a rising trend with increased pyrolysis temperatures, which the increase in aromatic ring concentrations could explain. Additionally, ball milling after pyrolysis increases the I_D/I_G ratio by introducing defects into the structure during the high-energy milling process.
8. The carbon-sulphur analysis reveals that the highest amount of carbon (41.3 wt.%) is preserved when pyrolysis is conducted at 700 °C under the argon atmosphere. Higher pyrolysis temperatures and partially reducing atmospheres have led to a higher amount of carbon loss.
9. XPS analysis conducted on the sample with the highest amount of carbon (700-Ar) shows that the Si 2p spectrum exhibits three peaks in order of their intensities: Si^{+2}, Si^{+3}, and Si^{+4}. This result shows that pyrolysis of rice husk leads to the successful partial reduction of silica and the formation of SiO_x.
10. TEM images and EDS analyses of pyrolyzed samples at 700 °C under argon and partially reducing atmospheres (Ar-H) show that dark-colored Si-rich particles are homogeneously distributed on the light-colored carbon matrix in both samples.

11. Cyclic voltammetry curves of pyrolyzed samples exhibit a shoulder around 0.7 V and a voltage plateau below 0.2 V, ascribed to SEI formation and lithiation reactions, respectively. The sample with the highest carbon content (700-Ar) delivers the best electrochemical performance as 1366, 800, 340, and 275 mAh/g specific capacities in the 1st, 5th, 100th, and 200th cycles. The results prove that samples deliver higher specific capacities as the carbon content increases. The sudden capacity drop after the first cycle seen in all samples could be explained by the formation of the SEI layer and irreversible lithium silicates.

12. Post-mortem cross-section SEM images of cycled and fresh 700-Ar samples show that the coating thickness increased from 2.5 to 10 microns after cycling. Additionally, active materials and conductive carbon chains are well-adherent in fresh and cycled electrodes. The continuous SEI layer is believed to hold the structure together by creating a network with few cracks due to volume exchanges during discharge/charge steps.

13. Electrochemical impedance spectroscopy analysis results support the galvanostatic test results, showing that the sample with the highest carbon content has the smallest impedance values, indicating improved electrical conductivity. When pyrolysis atmospheres are compared at the same temperature, it is seen that partially reducing atmospheres lead to higher impedance values. On the other hand, milling after pyrolysis slightly decreases impedance values, which could be explained by the decreased particle size.

14. The cyclic voltammetry curves taken at varying scan rates show that the energy storage mechanism of the 700-Ar sample is mainly diffusion-controlled with an increased capacitive contribution at higher scan rates.

15. The rate test of the 700-Ar sample shows the beneficial effects of capacitive contribution at higher current loads. The sample delivered 110 mAh/g specific capacity at a current load of 800 mA/g. When the current load is decreased to its initial values, a certain capacity loss is observed, which suggests that high current loads lead to permanent deformations in the structure.

16. Optimization of the slurry composition showed that preparing the SiO_x/C electrodes with the 60:25:15 ratio (active material:carbon:binder) leads to increased specific capacities compared to the 80:10:10 ratio due to its higher

carbon content. The increased binder ratio is also expected to result in a more homogeneous electrode.

17. The electrochemical activation method, referred to as formation in the experimental section, resulted in increased capacities by promoting the growth of a more homogeneous SEI layer during charging/discharging with low currents as well as increased lithiation/delithiation ratio with 48h holding at cut-off voltages.
18. FEC addition to the electrolyte resulted in higher capacity retention due to the increased stability of the SEI layer due to the deposition of components such as LiF, which stabilizes the surface without blocking the Li^+ ions.
19. To conclude, rice husk-derived anode active materials are successfully synthesized using precipitation and fast pyrolysis. Compared to precipitation, the fast pyrolysis method enables the production of nanocomposite biochars containing SiO_x and C in a short time, enabling fast and energy-efficient synthesis. This study is significant because it has the potential for scalability and commercial application. The optimized biochar delivers competitive specific capacities to graphite and could be a candidate for substitution. Further electrochemical performances could be obtained by doping.

REFERENCES

[1] **Statista** (2023) Primary energy consumption worldwide from 2000 to 2023.

[2] **United States Environmental Protection Agency** (2023) Inventory of U.S. Greenhouse Gas Emissions and Sinks: 1990-2021.

[3] **Jiao, M., Wang, Y., Ye, C., Wang, C., Zhang, W., and Liang, C.** (2020) High-capacity SiO_x ($0 \leq x \leq 2$) as promising anode materials for next-generation lithium-ion batteries. *Journal of Alloys and Compounds*. *842*, 155774.

[4] **Moon, D.-B., Kim, K.-H., and Ahn, H.-J.** (2023) Effect of hierarchically reduced SiO_x on anode performance of Li-ion batteries. *Korean Journal of Chemical Engineering*. *40*, (12), 3046–3051.

[5] **Zhang, H., Du, Y., Zhang, N., Lin, P., Liu, W., Wen, Z., et al.** (2022) Turning rice husks to a valuable boron and nitrogen co-doped porous C/SiO_x composite for high performance lithium-ion battery anodes. *Microporous and Mesoporous Materials*. *335*, 111794.

[6] **Askaruly, K., Korobeinyk, A. V., Azat, S., Yeleuov, M., Taurbekov, A., Toshtay, K., et al.** (2023) The electrochemical behavior of silica and activated carbon materials derived from the rice husk waste for li-ion cells. *Diamond and Related Materials*. *133*, 109759.

[7] **Lv, P., Zhao, H., Gao, C., Zhang, T., and Liu, X.** (2015) Highly efficient and scalable synthesis of SiO_x/C composite with core-shell nanostructure as high-performance anode material for lithium ion batteries. *Electrochimica Acta*. *152*, 345–351.

[8] **Dressler, R.A. and Dahn, J.R.** (2023) Simple Synthesis and Characterization of Ball Milled SiO_x for Use as a Negative Electrode Material. *Journal of The Electrochemical Society*. *170*, (8), 080505.

[9] **Fey, G.T.-K. and Chen, C.-L.** (2001) High-capacity carbons for lithium-ion batteries prepared from rice husk. *Journal of Power Sources*. *97–98*, (June 2000), 47–51.

[10] **Fey, G.T.K., Cho, Y.D., Chen, C.L., Huang, K.P., Lin, Y.C., Kumar, T.P., et al.** (2011) Pyrolytic Carbons from Porogen-treated Rice Husk as Lithium-insertion Anode Materials. *International Journal of Chemical Engineering and Applications*. (January 2011), 20–25.

[11] **Wang, L., Schnepp, Z., and Titirici, M.M.** (2013) Rice husk-derived carbon anodes for lithium ion batteries. *Journal of Materials Chemistry A*. *1*, (17), 5269.

[12] **Yu, K., Wang, Y., Wang, X., Liu, W., Liang, J., and Liang, C.** (2019) Preparation of porous carbon anode materials for lithium-ion battery from rice husk. *Materials Letters*. *253*, 405–408.

[13] **Li, Y., Huang, Y., Song, K., Wang, X., Yu, K., and Liang, C.** (2019) Rice Husk Lignin-Derived Porous Carbon Anode Material for Lithium-Ion Batteries. *Chemistry Select*. *4*, (14), 4178–4184.

[14] **Nilmoung, S., Limphirat, W., Siriroj, S., and Ausavasukhi, A.** (2024) Rice husk-activated carbon (RHAC) composited with V_2O_5 for lithium-ion batteries. *Applied Physics A*. *130*, (5), 305.

[15] **Amutha, K., Ravibaskar, R., and Sivakumar, G.** (2010) Extraction, Synthesis and Characterization of Nanosilica from Rice Husk Ash. *International Journal of Nanotechnology and Applications*. *4*, (1), 61–66.

[16] **Yuvakkumar, R., Elango, V., Rajendran, V., and Kannan, N.** (2014) High-purity nano silica powder from rice husk using a simple chemical method. *Journal of Experimental Nanoscience*. *9*, (3), 272–281.

[17] **Rafiee, E., Shahebrahimi, S., Feyzi, M., and Shaterzadeh, M.** (2012) Optimization of synthesis and characterization of nanosilica produced from rice husk (a common waste material). *International Nano Letters*. *2*, (1).

[18] **Dominguez, J.M., Terres, E., Vazquez, A.** (2003) High throughput study on the induction of radial distribution of nanotubes and spherical morphology in silica particles by short-chain polar co-solvents. *Microporous and Mesoporous Materials. 66*, 341–348.

[19] **Liu, N., Huo, K., McDowell, M.T., Zhao, J., and Cui, Y.** (2013) Rice husks as a sustainable source of nanostructured silicon for high performance Li-ion battery anodes. *Scientific Reports*. *3*, 1–7.

[20] **Liu, S.-F., Kuo, C.-H., Lin, C.-C., Lin, H.-Y., Lu, C.-Z., Kang, J.-W., et al.** (2022) Biowaste-derived Si@SiO_x/C anodes for sustainable lithium-ion batteries. *Electrochimica Acta*. *403*, 139580.

[21] **Zhao, Z., Cai, M., Zhao, H., Ma, Q., Xie, H., Xing, P., et al.** (2022) Zincothermic-Reduction-Enabled Harvesting of an Si/C Composite from Rice Husks for a Li-Ion Battery Anode. *ACS Sustainable Chemistry & Engineering*. *10*, (15), 5035–5042.

[22] **Wang, L., Xue, J., Gao, B., Gao, P., Mou, C., and Li, J.** (2014) Rice husk derived carbon-silica composites as anodes for lithium ion batteries. *RSC Advances*. *4*, (110), 64744–64746.

[23] **Feng, Y., Liu, X., Liu, L., Zhang, Z., Teng, Y., Yu, D., et al.** (2018) SiO_2/C Composite Derived from Rice Husks with Enhanced Capacity as Anodes for Lithium-Ion Batteries. *Chemistry Select*. *3*, (37), 10338–10344.

[24] **Zhang, H., Zhang, N., Man, J., Du, Y., Cui, J., and Sun, J.** (2022) A sustainable approach from rice husks to P,N-dual doping porous C/SiO_x composites for high-performance lithium-ion battery anodes. *Journal of Electroanalytical Chemistry*. *904*, (September 2021), 115939.

[25] **Cui, J., Qiu, Y., Zhang, H., Yao, Z., Zhao, W., Liu, Y., et al.** (2021) Sulfur- and nitrogen-doped rice husk-derived C/SiO_x composites as high-performance lithium-ion battery anodes. *Solid State Ionics*. *361*.

[26] **Linden, D. and Reddy, T.B.** (1995) *Handbook of batteries*. .

[27] **Eftekhari, A.** (2017) Low voltage anode materials for lithium-ion batteries. *Energy Storage Materials*. *7*, (December 2016), 157–180.

[28] **Fu, W., Wang, Y., Kong, K., Kim, D., Wang, F., and Yushin, G.** (2023) Materials and Processing of Lithium-Ion Battery Cathodes. *Nanoenergy Advances*. *3*, (2), 138–154.

[29] **Mizushima, K., Jones, P.C., Wiseman, P.J., and Goodenough, J.B.** (1980) Li_xCoO_2 ($0<x<-1$): A new cathode material for batteries of high energy density. *Materials Research Bulletin*. *15*, (6), 783–789.

[30] **Schipper, F., Erickson, E.M., Erk, C., Shin, J.-Y., Chesneau, F.F., and Aurbach, D.** (2017) Review—Recent Advances and Remaining Challenges for Lithium Ion Battery Cathodes. *Journal of The Electrochemical Society*. *164*, (1), A6220–A6228.

[31] **Ohzuku, T., Ueda, A., and Nagayama, M.** (1993) Electrochemistry and Structural Chemistry of $LiNiO_2$ (R3m) for 4 Volt Secondary Lithium Cells. *Journal of The Electrochemical Society*. *140*, (7), 1862–1870.

[32] **Armstrong, A.R. and Bruce, P.G.** (1996) Synthesis of layered $LiMnO_2$ as an electrode for rechargeable lithium batteries. *Nature*. *381*, (6582), 499–500.

[33] **Chakraborty, A., Kunnikuruvan, S., Kumar, S., Markovsky, B., Aurbach, D., Dixit, M., et al.** (2020) Layered Cathode Materials for Lithium-Ion Batteries: Review of Computational Studies on $LiNi_{1-x-y}Co_xMn_yO_2$ and $LiNi_{1-x-y}Co_xAl_yO_2$. *Chemistry of Materials*. *32*, (3), 915–952.

[34] **Erabhoina, H. and Thelakkat, M.** (2022) Tuning of composition and morphology of $LiFePO_4$ cathode for applications in all solid-state lithium metal batteries. *Scientific Reports*. *12*, (1), 5454.

[35] **Mauger, A. and Julien, C.** (2018) Olivine Positive Electrodes for Li-Ion Batteries: Status and Perspectives. *Batteries*. *4*, (3), 39.

[36] **Flamme, B., Rodriguez Garcia, G., Weil, M., Haddad, M., Phansavath, P., Ratovelomanana-Vidal, V., et al.** (2017) Guidelines to design organic electrolytes for lithium-ion batteries: environmental impact, physicochemical and electrochemical properties. *Green Chemistry*. *19*, (8), 1828–1849.

[37] **Hess, S., Wohlfahrt-Mehrens, M., and Wachtler, M.** (2015) Flammability of Li-Ion Battery Electrolytes: Flash Point and Self-Extinguishing Time Measurements. *Journal of The Electrochemical Society*. *162*, (2), A3084–A3097.

[38] **Wang, Q., Wang, H., Wu, J., Zhou, M., Liu, W., and Zhou, H.** (2021) Advanced electrolyte design for stable lithium metal anode: From liquid to solid. *Nano Energy*. *80*, (October 2020), 105516.

[39] **Ming, J., Cao, Z., Wu, Y., Wahyudi, W., Wang, W., Guo, X., et al.** (2019) New Insight on the Role of Electrolyte Additives in Rechargeable Lithium Ion Batteries. *ACS Energy Letters*. *4*, (11), 2613–2622.

[40] **Lee, H., Yanilmaz, M., Toprakci, O., Fu, K., and Zhang, X.** (2014) A review of recent developments in membrane separators for rechargeable lithium-ion batteries. *Energy Environ. Sci. 7*, (12), 3857–3886.

[41] **Costa, C.M., Lee, Y.-H., Kim, J.-H., Lee, S.-Y., and Lanceros-Méndez, S.** (2019) Recent advances on separator membranes for lithium-ion battery applications: From porous membranes to solid electrolytes. *Energy Storage Materials*. *22*, (July), 346–375.

[42] **Zhao, P., Yang, J., Shang, Y., Wang, L., Fang, M., Wang, J., et al.** (2015) Surface modification of polyolefin separators for lithium ion batteries to reduce thermal shrinkage without thickness increase. *Journal of Energy Chemistry*. *24*, (2), 138–144.

[43] **Foreman, E., Zakri, W., Hossein Sanatimoghaddam, M., Modjtahedi, A., Pathak, S., Kashkooli, A.G., et al.** (2017) A Review of Inactive Materials and Components of Flexible Lithium-Ion Batteries. *Advanced Sustainable Systems*. *1*, (11),.

[44] **Arora, P. and Zhang, Z. (John)** (2004) Battery Separators. *Chemical Reviews*. *104*, (10), 4419–4462.

[45] **Wu, X., Ji, G., Wang, J., Zhou, G., and Liang, Z.** (2023) Toward Sustainable All Solid-State Li–Metal Batteries: Perspectives on Battery Technology and Recycling Processes. *Advanced Materials*. *35*, (51), 1–37.

[46] **Zhang, H., Yang, Y., Xu, H., Wang, L., Lu, X., and He, X.** (2022) $Li_4Ti_5O_{12}$ spinel anode: Fundamentals and advances in rechargeable batteries. *InfoMat*. *4*, (4), 1–29.

[47] **Sharma, S.K., Sharma, G., Gaur, A., Arya, A., Mirsafi, F.S., Abolhassani, R., et al.** (2022) Progress in electrode and electrolyte materials: path to all-solid-state Li-ion batteries. *Energy Advances*. *1*, (8), 457–510.

[48] **Wang, Q., Liu, B., Shen, Y., Wu, J., Zhao, Z., Zhong, C., et al.** (2021) Confronting the Challenges in Lithium Anodes for Lithium Metal Batteries. *Advanced Science*. *8*, (17), 1–25.

[49] **Guan, X., Wang, A., Liu, S., Li, G., Liang, F., Yang, Y., et al.** (2018) Controlling Nucleation in Lithium Metal Anodes. *Small*. *14*, (37), 1–21.

[50] **Yan, K., Lu, Z., Lee, H.W., Xiong, F., Hsu, P.C., Li, Y., et al.** (2016) Selective deposition and stable encapsulation of lithium through heterogeneous seeded growth. *Nature Energy*. *1*, (3),.

[51] **Zou, P., Wang, Y., Chiang, S.W., Wang, X., Kang, F., and Yang, C.** (2018) Directing lateral growth of lithium dendrites in micro-compartmented anode arrays for safe lithium metal batteries. *Nature Communications*. *9*, (1).

[52] **Tikekar, M.D., Choudhury, S., Tu, Z., and Archer, L.A.** (2016) Design principles for electrolytes and interfaces for stable lithium-metal batteries. *Nature Energy*. *1*, (9), 1–7.

[53] **Tasaki, K., Kanda, K., Kobayashi, T., Nakamura, S., and Ue, M.** (2006) Theoretical Studies on the Reductive Decompositions of Solvents and Additives for Lithium-Ion Batteries near Lithium Anodes. *Journal of The Electrochemical Society*. *153*, (12), A2192.

[54] **Aurbach, D.** (2000) Review of selected electrode-solution interactions which determine the performance of Li and Li ion batteries. *Journal of Power Sources*. *89*, (2), 206–218.

[55] **Richards, W.D., Miara, L.J., Wang, Y., Kim, J.C., and Ceder, G.** (2016) Interface Stability in Solid-State Batteries. *Chemistry of Materials*. *28*, (1), 266–273.

[56] **Peled, E.** (1979) The Electrochemical Behavior of Alkali and Alkaline Earth Metals in Nonaqueous Battery Systems—The Solid Electrolyte Interphase Model. *Journal of The Electrochemical Society*. *126*, (12), 2047–2051.

[57] **Ghazi, Z.A., Sun, Z., Sun, C., Qi, F., An, B., Li, F., et al.** (2019) Key Aspects of Lithium Metal Anodes for Lithium Metal Batteries. *Small*. *15*, (32), 1–26.

[58] **Zhu, B., Jin, Y., Hu, X., Zheng, Q., Zhang, S., Wang, Q., et al.** (2017) Poly(dimethylsiloxane) Thin Film as a Stable Interfacial Layer for High-Performance Lithium-Metal Battery Anodes. *Advanced Materials*. *29*, (2), 2–7.

[59] **Sun, Y., Zhao, C., Adair, K.R., Zhao, Y., Goncharova, L. V., Liang, J., et al.** (2021) Regulated lithium plating and stripping by a nano-scale gradient inorganic–organic coating for stable lithium metal anodes. *Energy & Environmental Science*. *14*, (7), 4085–4094.

[60] **Chen, K., Pathak, R., Gurung, A., Adhamash, E.A., Bahrami, B., He, Q., et al.** (2019) Flower-shaped lithium nitride as a protective layer via facile plasma activation for stable lithium metal anodes. *Energy Storage Materials*. *18*, (November 2018), 389–396.

[61] **Chen, L., Connell, J.G., Nie, A., Huang, Z., Zavadil, K.R., Klavetter, K.C., et al.** (2017) Lithium metal protected by atomic layer deposition metal oxide for high performance anodes. *Journal of Materials Chemistry A*. *5*, (24), 12297–12309.

[62] **Zhu, W., Deng, W., Zhao, F., Liang, S., Zhou, X., and Liu, Z.** (2019) Graphene network nested Cu foam for reducing size of lithium metal towards stable metallic lithium anode. *Energy Storage Materials*. *21*, (August 2018), 107–114.

[63] **Liu, L., Yin, Y., Li, J., Wang, S., Guo, Y., and Wan, L.** (2018) Uniform Lithium Nucleation/Growth Induced by Lightweight Nitrogen-Doped Graphitic Carbon Foams for High-Performance Lithium Metal Anodes. *Advanced Materials*. *30*, (10), 1–8.

[64] **Wu, H., Jia, H., Wang, C., Zhang, J.G., and Xu, W.** (2021) Recent Progress in Understanding Solid Electrolyte Interphase on Lithium Metal Anodes. *Advanced Energy Materials*. *11*, (5), 1–35.

[65] **Li, S., Jiang, M., Xie, Y., Xu, H., Jia, J., and Li, J.** (2018) Developing High-Performance Lithium Metal Anode in Liquid Electrolytes: Challenges and Progress. *Advanced Materials*. *30*, (17), 1–29.

[66] **Wu, X., Pan, K., Jia, M., Ren, Y., He, H., Zhang, L., et al.** (2019) Electrolyte for lithium protection: From liquid to solid. *Green Energy & Environment*. *4*, (4), 360–374.

[67] **Wu, C. and Zeng, W.** (2022) Gel Electrolyte for Li Metal Battery. *Chemistry - An Asian Journal*. *17*, (23),.

[68] **Xie, L., Tang, C., Bi, Z., Song, M., Fan, Y., Yan, C., et al.** (2021) Hard Carbon Anodes for Next-Generation Li-Ion Batteries: Review and Perspective. *Advanced Energy Materials*. *11*, (38).

[69] **Asenbauer, J., Eisenmann, T., Kuenzel, M., Kazzazi, A., Chen, Z., and Bresser, D.** (2020) The success story of graphite as a lithium-ion anode material-fundamentals, remaining challenges, and recent developments including silicon (oxide) composites. *Sustainable Energy and Fuels*. *4*, (11), 5387–5416.

[70] **Bernal, J.D., Walker, S.J., Bernal, J.D., and Walker, S.J.** (1924) The structure of graphite. *Proceedings of the Royal Society of London. Series A, Containing Papers of a Mathematical and Physical Character*. *106*, (740), 749–773.

[71] **Song, X.Y., Kinoshita, K., and Tran, T.D.** (1996) Microstructural Characterization of Lithiated Graphite. *Journal of The Electrochemical Society*. *143*, (6), L120–L123.

[72] **Xu, K.** (2004) Nonaqueous Liquid Electrolytes for Lithium-Based Rechargeable Batteries. *Chemical Reviews*. *104*, (10), 4303–4418.

[73] **Winter, M., Besenhard, J.O., Spahr, M.E., and Novák, P.** (1998) Insertion Electrode Materials for Rechargeable Lithium Batteries. *Advanced Materials*. *10*, (10), 725–763.

[74] **Zaghib, K., Brochu, F., Guerfi, A., and Kinoshita, K.** (2001) Effect of particle size on lithium intercalation rates in natural graphite. *Journal of Power Sources*. *103*, (1), 140–146.

[75] **Yang, X.-G., Liu, T., Gao, Y., Ge, S., Leng, Y., Wang, D., et al.** (2019) Asymmetric Temperature Modulation for Extreme Fast Charging of Lithium-Ion Batteries. *Joule*. *3*, (12), 3002–3019.

[76] **Kim, J., Nithya Jeghan, S.M., and Lee, G.** (2020) Superior fast-charging capability of graphite anode via facile surface treatment for lithium-ion batteries. *Microporous and Mesoporous Materials*. *305*, (April), 110325.

[77] **Hai, Y., Cui, W., Lin, Y., Han, P., Chen, H., Zhu, Z., et al.** (2019) Surface modification of graphite by ion implantation for promoting the electrochemical property in Li-ion batteries. *Applied Surface Science*. *484*, (April), 726–731.

[78] **Beheshti, S.H., Javanbakht, M., Omidvar, H., Hosen, M.S., Hubin, A., Van Mierlo, J., et al.** (2022) Development, retainment, and assessment of the graphite-electrolyte interphase in Li-ion batteries regarding the functionality of SEI-forming additives. *IScience*. *25*, (3), 103862.

[79] **Wang, R., Li, X., Wang, Z., and Zhang, H.** (2017) Electrochemical analysis graphite/electrolyte interface in lithium-ion batteries: p-Toluenesulfonyl isocyanate as electrolyte additive. *Nano Energy*. *34*, (February), 131–140.

[80] **Wang, K., Xing, L., Zhi, H., Cai, Y., Yan, Z., Cai, D., et al.** (2018) High stability graphite/electrolyte interface created by a novel electrolyte additive: A theoretical and experimental study. *Electrochimica Acta*. *262*, 226–232.

[81] **Glazier, S.L., Li, J., Louli, A.J., Allen, J.P., and Dahn, J.R.** (2017) An Analysis of Artificial and Natural Graphite in Lithium Ion Pouch Cells Using Ultra-High Precision Coulometry, Isothermal Microcalorimetry, Gas Evolution, Long Term Cycling and Pressure Measurements. *Journal of The Electrochemical Society*. *164*, (14), A3545–A3555.

[82] **Surovtseva, D., Crossin, E., Pell, R., and Stamford, L.** (2022) Toward a life cycle inventory for graphite production. *Journal of Industrial Ecology*. *26*, (3), 964–979.

[83] **European Commission** (2014) Critical Raw Material List.

[84] **Weber, L.** (2023) On the security of graphite supply. *Mineralogy and Petrology*. *117*, (2), 387–399.

[85] **Natural Resources Canada** (2022) Graphite facts.

[86] **Sato, K., Noguchi, M., Demachi, A., Oki, N., and Endo, M.** (1994) A Mechanism of Lithium Storage in Disordered Carbons. *Science*. *264*, (5158), 556–558.

[87] **Zhang, L., Wang, W. (Alex), Lu, S., and Xiang, Y.** (2021) Carbon Anode Materials: A Detailed Comparison between Na-ion and K-ion Batteries. *Advanced Energy Materials*. *11*, (11), 1–15.

[88] **Zhao, L., Hu, Z., Lai, W., Tao, Y., Peng, J., Miao, Z., et al.** (2021) Hard Carbon Anodes: Fundamental Understanding and Commercial Perspectives for Na-Ion Batteries beyond Li-Ion and K-Ion Counterparts. *Advanced Energy Materials*. *11*, (1), 1–28.

[89] **Yang, G., Li, X., Guan, Z., Tong, Y., Xu, B., Wang, X., et al.** (2020) Insights into Lithium and Sodium Storage in Porous Carbon. *Nano Letters*. *20*, (5), 3836–3843.

[90] **Qian, Y., Jiang, S., Li, Y., Yi, Z., Zhou, J., Li, T., et al.** (2019) In Situ Revealing the Electroactivity of P-O and P-C Bonds in Hard Carbon for High-Capacity and Long-Life Li/K-Ion Batteries. *Advanced Energy Materials*. *9*, (34), 1–10.

[91] **Guo, Z., Wang, C., Chen, M., and Li, M.** (2013) Hard Carbon Derived from Coal Tar Pitch for Use as the Anode Material in Lithium Ion Batteries. *International Journal of Electrochemical Science*. *8*, (2), 2702–2709.

[92] **Chen, D., Cen, K., Zhuang, X., Gan, Z., Zhou, J., Zhang, Y., et al.** (2022) Insight into biomass pyrolysis mechanism based on cellulose, hemicellulose, and lignin: Evolution of volatiles and kinetics, elucidation of reaction pathways, and characterization of gas, biochar and bio-oil. *Combustion and Flame*. *242*, 112142.

[93] **Adams, R.A., Varma, A., and Pol, V.G.** (2019) Carbon Anodes for Nonaqueous Alkali Metal-Ion Batteries and Their Thermal Safety Aspects. *Advanced Energy Materials*. *9*, (35).

[94] **Kim, B.H., Kim, J.H., Kim, J.G., Im, J.S., Lee, C.W., and Kim, S.** (2017) Controlling the electrochemical properties of an anode prepared from pitch-based soft carbon for Li-ion batteries. *Journal of Industrial and Engineering Chemistry*. *45*, 99–104.

[95] **Ko, S., Lee, C.W., and Im, J.S.** (2016) Petrochemical-waste-derived high-performance anode material for Li-ion batteries. *Journal of Industrial and Engineering Chemistry*. *36*, 125–131.

[96] **Du, J., Ma, J., Liu, Z., Wang, W., Jia, H., Zhang, M., et al.** (2022) Investigation of the soft carbon microstructure in silicon/carbon anodes for superior lithium storage. *RSC Advances*. *12*, (32), 20672–20678.

[97] **Zhao, B., Ran, R., Liu, M., and Shao, Z.** (2015) A comprehensive review of $Li_4Ti_5O_{12}$-based electrodes for lithium-ion batteries : The latest advancements and future perspectives. *98*, 1–71.

[98] **Ohzuku, T., Ueda, A., and Yamamoto, N.** (1995) Zero-Strain Insertion Material of $Li[Li_{1/3}Ti_{5/3}]O_4$ for Rechargeable Lithium Cells. *Journal of The Electrochemical Society*. *142*, (5), 1431–1435.

[99] **Kavan, L., Procházka, J., Spitler, T.M., Kalbáč, M., Zukalová, M., Drezen, T., et al.** (2003) Li Insertion into $Li_4Ti_5O_{12}$ (Spinel). *Journal of The Electrochemical Society*. *150*, (7), A1000.

[100] **Murphy, D., Cava, R., Zahurak, S., and Santoro, A.** (1983) Ternary Li_xTiO_2 phases from insertion reactions. *Solid State Ionics*. *9–10*, (PART 1), 413–417.

[101] **Huang, S., Wen, Z., Lin, B., Han, J., and Xu, X.** (2008) The high-rate performance of the newly designed $Li_4Ti_5O_{12}$/Cu composite anode for lithium ion batteries. *Journal of Alloys and Compounds*. *457*, (1–2), 400–403.

[102] **Yao, X.L., Xie, S., Nian, H.Q., and Chen, C.H.** (2008) Spinel $Li_4Ti_5O_{12}$ as a reversible anode material down to 0V. *Journal of Alloys and Compounds*. *465*, (1–2), 375–379.

[103] **Hsieh, C.-T., Chen, I.-L., Jiang, Y.-R., and Lin, J.-Y.** (2011) Synthesis of spinel lithium titanate anodes incorporated with rutile titania nanocrystallites by spray drying followed by calcination. *Solid State Ionics*. *201*, (1), 60–67.

[104] **Scharner, S., Weppner, W., and Schmid-Beurmann, P.** (1999) Evidence of Two-Phase Formation upon Lithium Insertion into the $Li_{1.33}Ti_{1.67}O_4$ Spinel. *Journal of The Electrochemical Society*. *146*, (3), 857–861.

[105] **Venkateswarlu, M., Chen, C.H., Do, J.S., Lin, C.W., Chou, T.C., and Hwang, B.J.** (2005) Electrochemical properties of nano-sized $Li_4Ti_5O_{12}$ powders synthesized by a sol–gel process and characterized by X-ray absorption spectroscopy. *Journal of Power Sources*. *146*, (1–2), 204–208.

[106] **Khomane, R.B., Prakash, A.S., Ramesha, K., and Sathiya, M.** (2011) CTAB-assisted sol–gel synthesis of $Li_4Ti_5O_{12}$ and its performance as anode material for Li-ion batteries. *Materials Research Bulletin*. *46*, (7), 1139–1142.

[107] **Lin, C.-Y. and Duh, J.-G.** (2011) Porous $Li_4Ti_5O_{12}$ anode material synthesized by one-step solid state method for electrochemical properties enhancement. *Journal of Alloys and Compounds*. *509*, (8), 3682–3685.

[108] **Hu, X., Lin, Z., Yang, K., Huai, Y., and Deng, Z.** (2011) Effects of carbon source and carbon content on electrochemical performances of $Li_4Ti_5O_{12}$/C prepared by one-step solid-state reaction. *Electrochimica Acta*. *56*, (14), 5046–5053.

[109] **Huang, S., Wen, Z., Zhang, J., Gu, Z., and Xu, X.** (2006) $Li_4Ti_5O_{12}$/Ag composite as electrode materials for lithium-ion battery. *Solid State Ionics*. *177*, (9–10), 851–855.

[110] **Abouimrane, A., Belharouak, I., and Amine, K.** (2009) Sulfone-based electrolytes for high-voltage Li-ion batteries. *Electrochemistry Communications*. *11*, (5), 1073–1076.

[111] **Axel, H., Schafer, H., and Weiss, A.** (1965) Die Kristallstruktur von Lithiumsilicid Li2Si. *Angew. Chem. Int. 77*, (8), 379–380.

[112] **Axel, H., Schäfer, H., and Weiss, A.** (1966) Zur Kenntnis der Phase $Li_{22}Si_5$. *Z. Naturforsch. B. 21*, (2), 115–117.

[113] **Sharma, R.A. and Seefurth, R.N.** (1976) Thermodynamic properties of the lithium-silicon system. *Electrochemical Science And Technology*. *123*, 1763–1768.

[114] **Bourderau, S., Brousse, T., and Schleich, D..** (1999) Amorphous silicon as a possible anode material for Li-ion batteries. *Journal of Power Sources*. *81–82*, 233–236.

[115] **Li, H., Huang, X., Chen, L., Wu, Z., and Liang, Y.** (1999) High capacity nano-Si composite anode material for lithium rechargeable batteries. *Electrochemical and Solid-State Letters*. *2*, (11), 547–549.

[116] **Wilson, A.M., Way, B.M., Dahn, J.R., and Van Buuren, T.** (1995) Nanodispersed silicon in pregraphitic carbons. *Journal of Applied Physics*. *77*, (6), 2363–2369.

[117] **Chan, C.K., Peng, H., Liu, G., McIlwrath, K., Zhang, X.F., Huggins, R.A., et al.** (2008) High-performance lithium battery anodes using silicon nanowires. *Nature Nanotechnology*. *3*, (1), 31–35.

[118] **Yao, Y., McDowell, M.T., Ryu, I., Wu, H., Liu, N., Hu, L., et al.** (2011) Interconnected silicon hollow nanospheres for lithium-ion battery anodes with long cycle life. *Nano Letters*. *11*, (7), 2949–2954.

[119] **Liu, N., Wu, H., McDowell, M.T., Yao, Y., Wang, C., and Cui, Y.** (2012) A yolk-shell design for stabilized and scalable Li-ion battery alloy anodes. *Nano Letters*. *12*, (6), 3315–3321.

[120] **Wu, F., Dong, Y., Su, Y., Wei, C., Chen, T., Yan, W., et al.** (2023) Benchmarking the Effect of Particle Size on Silicon Anode Materials for Lithium-Ion Batteries. *Small*. *19*, (42), 1–17.

[121] **Paul, S., Rahman, M.A., Sharif, S. Bin, Kim, J.-H., Siddiqui, S.-E.-T., and Hossain, M.A.M.** (2022) TiO_2 as an Anode of High-Performance Lithium-Ion Batteries: A Comprehensive Review towards Practical Application. *Nanomaterials*. *12*, (12), 2034.

[122] **Aghamohammadi, H., Eslami-Farsani, R., and Castillo-Martinez, E.** (2022) Recent trends in the development of MXenes and MXene-based composites as anode materials for Li-ion batteries. *Journal of Energy Storage*. *47*, (October 2021), 103572.

[123] **Naguib, M., Come, J., Dyatkin, B., Presser, V., Taberna, P.-L., Simon, P., et al.** (2012) MXene: a promising transition metal carbide anode for lithium-ion batteries. *Electrochemistry Communications*. *16*, (1), 61–64.

[124] **Mou, H., Xiao, W., Miao, C., Li, R., and Yu, L.** (2020) Tin and Tin Compound Materials as Anodes in Lithium-Ion and Sodium-Ion Batteries: A Review. *Frontiers in Chemistry*. *8*, (March), 1–14.

[125] **Liu, H., Wang, S., Zhao, J., Zhang, B., Liu, L., Bao, R., et al.** (2024) Sn-based anode materials for lithium-ion batteries: From mechanism to modification. *Journal of Energy Storage*. *80*, (January), 109862.

[126] **Maiti, D., Aravindan, V., Madhavi, S., and Sujatha Devi, P.** (2015) Electrochemical performance of hematite nanoparticles derived from spherical maghemite and elongated goethite particles. *Journal of Power Sources*. *276*, 291–298.

[127] **Wang, Q., Chen, D., Chen, J., Lai, C., Li, L., and Wang, C.** (2015) Facile synthesis and electrochemical properties of Fe_3O_4 hexahedra for Li-ion battery anode. *Materials Letters*. *141*, (2015), 319–322.

[128] **Xu, J.S. and Zhu, Y.J.** (2012) Monodisperse Fe_3O_4 and γ-Fe_2O_3 Magnetic Mesoporous Microspheres as Anode Materials for Lithium-Ion Batteries. *ACS Applied Materials & Interfaces*. *4*, (9), 4752–4757.

[129] **Maibach, J., Lindgren, F., Eriksson, H., Edström, K., and Hahlin, M.** (2016) Electric Potential Gradient at the Buried Interface between Lithium-Ion Battery Electrodes and the SEI Observed Using Photoelectron Spectroscopy. *Journal of Physical Chemistry Letters*. *7*, (10), 1775–1780.

[130] **Casimir, A., Zhang, H., Ogoke, O., Amine, J.C., Lu, J., and Wu, G.** (2016) Silicon-based anodes for lithium-ion batteries: Effectiveness of materials synthesis and electrode preparation. *Nano Energy*. *27*, 359–376.

[131] **Limthongkul, P., Jang, Y. Il, Dudney, N.J., and Chiang, Y.M.** (2003) Electrochemically-driven solid-state amorphization in lithium-metal anodes. *Journal of Power Sources*. *119–121*, 604–609.

[132] **Key, B., Bhattacharyya, R., Morcrette, M., Seznéc, V., Tarascon, J.M., and Grey, C.P.** (2009) Real-time NMR investigations of structural changes in silicon electrodes for lithium-ion batteries. *Journal of the American Chemical Society*. *131*, (26), 9239–9249.

[133] **Liu, X.H., Wang, J.W., Huang, S., Fan, F., Huang, X., Liu, Y., et al.** (2012) In situ atomic-scale imaging of electrochemical lithiation in silicon. *Nature Nanotechnology*. *7*, (11), 749–756.

[134] **Limthongkul, P., Jang, Y. Il, Dudney, N.J., and Chiang, Y.M.** (2003) Electrochemically-driven solid-state amorphization in lithium-silicon alloys and implications for lithium storage. *Acta Materialia*. *51*, (4), 1103–1113.

[135] **Hasa, I. and Ivana Passerini, S.** (2021) *Silicon anode systems for lithium-ion batteries*. Elsevier Inc.

[136] **McDowell, M.T., Lee, S.W., Nix, W.D., and Cui, Y.** (2013) 25th anniversary article: Understanding the lithiation of silicon and other alloying anodes for lithium-ion batteries. *Advanced Materials*. *25*, (36), 4966–4985.

[137] **Zhang, L., Rajagopalan, R., Guo, H., Hu, X., Dou, S., and Liu, H.** (2016) A Green and Facile Way to Prepare Granadilla-Like Silicon-Based Anode Materials for Li-Ion Batteries. *Advanced Functional Materials*. *26*, (3), 440–446.

[138] **Son, I.H., Park, J.H., Kwon, S., Choi, J.W., and Rümmeli, M.H.** (2016) Graphene coating of silicon nanoparticles with CO_2-enhanced chemical vapor deposition. *Small*. *12*, (5), 658–667.

[139] **Rahman, M.A., Song, G., Bhatt, A.I., Wong, Y.C., and Wen, C.** (2016) Nanostructured silicon anodes for high-performance lithium-ion batteries. *Advanced Functional Materials*. *26*, (5), 647–678.

[140] **Agyeman, D.A., Song, K., Lee, G.H., Park, M., and Kang, Y.M.** (2016) Carbon-Coated Si Nanoparticles Anchored between Reduced Graphene Oxides as an Extremely Reversible Anode Material for High Energy-Density Li-Ion Battery. *Advanced Energy Materials*. *6*, (20), 1–10.

[141] **Zuo, X., Xia, Y., Ji, Q., Gao, X., Yin, S., Wang, M., et al.** (2017) Self-Templating Construction of 3D Hierarchical Macro-/Mesoporous Silicon from 0D Silica Nanoparticles. *ACS Nano*. *11*, (1), 889–899.

[142] **Heiskanen, S.K., Kim, J., and Lucht, B.L.** (2019) Generation and Evolution of the Solid Electrolyte Interphase of Lithium-Ion Batteries. *Joule*. *3*, (10), 2322–2333.

[143] **Kwon, T.W., Choi, J.W., and Coskun, A.** (2018) The emerging era of supramolecular polymeric binders in silicon anodes. *Chemical Society Reviews*. *47*, (6), 2145–2164.

[144] **Ma, T., Xu, H., Yu, X., Li, H., Zhang, W., Cheng, X., et al.** (2019) Lithiation behavior of coaxial hollow nanocables of carbon-silicon composite. *ACS Nano*. *13*, (2), 2274–2280.

[145] **Lin, L., Xu, X., Chu, C., Majeed, M.K., and Yang, J.** (2016) Mesoporous Amorphous Silicon: A Simple Synthesis of a High-Rate and Long-Life Anode Material for Lithium-Ion Batteries. *Angewandte Chemie - International Edition*. *55*, (45), 14063–14066.

[146] **Polat, D.B., Keles, O., and Amine, K.** (2016) Compositionally-graded silicon-copper helical arrays as anodes for lithium-ion batteries. *Journal of Power Sources*. *304*, 273–281.

[147] **Zhang, Z., Wang, Y., Ren, W., Tan, Q., Chen, Y., Li, H., et al.** (2014) Scalable synthesis of interconnected porous silicon/carbon composites by the rochow reaction as high-performance anodes of lithium ion batteries. *Angewandte Chemie - International Edition*. *53*, (20), 5165–5169.

[148] **Pathak, A.D., Chanda, U.K., Samanta, K., Mandal, A., Sahu, K.K., and Pati, S.** (2019) Selective leaching of Al from hypereutectic Al-Si alloy to produce nano-porous silicon (NPS) anodes for lithium ion batteries. *Electrochimica Acta*. *317*, 654–662.

[149] **Jia, H., Zheng, J., Song, J., Luo, L., Yi, R., Estevez, L., et al.** (2018) A novel approach to synthesize micrometer-sized porous silicon as a high performance anode for lithium-ion batteries. *Nano Energy*. *50*, (May), 589–597.

[150] **Xu, Y., Yin, G., Ma, Y., Zuo, P., and Cheng, X.** (2010) Nanosized core/shell silicon@carbon anode material for lithium ion batteries with polyvinylidene fluoride as carbon source. *Journal of Materials Chemistry*. *20*, (16), 3216–3220.

[151] **Zhou, X.Y., Tang, J.J., Yang, J., Xie, J., and Ma, L.L.** (2013) Silicon@carbon hollow core-shell heterostructures novel anode materials for lithium ion batteries. *Electrochimica Acta*. *87*, 663–668.

[152] **Zhou, J., Qian, T., Wang, M., Xu, N., Zhang, Q., Li, Q., et al.** (2016) Core-Shell Coating Silicon Anode Interfaces with Coordination Complex for Stable Lithium-Ion Batteries. *ACS Applied Materials and Interfaces*. *8*, (8), 5358–5365.

[153] **Zhang, W., Shi, H., Wang, C., Wang, J., Wang, Z., Jiang, H., et al.** (2023) Synthesizing copper-doped silicon/carbon composite anode as cost-effective active materials for Li-ion batteries. *Journal of Physics and Chemistry of Solids*. *179*, (February), 111387.

[154] **Nulu, A., Nulu, V., and Sohn, K.Y.** (2022) Influence of transition metal doping on nano silicon anodes for Li-ion energy storage applications. *Journal of Alloys and Compounds*. *911*, 164976.

[155] **Qi, C., Li, S., Yang, Z., Xiao, Z., Zhao, L., Yang, F., et al.** (2022) Suitable thickness of carbon coating layers for silicon anode. *Carbon*. *186*, 530–538.

[156] **Mabery, C. F.** (1886) The composition of certain products from the cowles electrical furnace. *Am. Chem. J. 9*, 11–15.

[157] **Sindland, C. and Tangstad, M.** (2021) Production Rate of SiO Gas from Industrial Quartz and Silicon. *Metallurgical and Materials Transactions B*. *52*, (3), 1755–1771.

[158] **Hohl, A., Wieder, T., van Aken, P.., Weirich, T.., Denninger, G., Vidal, M., et al.** (2003) An interface clusters mixture model for the structure of amorphous silicon monoxide (SiO). *Journal of Non-Crystalline Solids*. *320*, (1–3), 255–280.

[159] **Lee, J.K., Yoon, W.Y., and Kim, B.K.** (2014) Kinetics of Reaction Products of Silicon Monoxide with Controlled Amount of Li-Ion Insertion at Various Current Densities for Li-Ion Batteries. *Journal of The Electrochemical Society*. *161*, (6), A927–A933.

[160] **Nagao, Y., Sakaguchi, H., Honda, H., Fukunaga, T., and Esaka, T.** (2004) Structural Analysis of Pure and Electrochemically Lithiated SiO Using Neutron Elastic Scattering. *Journal of The Electrochemical Society*. *151*, (10), A1572.

[161] **Guo, L., He, H., Ren, Y., Wang, C., and Li, M.** (2018) Core-shell SiO@F-doped C composites with interspaces and voids as anodes for high-performance lithium-ion batteries. *Chemical Engineering Journal*. *335*, (July 2017), 32–40.

[162] **Jung, S.C., Kim, H.-J., Kim, J.-H., and Han, Y.-K.** (2016) Atomic-Level Understanding toward a High-Capacity and High-Power Silicon Oxide (SiO) Material. *The Journal of Physical Chemistry C*. *120*, (2), 886–892.

[163] **Yang, H., Zhang, Z., Cai, J., Yang, B., Fan, D., and Zhao, F.** (2022) Preparation and electrochemical properties of porous SiO/Ni anode materials for lithium-silicon batteries. *Journal of Alloys and Compounds*. *923*, 166396.

[164] **Park, D., Kim, H.-S., Seo, H., Kim, K., and Kim, J.-H.** (2020) Porous SiO composite tailored by scalable mechanochemical oxidation of Si for Li-ion anodes. *Electrochimica Acta*. *357*, 136862.

[165] **Woo, J. and Baek, S.-H.** (2017) A comparative investigation of different chemical treatments on SiO anode materials for lithium-ion batteries: towards long-term stability. *RSC Advances*. *7*, (8), 4501–4509.

[166] **Miyachi, M., Yamamoto, H., and Kawai, H.** (2007) Electrochemical Properties and Chemical Structures of Metal-Doped SiO Anodes for Li-Ion Rechargeable Batteries. *Journal of The Electrochemical Society*. *154*, (4), A376.

[167] **Li, Z., Du, M., Guo, X., Zhang, D., Wang, Q., Sun, H., et al.** (2023) Research progress of SiO_x-based anode materials for lithium-ion batteries. *Chemical Engineering Journal*. *473*, (May), 145294.

[168] **Hirata, A., Kohara, S., Asada, T., Arao, M., Yogi, C., Imai, H., et al.** (2016) Atomic-scale disproportionation in amorphous silicon monoxide. *Nature Communications*. *7*, (May), 1–7.

[169] **Wetzel, S., Klevenz, M., Pucci, A., and Gail, H.P.** (2012) The temperature-dependent decomposition of SiO studied by infrared vibrational spectroscopy. *Applied Spectroscopy*. *66*, (9), 1061–1066.

[170] **Moon, J.** (2021) Tailoring the oxygen content in lithiated silicon oxide for lithium-ion batteries. *International Journal of Energy Research*. *45*, (5), 7315–7325.

[171] **Li, Z., He, Q., He, L., Hu, P., Li, W., Yan, H., et al.** (2017) Self-sacrificed synthesis of carbon-coated SiO_x nanowires for high capacity lithium ion battery anodes. *Journal of Materials Chemistry A*. *5*, (8), 4183–4189.

[172] **Meng, Q., Li, G., Yue, J., Xu, Q., Yin, Y.-X., and Guo, Y.-G.** (2019) High-Performance Lithiated SiO_x Anode Obtained by a Controllable and Efficient Prelithiation Strategy. *ACS Applied Materials & Interfaces*. *11*, (35), 32062–32068.

[173] **Yu, B.-C., Hwa, Y., Kim, J.-H., and Sohn, H.-J.** (2014) A New Approach to Synthesis of Porous SiO_x Anode for Li-ion Batteries via Chemical Etching of Si Crystallites. *Electrochimica Acta*. *117*, 426–430.

[174] **Jung, H., Yeo, B.C., Lee, K.R., and Han, S.S.** (2016) Atomistics of the lithiation of oxidized silicon (SiO_x) nanowires in reactive molecular dynamics simulations. *Physical Chemistry Chemical Physics*. *18*, (47), 32078–32086.

[175] **Liu, Z., Yu, Q., Zhao, Y., He, R., Xu, M., Feng, S., et al.** (2019) Silicon oxides: A promising family of anode materials for lithium-ion batteries. *Chemical Society Reviews*. *48*, (1), 285–309.

[176] **Chou, C.-Y. and Hwang, G.S.** (2013) Lithiation Behavior of Silicon-Rich Oxide ($SiO_{1/3}$): A First-Principles Study. *Chemistry of Materials*. *25*, (17), 3435–3440.

[177] **Tang, J., Hou, L., Hu, T., Fan, S., Zhou, X., and Yang, J.** (2021) Influence of oxygen content on the electrochemical behavior of SiO_x@C anodes for Li-ion battery. *Composites Communications*. *23*, (October 2020), 100544.

[178] **Sun, L., Jiang, X., and Jin, Z.** (2023) Interfacial engineering of porous SiO_x@C composite anodes toward high-performance lithium-ion batteries. *Chemical Engineering Journal*. *474*, (September), 145960.

[179] **Wang, K., Tan, Y., Li, P., and Sun, J.** (2020) Scalable 3D porous residual Al-doped Si/SiO_x composites for high performance anodes: Coupling effects of porosity, conductive sites and oxide layer. *Electrochimica Acta*. *353*, 136538.

[180] **Im, J., Kwon, J., Kim, D., Yoon, S., and Cho, K.Y.** (2022) P-Doped SiO_x /Si/SiO_x Sandwich Anode for Li-Ion Batteries to Achieve High Initial Coulombic Efficiency and Low Capacity Decay. *Small Methods*. *6*, (3), 1–11.

[181] **Kwon, M.-J., Maniyazagan, M., Yang, H.-W., Kang, W.S., and Kim, S.-J.** (2020) A facile synthesis of vanadium-doped SiO_x composites for high-performance Li-ion battery anodes. *Journal of Alloys and Compounds*. *842*, 155900.

[182] **Ma, H., Jin, C., Xu, G., Wen, L., Tu, C., Sun, F., et al.** (2023) High-performance free-standing N-doped C/SiO_x film anode materials for lithium ion batteries. *Electrochimica Acta*. *471*, (August), 143402.

[183] **Xie, H., Hou, C., Yue, Z., Zhai, L., Sun, H., Lu, H., et al.** (2023) Facile synthesis of C, N, P co-doped SiO_x as anode material for lithium-ion batteries with excellent rate performance. *Journal of Energy Storage*. *64*, (February), 107147.

[184] **Huang, H., Kelder, E.., Chen, L., and Schoonman, J.** (1999) Electrochemical characteristics of $Sn_{1-x}Si_xO_2$ as anode for lithium-ion batteries. *Journal of Power Sources*. *81–82*, 362–367.

[185] **Gao, B., Sinha, S., Fleming, L., and Zhou, O.** (2001) Alloy Formation in Nanostructured Silicon. *Advanced Materials*. *13*, (11), 816–819.

[186] **Chang, W.-S., Park, C.-M., Kim, J.-H., Kim, Y.-U., Jeong, G., and Sohn, H.-J.** (2012) Quartz (SiO_2): a new energy storage anode material for Li-ion batteries. *Energy & Environmental Science*. *5*, (5), 6895.

[187] **Zhang, Y., Li, Y., Wang, Z., and Zhao, K.** (2014) Lithiation of SiO_2 in Li-Ion Batteries: In Situ Transmission Electron Microscopy Experiments and Theoretical Studies. *Nano Letters*. *14*, (12), 7161–7170.

[188] **Lener, G., Otero, M., Barraco, D.E., and Leiva, E.P.M.** (2018) Energetics of silica lithiation and its applications to lithium ion batteries. *Electrochimica Acta*. *259*, 1053–1058.

[189] **Guo, B., Shu, J., Wang, Z., Yang, H., Shi, L., Liu, Y., et al.** (2008) Electrochemical reduction of nano-SiO_2 in hard carbon as anode material for lithium ion batteries. *Electrochemistry Communications*. *10*, (12), 1876–1878.

[190] **Liang, C., Zhou, C., Chen, Z., Gan, Y., Xia, Y., Huang, H., et al.** (2018) Electrochemical lithium storage properties of desert sands. *Ionics*. *24*, (8), 2233–2239.

[191] **Han, Y., Liu, X., and Lu, Z.** (2018) Systematic investigation of prelithiated SiO_2 particles for high-performance anodes in lithium-ion battery. *Applied Sciences (Switzerland)*. *8*, (8),.

[192] **Lepoivre, F., Larcher, D., and Tarascon, J.-M.** (2016) Electrochemical Activation of Silica for Enhanced Performances of Si-Based Electrodes. *Journal of The Electrochemical Society*. *163*, (13), A2791–A2796.

[193] **Yan, N., Wang, F., Zhong, H., Li, Y., Wang, Y., Hu, L., et al.** (2013) Hollow Porous SiO_2 Nanocubes Towards High-performance Anodes for Lithium-ion Batteries. *Scientific Reports*. *3*, (1), 1568.

[194] **Yu, Q., Wang, P., Hu, S., Hui, J., Zhuang, J., and Wang, X.** (2011) Hydrothermal synthesis of hollow silica spheres under acidic conditions. *Langmuir*. *27*, (11), 7185–7191.

[195] **Cao, X., Chuan, X., Li, S., Huang, D., and Cao, G.** (2016) Hollow Silica Spheres Embedded in a Porous Carbon Matrix and Its Superior Performance as the Anode for Lithium-Ion Batteries. *Particle & Particle Systems Characterization*. *33*, (2), 110–117.

[196] **Liu, X., Chen, Y., Liu, H., and Liu, Z.-Q.** (2017) SiO_2@C hollow sphere anodes for lithium-ion batteries. *Journal of Materials Science & Technology*. *33*, (3), 239–245.

[197] **Lv, P., Zhao, H., Wang, J., Liu, X., Zhang, T., and Xia, Q.** (2013) Facile preparation and electrochemical properties of amorphous SiO_2/C composite as anode material for lithium ion batteries. *Journal of Power Sources*. *237*, 291–294.

[198] **European Commission,** Fit for 55: EU reaches new milestone to make all new cars and vans zero-emission from 2035.

[199] **European Commission,** The European Green Deal: Striving to be the first climate-neutral continent.

[200] **International Energy Agency.** (2023) Batteries and Secure Energy Transitions.

[201] **Naskar, A.K., Bi, Z., Li, Y., Akato, S.K., Saha, D., Chi, M., et al.** (2014) Tailored recovery of carbons from waste tires for enhanced performance as anodes in lithium-ion batteries. *RSC Advances*. *4*, (72), 38213.

[202] **Veldevi, T., Raghu, S., Kalaivani, R.A., and Shanmugharaj, A.M.** (2022) Waste tire derived carbon as potential anode for lithium-ion batteries. *Chemosphere*. *288*, (P1), 132438.

[203] **Shilpa, Kumar, R., and Sharma, A.** (2018) Morphologically tailored activated carbon derived from waste tires as high-performance anode for Li-ion battery. *Journal of Applied Electrochemistry*. *48*, (1), 1–13.

[204] **Ding, K., Zhou, L., Qu, R., Zhang, D., Chen, J., He, X., et al.** (2020) Honeycomb-shaped carbon particles prepared from bicycle waste tires for anodes in lithium ion batteries. *Materials Chemistry and Physics*. *251*, (April), 123202.

[205] **Bao, Q., Huang, Y.-H., Lan, C.-K., Chen, B.-H., and Duh, J.-G.** (2015) Scalable Upcycling Silicon from Waste Slicing Sludge for High-performance Lithium-ion Battery Anodes. *Electrochimica Acta*. *173*, (2015), 82–90.

[206] **Kasukabe, T., Nishihara, H., Kimura, K., Matsumoto, T., Kobayashi, H., Okai, M., et al.** (2017) Beads-Milling of Waste Si Sawdust into High-Performance Nanoflakes for Lithium-Ion Batteries. *Scientific Reports*. *7*, (1), 42734.

[207] **Wang, K., Xue, B., Tan, Y., Sun, J., Li, Q., Shi, S., et al.** (2019) Recycling of micron-sized Si powder waste from diamond wire cutting and its application in Li-ion battery anodes. *Journal of Cleaner Production*. *239*, 117997.

[208] **Sreenarayanan, B., Vicencio, M., Bai, S., Lu, B., Mao, O., Adireddy, S., et al.** (2023) Recycling silicon scrap for spherical Si–C composite as high-performance lithium-ion battery anodes. *Journal of Power Sources*. *578*, (June), 233245.

[209] **Wang, S.E., Jang, I.-S., Kang, Y.C., Chun, J., and Jung, D.-S.** (2021) Residual silica removal and nanopore generation on industrial waste silicon using ammonium fluoride and its application to lithium-ion battery anodes. *Chemical Engineering Journal*. *419*, (December 2020), 129389.

[210] **Zhang, C., Ma, Q., Cai, M., Zhao, Z., Xie, H., Ning, Z., et al.** (2021) Recovery of porous silicon from waste crystalline silicon solar panels for high-performance lithium-ion battery anodes. *Waste Management*. *135*, (May), 182–189.

[211] **Sim, Y., Tay, Y.B., Ankit, Lin, X., and Mathews, N.** (2023) Simplified silicon recovery from photovoltaic waste enables high performance, sustainable lithium-ion batteries. *Solar Energy Materials and Solar Cells*. *257*, (May), 112394.

[212] **Chun, J., An, S., and Lee, J.** (2015) Highly mesoporous silicon derived from waste iron slag for high performance lithium ion battery anodes. *Journal of Materials Chemistry A*. *3*, (43), 21899–21906.

[213] **Yang, K., Gong, P., Xin, X., Tian, Z., and Lai, Y.** (2020) Purifying spent carbon anode (SCA) from aluminum reduction industry by alkali fusion method to apply for Li-ion batteries anodes: From waste to resource. *Journal of the Taiwan Institute of Chemical Engineers*. *116*, 121–127.

[214] **Karahan, B.D.** (2023) Rational fabrication of low carbon foot-print electrode materials for lithium-ion batteries from electric arc furnace dust via integrated hydrometallurgical process. *Materials Chemistry and Physics*. *302*, (April), 127734.

[215] **Karahan, B.D.** (2022) Carbon coated electric arc furnace dust prepared by one-pot pyrolysis: An efficient, low carbon footprint electrode material for lithium-ion batteries. *Materials Chemistry and Physics*. *287*, (December 2021), 126178.

[216] **Gülcan, M.F. and Karahan, B.D.** (2024) Waste to Resource: Surface Modification of Electric Arc Furnace Flue Dust by Ball Milling and In Situ Carbonization. *Journal of Sustainable Metallurgy*. *10*, (2), 472–485.

[217] **Cao, L., Xiao, R., Wang, J., Li, S., Xu, J., and Huang, T.** (2022) Recycling Waste Al–Si Alloy for Micrometer-Sized Spongy Si with High Areal/Volumetric Capacity and Stability in Lithium-Ion Batteries. *ACS Sustainable Chemistry & Engineering*. *10*, (25), 8143–8150.

[218] **Liu, Y., Zhong, Y., Zeng, Z., Zhang, P., Zhang, H., Zhang, Z., et al.** (2023) Scalable Synthesis of a Porous Micro Si/Si-Ti Alloy Anode for Lithium-Ion Battery from Recovery of Titanium-Blast Furnace Slag. *ACS Applied Materials & Interfaces*. *15*, (47), 54539–54549.

[219] **Hou, L., Xing, B., Zeng, H., Kang, W., Guo, H., Cheng, S., et al.** (2022) Aluminothermic reduction synthesis of Si/C composite nanosheets from waste vermiculite as high-performance anode materials for lithium-ion batteries. *Journal of Alloys and Compounds*. *922*, 166134.

[220] **Li, C., Liu, C., Wang, W., Mutlu, Z., Bell, J., Ahmed, K., et al.** (2017) Silicon Derived from Glass Bottles as Anode Materials for Lithium Ion Full Cell Batteries. *Scientific Reports*. *7*, (1), 917.

[221] **Ehi-Eromosele, C.O., Onwucha, C.N., Ajayi, S.O., Melinte, G., Hansen, A.-L., Indris, S., et al.** (2022) Ionothermal synthesis of activated carbon from waste PET bottles as anode materials for lithium-ion batteries. *RSC Advances*. *12*, (53), 34670–34684.

[222] **Sun, P., Lu, H., Zhang, W., Wu, H., Sun, S., and Liu, X.** (2018) Poly(ethylene terephthalate): Rubbish could be low cost anode material of lithium ion battery. *Solid State Ionics*. *317*, (December 2017), 164–169.

[223] **Villagómez-Salas, S., Manikandan, P., Acuña Guzmán, S.F., and Pol, V.G.** (2018) Amorphous Carbon Chips Li-Ion Battery Anodes Produced through Polyethylene Waste Upcycling. *ACS Omega*. *3*, (12), 17520–17527.

[224] **Agarkar, S., Yadav, P., Fernandes, R., Kothari, D., Suryawanshi, A., and Ogale, S.** (2016) Minute-made activated porous carbon from agro-waste for Li-ion battery anode using a low power microwave oven. *Electrochimica Acta*. *212*, 535–544.

[225] **Zheng, F., Liu, D., Xia, G., Yang, Y., Liu, T., Wu, M., et al.** (2017) Biomass waste inspired nitrogen-doped porous carbon materials as high-performance anode for lithium-ion batteries. *Journal of Alloys and Compounds*. *693*, 1197–1204.

[226] **Sankar, S., Saravanan, S., Ahmed, A.T.A., Inamdar, A.I., Im, H., Lee, S., et al.** (2019) Spherical activated-carbon nanoparticles derived from biomass green tea wastes for anode material of lithium-ion battery. *Materials Letters*. *240*, 189–192.

[227] **Sekar, S., Lee, Y., Kim, D.Y., and Lee, S.** (2019) Substantial LIB anode performance of graphitic carbon nanoflakes derived from biomass green-tea waste. *Nanomaterials*. *9*, (6),.

[228] **Hernández-Rentero, C., Marangon, V., Olivares-Marín, M., Gómez-Serrano, V., Caballero, Á., Morales, J., et al.** (2020) Alternative lithium-ion battery using biomass-derived carbons as environmentally sustainable anode. *Journal of Colloid and Interface Science*. *573*, 396–408.

[229] **Yu, K., Wang, J., Wang, X., Liang, J., and Liang, C.** (2020) Sustainable application of biomass by-products: Corn straw-derived porous carbon nanospheres using as anode materials for lithium ion batteries. *Materials Chemistry and Physics*. *243*, (November 2019), 122644.

[230] **Cheng, Y., Huang, J., Li, J., Xie, H., Wang, Y., Yu, F., et al.** (2020) Turning waste makeup cotton to a hollow structured carbon as anode for high-performance lithium ions batteries. *Micro & Nano Letters*. *15*, (15), 1095–1098.

[231] **Jagdale, P., Nair, J.R., Khan, A., Armandi, M., Meligrana, G., Hernandez, F.R., et al.** (2021) Waste to life: Low-cost, self-standing, 2D carbon fiber green Li-ion battery anode made from end-of-life cotton textile. *Electrochimica Acta*. *368*, 137644.

[232] **Muruganantham, R., Wang, F.-M., Yuwono, R.A., Sabugaa, M., and Liu, W.-R.** (2021) Biomass Feedstock of Waste Mango-Peel-Derived Porous Hard Carbon for Sustainable High-Performance Lithium-Ion Energy Storage Devices. *Energy & Fuels*. *35*, (13), 10878–10889.

[233] **Salimi, P., Tieuli, S., Taghavi, S., Venezia, E., Fugattini, S., Lauciello, S., et al.** (2022) Sustainable lithium-ion batteries based on metal-free tannery waste biochar. *Green Chemistry*. *24*, (10), 4119–4129.

[234] **Soltani, N., Bahrami, A., Pech-Canul, M.I.I., and González, L.A.A.** (2015) Review on the physicochemical treatments of rice husk for production of advanced materials. *Chemical Engineering Journal*. *264*, 899–935.

[235] **Bazargan, A., Wang, Z., Barford, J.P., Saleem, J., and McKay, G.** (2020) Optimization of the removal of lignin and silica from rice husks with alkaline peroxide. *Journal of Cleaner Production*. *260*, 120848.

[236] **Mussatto, S. and Teixeira, J.** (2010) Lignocellulose as raw material in fermentation processes. *Applied Microbiology an Microbial Biotechnology*. *2*, 897–907.

[237] **Patel, M., Karera, A., and Prasanna, P.** (1987) Effect of thermal and chemical treatments on carbon and silica contents in rice husk. *Journal of Materials Science*. *22*, (7), 2457–2464.

[238] **Toda, I., Komatsu, K., Watanabe, T., Toda, H., Akasaka, H., Ohshio, S., et al.** (2018) Effect of meso- and micropore structures on the hydrogen storage properties of nanoporous carbon materials. *Journal of Porous Materials*. *25*, (6), 1765–1770.

[239] **Araque, O., Arzola, N., and Cerón, I.X.** (2024) Microstructure and Mechanical Characterization of Rice Husks from the Tolima Region of Colombia. *Resources*. *13*, (1),.

[240] **Matinfar, M. and Nychka, J.A.** (2023) A review of sodium silicate solutions: Structure, gelation, and syneresis. *Advances in Colloid and Interface Science*. *322*, 103036.

[241] **Iler, R.K.** (1979) *The chemistry of silica*. ISBN: 978-0-471-02404-0

[242] **Andreola, F., Barbieri, L., and Lancellotti, I.** (2020) The Environmental Friendly Route to Obtain Sodium Silicate Solution from Rice Husk Ash: A Comparative Study with Commercial Silicates Deflocculating Agents. *Waste and Biomass Valorization*. *11*, (11), 6295–6305.

[243] **Tong, K.T., Vinai, R., and Soutsos, M.N.** (2018) Use of Vietnamese rice husk ash for the production of sodium silicate as the activator for alkali-activated binders. *Journal of Cleaner Production*. *201*, 272–286.

[244] **Knight, C.T.G., Balec, R.J., and Kinrade, S.D.** (2007) The Structure of Silicate Anions in Aqueous Alkaline Solutions. *Angewandte Chemie*. *119*, (43), 8296–8300.

[245] **Andersson, K.R., Dent Glasser, L.S., and Smith, D.N.** (1982) Polymerization and Colloid Formation in Silicate Solutions. 115–131.

[246] **Zarzycki, J., Prassas, M., and Phalippou, J.** (1982) Synthesis of glasses from gels: the problem of monolithic gels. *Journal of Materials Science*. *17*, (11), 3371–3379.

[247] **Wijnen, P.W.J.G., Beelen, T.P.M., and van Santen, R.A.** (2005) Silica gels from aqueous silicate solutions: Combined 29Si NMR and small-angle X-ray scattering spectroscopic study. *Colloidal Silica: Fundamentals and Applications*. 597–604.

[248] **Schlomach, J. and Kind, M.** (2004) Investigations on the semi-batch precipitation of silica. *Journal of Colloid and Interface Science*. *277*, (2), 316–326.

[249] **Gorrepati, E.A., Wongthahan, P., Raha, S., and Fogler, H.S.** (2010) Silica precipitation in acidic solutions: Mechanism, pH effect, and salt effect. *Langmuir*. *26*, (13), 10467–10474.

[250] **BaŁdyga, J., Jasińska, M., Jodko, K., and Petelski, P.** (2012) Precipitation of amorphous colloidal silica from aqueous solutions-Aggregation problem. *Chemical Engineering Science*. *77*, 207–216.

[251] **Hessien, M.M., Rashad, M.M., Zaky, R.R., Abdel-Aal, E.A., and El-Barawy, K.A.** (2009) Controlling the synthesis conditions for silica nanosphere from semi-burned rice straw. *Materials Science and Engineering: B*. *162*, (1), 14–21.

[252] **Al-Abboodi, S.M.T., Al-Shaibani, E.J.A., and Alrubai, E.A.** (2020) Preparation and Characterization of Nano silica Prepared by Different Precipitation Methods. *IOP Conference Series: Materials Science and Engineering*. *978*, (1), 0–12.

[253] **Domínguez, J.M., Terrés, E., and Vázquez, A.** (2003) High throughput study on the induction of radial distribution of nanotubes and spherical morphology in silica particles by short-chain polar co-solvents. *Microporous and Mesoporous Materials*. *66*, (2–3), 341–348.

[254] **Godoi, R.H.M., Fernandas, L., Jafelicci, M., Marques, R.C., Varanda, L.C., and Davolos, M.R.** (1999) Investigation of the systems silica and silica containing chromium in alcohol medium. *Journal of Non-Crystalline Solids*. *247*, (1–3), 141–145.

[255] **Jung, C.Y., Kim, J.S., Chang, T.S., Kim, S.T., Lim, H.J., and Koo, S.M.** (2010) One-step synthesis of structurally controlled silicate particles from sodium silicates using a simple precipitation process. *Langmuir*. *26*, (8), 5456–5461.

[256] **Harris, M.T., Brunson, R.R., and Byers, C.H.** (1990) The base-catalyzed hydrolysis and condensation reactions of dilute and concentrated TEOS solutions. *Journal of Non-Crystalline Solids*. *121*, (1–3), 397–403.

[257] **Wen, B., Huo, C., Li, C., and Zhang, L.** (2013) Preparation of the silica micro-spheres by chemical precipitation process. *Advanced Materials Research*. *602–604*, 259–264.

[258] **Kumari, A., Singh, R.K., Kumar, N., Kumari, R., Monalisa, and Sharma, S.** (2023) Green synthesis and physical properties of crystalline silica engineering nanomaterial from rice husk (agriculture waste) at different annealing temperatures for its varied applications. *Journal of the Indian Chemical Society*. *100*, (5), 100982.

[259] **Keiluweit, M., Nico, P.S., Johnson, M., and Kleber, M.** (2010) Dynamic molecular structure of plant biomass-derived black carbon (biochar). *Environmental Science and Technology*. *44*, (4), 1247–1253.

[260] **Bourke, J., Manley-Harris, M., Fushimi, C., Dowaki, K., Nunoura, T., and Antal, M.J.** (2007) Do all carbonized charcoals have the same chemical structure? 2. A model of the chemical structure of carbonized charcoal. *Industrial and Engineering Chemistry Research*. *46*, (18), 5954–5967.

[261] **Ludueña, L., Fasce, D., Alvarez, V.A., and Stefani, P.M.** (2011) Nanocellulose from rice husk following alkaline treatment to remove silica. *BioResources*. *6*, (2), 1440–1453.

[262] **Singh Karam, D., Nagabovanalli, P., Sundara Rajoo, K., Fauziah Ishak, C., Abdu, A., Rosli, Z., et al.** (2022) An overview on the preparation of rice husk biochar, factors affecting its properties, and its agriculture application. *Journal of the Saudi Society of Agricultural Sciences*. *21*, (3), 149–159.

[263] **Collard, F.X. and Blin, J.** (2014) A review on pyrolysis of biomass constituents: Mechanisms and composition of the products obtained from the conversion of cellulose, hemicelluloses and lignin. *Renewable and Sustainable Energy Reviews*. *38*, 594–608.

[264] **Bridgwater, A. V.** (2003) Renewable fuels and chemicals by thermal processing of biomass. *Chemical Engineering Journal*. *91*, (2–3), 87–102.

[265] **Goyal, H.B., Seal, D., and Saxena, R.C.** (2008) Bio-fuels from thermochemical conversion of renewable resources: A review. *Renewable and Sustainable Energy Reviews*. *12*, (2), 504–517.

[266] **Claoston, N., Samsuri, A.W., Ahmad Husni, M.H., and Mohd Amran, M.S.** (2014) Effects of pyrolysis temperature on the physicochemical properties of empty fruit bunch and rice husk biochars. *Waste Management and Research*. *32*, (4), 331–339.

[267] **Hidayat, Rahmat, A., Nissa, R.C., Sukamto, Nuraini, L., Nurtanto, M., et al.** (2023) Analysis of rice husk biochar characteristics under different pyrolysis temperature. *IOP Conference Series: Earth and Environmental Science*. *1201*, (1), 012095.

[268] **Gao, X., Zhang, Y., Xu, F., Yin, Z., Wang, Y., Bao, F., et al.** (2019) Experimental and kinetic studies on the intrinsic reactivities of rice husk char. *Renewable Energy*. *135*, 608–616.

[269] **Morin, M., Pécate, S., Hémati, M., and Kara, Y.** (2016) Pyrolysis of biomass in a batch fluidized bed reactor: Effect of the pyrolysis conditions and the nature of the biomass on the physicochemical properties and the reactivity of char. *Journal of Analytical and Applied Pyrolysis*. *122*, 511–523.

[270] **Phuong, H.T., Uddin, M.A., and Kato, Y.** (2015) Characterization of Biochar from Pyrolysis of Rice Husk and Rice Straw. *Journal of Biobased Materials and Bioenergy*. *9*, (4), 439–446.

[271] **Tsai, W.T., Lee, M.K., and Chang, Y.M.** (2007) Fast pyrolysis of rice husk: Product yields and compositions. *Bioresource Technology*. *98*, (1), 22–28.

[272] **Petreanu, I., Niculescu, V.-C., Enache, S., Iacob, C., and Teodorescu, M.** (2023) Structural Characterization of Silica and Amino-Silica Nanoparticles by Fourier Transform Infrared (FTIR) and Raman Spectroscopy. *Analytical Letters*. *56*, (2), 390–403.

[273] **Sankar, S., Sharma, S.K., Kaur, N., Lee, B., Kim, D.Y., Lee, S., et al.** (2016) Biogenerated silica nanoparticles synthesized from sticky, red, and brown rice husk ashes by a chemical method. *Ceramics International*. *42*, (4), 4875–4885.

[274] **Kim, S., Park, J.Y., Gu, Y.M., Jang, I.-S., Park, H., Oh, K.K., et al.** (2021) Eco-friendly and facile synthesis of size-controlled spherical silica particles from rice husk. *Nanoscale Advances*. *3*, (24), 6965–6973.

[275] **Cui, J., Sun, H., Luo, Z., Sun, J., and Wen, Z.** (2015) Preparation of low surface area SiO2 microsphere from wheat husk ash with a facile precipitation process. *Materials Letters*. *156*, 42–45.

[276] **Wilhelm, S. and Kind, M.** (2015) Influence of pH, temperature and sample size on natural and enforced syneresis of precipitated silica. *Polymers*. *7*, (12), 2504–2521.

[277] **Jiao, M., Liu, K., Shi, Z., and Wang, C.** (2017) SiO_2/Carbon Composite Microspheres with Hollow Core–Shell Structure as a High-Stability Electrode for Lithium-Ion Batteries. *ChemElectroChem*. *4*, (3), 542–549.

[278] **Al Ja'farawy, M.S., Hikmah, D.N., Riyadi, U., Purwanto, A., and Widiyandari, H.** (2021) A Review: The Development of SiO_2/C Anode Materials for Lithium-Ion Batteries. *Journal of Electronic Materials*. *50*, (12), 6667–6687.

[279] **Li, Y., Liu, L., Liu, X., Feng, Y., Yu, L., He, Z., et al.** (2022) Core–shell structured C/SiO_2 composites derived from Si-rich biomass as anode materials for lithium-ion batteries. *Ionics*. *28*, (1), 151–160.

[280] **Sivonxay, E., Aykol, M., and Persson, K.A.** (2020) The lithiation process and Li diffusion in amorphous SiO_2 and Si from first-principles. *Electrochimica Acta*. *331*, 135344.

[281] **Guo, Y., Chen, X., Liu, W., Wang, X., Feng, Y., Li, Y., et al.** (2020) Preparation of Rice Husk-Based C/SiO_2 Composites and Their Performance as Anode Materials in Lithium Ion Batteries. *Journal of Electronic Materials*. *49*, (2), 1081–1089.

[282] **Lee, T., Othman, R., and Yeoh, F.-Y.** (2013) Development of photoluminescent glass derived from rice husk. *Biomass and Bioenergy*. *59*, 380–392.

[283] **Ju, Y., Tang, J.A., Zhu, K., Meng, Y., Wang, C., Chen, G., et al.** (2016) SiO_x/C composite from rice husks as an anode material for lithium-ion batteries. *Electrochimica Acta*. *191*, 411–416.

[284] **Bhagiyalakshmi, M., Yun, L.J., Anuradha, R., and Jang, H.T.** (2010) Synthesis of chloropropylamine grafted mesoporous MCM-41, MCM-48 and SBA-15 from rice husk ash: their application to CO_2 chemisorption. *Journal of Porous Materials*. *17*, (4), 475–484.

[285] **Zhang, H., Yang, Z., Zhang, N., Qiao, K., Liu, Y., He, W., et al.** (2022) Boron-doped rice husk-derived C/SiO_x composites as high-property anode for Li-ion batteries. *Ionics*. *28*, (9), 4159–4167.

[286] **Yu, G., Jing, J., Li, C., Li, Q., Yang, Z., Yao, S., et al.** (2023) A review on recent progress of non-stoichiometric SiO_x anodes based on lithium ion batteries. *Progress in Natural Science: Materials International*. *33*, (1), 47–54.

[287] **Wang, G., Zhang, J., Chang, W., Li, R., Li, Y., and Wang, C.** (2018) Structural features and gasification reactivity of biomass chars pyrolyzed in different atmospheres at high temperature. *Energy*. *147*, 25–35.

[288] **Jo, M., Sim, S., Kim, J., Oh, P., and Son, Y.** (2022) Micron-Sized SiO_x-Graphite Compound as Anode Materials for Commercializable Lithium-Ion Batteries. *Nanomaterials*. *12*, (12),.

[289] **Lee, S.H., Cho, Y., Jeon, Y.P., Chang, Y., Lee, K.S., Hong, D., et al.** (2023) Sustainable eco-friendly sub-micron NaCl crystal powder-assisted method to synthesize SiO_x/C as anode materials originated from rice husk for lithium-ion batteries. *EcoMat*. *5*, (11), 1–17.

[290] **Liang, C., Zhou, L., Zhou, C., Huang, H., Liang, S., Xia, Y., et al.** (2017) Submicron silica as high−capacity lithium storage material with superior cycling performance. *Materials Research Bulletin*. *96*, 347–353.

[291] **Liu, L. and Zhu, M.** (2014) Modeling of SEI Layer Growth and Electrochemical Impedance Spectroscopy Response using a Thermal-Electrochemical Model of Li-ion Batteries. *ECS Transactions*. *61*, (27), 43–61.

[292] **Min, K., Kim, K., An, H., Go, Y., Lee, Y., Lim, D., et al.** (2022) Yolk-shell-structured SiO_2@N, P co-doped carbon spheres as highly stable anode materials for lithium ion batteries. *Journal of Power Sources*. *543*,.

[293] **Sui, D., Yao, M., Si, L., Yan, K., Shi, J., Wang, J., et al.** (2023) Biomass-derived carbon coated SiO_2 nanotubes as superior anode for lithium-ion batteries. *Carbon*. *205*, 510–518.

[294] **Orozco-Gallo, D.C., Vásquez-Arroyave, F.A., and Calderón-Gutierréz, J.A.** (2023) Carbon-slurry optimization for lithium-ion batteries customization. *Electrochimica Acta*. *467*, (June),.

[295] **Wang, Z., Deng, R., Wang, Y., and Pan, F.** (2024) Comparison of Construction Strategies of Solid Electrolyte Interface (SEI) in Li Battery and Mg Battery-A Review. *Molecules (Basel, Switzerland)*. *29*, (19),.

[296] **Renman, V., Blanco, M.V., Norberg, A.N., Vullum-Bruer, F., and Svensson, A.M.** (2021) Electrochemical activation of a diatom-derived SiO_2/C composite anode and its implementation in a lithium ion battery. *Solid State Ionics*. *371*, (September 2020), 115766.

[297] **Liu, X., Gao, M., Zhao, J., Sun, X., Li, Z., Li, Q., et al.** (2021) Effects of charging protocols on the cycling performance for high-energy lithium-ion batteries using a graphite-SiO_x composite anode and Li-rich layered oxide cathode. *Journal of Power Sources*. *495*, (November 2020), 229793.

[298] **Li, R., Cui, B., Zhou, Q., Mu, X., Gao, Y., Yin, G., et al.** (2023) Stabilizing electrode-electrolyte interface for high-performance SiO_x anode by dual electrolyte additive. *Journal of Energy Chemistry*. *86*, 32–40.

[299] **Jung, R., Metzger, M., Haering, D., Solchenbach, S., Marino, C., Tsiouvaras, N., et al.** (2016) Consumption of Fluoroethylene Carbonate (FEC) on Si-C Composite Electrodes for Li-Ion Batteries. *Journal of The Electrochemical Society*. *163*, (8), A1705–A1716.

[300] **Shin, H., Park, J., Sastry, A.M., and Lu, W.** (2015) Effects of Fluoroethylene Carbonate (FEC) on Anode and Cathode Interfaces at Elevated Temperatures. *Journal of The Electrochemical Society*. *162*, (9), A1683–A1692.

[301] **Jaumann, T., Balach, J., Langklotz, U., Sauchuk, V., Fritsch, M., Michaelis, A., et al.** (2017) Lifetime vs. rate capability: Understanding the role of FEC and VC in high-energy Li-ion batteries with nano-silicon anodes. *Energy Storage Materials*. *6*, (August 2016), 26–35.

CURRICULUM VITAE

Name Surname **:** İpek TUNÇ

EDUCATION :

- **B.Sc.** **:** 2016, Yıldız Technical University, Faculty of Chemical Metallurgical Engineering, Metallurgical and Materials Engineering Department
- **M.Sc.** **:** 2017, Yıldız Technical University, Faculty of Chemical Metallurgical Engineering, Metallurgical and Materials Engineering Department

PROFESSIONAL EXPERIENCE AND REWARDS:

April 2017 – current: Research Assistant at ITU, Faculty of Chemical Metallurgical Engineering, Metallurgical and Materials Engineering Department

PUBLICATIONS, PRESENTATIONS AND PATENTS ON THE THESIS:

- **Tunc, I.**, Karahan, B. D., Keles, O. 2024. Biomass-derived SiO_x/C nanocomposite anode synthesis by induction heating for lithium ion battery, *Applied Physics A*, 13, 677.
- **Tunc, I.**, Keles, O. 2023: Rice Husk-Derived Silica Anodes for Lithium-Ion Batteries. 3rd International Materials Technologies and Metallurgy Conference, October 11-13, 2023 Istanbul, Türkiye.

OTHER PUBLICATIONS, PRESENTATIONS AND PATENTS:

- **Tunc, I.,** Eroglu, O., Bulut, D. M., Ozen, S., Bayram, E., Yilmaz, C. H., Karatepe Yavuz, N., 2024. Lithium-ion Batteries in Electric Vehicles, Anode Materials - Book chapter, OTEP, ISBN: 978-625-00-7899-0.

- Tezgel, Y., **Tunc, I.,** Kaya, O., Yesilcubuk, A., Mutlu, M., Keles, O. 2021. Investigating the Tribological Behavior of Aluminum Alloys Produced by a Novel Method Gas Induced Semi-Solid (GISS) Casting Technology, *International Journal of Metalcasting*, 16, 458-472.
- **Tunc, I.,** Karahan, B. D., Keles, O. 2020. A Study on the Corrosion Behaviour of Clad Aluminum Alloys in Different Media, *Journal of Materials Engineering and Performance*, 29, 4506-4514.
- Senyurt, G. Z., Burumlu, Y., Yılmaz, M., **Tunc, I.**, Karahan, B. D., Keles, O. 2023: Cobalt free cathodes for high performance lithium-ion batteries. 3rd International Materials Technologies and Metallurgy Conference, October 11-13, 2023 Istanbul, Türkiye.
- Sert, T., Afsin, P., **Tunc, I.,** Akyil, C., Karahan, B. D., Mutlu, M., Ozcan, O., Kurual, I., Keles, O. 2023: Corrosion Behavior of Trivalent Chromium Process (TCP) Coating on Modified Die Casting Alloys. 11th International Aluminum Symposium, October 12-13, 2023 Istanbul, Türkiye.
- Sarikas, E., **Tunc, I.,** Karahan, B. D., Keles**,** O. 2022: High Capacity Iron Oxide Anode Active Materials from Na-based Rinsing Waters for Lithium Ion Batteries. International Conference on Advanced Lithium Batteries for Automobile Applications (ABAA-13), October 16-19, 2022 Marrakesh, Morocco.
- Sarikas, E., **Tunc, I.,** Keles**,** O. 2022: Investigating the Electrochemical Performance of Double Shell Cathode Active Materials for Lithium Ion Batteries. 21th International Metallurgy and Materials Conference (IMMC'22), October 6-8, 2022 Istanbul, Türkiye.
- **Tunc, I.,** Keles**,** O. 2019: Anodization Behaviour of Clad Aluminum. 28th Annual Anodizing Conference & Exposition, October 1-3, 2019 Houston, Texas, USA.
- Sivlin, D., **Tunc, I.,** Mutlu, M., Polat Karahan, B. D., Keles, O. 2018: Anodization of EN 46000 Alloy Produced with and without Gas Induced Semi-Solid Method. 27th Annual Anodizing Conference & Exposition, October 2-4, 2018 Minneapollis, Minnesota, USA.
- **Tunc, I.,** Ersundu, A. E., Aydin, S., Celikbilek Ersundu, M., 2017: Synthesis and Growth Kinetic Studies of ZnTe Quantum Dot-doped Glass Nanocomposites. 12th International Symposium on Crystallization in Glasses and Liquids, September 10-13, 2017 Segovia, Spain.